

# Development of Novel Standardized Structural Timber Elements Using Wood-Wood Connections

Présentée le 11 septembre 2020

à la Faculté de l'environnement naturel, architectural et construit  
Laboratoire de construction en bois  
Programme doctoral en génie civil et environnement

pour l'obtention du grade de Docteur ès Sciences

par

**Julien GAMERRO**

Acceptée sur proposition du jury

Prof. D. Lignos, président du jury  
Prof. Y. Weinand, Dr J.-F. Bocquet, directeurs de thèse  
Dr J. Gattas, rapporteur  
Dr N. Sauvat, rapporteur  
Prof. C. Fivet, rapporteur



Science sans conscience n'est que ruine de l'âme.  
— Rabelais

*To the memory of my father, Denis*

*To my mother, Laurence*

*With love and eternal appreciation*





# Acknowledgments

First, I would like to thank my thesis director, Prof. Dr. Yves Weinand, who has given me the opportunity to work in such a stimulating and inspiring environment within the Laboratory for Timber Constructions IBOIS at EPFL and for his trust throughout these four years. I would also like to express my deepest gratitude to my thesis co-supervisor, Dr. Jean-François Bocquet, for his unconditional support and patience, his invaluable guidance, and tireless discussions on timber engineering and life.

I extend my sincere appreciation to the president of the thesis jury, Prof. Dr. Dimitrios Lignos, and to the jury members, Prof. Dr. Corentin Fivet, Dr. Joe Gattas, and Dr. Nicolas Sauvat, for their commitment to review this research work and their insightful feedback and comments to improve it.

Many thanks also to all my colleagues, co-authors and friends from IBOIS with whom I had the pleasure of discussing research, exchanging ideas, and sharing wonderful times in Lausanne: Andrea, Anh Chi, Aryan, Christopher, Francine, Ingebrigt, Martin, Nicolas, Petras, and Stéphane. Furthermore, Anh Chi deserves my special thanks for kindly proofreading the entire document. Special thanks also to Martin who spent more than two years collaborating with me on many topics, always in a very friendly manner.

I spent countless hours in the experimental hall and I would like to thank all the technical staff, including Armin, François, Frédéric, Gérald, Gilles, Serge, and Sylvain, who helped me to set up all my tests and contributed greatly to this work. A particular thanks goes to François for his vast knowledge of the carpentry trade and our friendly conversations.

Finally, I wish to express my deepest gratitude to my loved ones for their great support and love: especially to my mother, Laurence; my brother, Rémi; and my grandparents, Françoise, Michel, and Yvette. There are no words strong enough to thank my mother for her unconditional love and encouragement throughout my life, in both good and bad times. I owe her everything I am today or ever hope to be one day. This work would not have been possible without her and my brother, who always believed in me.

*Lausanne, July 16, 2020*

J. G.



# Abstract

Traditional wood-wood connections, widely used in the past, have been progressively replaced by steel fasteners and bonding processes in modern timber constructions with the standardization of the industry. However, the emergence of digital fabrication and innovative engineered timber products have offered new design possibilities for wood-wood connections, particularly for timber plate structures. The typical design-to-production workflow has evolved considerably over the last few decades, such that a large number of connections with various geometries can now be easily produced. These connections have become a cost-competitive alternative for the edgewise connection of thin timber panels. Numerous research studies on this topic have led to the realization of prototypes and pavilions, but this has mainly occurred for complex geometrical shapes. Several challenges remain in order to broaden the use of this specific joining technique into common timber construction practice: (i) prove the applicability at the building scale, (ii) propose a standardized construction system, (iii) develop a convenient calculation model for practice, and (iv) investigate the mechanical behavior of wood-wood connections.

The first building implementation of digitally produced through-tenon connections for a folded-plate structure is presented in this work. Specific computational tools for the design and manufacture of more than 300 different plates were efficiently applied in a multi-stakeholder project environment. In addition to the laminated lumber veneer panels generally employed in previous research, cross-laminated timber panels were investigated for the first time, and the potential of such connections was demonstrated for different engineered timber products. Moreover, this work demonstrated the feasibility of this construction system at the building scale.

For a more resilient and locally distributed construction process, a standardized system using through-tenon connections and commonly available small panels was developed to reconstitute basic housing components, such as slab and roof elements. Based on a case-study with industry partners, the fabrication and assembly processes were validated with prototypes made of oriented strand board. Their structural performance was investigated by means of a numerical model and a comparison with glued and nailed assemblies. The results showed that through-tenon connections are a viable alternative to commonly used mechanical fasteners.

So far, the structural analysis of such construction systems has been mainly achieved with sophisticated, computationally expensive, and time-consuming finite element models, not in

## Abstract

---

line with the simplicity of basic housing elements. A convenient calculation model for practice, which can capture the semi-rigid behavior of the connections and predict the effective bending stiffness, was thus introduced and subjected to large-scale bending as well as vibration tests. The proposed model was in good agreement with the experimental results, highlighting the importance of the connection behavior.

The in-plane behavior of through-tenon connections for several timber panel materials was characterized through an experimental campaign to determine the load-carrying capacity and slip modulus required for calculation models. Based on the test results, existing guidelines were evaluated to safely apply these connections in structural elements while a finite element model was developed to approximate their performance. This work constitutes a firm basis for the optimization of design guidelines and the creation of an extensive database on digitally produced wood-wood connections.

Finally, this thesis provides a convenient design framework for the newly developed standardized timber construction system and a solid foundation for research into digitally produced wood-wood connections.

**Keywords:** *timber construction, wood-wood connections, digital fabrication, design for manufacture and assembly, structural design framework, calculation model, semi-rigidity, experimental research, shear strength, compression strength*

# Résumé

Les assemblages bois traditionnels couramment utilisés dans le passé ont progressivement été remplacés par des fixations métalliques et des procédés de collage du fait de la standardisation de l'industrie. Toutefois, l'émergence de la conception et de la fabrication assistées par ordinateur ainsi que l'évolution des matériaux d'ingénierie bois ont engendré de nouvelles possibilités pour ces assemblages, en particulier pour les structures principalement composées de panneaux. Au cours des dernières décennies, le processus classique de la conception à la production a considérablement évolué, de sorte que de nombreuses connexions avec un large éventail de géométries possibles peuvent désormais être facilement réalisées. Ces assemblages sont donc devenus une alternative concurrentielle dans certains domaines comme dans l'assemblage de panneaux de bois fins. De nombreuses recherches sur ce sujet ont mené à la réalisation de prototypes et de pavillons, mais principalement pour des structures avec des formes géométriques complexes. Malgré ces avancées, plusieurs défis restent à relever pour étendre l'utilisation de cette technique d'assemblage à la pratique courante pour les constructions bois : (i) démontrer son applicabilité à l'échelle d'un bâtiment, (ii) proposer un système de construction standardisé, (iii) développer un modèle de calcul adéquat pour la pratique et enfin, (iv) étudier le comportement mécanique des assemblages bois-bois.

Ce travail présente la première réalisation d'un bâtiment utilisant des tenons traversants produits numériquement pour une structure plissée en panneaux de bois. Des outils informatiques spécifiques pour la conception et la fabrication de plus de 300 plaques différentes ont été utilisés efficacement dans un environnement de projet regroupant de nombreux acteurs. En plus des panneaux lamibois généralement utilisés dans les recherches précédentes, des panneaux en bois lamellé croisé ont été introduits pour la première fois, permettant de démontrer le potentiel de ces connexions pour différents produits d'ingénierie bois. De plus, ce travail a permis de prouver la faisabilité de ce système de construction utilisant des connexions bois-bois à l'échelle d'un bâtiment.

Afin d'obtenir un processus de construction plus résilient et applicable facilement à l'échelle locale, un système standardisé utilisant des tenons traversants et des panneaux de petite taille a été développé afin de reconstituer les éléments basiques de construction tels que les éléments de dalles et de toits. Selon une étude de cas menée en collaboration avec des partenaires industriels, des prototypes constitués de panneaux de particules orientées ont permis de valider le procédé de fabrication et d'assemblage. Leurs performances structurelles ont été

étudiées au moyen d'un modèle numérique et d'une comparaison avec des assemblages collés et cloués. Les résultats ont montré que les assemblages par tenon traversant constituent une alternative viable aux fixations mécaniques couramment utilisées.

Jusqu'à présent, l'analyse structurelle de ce type de système constructif a été principalement réalisée à l'aide de modèles éléments finis sophistiqués, complexes à modéliser et coûteux en temps de calcul. Par conséquent, ils sont peu adaptés pour la modélisation d'éléments basiques de construction. Un modèle de calcul plus adapté pouvant traduire le comportement semi-rigide des connexions bois-bois a donc été développé. Ce modèle a été évalué avec des tests de flexion et de vibration sur des éléments de grandes tailles. Le modèle a finalement démontré être en adéquation avec les résultats expérimentaux, soulignant l'importance du comportement des connexions.

Le comportement des tenons traversants a été caractérisé pour différents types de panneau bois. Une campagne expérimentale a permis de déterminer la capacité de résistance admissible ainsi que le module de glissement nécessaire aux modèles de calcul. À partir des résultats obtenus, les normes existantes ont été évaluées pour appliquer en toute sécurité ces connexions dans les éléments structurels. De plus, un modèle éléments finis a été développé pour estimer leurs performances. Ce travail constitue un point de départ pour l'optimisation des normes existantes et pour la création d'une base de données sur les propriétés mécaniques des connexions bois-bois.

Enfin, cette thèse fournit un cadre de conception pratique pour le système de construction en bois nouvellement développé ainsi qu'une base solide pour les recherches sur les connexions bois-bois produites numériquement.

**Mots clés :** *construction bois, assemblage bois-bois, fabrication numérique, conception pour la fabrication et l'assemblage, cadre de conception, modèle de calcul, semi-rigidité, tests, cisaillement, compression*

# Contents

<b>Acknowledgments</b>	<b>v</b>
<b>Abstract (English/Français)</b>	<b>vii</b>
<b>List of figures</b>	<b>xv</b>
<b>List of tables</b>	<b>xxiii</b>
<b>List of abbreviations</b>	<b>xxv</b>
<b>1 Introduction</b>	<b>1</b>
1.1 Research context . . . . .	1
1.1.1 Construction and sustainability . . . . .	1
1.1.2 Digital fabrication and timber construction . . . . .	2
1.1.3 Wood-wood connections for timber plate structures . . . . .	3
1.1.4 Standardized building components . . . . .	8
1.2 Research motivation . . . . .	9
1.2.1 Problem statement . . . . .	9
1.2.2 Approach and objectives . . . . .	10
1.3 List of publications . . . . .	11
<b>2 Large-scale building implementation: the Vidy theater</b>	<b>13</b>
2.1 Introduction . . . . .	13
2.2 Construction system . . . . .	15
2.3 Automatic design-to-production workflow . . . . .	17
2.4 Experimental investigations of single-layered connections . . . . .	20
2.4.1 Methods . . . . .	20
2.4.2 Samples . . . . .	20
2.4.3 Results of the CLT panel (1) . . . . .	22
2.4.4 Results of the CLT panel (2) . . . . .	24
2.4.5 Comparative analysis of materials . . . . .	25
2.5 Experimental investigations of double-layered connections . . . . .	28
2.5.1 Methods . . . . .	28
2.5.2 Samples . . . . .	28
2.5.3 Results and discussions . . . . .	29

2.6	Conclusions . . . . .	31
<b>3</b>	<b>Standardized construction system: development and potential</b>	<b>33</b>
3.1	Introduction . . . . .	33
3.2	State-of-the-art . . . . .	34
3.3	Proposal of a standardized construction system . . . . .	36
3.3.1	Scope . . . . .	37
3.3.2	The construction system . . . . .	38
3.4	Case-study . . . . .	42
3.5	Numerical model . . . . .	44
3.5.1	Modeling approach . . . . .	45
3.5.2	Connection parameters . . . . .	48
3.6	Results and discussions . . . . .	52
3.7	Conclusions . . . . .	55
<b>4</b>	<b>Simplified calculation method: development and validation</b>	<b>57</b>
4.1	Introduction . . . . .	57
4.2	State-of-the-art . . . . .	58
4.2.1	Analytical theories . . . . .	59
4.2.2	Numerical models . . . . .	60
4.3	Materials and experimental methods . . . . .	61
4.3.1	Large-scale specimens . . . . .	61
4.3.2	Methods . . . . .	62
4.4	Simplified calculation model . . . . .	65
4.4.1	Modeling approach . . . . .	66
4.4.2	Connection parameters . . . . .	68
4.5	Results and discussion . . . . .	70
4.5.1	Effective bending stiffness . . . . .	70
4.5.2	Panel discontinuities . . . . .	72
4.5.3	Failure mode in tension . . . . .	74
4.6	Conclusions . . . . .	76
<b>5</b>	<b>Mechanical characterization of through-tenon joints</b>	<b>79</b>
5.1	Introduction . . . . .	79
5.2	State-of-the-art . . . . .	82
5.2.1	Design guidelines for wood-wood connections . . . . .	82
5.2.2	Experimental protocols for the shear behavior of timber . . . . .	83
5.3	Materials . . . . .	85
5.3.1	General . . . . .	85
5.3.2	Moisture content and properties . . . . .	86
5.3.3	Compression strength characterization . . . . .	86
5.4	Experimental methods . . . . .	88
5.4.1	Compression tests . . . . .	88



5.4.2	Shear tests . . . . .	90
5.4.3	Loading procedure . . . . .	93
5.5	Compression tests . . . . .	94
5.6	Shear tests . . . . .	97
5.6.1	Results . . . . .	97
5.6.2	Results vs. numerical model . . . . .	106
5.7	Design guidelines . . . . .	118
5.8	Conclusions . . . . .	121
<b>6</b>	<b>Conclusions and outlook</b>	<b>123</b>
6.1	Conclusions . . . . .	123
6.2	Outlook . . . . .	127
	<b>Funding</b>	<b>129</b>
<b>A</b>	<b>Appendix of Chapter 3</b>	<b>131</b>
A.1	Detailed geometry of roof element for the case-study . . . . .	132
A.2	Experimental curves of the push-out tests performed on OSB TT joints for the specific case-study . . . . .	133
<b>B</b>	<b>Appendix of Chapter 4</b>	<b>135</b>
B.1	Detailed plans of large-scale specimens . . . . .	136
B.2	Gamma method calculations . . . . .	138
B.3	Creep behavior . . . . .	140
B.3.1	Introduction . . . . .	140
B.3.2	Material and methods . . . . .	142
B.3.3	Loading procedure . . . . .	144
B.3.4	Calculation models . . . . .	145
B.3.5	Results . . . . .	145
B.3.6	Conclusions . . . . .	148
<b>C</b>	<b>Appendix of Chapter 5</b>	<b>149</b>
C.1	Material compression tests . . . . .	150
C.1.1	Method and specimens . . . . .	150
C.1.2	Methodology for calculating the 5% fractile values . . . . .	151
C.2	Statistical distribution of compression tests of TT connections . . . . .	152
C.3	Statistical distribution of shear tests of TT connections . . . . .	153
C.4	Numerical model for TT connections . . . . .	155
C.4.1	Material model . . . . .	155
C.4.2	Continuum damage model . . . . .	155
C.4.3	Failure modes . . . . .	157
C.4.4	Damage evolution . . . . .	159
C.4.5	Subroutine algorithm . . . . .	160
C.4.6	Contact modeling . . . . .	162

## Contents

---

C.4.7 Mesh . . . . .	163
C.4.8 Material properties . . . . .	165
<b>Bibliography</b>	<b>169</b>
<b>Curriculum Vitae</b>	<b>185</b>

# List of figures

<b>1</b>	<b>Introduction</b>	<b>1</b>
1.1	(left) Global urban population data according to the HYDE database / (right) Carbon dioxide from firn and ice-core records (Law Dome, Antarctica and Cape Grim, Australia). Based on [151]. . . . .	1
1.2	Development of manufacturing techniques over the history of humankind. Based on [137]. . . . .	3
1.3	Digitally produced wood-wood connections: (a) Multiple-tab-and-slot joint (MTSJ) / (b) Through-tenon (TT). Based on [173]. . . . .	4
1.4	Evolution of IBOIS prototypes: (a) Single-layered origami prototype using MTSJ [123] / (b) Double-layered prototype using snap-fit joints [121] / (c) Double-layered Miura-Ori pattern prototype using TT [126] / (d) Double-layered free-form shell prototype using TT [120]. . . . .	5
1.5	Pavilions: (a) Curved CLT pavilion, Academy of Architecture in Mendrisio, Switzerland, 2013 [122] / (b) ICD/ITKE Research Pavilion, Stuttgart, Germany, 2011 [83, 84, 145] / (c) Landesgartenschau Exhibition Hall, Schwäbisch Gmünd, Germany, 2014 [81, 88]. . . . .	6
1.6	Principle of deformation for the different basic assemblies used in modern timber structures. Based on [162]. . . . .	7
1.7	View of a prefabricated roof element made with laminated-veneer lumber by the company Metsä Wood: Kerto Ripa®. . . . .	8
<b>2</b>	<b>Large-scale building implementation: the Vidy theater</b>	<b>13</b>
2.1	Saint-Loup chapel, Pompaples, Switzerland 2008: (a) Exterior view during construction with metal fasteners / (b) Final exterior view of the building. <i>[Photograph credit: IBOIS, Fred Hatt]</i> . . . . .	14
2.2	Vidy theater pavilion, Lausanne, Switzerland, 2017: (a) Exterior view / (b) Interior view during construction. <i>[Photograph credit: Ilka Kramer Photography]</i> . . . .	15
2.3	Assembly process of a building segment. Steps 1 to 4: prefabrication process of the roof element. Steps 5 to 6: onsite assembly of the wall and roof elements to obtain a complete building segment. . . . .	16

## List of figures

---

2.4	Photographs of the construction system process: (a) Prefabrication of a roof element / (b) Transport of a roof element / (c) Onsite assembly of the roof and wall elements. . . . .	16
2.5	(a) Grasshopper® interface of the CAD plugin (DLFP) for the 3D plate geometry and 2D plate matrix for fabrication / (b) Base geometry polygon mesh (DCEL mesh), plate ID numbers are visualized in blue color, edge ID numbers are shown in black color. . . . .	18
2.6	Double-layered folded-plate assembly principle, and tool alignment angle $\beta$ results from the fold angles deviation from 90°. Very obtuse or acute fold angles require a large inclination of the tool during cutting. . . . .	19
2.7	Automatically generated 2D matrix of 308 individually shaped plates. . . . .	19
2.8	Rotational setup for single-layered TT connections: (1) inclinometers, (2) lever arm, (3) four load cells, (4) wall panel, and (5) roof panel. . . . .	20
2.9	Sample geometries for single-layered TT connections: (a) Axonometry of the different samples / (b) Grain orientation of the samples / (c) Lay-up of the different panels. . . . .	21
2.10	(a) Mechanical behavior of the 40-mm CLT single-layered TT joint in rotation / (b) Results for samples without tenon inclination / (c) Results for samples with tenon inclination / (d) Elastic stiffness for all samples (10 to 40% of the ultimate moment). . . . .	22
2.11	Failure modes of the 40-mm CLT joint in rotation. . . . .	23
2.12	(a) Mechanical behavior of the 45 mm CLT single-layered TT joint in rotation / (b) Results for samples without tenon inclination / (c) Results for samples with tenon inclination / (d) Elastic stiffness for all the samples (10 to 40% of the ultimate moment). . . . .	24
2.13	Failure modes of the 45 mm CLT joint in rotation. . . . .	25
2.14	Average moment-rotation curves per material type for single-layered TT joint in rotation (no screws or tenon inclination). . . . .	27
2.15	Failure mode of the 39-mm spruce LVL joint in rotation. . . . .	27
2.16	(a) Rotational setup for double-layered TT connections: (1) load cell and hydraulic jack, (2) displacement sensors, (3) roof layers, (4) four bolts Ø24 mm, and (5) wall layers / (b) Double-layered samples: (6) location of screws. . . . .	28
2.17	Finite element model representation with the most loaded connection in rotation. . . . .	29
2.18	Failure mode of a double-layered joint in rotation. . . . .	30
2.19	Moment-rotation curves per sample type for the double-layered joints. . . . .	30
<b>3</b>	<b>Standardized construction system: development and potential</b>	<b>33</b>
3.1	DfMA product-based approach: comparison of the construction with car and furniture industries. Based on [155]. . . . .	34
3.2	Construction methods: (a) Off-site / (b) Prefabricated panel / (c) Mass panel / (d) Flat-pack. Based on [155]. . . . .	35

3.3	Flat-pack system: (a) 3D structure / (b) Part of the 3D structure / (c) Decomposition of the 3D element into standard panels / (d) Panels and cuts needed to reconstitute the structural element. Based on [133]. . . . .	35
3.4	(a) WikiHouse [165] / (b) Wood Frame Grammar system [133] / (c) X-Frame system [168] / (d) Sim[PLY] system [149] / (e) Facit Homes system [40]. . . . .	36
3.5	Production tools at IBOIS / (a) five-axis CNC machine / (b) Zoom on the cutting tool during the machining process / (c) six-axis robot when manipulating a panel.	37
3.6	Engineered timber products. Based on [112]. . . . .	37
3.7	Construction system: (1) top flange exterior layer, (2) top flange interior layer, (3) through-tenon connection, (4) transversal beam, (5) web first layer, (6) web second layer, (7) longitudinal connection for web, (8) bottom flange interior layer, (9) bottom flange exterior layer, (10) discontinuities between flanges, and (11) discontinuities between webs. . . . .	38
3.8	Through-tenon joint parameters: (a) Effective tenon length as function of notch position (front view) / (b) Effective mortise length as function of notch position (top view) / (c) Possible insertion angles (front view and side view for c.3) / (d) Bottom joint for tensile forces (side view). . . . .	39
3.9	Assembly sequence for bottom TT joints. . . . .	41
3.10	Longitudinal connections for web: (a) Finger joint / (b) Dovetail joint / (c) Butterfly spline / (d) Round joint / (e) Dumb-bell spline. . . . .	41
3.11	MOBIC SA industrial-hall project. . . . .	43
3.12	Prefabrication at MOBIC SA: (a) OSB prefabricated element during fabrication / (b) Robotic line equipped with special tools for OSB panels. <i>[Photograph credit: Cedric Moutschen, MOBIC SA]</i> . . . . .	43
3.13	Automatic pipelines from CAD to FE analysis software packages. . . . .	44
3.14	Simplified shell geometry the FE analysis: (a) Exploded view of the studied roof element / (b) Detail of the rigid connection between transversal and longitudinal beams / (c) Model representation of the two longitudinal beam layers as one shell element / (d) Model representation of the two flange layers as one shell element. The red lines represent the shell partition for the connections. . . . .	46
3.15	Generation of the simplified geometry for the FE analysis software. . . . .	48
3.16	Model representation in the FE analysis software Abaqus <sup>TM</sup> . . . . .	48
3.17	Sample geometry: (a) Axonometry / (b) Side view / (c) Top view. . . . .	49
3.18	Experimental Setup: (a) Axonometry view / (b) Front view / (c) Side view. . . . .	50
3.19	Histogram of the average result per sample for the maximum load ( $F_{max,sample}$ ) and the experimental stiffness ( $K_{y,sample}$ ). . . . .	51
3.20	Vertical displacement of the element configuration with a web thickness of 18 mm and TT connections. . . . .	53

#### 4 Simplified calculation method: development and validation 57

## List of figures

4.1	Deflection and bending stress distribution of an interconnected timber element with multiple rectangular cross-sections: (A) using rigid connections, (B) using semi-rigid connections, and (C) without connections. Reproduced from [10]. . . . .	58
4.2	Interconnected beam with three elements according to the gamma method. Reproduced from [10]. . . . .	60
4.3	FE model: (a) Timber plates connected by TT joints / (b) Plate as shell element / (c) Connection as strip element / (d) Connection as spring element. Reproduced from [153]. . . . .	61
4.4	Large-scale specimens produced in the laboratory: (1) top flange exterior layer, (2) top flange interior layer, (3) transversal beam, (4) web double-layered, and (5) discontinuities along the length. . . . .	62
4.5	Four-point bending test setup for large-scale specimens: (a) Photograph of the setup during a test / (b) Technical drawing, axonometry / (c) Side view / (d) Front view. . . . .	64
4.6	Vibration test on one specimen: (a) acceleration at mid-span over time / (b) Frequency spectrum of the acceleration. . . . .	65
4.7	(a) Representation of the proposed calculation model (black lines) for the I-beam using TT connections (3D gray solid) / (b) Axonometry of one TT joint / (c) Modeling of this joint with beam elements and springs. . . . .	67
4.8	(a) Axonometry of the experimental setup for TT joints / (b) Side view / (c) Photograph of the experimental setup with LVDTs. . . . .	68
4.9	Experimental curves for the specific TT connections made of spruce LVL and OSB. . . . .	69
4.10	Deflection-load curves at mid-span for tests and calculation models. . . . .	72
4.11	Displacement comparison between the tests and SR model caused by flange discontinuities: (a) DIC 4 area, near support of the element / (b) DIC 2 area, middle of the element / (c) Average of DIC 1 and 3 areas, under hydraulic jacks. . . . .	73
4.12	Tensile failure profile of OSB bottom flange panels. . . . .	75
<b>5</b>	<b>Mechanical characterization of through-tenon</b>	<b>79</b>
5.1	Geometry and parameters of a TT connection: (a) Axonometry of a single-layered connection / (b) Axonometry of a double-layered connection / (c) Side view of a connection. . . . .	80
5.2	Possible failure modes of a TT connection: (a) Axonometry of a TT joint loaded in its length direction / (b) Shear failure area in tenon part / (c) Compression failure area in tenon part / (d) Shear failure area in mortise part / (e) Compression failure area in mortise part. . . . .	81
5.3	Failure modes studied: (a) Shear failure in tenon part / (b) Compression failure in tenon part / (c) Compression failure in mortise part / (d) Expected compression spreading in tenon part. . . . .	83
5.4	Shear experimental setup for timber: (a) EN 408 [37] / (b) EN 16351 Annex E3.3 [30] / (c) EN 16351 Annex D [30] / (d) EN 789 [38] / (e) NF B51-032 [99]. . . . .	84

5.5	Materials used for the experimental investigation on TT connections: (1) OSB type 3 25 mm / (1') OSB type 3 18 mm / (2) Spruce LVL 21 mm / (3) Spruce LVL 39 mm / (4) Beech LVL 40 mm / (5) Spruce MSW 27 mm. . . . .	85
5.6	Compression experimental setup for TT connections: (a) Side view: (8) two LVDTs sensors and (9) steel plate 10 mm / (b) Technical axonometry: (1) tenon part of the specimen, (2) mortise part of the specimen, (3) lateral restraints, (4) support plate, (5) support plate, (6) steel plate 10 mm, and (7) bolt $\varnothing 24$ mm / (c) Specimen: $d$ is the measured area. . . . .	88
5.7	TT compression specimens: (a) Front view: (1) tenon part and (2) mortise part / (b) Front view with only (1), the gray part represents the TT connection / (c) Side view / (d) Side view with only (2). . . . .	90
5.8	Side view of the shear experimental setup for TT connections: (a) Photograph / (b) Technical drawing: (1) steel plate 40 mm, (2) bolt $\varnothing 24$ mm, (3) steel plate 15 mm, (4) tenon part, (5) mortise part, (6) steel plate 5 mm, (7) beech LVL 40 mm, (8) steel plate 20 mm, (9) bolt $\varnothing 12$ mm, (10) two Teflon plates, and (11) steel bracket 20 mm with 8 bolts $\varnothing 12$ mm / (c) Schematic drawing: (12) two LVDTs sensors. . . . .	91
5.9	TT shear specimens: (a) Axonometry of single-layered type / (b) Axonometry of double-layered type / (b) Front view / (c) Side view. . . . .	92
5.10	(a) Loading procedure / (b) Idealized load-deformation curve and measurements according to EN 26891 [35]. . . . .	93
5.11	Load-displacement curves of all specimens for compression tests: (a) EM1 / (b) EM2 / (c) EM3 / (d) EM4 / (e) EM5. . . . .	96
5.12	Failure pictures of all TT specimens in compression: (a) EM1 / (b) EM2 / (c) EM3 / (d) EM4 / (e) EM5. . . . .	96
5.13	Load-displacement curves: (a) T1-50 / (b) T1-65 / (c) T1-80. . . . .	98
5.14	Failure pictures of T1 specimens: (a) Front view of T1-50 / (b) Side view of T1-50 / (c) Front view of T1-80 / (d) Side view of T1-80. . . . .	99
5.15	Failure pictures of T2 specimens: (a) Axonometry / (b) Front view T2-50 / (c) Front view T2-100. . . . .	99
5.16	Load-displacement curves: (a) T2-50 / (b) T2-100 / (c) T2-150. . . . .	100
5.17	Load-displacement curves: (a) T3-50 / (b) T3-100 / (c) T3-150. . . . .	101
5.18	Failure pictures of T3 specimens: (a) Axonometry side 1 / (b) Axonometry side 2 / (c) Front view. . . . .	102
5.19	Load-displacement curves: (a) T4-50 / (b) T4-100 / (c) T4-150. . . . .	102
5.20	Failure pictures of T4 specimens: (a) Side view / (b) Axonometry / (c) Front view. . . . .	103
5.21	Load-displacement curves: (a) T5-50 / (b) T5-100 / (c) T5-150. . . . .	104
5.22	Failure pictures of T5 specimens: (a) Axonometry / (b) Side view 1 / (c) Side view 2. . . . .	105
5.23	(a) Elastic-brittle behavior / (b) low-ductility behavior. . . . .	106
5.24	(a) General shape of the load-displacement curves / (b) Tiny asperities at the surface of the faces in contact that are crushed during the first loading. . . . .	107

## List of figures

---

5.25	Load-displacement curves vs. model: (a) T1-50 / (b) T1-65 / (c) T1-80. . . . .	108
5.26	Shear stress distribution along the tenon for T1 specimens. . . . .	109
5.27	Load-displacement curves vs. model: (a) T2-50 / (b) T2-100 / (c) T2-150. . . . .	110
5.28	Shear stress distribution along the tenon for T2-150 specimens. . . . .	110
5.29	Load-displacement curves vs. model: (a) T3-50 / (b) T3-100 / (c) T3-150. . . . .	111
5.30	Shear stress distribution along the tenon for T3-150 specimens. . . . .	112
5.31	Load-displacement curves vs. model: (a) T4-50 / (b) T4-100 / (c) T4-150. . . . .	113
5.32	Shear stress distribution along the tenon for T4-150 specimens. . . . .	114
5.33	Load-displacement curves vs. model: (a) T5-50 / (b) T5-100 / (c) T5-150. . . . .	115
5.34	Shear stress distribution along the tenon for T5-150 specimens. . . . .	115
5.35	Shear strength comparison between characteristic values ( $f_{v,k}$ ), tested values ( $\tau_{v,k,TT}$ ), and FE model values ( $\tau_{v,k,model}$ ): (a) T1 / (b) T2 / (c) T3 / (d) T4 / (e) T5.	116
5.36	Connection stiffness comparison between slip modulus ( $k_s$ ), slip modulus after first loading ( $k_{s,model}$ ), and FE model slip modulus values ( $k_{model}$ ): (a) T1 / (b) T2 / (c) T3 / (d) T4 / (e) T5. . . . .	117
5.37	Load-carrying capacity of TT connections as a function of tenon length. . . . .	119
<b>A</b>	<b>Appendix of Chapter 3</b>	<b>131</b>
A.1	Detailed plan of the case-study roof element. . . . .	132
A.2	Detailed plan of the top and bottom TT geometry of the case-study roof element.	133
A.3	Experimental curves of the push-out tests performed on OSB TT joints: (a) Stiffness curves $K_{y,sample}$ / (b) Comparison of the stiffness curves $K_{y,sample}$ . . . . .	133
<b>B</b>	<b>Appendix of Chapter 4</b>	<b>135</b>
B.1	Detailed plan of large-scale specimens: part 1. . . . .	136
B.2	Detailed plan of large-scale specimens: part 2. . . . .	137
B.3	(a) Creep strain curve for different stress levels / (b) Different stress levels compared to the limit of linearity (LL). . . . .	140
B.4	Photograph of the experimental setup in outdoor conditions. . . . .	142
B.5	Experimental setup details: (a) Front view / (b) Side view / (c) Axonometry / (d) Punctual load on OSB panel / (e) Displacement targets on top and bottom flanges / (f) Displacement target on web / (g) Displacement targets on support conditions of OSB panels. . . . .	143
B.6	Loading calculation method for the creep test. . . . .	144
B.7	Maximum displacement $w_{max}$ over time for the LSS and CPs. . . . .	146
B.8	Humidity and temperature measured under the ventilated shelter. . . . .	146
<b>C</b>	<b>Appendix of Chapter 5</b>	<b>149</b>
C.1	Compression setup: (a) EN789 [38]: (1) spherical seated, (2) transducer, and (3) test piece / (b) OSB specimen / (c) Spruce LVL specimen / (d) Beech LVL specimen. . . . .	150



C.2	Boxplot of $F_{max}$ values per specimen type for the compression tests of TT connections. The box-plot represents the median with the red central mark and the 25 <sup>th</sup> and 75 <sup>th</sup> percentiles with the bottom and top edges of the box, respectively.	152
C.3	Boxplot of $k_s$ values per specimen type for the compression tests of TT connections.	152
C.4	Boxplot of $k_s$ values per specimen type for the shear tests of TT connections.	153
C.5	Boxplot of $k_s$ and $k_{smod}$ values per specimen type for the shear tests of TT connections with a tenon length of 50 mm.	153
C.6	Boxplot of $F_{max}$ values per specimen type for the shear tests of TT connections.	154
C.7	Definition of the material directions 1, 2, and 3.	155
C.8	Damage evolution laws: (a) Elastic perfectly plastic for damage parameters associated with ductile failure modes (b) Fracture-energy-based tension softening for damage parameters associated with brittle failure modes.	160
C.9	Flow chart illustrating the algorithm of the USDFLD subroutine for the continuum damage model.	161
C.10	Contact modeling using surface-to-surface interactions illustrated for specimen T2-50: (a) Friction coefficient $\mu_{edge} = 0.26$ with separation allowed after contact for the surfaces of the tenon and mortise parts ①, ②, and ③ (b) Friction coefficient $\mu_{edge} = 0.26$ with no separation allowed after contact between the loaded face of the tenon part and the corresponding face of the mortise part ④ (c) For two-layered specimens, friction coefficient $\mu_{flat} = 0.40$ with separation allowed between the panels of the mortise part ⑤ and the tenon part ⑥.	163
C.11	Mesh convergence study performed for specimen T3-50 under a load of 25% $F_{max}$ : (a) Vertical displacement converge (b) Maximum shear stresses do not converge.	163
C.12	Stresses along a path passing through the notches (dotted line), which represent singularity points with theoretically infinite stresses, for mesh sizes varying from 10 to 2 mm in steps of 1 mm: (a) Shear stresses (b) Normal stresses.	164
C.13	Mesh for the sample T3-50 - Refined-mesh element size of 2 mm in the vicinity of the tenon and coarse-mesh element size of 16 mm away from this region of interest.	164
C.14	Normal distribution with mean $\mu$ and a standard deviation $\sigma$ for material property parameters $X$ .	165



# List of tables

<b>2</b>	<b>Large-scale building implementation: the Vidy theater</b>	<b>13</b>
2.1	Evolution of digitally produced wood-wood connections for the assembly of folded-plate structures. . . . .	14
2.2	Materials investigated in the rotational tests on TT connections. . . . .	21
2.3	Results for 40-mm single-layered CLT connections in rotation. . . . .	23
2.4	Results for 45-mm single-layered CLT connections in rotation. . . . .	25
2.5	Results per material type for one geometry without screws or tenon inclination. . . . .	26
2.6	Results for the 45-mm CLT joint using the 40-mm CLT joint as reference. . . . .	27
2.7	Results for the double-layered TT connections in rotation. . . . .	30
<b>3</b>	<b>Standardized construction system: development and potential</b>	<b>33</b>
3.1	Material properties of OSB type 4 for numerical modeling. . . . .	46
3.2	Sample properties. . . . .	49
3.3	Experimental average results per sample. . . . .	52
3.4	Maximum vertical displacement for the different element configurations. . . . .	53
3.5	Computation times for the different configurations of elements. . . . .	54
<b>4</b>	<b>Simplified calculation method: development and validation</b>	<b>57</b>
4.1	Material properties. . . . .	63
4.2	Model properties according to Fig. 4.7. . . . .	67
4.3	Results of effective bending stiffness ( $EI_{ef}$ ) and natural frequency ( $f$ ). . . . .	71
4.4	Results for tensile failure in the OSB bottom flange for each specimen. . . . .	75
<b>5</b>	<b>Mechanical characterization of through-tenon</b>	<b>79</b>
5.1	Material properties for the experimental investigation of TT connections. . . . .	85
5.2	Tested material densities compared to the manufacturer's values. . . . .	86
5.3	Results of compression tests per material according to EN 789 [38]. . . . .	87
5.4	Specimen properties for compression tests on TT as described in Fig. 5.7. . . . .	89
5.5	Specimen properties for shear tests on TT as described in Fig. 5.9. . . . .	92
5.6	Experimental results for compression tests on TT connections. . . . .	95
5.7	Results for T1 specimens. . . . .	98

## List of tables

---

5.8	Results for T2 specimens. . . . .	100
5.9	Results for T3 specimens. . . . .	101
5.10	Results for T4 specimens. . . . .	103
5.11	Results for T5 specimens. . . . .	104
5.12	Results for T1 specimens vs. model. . . . .	108
5.13	Results for T2 specimens vs. model. . . . .	110
5.14	Results for T3 specimens vs. model. . . . .	112
5.15	Results for T4 specimens vs. model. . . . .	113
5.16	Results for T5 specimens vs. model. . . . .	115
5.17	Summary of the test results for TT connections. . . . .	118
<b>B</b>	<b>Appendix of Chapter 4</b>	<b>135</b>
B.1	Material properties with the reduction coefficient $k_{def}$ applied. . . . .	145
B.2	Maximum displacement $w_{max}$ over time for the LSS test and CP average. . . . .	147
B.3	Comparison between test and calculation models for the maximum displacement $w_{max}$ of the LSS. . . . .	147
<b>C</b>	<b>Appendix of Chapter 5</b>	<b>149</b>
C.1	Specimen properties for compression tests according to EN 789 [38]. . . . .	150
C.2	Test results of the maximum load ( $F_{max}$ ) for the material compression tests. . . . .	151
C.3	Elastic properties (mean values). . . . .	166
C.4	Poisson's ratio values from the literature on spruce and spruce LVL. . . . .	166
C.5	Mechanical properties (characteristic values) in MPa [163]. . . . .	167
C.6	Fracture energy values in N/mm for spruce and beech [131]. . . . .	167

## List of abbreviations

AEC	Architecture, engineering, and construction
BIM	Building information modeling
CAD	Computer-aided design
CAM	Computer-aided manufacturing
CLT	Cross-laminated timber
CNC	Computer numerical control
DfMA	Design for manufacture and assembly
DIC	Digital image correlation
DOF	Degree-of-freedom
EC5	Eurocode 5
$EI_{ef}$	Effective bending stiffness
FE	Finite element
GHG	Greenhouse gas
GLT	Glued laminated timber
HSSSD	Hammock-shape shear-stress distribution
IPCC	Intergovernmental Panel on Climate Change
LL	Limit of linearity
LVDT	Linear variable differential transformers
LVL	Laminated-veneer lumber
MSW	Multiply solid wood
MTSJ	Multiple-tab-and-slot joint
OSB	Oriented strand board
SLS	Serviceability limit state
SMEs	Small and medium-sized enterprises
TT	Through-tenon



# 1 Introduction

## 1.1 Research context

### 1.1.1 Construction and sustainability

Since the Paris agreement was signed in 2016 [158], it has been firmly established that global warming is one of the most important threats to modern society. A report published in 2018 by the Intergovernmental Panel on Climate Change (IPCC) [70] emphasized the importance of limiting greenhouse gas (GHG) emissions in order to maintain warming within 1.5°C of pre-industrial levels. Nonetheless, human activities continue to accelerate since 1950, putting pressure on priceless natural resources [151]. The world population, especially in urban areas, is also increasing at a high rate, and the construction industry must fulfill demand in a sustainable manner (see Fig. 1.1). Currently, concrete and metals (iron, aluminum, copper, zinc, lead, nickel, and manganese) are the most-used construction materials even though they are responsible for approximately 15% of total GHG emissions and represent one-sixth of cumulative energy demand [104].

In 1996, the IPCC declared that wood products require less energy than other alternative

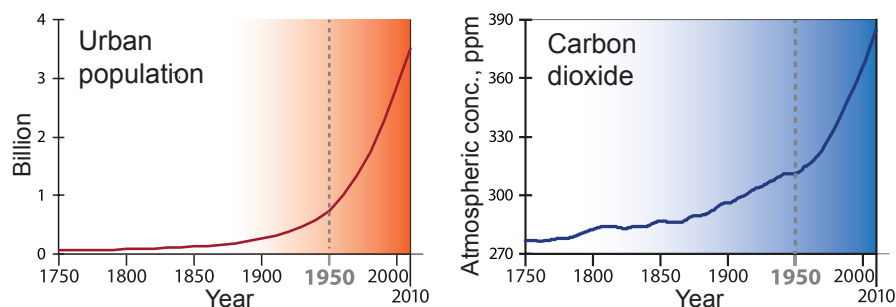


Figure 1.1 – (left) Global urban population data according to the HYDE database / (right) Carbon dioxide from firn and ice-core records (Law Dome, Antarctica and Cape Grim, Australia). Based on [151].

products. This statement has been confirmed by the construction industry in several examples of concrete versus timber buildings [12, 55, 62, 87, 96]. Generally, timber is less carbon-intensive to transform and manufacture, even if each case should be evaluated considering key parameters such as the end-of-life planning of the structure [61, 63]. In this context, timber can mitigate the impact of the industry on global GHG emissions, as it is a renewable resource that can absorb and store carbon dioxide from the atmosphere. In Europe, if the use of wood products in construction was increased by 100 million cubic meters, approximately 100 million tons of CO<sup>2</sup> would be saved, which represents 4% of the total expected carbon budget in accordance with the Paris agreement [156]. In addition, forest policy and strategy should be enhanced, as average yearly gross deforestation in Europe is about 97,000 ha, mainly due to urban sprawl and expansion of transport, infrastructures, and natural disasters such as fires [95].

This work is part of the efforts undertaken to bring more timber products into the architecture, engineering, and construction (AEC) industry to create a sustainable built environment.

### 1.1.2 Digital fabrication and timber construction

In addition to the increasing demand for sustainable products in construction such as wood, new technologies can help optimize the use of this precious renewable resource.

Since humans started to work with wood material, carpenters mostly used handcrafting techniques until the industrial revolution in the 19<sup>th</sup> century. At that time, machine tools were developed thanks to the mechanization and standardization of the industry, which resulted in faster processing speed, efficient prefabrication for timber housing, and new engineered timber products. In the middle of the 20<sup>th</sup> century, automation replaced not only physical labor like machine tools but also intellectual labor (see Fig. 1.2). This transformation is called information-tool technology according to Schindler [137]<sup>1</sup>: “*Man becomes the creator of the process while the machine is the creator of the products.*” As a result, computer numerical control (CNC) machines, as well as computer-aided design and manufacturing (CAD/CAM), were developed in various industries. Such tools were widely integrated in the 1980s with Hundegger machines (Hans Hundegger AG, Hawangen, Germany) for joinery and timber construction. However, a considerable range of such tools now exists, from large-scale five-axis CNC machines to six-axis robotic arms from different producers. The universality of programming codes [73], the automated positioning of cutting parts, and a large repertoire of cutting movements have allowed high flexibility in the production process and a vast range of design possibilities. The workflow of design-to-production has evolved considerably and numerous research studies have been conducted on this topic [7, 154]. Moreover, new engineered wood products such as cross-laminated timber (CLT) and laminated-veneer lumber (LVL) have led to the panelization of the industry alongside the continued use of common timber

---

<sup>1</sup>Approximately during the same period, Eastman started to describe building information modeling (BIM), which is now well known in the AEC industry and has a similar philosophy [28].



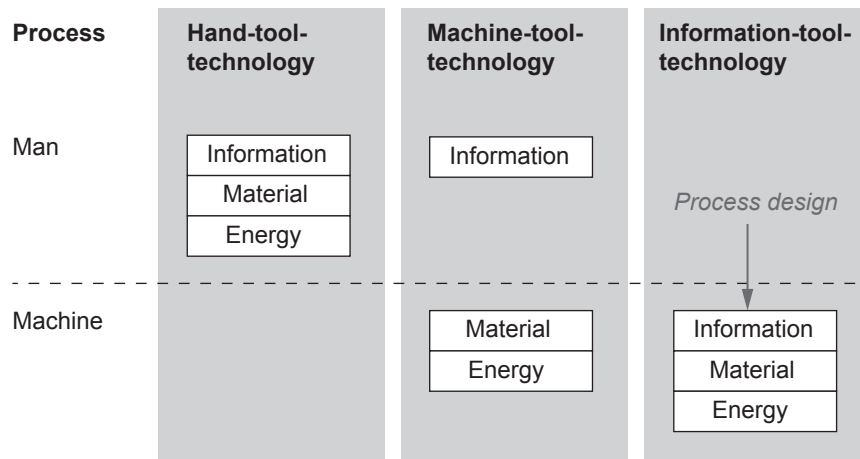


Figure 1.2 – Development of manufacturing techniques over the history of humankind. Based on [137].

frame buildings. In parallel, new ways of using round timber have also been explored using automated processes and new technologies [16], even if it represents a small part of the set of timber constructions. The last step is the assembly process, which is also investigated through digital fabrication and, more specifically, with robots. There is ongoing research on timber frame systems [1, 166], together with panel systems [119], to achieve a fully automated process. Finally, automation and new technologies are increasingly present in the design, fabrication, and assembly steps in the timber industry and, more generally, in the AEC industry.

### 1.1.3 Wood-wood connections for timber plate structures

With the standardization of the construction industry, traditional wood-wood assemblies have been replaced by steel fasteners and adhesive bonding, which are now generally used as connections in modern timber structures. Nevertheless, as discussed in Section 1.1.2, the emergence of digital fabrication and engineered timber materials have opened new design possibilities for wood-wood connections, especially for timber plate structures.

In this context, improved timber plate connections were proposed by Robeller [117]. He developed innovative wood-wood connections inspired by traditional joinery which can be designed and produced using digital manufacturing techniques [118]. Two main connection types, called multiple-tab-and-slot joint (MTSJ) and through-tenon (TT), were established for the edgewise connection of thin panels, as shown in Fig. 1.3. Such connections are an integral part of the panels and require a customized automated prefabrication. A large number of connections with various geometries can be easily designed with CAD and manufactured with CAM in a single operation using CNC machines [125]. The single degree-of-freedom (DOF) of MTSJ and TT allows for their fast and precise assembly since only one insertion vector is possible for their positioning. Various assembly sequences for simple as well as complex structural shapes can be defined which thus increases the efficiency of the assembly process in

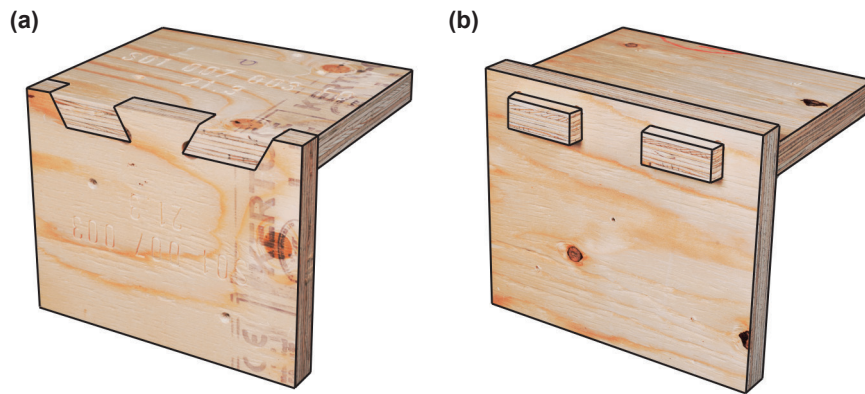


Figure 1.3 – Digitally produced wood-wood connections: (a) Multiple-tab-and-slot joint (MTSJ) / (b) Through-tenon (TT). Based on [173].

construction, either on-site or in workshops. Additional costs linked to temporary formwork can also be saved. The high levels of automation and prefabrication make digitally produced wood-wood connections a cost-competitive assembly for timber structures. Moreover, these connections provide a substantial load-bearing capacity, which could reduce or eliminate the use of bonding and metal fasteners. As a result, different research has been conducted on prototypes and pavilions.

### Prototypes

Research was first performed on origami-shaped structures made of timber panels [18]. The particular arrangement of folds that would enable the spanning of long distances with thin panels was investigated. Mechanical fasteners, such as screws, were first used for the edgewise connections of different prototypes [17]. The failures were thus located in assembly areas because of the low thickness of panels. As a result, a single-layered folded-plate prototype using MTSJ was built (see Fig. 1.4a) to enhance the resistance of such origami-shaped structures [123]. The vault, with a 3 m span, was digitally produced using exclusively 21-mm thick LVL panels without bonding or metal fasteners. The load-bearing capacity of such structures can also be enhanced by the addition of another layer, as performed for the prototype presented at the ACADIA conference in 2014 (see Fig. 1.4b) [121]. The double-layered pattern, connected by wood-wood connections, increases the inertia of the structure. A particular type of TT, called through snap-fit joints, was used for this prototype to demonstrate the possible disassembly and ease of the recycling process using this type of connection. In 2016, a single-curved and double-layered prototype using TT was fabricated (see Fig. 1.4c) [126]. Beech LVL panels of 12-mm thickness with a distance between layers of 48 mm were used to span a distance of 3.25 m. Based on this work, a double-curved and double-layered construction system using both MTSJ and TT was developed (see Fig. 1.4d) [120]. A span of approximately 7 m was achieved with a height varying from 0.7 to 1.2 m. The construction system consisted of a series of prefabricated boxes assembled with TT and only one possible insertion vector.

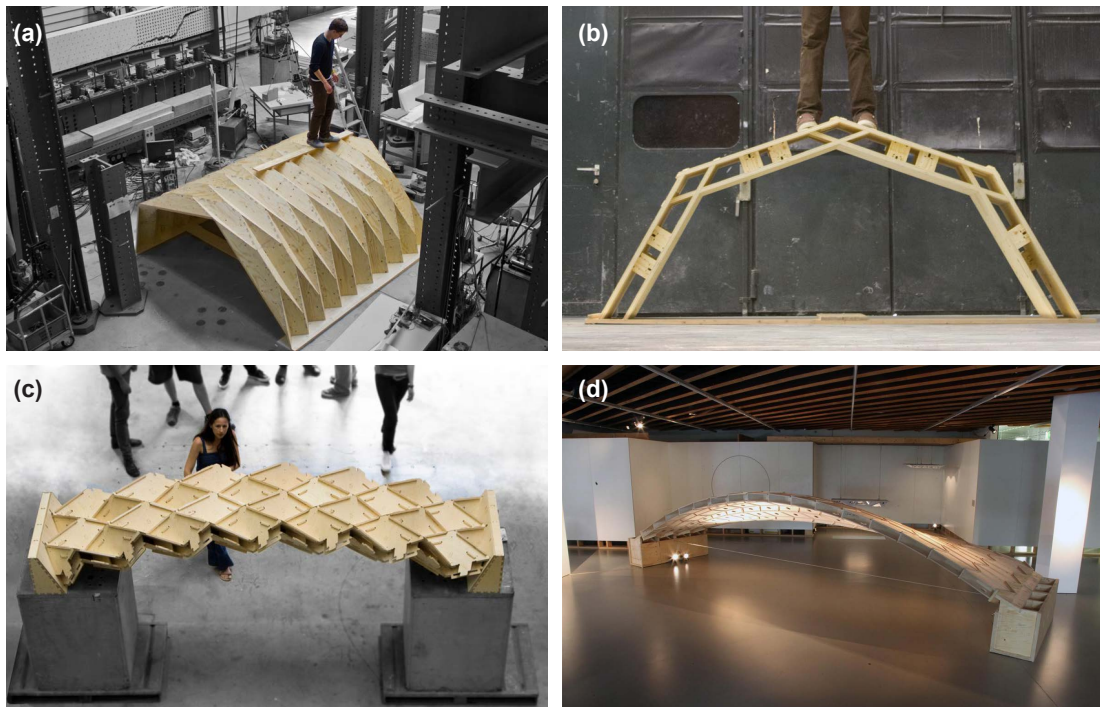


Figure 1.4 – Evolution of IBOIS prototypes: (a) Single-layered origami prototype using MTSJ [123] / (b) Double-layered prototype using snap-fit joints [121] / (c) Double-layered Miura-Ori pattern prototype using TT [126] / (d) Double-layered free-form shell prototype using TT [120].

Birch plywood of 15-mm thickness was used with a spacing between layers of 100 mm. All these prototypes were produced at the laboratory for timber constructions (IBOIS) of the École Polytechnique Fédérale de Lausanne (EPFL) with a five-axis CNC machine. The maximum size of the CNC (2.5 by 1.5 m) limited the fabrication possibilities for the different prototypes. Nonetheless, larger pavilions have been built based on the same construction technique.

## Pavilions

In 2013, a single-layered and double-curved pavilion [122] was presented at the exhibition of the Academy of Architecture in Mendrisio, Switzerland (see Fig. 1.5a). It comprised curved CLT panels with a thickness of 77 mm, connected by MTSJ at the structure's corners. Continuity between the different panels was achieved with small glued LVL joints to span a total length of 13.5 m. The manufacturing process for the different prefabricated parts was performed by a seven-axis robot arm to allow the cutting of large size panels.

The Institute for Computational Design (ICD) at the University of Stuttgart also performed research on the applicability of wood-wood connections in timber plate structures. In 2011, they built a double-layered shell-shaped pavilion inspired by a natural generation scheme [83, 84, 145] in collaboration with the Institute of Building Structures and Structural Design (ITKE,

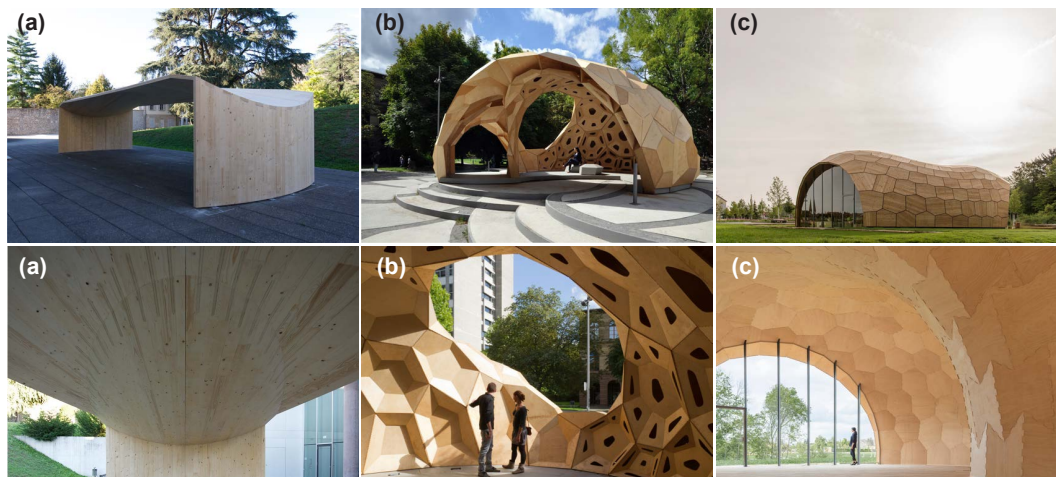


Figure 1.5 – Pavilions: (a) Curved CLT pavilion, Academy of Architecture in Mendrisio, Switzerland, 2013 [122] / (b) ICD/ITKE Research Pavilion, Stuttgart, Germany, 2011 [83, 84, 145] / (c) Landesgartenschau Exhibition Hall, Schwäbisch Gmünd, Germany, 2014 [81, 88].

Stuttgart). The ICD/ITKE research pavilion covered an area of approximately 10 m in diameter on the ground for a height of 4 m, as shown in Fig. 1.5b. The vault structure was composed of prefabricated boxes assembled on-site with bolts. Each prefabricated box was made of 6.5-mm thick birch plywood connected on each side by multiple finger joints similar to the MTSJ developed at IBOIS. These joints had several DOFs and they were thus used exclusively as locators. The rigidity of the prefabricated boxes was achieved by gluing each element together. The prefabrication of all the elements was also realized using robots. In 2014, the same collaboration between the ICD and ITKE resulted in the construction of an actual building [81, 88], the Landesgartenschau exhibition hall located in Schwäbisch Gmünd, Germany (see Fig. 1.5c). The single-layered shell structure is composed of 50-mm thick beech LVL panels in form of a double-domed pavilion. All 243 panels were robotically prefabricated and directly assembled on-site. Edgewise connections are made of multiple finger joints to resist in-plane shear and self-tapping screws to resist axial forces as well as out-of-plane shear. The overall dimensions of the pavilion are 17 m in length, 11 m in width, and 6 m in height.

### Mechanical behavior

The structural design of these prototypes and pavilions using digitally produced wood-wood connections was always performed with finite element (FE) models [88, 122, 173], which are computationally expensive and time-consuming. In some cases, complex geometries were automatically transferred from CAD to FE analysis software to accelerate the calculation process and reduce the engineering time required for the projects [101, 153]. The FE analysis was preferred mainly due to the singular structural shapes and high number of elements. In addition, simpler analytical solutions generally do not exist for this type of construction technology. For all of these structures, experiments were conducted to determine the performance

of the connections.

In fact, the mechanical behavior of connections is an essential parameter for the prediction of the structural response of timber structures, as it largely influences its displacement, stress distribution, and failure modes. However, current timber building standards (Eurocode 5 [33] or SIA 265 [146]) only define basic steel fastener assemblies generally used in modern timber constructions, as shown in Fig. 1.6. Wood-wood connections can be competitive in terms of performance, but their mechanical behavior has not yet been characterized: few studies have been conducted on their behavior in terms of stiffness and load-carrying capacity. Experimental tests were performed on specific case-studies for finger joints used by the ICD and ITKE research groups for the pavilions presented in Fig. 1.5b and c [81, 83]. The shear behavior of MTSJ was also experimentally studied by Dedijer [22] for specific configurations made exclusively of spruce LVL panels. With a more general approach, Roche [128, 129, 127] developed a simplified analytical model to estimate the stiffness and load-carrying capacity in rotation of MTSJ. The experimental campaign also focused on spruce LVL panels but for a wider range of geometrical configurations. Finally, further guidelines on the load-carrying capacity of wood-wood connections have been developed in the field of built heritage restoration for the assessment and restoration of old timber frame connections, which are considerably different from the new digitally produced MTSJ and TT connections of interest in this work.

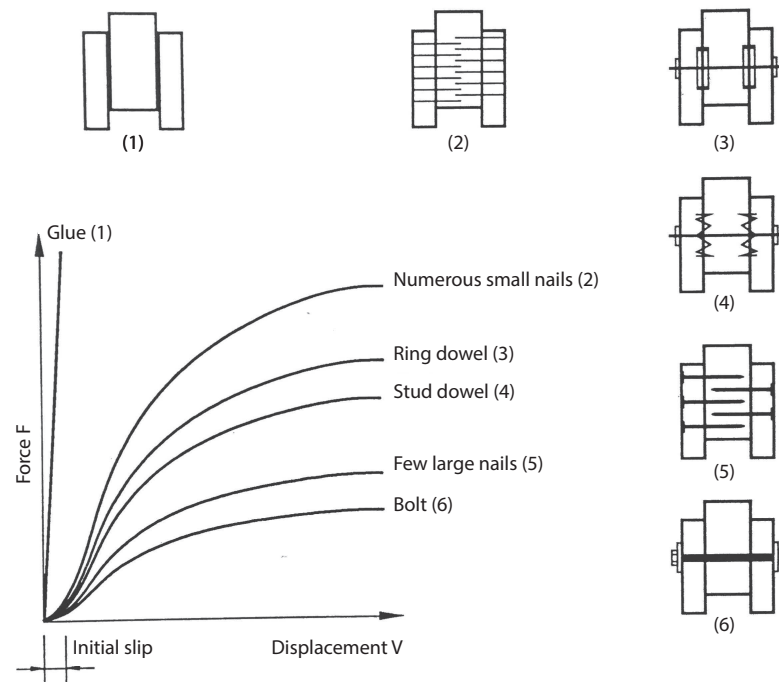


Figure 1.6 – Principle of deformation for the different basic assemblies used in modern timber structures. Based on [162].



### 1.1.4 Standardized building components

Until now, most of the research performed on digitally produced wood-wood connections has focused on folded-plate or free-form structures, which are very specific geometries. However, with all the gained knowledge from research, the possibility exists to use this assembly technique for standardized building elements.

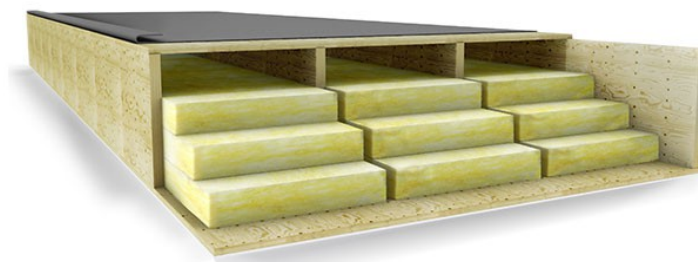


Figure 1.7 – View of a prefabricated roof element made with laminated-veneer lumber by the company Metsä Wood: Kerto Ripa®.

This type of prefabricated element is highly efficient since constraints and regulations related to new buildings have evolved considerably in recent decades. Many factors must be considered, such as thermal, waterproofing, and structural performance. Moreover, economic constraints and an increasingly competitive environment have pushed manufacturers to find new constructive solutions to more easily fulfill these requirements. In this context, various prefabricated timber elements have been developed in the past 15 years by manufacturers such as Kerto Ripa® (Metsä Wood, Espoo, Finland) as shown in Figure 1.7, Lignotrend® (Lignotrend Produktions GmbH, Weilheim-Bannholz, Germany), and Lignature® (Lignatur AG, Waldstatt, Switzerland). Such timber elements can fulfill different functions (structural, thermal, etc.) in a single element delivered directly to the construction site. All these elements are factory-produced through industrial processes using engineered timber products and structural bonding. These production methods involve important materials and investments, while the timber construction industry is largely composed of small and medium-sized enterprises (SMEs). Moreover, structural bonding is difficult to achieve and an important quality control must be passed [33]. The production line is also exclusively dedicated to one standard element and cannot easily be changed, which removes the required production flexibility of SMEs.

In contrast, multiple-axis CNC machines are commonly found in small and medium-scale carpentry companies [152]. As a result, wood-wood connections for structural timber elements can offer an alternative to structural bonding. The flexibility of the production process remains, since there is no need for the strict quality control required for the bonding process. Other timber construction systems can thus be manufactured at the same location. Moreover, timber products assembled with a reduced amount of fasteners and glue have many advantages with respect to the recycling process [148].

## **1.2 Research motivation**

### **1.2.1 Problem statement**

The rise of digital fabrication has made the development of alternative assembly techniques inspired by traditional carpentry possible for timber plate structures. Digitally produced wood-wood connections, presented in Subsection 1.1.3, have thus been increasingly investigated and a large quantity of research has been performed on this topic. Nevertheless, several challenges remain in order to broaden the use of this specific construction technique in the timber industry.

#### **Large-scale building implementation**

Both multiple-tab-and-slot and through-tenon joints have shown their applicability for small-scale research prototypes and pavilions. Origami and free-form shaped structures with single or double layers have been designed and built over the past few decades. However, their feasibility at the building scale has not yet been proven. Computational tools for the design and experimental research necessary for the structure's mechanical characterization must be confronted on a larger scale.

#### **Development of a standardized construction system**

Past research has tended to mostly focus on specific geometrical problems such as free-form and folded structures. However, wood-wood connections can also be used for more standardized building elements with basic geometry, such as roof or slab components. Such connections can offer an alternative to bonding process and steel fasteners for SMEs, which generally have the required production tools (CAD, CAM, and CNC). Therefore, research should be conducted on the implementation of digitally produced wood-wood connections for basic building components.

#### **Simplified calculation model for structural design**

The structural performance of timber plate structures using wood-wood connections has mainly been evaluated for complex geometrical shapes. As a result, their structural analysis has been conducted with sophisticated FE models. These models are generally time-consuming and complex to implement in FE analysis software. They are thus not convenient to use in practice for standardized building components. More practical design methodologies should be investigated to capture the specifics of the developed standardized construction system.

## **Chapter 1. Introduction**

---

### **Behavior of through-tenon connections**

Few systemic studies have been performed on MTSJ and TT connections in the past. Rotational behavior has primarily been the focus of investigation, as it is an important parameter for folded-plate structures. However, it is essential to characterize their in-plane behavior for standardized interconnected timber elements. In-depth investigation should therefore be conducted on this topic.

### **1.2.2 Approach and objectives**

The main objective of this research is to bring digitally produced wood-wood connections for timber plate structures into common practice through the development of standardized structural timber elements. This work is decomposed into the following research steps with different sub-objectives:

#### **Step 1 - Proof of concept at the building scale - Chapter 2**

---

- Prove the feasibility of construction systems using TT connections at the building scale.
- Implement TT connections at the building scale.
- Implement computational design methods at the building scale.
- Experimentally determine the most appropriate engineered timber panels.
- Assess the rotational load-carrying capacity of the connection.

#### **Step 2 - Development of a standardized construction system - Chapter 3**

---

- Review existing standardized systems using wood-wood connections.
- Develop a novel standardized construction system.
- Select appropriate TT joint with key parameters according to fabrication constraints.
- Perform a preliminary investigation through a case-study.
- Evaluate the feasibility of the construction system.
- Determine the structural performance of the novel system compared to glued and nailed connections through the development of a numerical modeling approach.

#### **Step 3 - Calculation methodology and validation - Chapter 4**

---

- Review existing calculation methods for interconnected timber elements.
- Propose a convenient calculation model for the developed construction system.
- Describe the modeling of the connection.
- Validate the concept with the fabrication of large-scale specimens.
- Experimentally determine the failure modes and flexural capacity.
- Validate the proposed calculation model and proof of concept.



#### Step 4 - Mechanical characterization of through-tenon - Chapter 5

---

- Review existing guidelines and experimental protocols for wood-wood connections.
- Experimentally investigate the failure modes, load-bearing capacity, and semi-rigidity of TT connections for in-plane loading configurations.
- Develop specific experimental setups for TT connections.
- Compare test results to existing guidelines and a numerical model.
- Expand knowledge of commonly available engineered timber panels.
- Define guidelines for the structural design of TT connections.

### 1.3 List of publications

This thesis is based on several scientific articles published during the PhD:

- J. Gamero, J. F. Bocquet and Y. Weinand. Experimental investigations on the load-carrying capacity of digitally produced wood-wood connections. *Engineering Structures*, 213:110576, 2020. doi:10.1016/j.engstruct.2020.110576.
- J. Gamero, J. F. Bocquet and Y. Weinand. A Calculation Method for Interconnected Timber Elements Using Wood-Wood Connections. *Buildings*, 10(3):61, 2020. doi:10.3390/buildings10030061
- J. Gamero, M. Nakad, J. F. Bocquet and Y. Weinand. Case-study on the creep behavior of interconnected elements using wood-wood connections. In *Proceedings of the World Conference on Timber Engineering*. Santiago, Chile, 2020. Abstract submitted.
- J. Gamero, I. Lemaître and Y. Weinand. Mechanical Characterization of Timber Structural Elements using Integral Mechanical Attachments. In *Proceedings of the World Conference on Timber Engineering*. Seoul, South Korea, 2018.
- J. Gamero, C. Robeller, and Y. Weinand. Rotational mechanical behavior of wood-wood connections with application to double-layered folded timber plate structure. *Construction and Building Materials*, 165:434-442, 2018. doi:10.1016/j.conbuildmat.2017.12.178
- C. Robeller, J. Gamero and Y. Weinand. Théâtre Vidy Lausanne - A Double-Layered Timber Folded Plate Structure. *Journal of the International Association for Shell and Spatial Structures*, 58:295-314, 2017. doi:10.20898/j.iass.2017.194.864



## 2 Large-scale building implementation: the Vidy theater

---

This chapter is based on:

J. Gamero, C. Robeller, and Y. Weinand. Rotational mechanical behavior of wood-wood connections with application to double-layered folded timber plate structure. *Construction and Building Materials*, 165:434-442, 2018. doi:10.1016/j.conbuildmat.2017.12.178

&

C. Robeller, J. Gamero and Y. Weinand. Théâtre Vidy Lausanne - A Double-Layered Timber Folded Plate Structure. *Journal of the International Association for Shell and Spatial Structures*, 58:295-314, 2017. doi:10.20898/j.iass.2017.194.864

---

### 2.1 Introduction

Timber folded-plate structures were the first to implement multiple digitally produced wood-wood connections at the building scale. One of the first building implementations of a timber folded-plate structure was the Saint-Loup chapel located in Switzerland (see Fig. 2.1). The chapel was designed by Hans Buri and Yves Weinand and built as a temporary structure in 2008, but it eventually became permanent. All connections between plates were achieved with custom steel-plate connectors and self-tapping screws for a span of 9 m, as shown in Fig. 2.1a. No digitally produced wood-wood connections had been developed at that time. After many years of consistent development of joining techniques and computational design, several timber prototypes and pavilions using digitally produced wood-wood connections have since been made with a strong emphasis on folded and free-form structures, as described in Section 1.1.3. The first step in the evolution of such a structure was the proposing of a single-layered folded-plate prototype connected uniquely with MTSJ, as shown in Fig. 1.4a. A double curvature was then added to increase load-bearing performance by 40% compared to the equivalent single-curved variant [124]. The second evolution was the double-layered timber folded-plate prototype displayed in Fig. 1.4c. The double TT joint can connect four panels at once to achieve a double-layering of the structure [126]. The evolution of digitally produced joining techniques for folded-plate structures is summarized in Table 2.1.

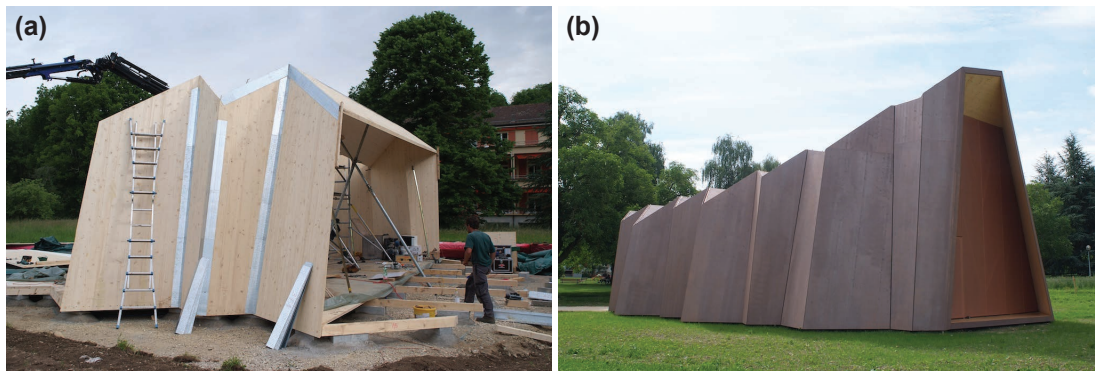


Figure 2.1 – Saint-Loup chapel, Pommaples, Switzerland 2008: (a) Exterior view during construction with metal fasteners / (b) Final exterior view of the building. *[Photograph credit: IBOIS, Fred Hatt]*

Table 2.1 – Evolution of digitally produced wood-wood connections for the assembly of folded-plate structures.

Project	Number of plates	Differently shaped plates	Differently shaped edge joints
Origami Folded Plate, 2006 [17]	144	8	4
St-Loup chapel, 2010, Fig. 2.1	39	39	67
Interlocking Folded Plate, 2014, Fig. 1.4a	107	107	239
Théâtre Vidy Lausanne, 2017	304	304	456

Based on this evolution, the Vidy theater is the first building implementation of a large-scale double-layered and double-curved timber folded-plate structure using TT joints (see Fig. 2.2). The building is located in Lausanne and was inaugurated in 2017. This project was the result of a collaboration between the IBOIS laboratory and the Bureau d'Etudes Weinand (Liège, Belgium), responsible for the architecture and engineering. The main objective was to implement the knowledge gained from research in a real application. In this project, TT joints were used for the first time at the building scale, as was the workflow from design-to-production and the customized prefabrication of these joints. The first challenge was to develop and apply customized computational tools for the automated design and production of the building while collaborating with several industry partners. In addition, the structural design of the theater was complex due to its folded shape and the anisotropic characteristics of wood material. As a result, experimental tests were performed on TT joints to assist the Bureau d'Etudes Weinand, who was in charge of global structural design. The mechanical behavior and potential load-carrying capacity of similar types of connections have been investigated by Roche since 2015 [130]. In particular, the rotational stiffness has been studied [127], as it is an important parameter of a folded-plate structure [173]. In previous research, only LVL panels were considered because of their low thickness, homogeneity, and relatively high resistance. However, the use of Swiss wood panels was an essential condition for the sustainable policy

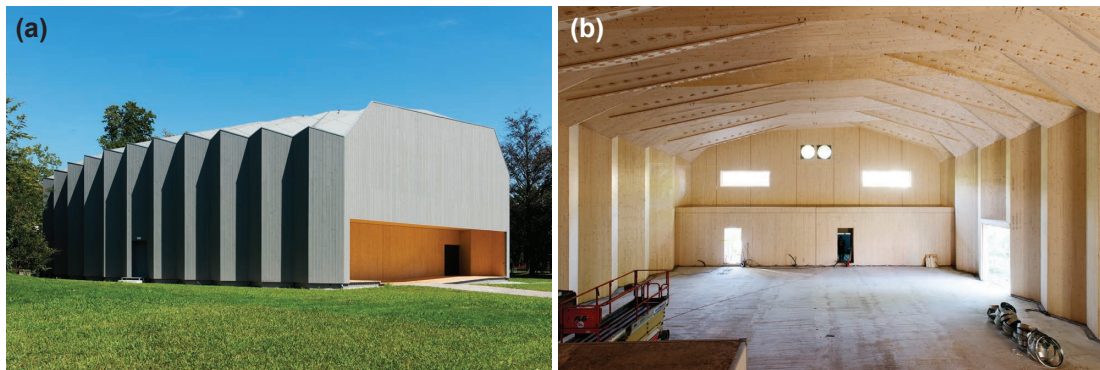


Figure 2.2 – Vidy theater pavilion, Lausanne, Switzerland, 2017: (a) Exterior view / (b) Interior view during construction. *[Photograph credit: Ilka Kramer Photography]*

of the project, and no manufacturers produce LVL in Switzerland. For the first time, CLT panels were therefore considered for the manufacturing of TT joints. Based on the project requirements, different CLT panels were tested to select the optimal option and verify the rotational load-carrying capacity in the most loaded connections.

This chapter is structured as follows:

- Section 2.2 presents the construction system of the Vidy theater.
- Section 2.3 introduces the automated design workflow.
- Sections 2.4 and 2.5 describe and discuss the experimental investigations of single- and double-layered TT connections in rotation.
- Section 2.6 summarizes the main conclusions on the first building implementation using TT joints.

## 2.2 Construction system

The overall dimensions of the building are 30 m in length, 20 m in width, and 11 m in height. The large span of 20 m is achieved with CLT panels of just 45 mm in thickness thanks to the double-layered construction system illustrated in Fig. 2.3. The two layers are spaced 210 mm apart and connected exclusively with single and double TT connections to obtain a total cross-section of 300 mm in height. The insulation is also placed between the layers directly onsite using a blowing process, which makes this solution highly competitive with single-layered options in terms of structural and cost optimizations.

The theater is composed of 11 building segments, as shown in Fig. 2.3. Roof and wall elements were prefabricated in a workshop and subsequently assembled onsite. The prefabrication process of a roof element can be decomposed into four steps, as presented in Fig. 2.3 (steps 1 to 4). The plates are connected by TT connections, each with different tenon geometry depending on the insertion angle and the number of layers to be joined. In addition to their load-bearing function, these connections allow rapid positioning of the different panels for

## Chapter 2. Large-scale building implementation: the Vidy theater

the assembly. The same process was used for the wall prefabrication. Once the prefabrication of these three parts was completed, they were delivered and assembled directly onsite, as shown in Fig. 2.3 (steps 5 to 6) and Fig. 2.4. However, the 11 building segments were assembled onsite using bolts.

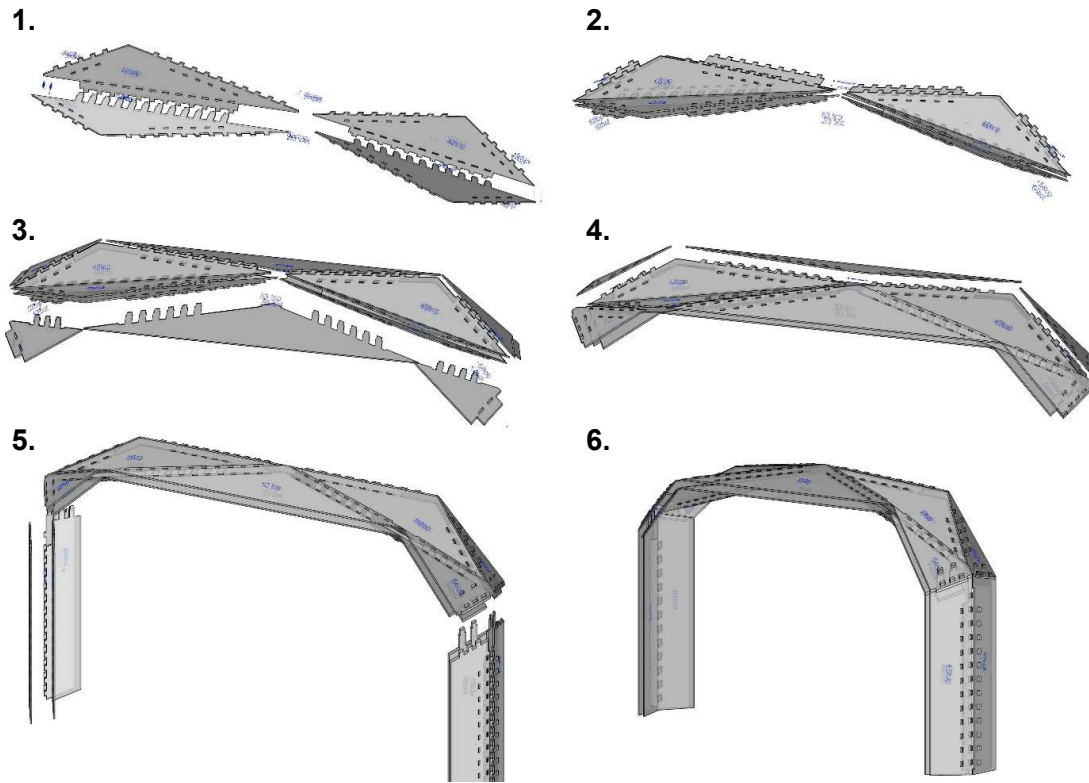


Figure 2.3 – Assembly process of a building segment. Steps 1 to 4: prefabrication process of the roof element. Steps 5 to 6: onsite assembly of the wall and roof elements to obtain a complete building segment.



Figure 2.4 – Photographs of the construction system process: (a) Prefabrication of a roof element / (b) Transport of a roof element / (c) Onsite assembly of the roof and wall elements.

## 2.3 Automatic design-to-production workflow <sup>1</sup>

Digital fabrication is the key to success in such a project as there are more than 300 differently shaped plates with a total of 456 different edge-joint geometries, which would be infeasible or highly time-consuming to draw manually in a CAD software. The generation of plate components is performed automatically using a CAD plugin (DLFP) that was custom-built for the Vidy theater project using the software development kit (SDK) Rhino Commons<sup>®</sup> (Robert McNeel & Associates, Seattle, USA) and the programming language C#. The Grasshopper<sup>®</sup> software (Robert McNeel & Associates, Seattle, USA) is employed as a user interface, through which the input parameters of the design can be edited and modified (see Fig. 2.5a) and which includes a real-time preview of the 3D components. The parameters of the project-generation CAD plugin are as follows:

1. A single-layer polygon mesh with planar triangular surfaces for the roof elements and planar quadrangular surfaces for the wall elements (see Fig. 2.5b). Using this surface model, the identification numbers are managed for all components and edge connections. This identification is made possible through the use of a doubly connected edge list (DCEL) data structure, which allows for neighborhood requests. These requests are crucial for automated geometry generation through the algorithmic tool.
2. The plate thickness ( $t_{\text{plate}}$ ), which was set to 45 mm for the final building components.
3. The total thickness of the double-layer elements. This offset ( $t_{\text{offset}}$ ) starts at the bottom side of the lower plate, which lies exactly on the surfaces of the DCEL polygon mesh and ends at the upper side of the upper plate. The offset therefore includes the two plate thicknesses and is not influenced by changes of the  $t_{\text{plate}}$  value. The  $t_{\text{offset}}$  for the final project was 300 mm.
4. The type of joints, managed through an Excel spreadsheet file containing data for the parameters, which are assigned automatically by the algorithm.
5. The fold type indicates whether a joint is a positive or negative fold, considering all the outward-facing normals of the base polygon mesh. Negative folds are treated differently by the algorithm.
6. Two insert vectors for each regular joint. These 3D vectors are calculated with a separate algorithmic tool, which ensures that plates can be inserted. This requires that multiple edges per plate, which must be joined simultaneously, must share the same insertion vector.

Outputs include a 3D preview of the plate geometry that includes all joints, as well as a visualization of the insertion directions for each regular joint edge in the polygon mesh. Once the parameters have been adjusted, the geometry can be output into the CAD program through three switches for different representations. In addition to the 3D plate contours, boundary representation solids (BREPS) can be output, which is required for the evaluation of masses and visualization purposes. Furthermore, all plates can be sorted and arranged on the world XY plane in preparation for the fabrication (see Fig. 2.7).

<sup>1</sup>This part was performed by the co-author and author of the publications, C. Robeller.



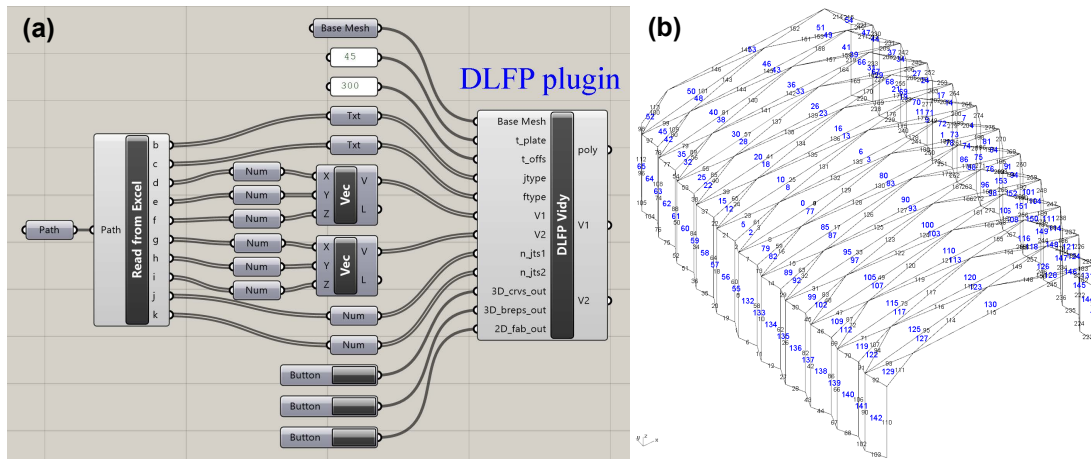


Figure 2.5 – (a) Grasshopper<sup>®</sup> interface of the CAD plugin (DLFP) for the 3D plate geometry and 2D plate matrix for fabrication / (b) Base geometry polygon mesh (DCEL mesh), plate ID numbers are visualized in blue color, edge ID numbers are shown in black color.

One of the most critical parameters for fabrication is the cutting angle at which the tool must be inclined to produce the plate components. This angle,  $\beta$ , results from the dihedral fold angles,  $\phi$ , in the basic polygon mesh. If the dihedral angle  $\phi = 90^\circ$ , no alignment of the tool is required. Furthermore, such orthogonal folds are structurally beneficial. However, it is not possible or feasible to achieve the overall geometry without a deviation  $\beta$  from these orthogonal angles (see Fig. 2.6). On the CNC machine used for the cutting of the plates at the plate manufacturer and wood-processing facilities, the maximum tool alignment angle was  $\beta = 60^\circ$ . This allows for a maximum fold angle of  $150^\circ$ . Considering the tool-holder profile, in this case a slim thermo-shrink chuck, the required clamping length of the shank-type milling cutter can be calculated. This protrusion is to be kept as small as possible because it makes the cutting prone to vibrations, which reduce cutting speed and quality. Larger protrusions therefore require larger milling cutter diameters; however, this increase in diameter would have a negative effect on the notches, which are required for the cutting of the concave corners of the plate contours.

Due to the 456 differently shaped edge joints, various slanting cuts are required for the fabrication of the components. The parts were thus manufactured with a five-axis CNC NC-PMT/190-TUCU/ISO40 machining center (anno 2000) from the manufacturer CMS (SCM Group, Rimini, Italy), which was available at the facilities of the timber-plate manufacturer Schilliger Holz AG (Küssnacht, Switzerland). With an X-axis length of 28.5 m, the machine allowed the cutting of raw plates of up to 15 m long. The necessary five-axis CNC machining, which is required at approximately 500 different component edges with thousands of differently inclined tenon geometries, could not be efficiently generated with standard CAM software solutions for regular timber construction tasks. Instead, a custom-developed CAD plugin for the automated ISO G-code [73] generation of integrally inserted wood-based panels



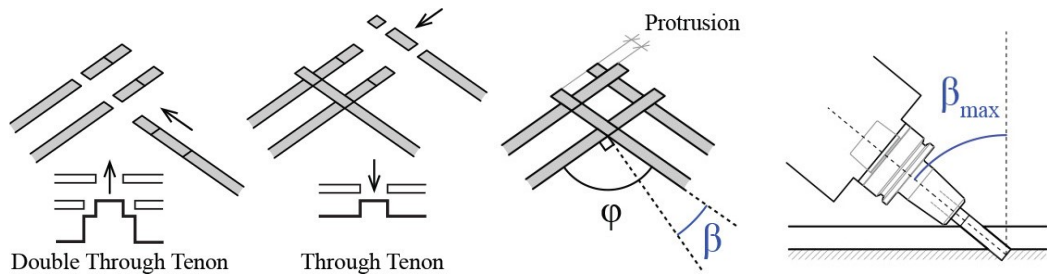


Figure 2.6 – Double-layered folded-plate assembly principle, and tool alignment angle  $\beta$  results from the fold angles deviation from  $90^\circ$ . Very obtuse or acute fold angles require a large inclination of the tool during cutting.

was developed. The underlying algorithm has already been used in previous projects and was further improved and adapted for the Vidy theater [125]. One of the necessary adaptations was a special postprocessor for the CMS machine of the industry partner company. Using the CAD plugin, various special details of integral connections can be created automatically. These include, for example, notch cuts in the concave corners, which are necessary for the insertion of sharp corners on the inserted tenons. This interface allowed for the automatic conversion of the plate contour data out of the 2D plate matrix shown in Fig. 2.7 into ISO G-code, which can be sent to the machining center's control system simply by hatch selection.

Finally, plates geometries, wood-wood connection geometries, and CNC G-code for the production were automatically generated as function of inputs parameters defined by the project designer. The resulting files and information were exchanged with the different partners as well as the company in charge of the manufacturing part. This is a good example of a new workflow of design-to-production described in Section 1.1.2 and Fig. 1.2.

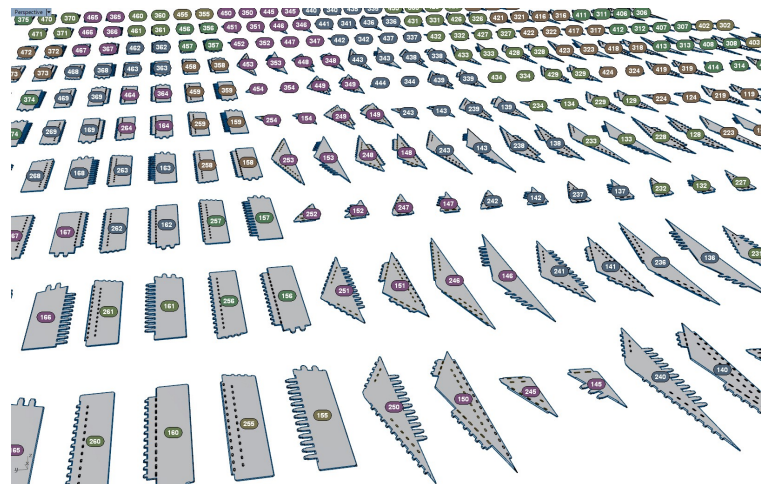


Figure 2.7 – Automatically generated 2D matrix of 308 individually shaped plates.

### 2.4 Experimental investigations of single-layered connections

With the construction system of the Vidy theater, single- and double-layered TT connections were used to join the different building components. In addition, CLT panels were considered for the first time, since LVL panels were generally preferred for their low thickness and good structural performance. The connections should also be able to withstand large forces, especially at the corner of the structure between the roof and wall joints. The rotational behavior of single-layered TT connections was thus investigated for different CLT panels to select the optimal option for the project.

#### 2.4.1 Methods

Samples were tested using a setup developed especially for the rotational-mechanical characterization of single-layered TT joints (see Fig. 2.8) [127]. A 20-kN cylinder pressing on a steel lever arm was used to transmit rotation to the roof panel, which was in contact with the surface of the wall panel. The lever arm maintained the load perpendicular to the roof panel in any position. The wall panel was rigidly fixed using four bolts. The rotation and load were recorded using two inclinometers and four load cells fixed at each connection point of the roof panel. During these tests, the rotation was limited to  $30^\circ$ . A connection with a greater rotation is not relevant because the rotation causes large deflections and does not satisfy the serviceability limit states (SLS) of current European timber building codes, such as Eurocode 5 [33]. All results were obtained based on the EN 789 standard [38] for the determination of mechanical properties of wood-based panels.

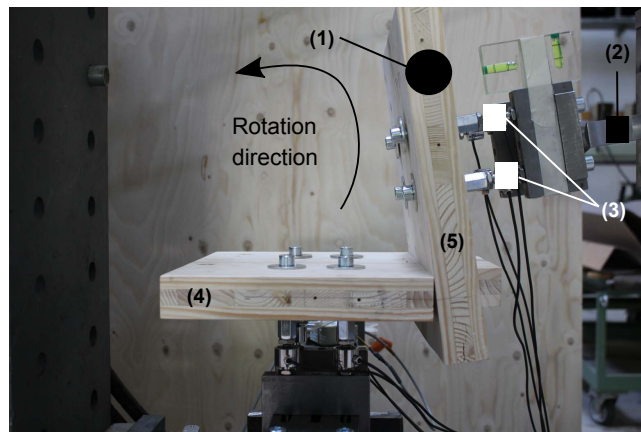


Figure 2.8 – Rotational setup for single-layered TT connections: (1) inclinometers, (2) lever arm, (3) four load cells, (4) wall panel, and (5) roof panel.

#### 2.4.2 Samples

All tests were performed with the grain orientation perpendicular to the joint length of 150 mm and with a dihedral angle equal to  $90^\circ$  (see Fig. 2.9a and b). This configuration is used in the

## 2.4. Experimental investigations of single-layered connections

connections between the walls and roof of the project building. Four series, each with different geometries and properties, were tested for a total of 12 specimens per panel type and a total amount of 36 specimens. The influence of tenon inclination ( $0^\circ$  or  $15^\circ$ ) and screw usage was investigated (see Fig. 2.9a). Screws for timber construction with an asymmetrical double-threaded portion and a length of 90 mm (reference: 0170 655 90, Würth Group, Künzelsau, Germany) were used. In this study, the influence of the dihedral angle was not investigated. However, Roche et al. [128] have already tested different angles with LVL panels in 2016. For the materials, two types of spruce CLT were investigated and compared to one type of spruce LVL. The material properties of the different panels are summarized in Table 2.2 and the lay-up is shown in Fig. 2.9c. The CLT panel (1) was the first proposition for designing the project. It comprises two external layers of 12.5 mm each and a middle layer of 15 mm. On the other hand, the CLT panel (2) is composed of five 9-mm thick layers and has a total thickness of 45 mm. Both of these panels are produced by the Swiss company Schilliger Holtz AG (Küssnacht, Switzerland) and possess a European Technical Approval (ETA) [39] to describe their mechanical properties. The spruce LVL is a Kerto Q<sup>®</sup> panel produced by Metsä Wood (Espoo, Finland) and its mechanical properties are described in the VTT certificate [163].

Table 2.2 – Materials investigated in the rotational tests on TT connections.

Designation	CLT (1)	CLT (2)	LVL (3)
Thickness	40 mm	45 mm	39 mm
Lay-up	–	–   –	–     –     –
Lay-up	12.5/15/12.5 mm	5 × 9 mm	13 × 3 mm

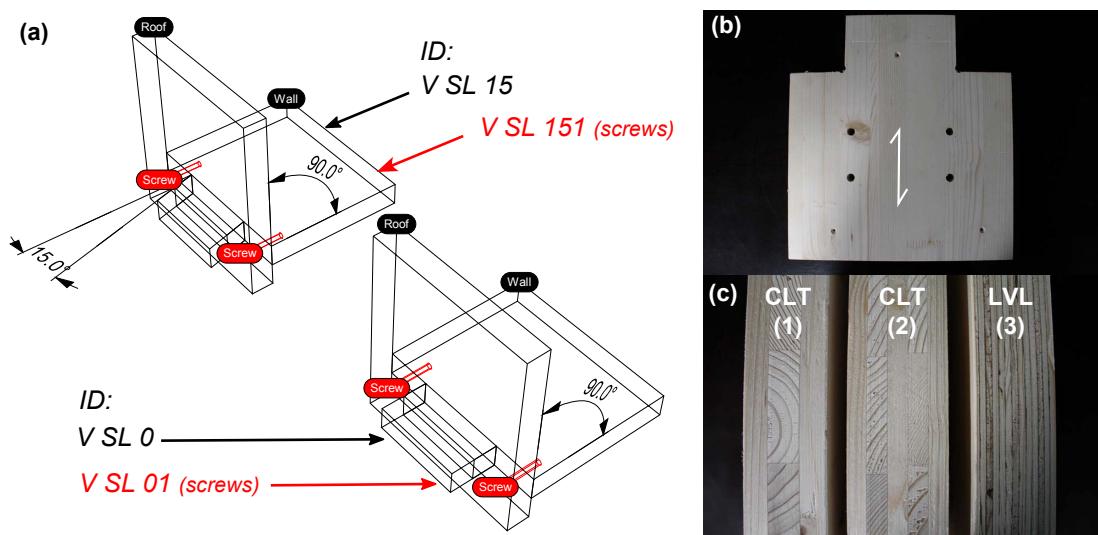


Figure 2.9 – Sample geometries for single-layered TT connections: (a) Axonometry of the different samples / (b) Grain orientation of the samples / (c) Lay-up of the different panels.

### 2.4.3 Results of the CLT panel (1)

#### Mechanical behavior of the joint

From the tests, a general mechanical behavior of the joint was observed for all samples made with CLT panels (1), as shown in Fig. 2.10a. The ultimate moment was observed as a block failure appearing in the external layer of the panel. This block could not follow the rotation of the roof because of the wall tenon. The external-layer grain orientation, perpendicular to the joint length, caused a block shear failure (see Fig. 2.11a). Despite this failure mode, the rupture was not fragile because the internal and middle layers were still intact at this moment. However, when the rotation continued, the excessive rolling shear caused the failure of the middle layer (see Fig. 2.11b, c, and d). In addition, the bonding surface between the external and middle layers broke when the rolling shear increased (see Fig. 2.11c). For the internal layer, the failure mode was similar to that of a clamped beam in bending, as observed in Fig. 2.11b. The stress distribution in the panel depends on the grain orientation in each layer, which is determined before gluing and pressing each wood piece during the manufacturing of CLT in the factory. The manufacturing process is therefore crucial to the failure mode of the CLT, and each manufacturing step must thus be meticulously controlled.

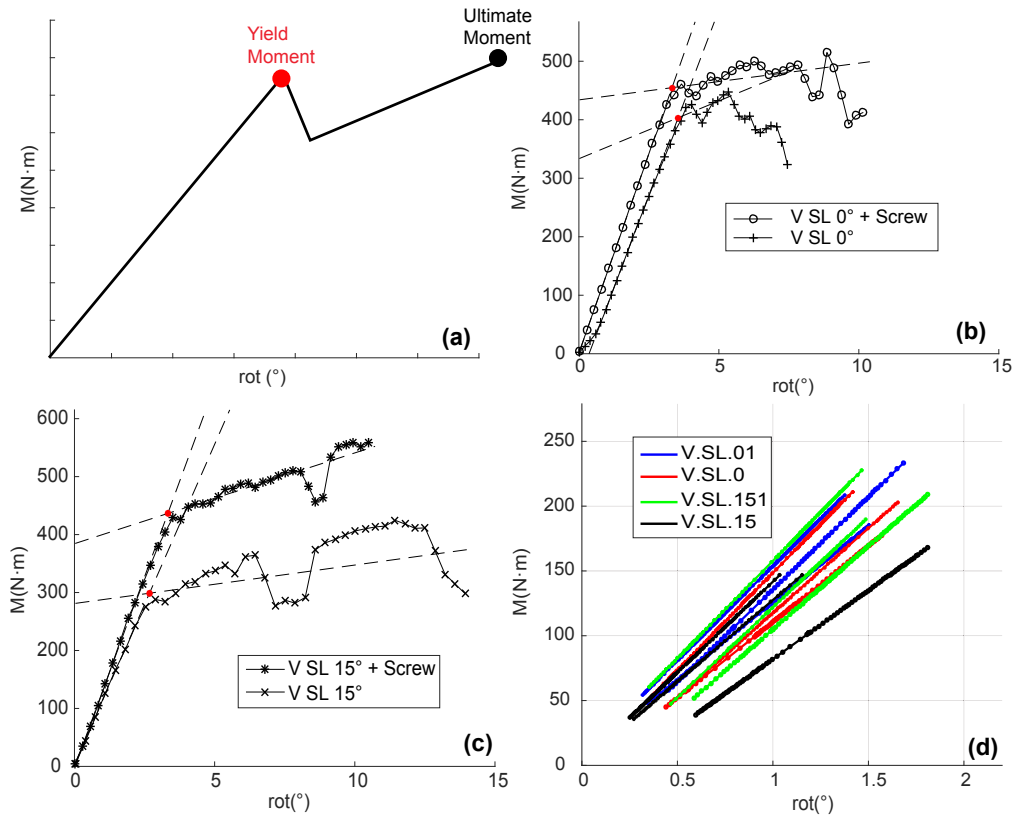


Figure 2.10 – (a) Mechanical behavior of the 40-mm CLT single-layered TT joint in rotation / (b) Results for samples without tenon inclination / (c) Results for samples with tenon inclination / (d) Elastic stiffness for all samples (10 to 40% of the ultimate moment).

## 2.4. Experimental investigations of single-layered connections

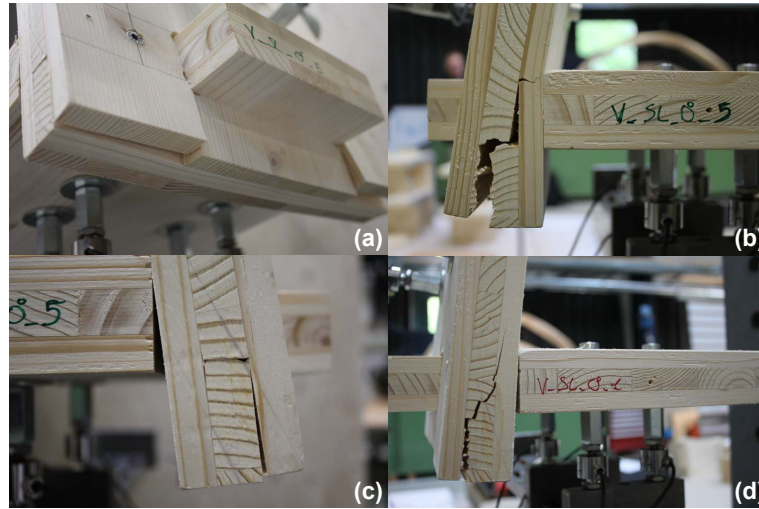


Figure 2.11 – Failure modes of the 40-mm CLT joint in rotation.

### Stiffness and load-carrying capacity

The ultimate moment and rotation were determined alongside the elastic stiffness, which was defined by a linear regression from 10 to 40% of the ultimate moment. The average results for each sample are listed in Table 2.3, and the full moment-rotation curves are displayed in Fig. 2.10b and c. Overall, the joint with no tenon inclination had superior mechanical characteristics. However, the results were highly homogeneous for the elastic stiffness (see Fig. 2.10d). All screwed samples behaved similarly. Screws can therefore be used to homogenize the joint behavior and avoid gaps by keeping wood surfaces in contact. However, there were significant differences between non-screwed samples. With a tenon inclination of 15°, the elastic stiffness and the ultimate moment decreased by 15% and 35%, respectively. Therefore, particular attention has to be paid to the double-layered joints with inclined tenons present in the roof central panel. In addition, tenon inclination is not relevant for preventing the disassembly of two parts as this phenomenon was not observed during the tests.

Table 2.3 – Results for 40-mm single-layered CLT connections in rotation.

ID	Screw	Tenon inclination (°)	Elastic stiffness (N·m/°)	Yield moment (N·m)	Ultimate rotation (°)	Ultimate moment (N·m)
V SL 0	No	0	126.74	403.46	3.55	448.95
V SL 01	Yes	0	136.46	454.81	3.32	515.78
V SL 15	No	15	110.53	298.83	2.68	425.22
V SL 151	Yes	15	131.74	436.45	3.33	559.18

#### 2.4.4 Results of the CLT panel (2)

##### Mechanical behavior of the joint

The general behavior of the samples made of CLT panels (2) was also observed (see Fig. 2.12a). The shape of the curve was more ductile compared to the brittle block shear failure occurring at the yield moment of CLT panel (1) samples. A significant decrease of the performance was not observed after the failure of the first layer. However, the failure mode was exactly the same, except that it was repeated over several layers. A block shear failure occurred in the layers with the grain orientation perpendicular to the joint length (see Fig. 2.13a and b), while a rolling shear failure occurred in the other layers (see Fig. 2.13c and d). Overall, the behavior of the CLT panel (2) connections of 9-mm-thick layers is superior as it prevents weak failures after the yield point and maximum bending moment.

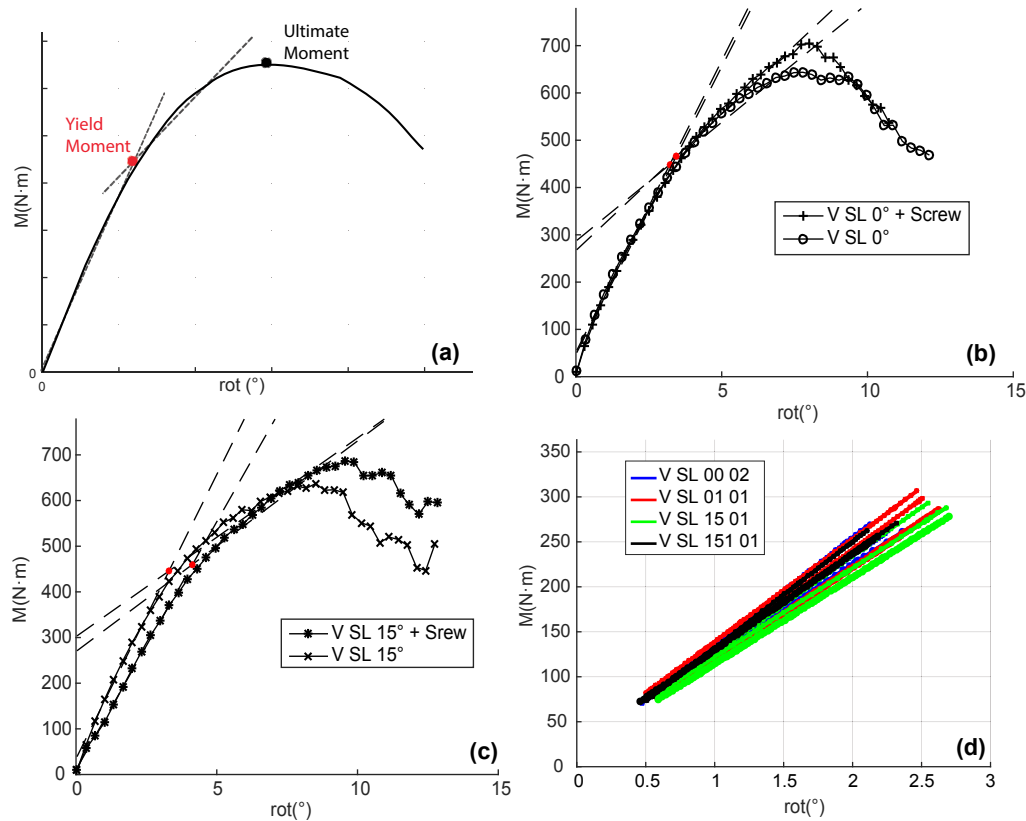


Figure 2.12 – (a) Mechanical behavior of the 45 mm CLT single-layered TT joint in rotation / (b) Results for samples without tenon inclination / (c) Results for samples with tenon inclination / (d) Elastic stiffness for all the samples (10 to 40% of the ultimate moment).

##### Stiffness and load-carrying capacity

The elastic stiffness, ultimate moment, and ultimate rotation were determined in the same manner as for the CLT panel (1) connections. The average results of each sample are listed in



## 2.4. Experimental investigations of single-layered connections

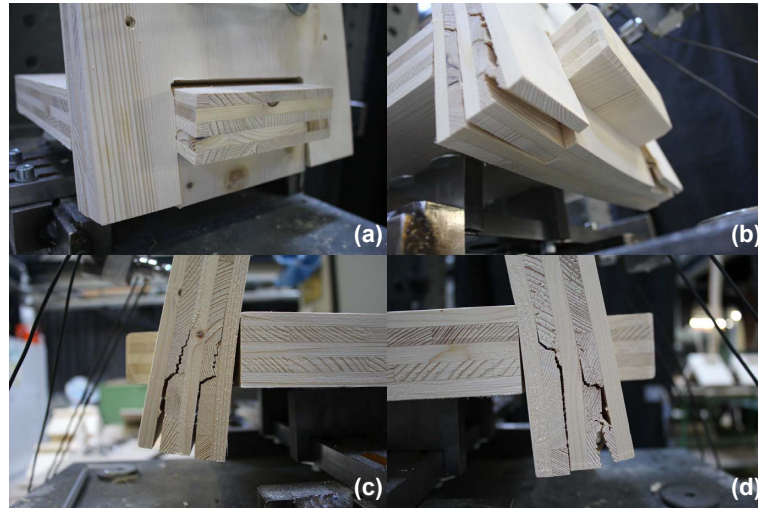


Figure 2.13 – Failure modes of the 45 mm CLT joint in rotation.

Table 2.4 – Results for 45-mm single-layered CLT connections in rotation.

ID	Screw	Tenon inclination (°)	Elastic stiffness (N·m/°)	Yield moment (N·m)	Ultimate rotation (°)	Ultimate moment (N·m)
V SL 0	No	0	123.23	448.21	3.21	644.73
V SL 01	Yes	0	121.55	465.75	3.44	707.60
V SL 15	No	15	124.43	445.68	3.30	638.11
V SL 151	Yes	15	108.60	460.36	4.14	691.78

Table 2.4 and the full moment-rotation curves are displayed in Fig. 2.12b and c. With this panel, the behavior was more homogeneous, even with a tenon inclination. The elastic stiffness was almost the same for every configuration except for the screwed joint with an inclined tenon, which had a 10% lower elastic stiffness than the others (see Fig. 2.12d). However, the yield and ultimate moment for the screwed samples were both 10% higher than for the non-screwed samples. Therefore, screws are a good option to maintain the contact between the panels and prevent any gap in the structure. Furthermore, the 15° tenon inclination does not depreciate the mechanical properties of the joint for this CLT panel type.

### 2.4.5 Comparative analysis of materials

In order to conduct a comparison with the material generally used for IBOIS's research and projects, the spruce LVL (3) Kerto Q<sup>®</sup> was tested with three samples of one geometry (V SL 0, no tenon inclination, and no screws). The comparative graph for the samples without screws and tenon inclination is shown in Fig. 2.14. The behavior of the LVL (3) joint for this geometry was quite similar to the 45-mm-thick CLT (2) joint because, unlike the 40-mm-thick CLT (1) joint, there was no weak point after the yield moment. After the ultimate moment,

Table 2.5 – Results per material type for one geometry without screws or tenon inclination.

Material	Screw	Tenon Inclination (°)	Elastic stiffness (N·m/°)	Yield moment (N·m)	Ultimate rotation (°)	Ultimate moment (N·m)
CLT 40 mm	No	0	126.74	403.46	3.55	448.95
CLT 45 mm	No	0	123.23	448.21	3.21	644.73
LVL 39 mm	No	0	50.98	195.85	4.59	302.22

the decrease in performance was smaller and continued at a larger rotation than with the 45-mm-thick CLT panels (2). The behavior of this material was more ductile but less efficient from a mechanical performance perspective. Furthermore, the failure mode was different from that of the CLT samples (see Fig. 2.15). The grain orientation of the LVL panels was perpendicular to the joint length, except for three layers in which the grain orientation was parallel to the joint length. A block shear failure occurred in the layers perpendicular to the joint length (see Fig. 2.15a), while a delamination occurred in the layers parallel to the joint length (see Fig. 2.15b). In general, CLT panels (1) and (2) were stronger than LVL panels. The elastic stiffness, yield moment, and ultimate moment of the 40-mm-thick CLT panel were 60%, 51%, and 33% higher than the LVL panel performance, respectively (see Table 2.5). LVL connections allow for a larger rotation, which is, however, not relevant considering the SLS of the structure.

Concerning the two CLT panel types, their results are compared in Table 2.6. For the samples without screws or tenon inclinations (V SL 0), the elastic stiffness was almost the same but the yield and ultimate moment were 11% and 44% higher for the 45-mm-thick CLT panel (2), respectively. For the samples without screws and with a tenon inclination of 15°, the elastic stiffness, yield moment, and ultimate moment were 13%, 49%, and 50% higher for the 45-mm-thick CLT panel (2), respectively. The inclination of the tenon had a limited influence on the mechanical behavior in rotation for the 45-mm-thick CLT panel (2), while the yield moment decreased by 35% for the 40-mm-thick CLT panel (1). For the screwed samples (V SL 01 and 151), the yield moment was quite similar and the difference in ultimate moment was reduced.

Finally, the tests on single-layered joints showed that CLT panels have superior rotational performance for the considered joint geometries than the LVL panels generally used for IBOIS's research. Therefore, the 45-mm-thick CLT panel (2) is the best option for the Vidy theater project for multiple reasons:

- It has a greater stiffness than the 40-mm CLT panel (1).
- It has a greater yield moment.
- It can withstand a larger rotation in elastic part compared to the 40-mm CLT panel (1).
- Its ultimate moment is greater than CLT 40-mm (almost double).
- It demonstrates homogeneous behavior even with tenon inclination (between 0° to 15°).



## 2.4. Experimental investigations of single-layered connections

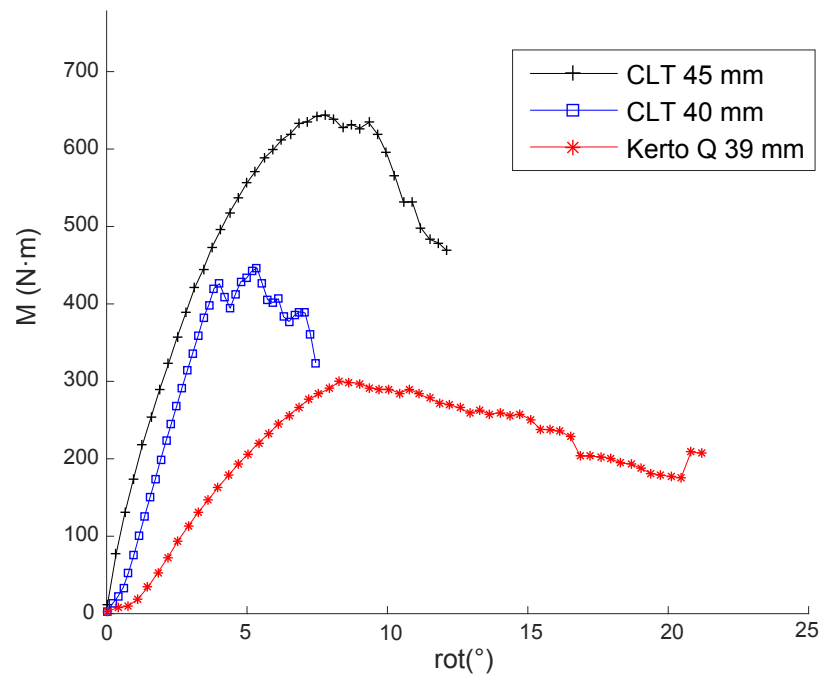


Figure 2.14 – Average moment-rotation curves per material type for single-layered TT joint in rotation (no screws or tenon inclination).

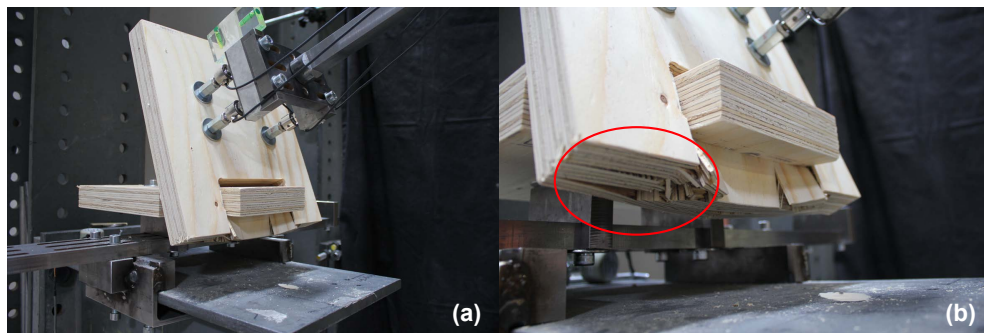


Figure 2.15 – Failure mode of the 39-mm spruce LVL joint in rotation.

Table 2.6 – Results for the 45-mm CLT joint using the 40-mm CLT joint as reference.

ID	Screw	Tenon inclination (°)	Elastic stiffness (%)	Yield moment (%)	Ultimate rotation (%)	Ultimate moment (%)
V SL 0	No		-3	11	-10	44
V SL 01	Yes	0	-11	2	4	37
V SL 15	No	15	13	49	2	50
V SL 151	Yes	15	-18	5	24	24

## 2.5 Experimental investigations of double-layered connections

In this section, the work was focused on the rotational load-carrying capacity of the double-layered TT joint connecting wall and roof elements as it is the most critical part of the structure according to the Bureau d'Etudes Weinand, who was in charge of the design calculations. The experimental research was performed with 40-mm-thick CLT due to time constraints of the project as well as manufacturer supply constraints.

### 2.5.1 Methods

Since the rotational setup designed for the single-layered TT joint was too small, another experimental setup that considered the geometrical constraints imposed by double-layered joints was used (see Fig. 2.16a). In this setup, the force from a 50-kN hydraulic jack was applied directly to the specimens with a wood stiffener screwed between the roof layers to transmit the load homogeneously to the joint. The wall panels were rigidly fastened with four bolts crossing the two layers, and the spacing between layers was maintained with two wood stiffeners. The displacement and loads were recorded using four linear variable differential transformer (LVDT) sensors and one load cell attached to the hydraulic jack, respectively.

### 2.5.2 Samples

Two different series of samples were tested as shown in Fig. 2.16b, for a total of 10 specimens. The joint lengths were of 250 and 150 mm for the double and single tenons, respectively. Dihedral angles of 90° and 110° were studied to observe the influence of this parameter, with the latter angle corresponding to the angle between wall and roof elements in the project. Specific screws (reference: 016536, type: assy, Würth Group, Künzelsau, Germany) were used to enhance the joint behavior, especially in traction. As mentioned previously, 40-mm-thick CLT panels were used for the tests, with a grain orientation perpendicular to the joint length.

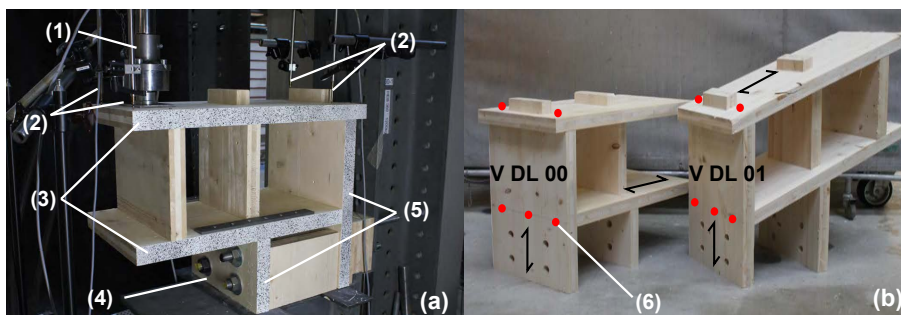


Figure 2.16 – (a) Rotational setup for double-layered TT connections: (1) load cell and hydraulic jack, (2) displacement sensors, (3) roof layers, (4) four bolts Ø24 mm, and (5) wall layers / (b) Double-layered samples: (6) location of screws.

### 2.5.3 Results and discussions

The failure mode of double-layered joints was found to be different from that of single-layered joints, as observed in Fig. 2.18. Double-layered joints were highly rigid, as the wall part did not follow the applied rotation. The roof section was thus blocked and reacted like a clamped beam. Therefore, only the cantilevered section of the roof exhibited deflections (see Fig. 2.18a). The cross-section of the roof panel, which was reduced due to the tenon length, failed at the bottom and top panels during the rotation (see Fig. 2.18b and c). The reduced sections of the bottom and top panels were 50 and 100 mm, respectively. The average results of each sample type are listed in Table 2.7 and shown in Fig. 2.19. The elastic stiffness, yield moment, and ultimate moment were 60%, 20%, and 36% greater, respectively, for the double-layered joint with a 90° dihedral angle than for a 110° dihedral angle. The dihedral angle is thus an important parameter that significantly influences the mechanical behavior of this joint.

A FE model was built by the Bureau d'Etudes Weinand, which was in charge of the design calculations for the Vidy theater. Based on this model, the maximum moment in a TT joint was located in the corner of a building segment with a value of 4.33 kN·m (see Fig. 2.17). From the tests, the maximum moment was 7.40 kN·m for the corresponding joint configuration. The 5% fractile characteristic value was 6.28 kN·m, following the calculation protocol of annex D of Eurocode 0 [31] (design assisted by testing). The characteristic value determined by tests was 45% greater than the FE model value. In addition, 40-mm-thick CLT was tested whereas 45-mm-thick CLT used for the project has greater rotational mechanical characteristics, as shown in Section 2.4.5. Moreover, the reduced section of 50 mm used in the tests (see Fig. 2.18a), due to geometrical and experimental constraints, is equal to 250 mm in the project. The double-layered TT connection can therefore be considered conservative with respect to the rotational load-carrying capacity for the Vidy theater project.

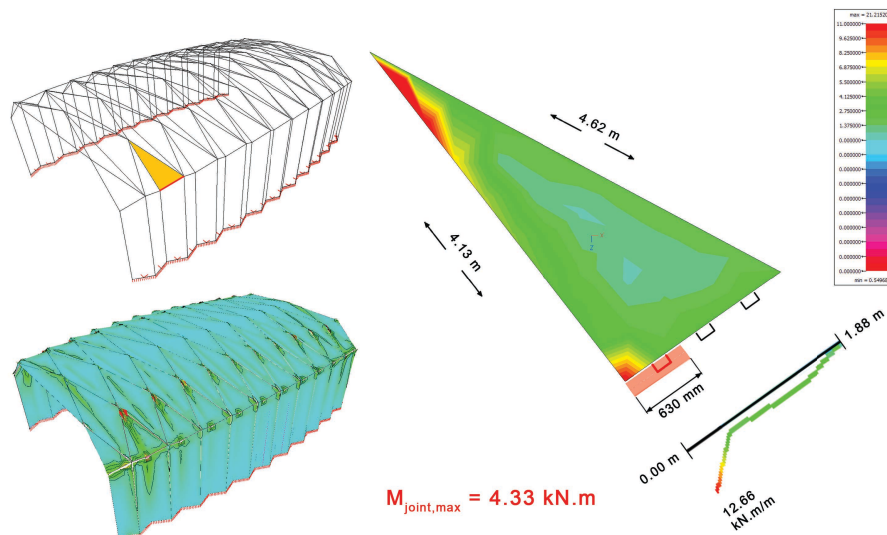


Figure 2.17 – Finite element model representation with the most loaded connection in rotation.

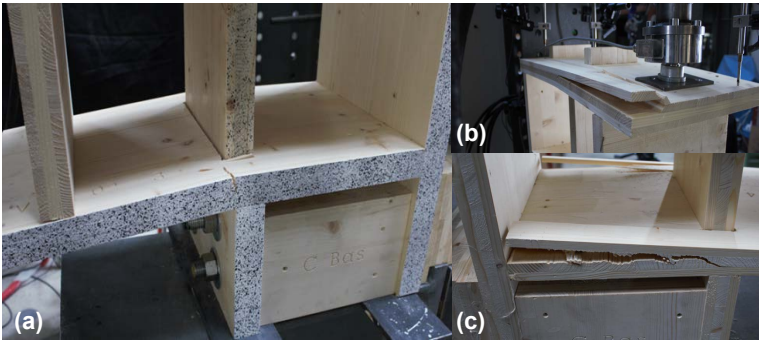


Figure 2.18 – Failure mode of a double-layered joint in rotation.

Table 2.7 – Results for the double-layered TT connections in rotation.

ID	Elastic stiffness (kN·m/°)	Yield moment (kN·m)	Ultimate rotation (°)	Ultimate moment (kN·m)
V DL 00	4.04	6.15	1.71	10.09
V DL 01	2.52	5.14	2.04	7.40
Difference	60%	20%	19%	36%

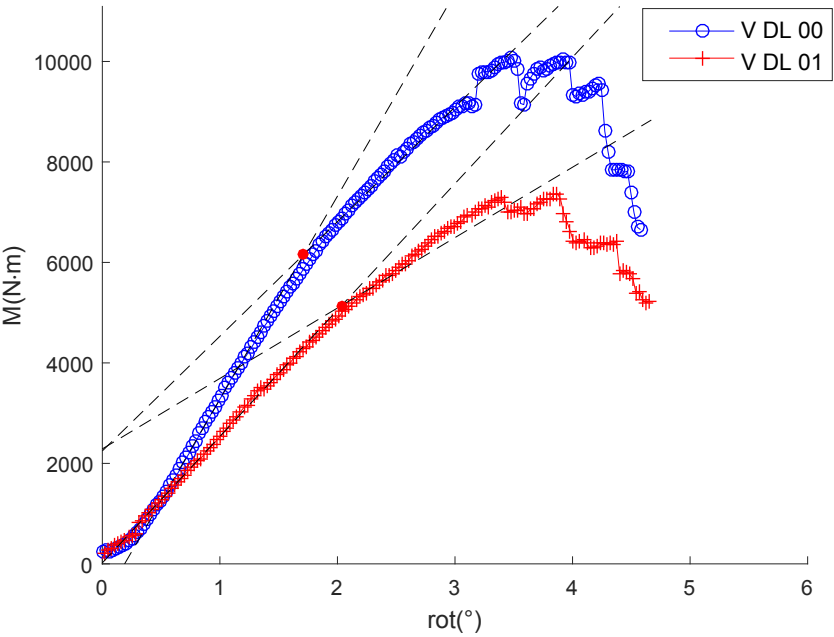


Figure 2.19 – Moment-rotation curves per sample type for the double-layered joints.

## **2.6 Conclusions**

This chapter presents the first building implementation of a double-layered timber folded-plate structure using digitally produced TT connections: the Vidy theater. Many years of research have successfully contributed to the design of this structure composed of 308 different plate shapes, 456 different joint angles, and over 3 000 TT connections.

The complexity of such a project can be managed through new design-to-production workflows, linking the fabrication process and its capabilities to the architectural design and planning processes. Specific CAD plugins were thus developed to automatically generate and fabricate the different structural parts based on input parameters, such as the folding form, plate thickness, and offset between the layers. These parameters remained variable, allowing great flexibility in the design during the project. Algorithms were packaged into custom-made software tools and were used by a number of collaborators, from the project designers (for the 3D geometry) to the CNC technicians (for the fabrication process). Specific computational tools for the design of digitally produced TT connections were efficiently used in a project environment with multiple stakeholders.

Concerning the structural design of the theater, experimental research was conducted on the rotational behavior of single- and double-layered TT connections. CLT panels were investigated for the first time and demonstrated superior rotational performance for this specific TT geometry than LVL panels generally used for such structures. As a result, CLT with a thickness of 45 mm was selected for the project. This highlights the potential of other engineered timber products for wood-wood connections.

The global structural verifications were performed by the Bureau d'Etudes Weinand with an FE model. No automated pipelines between the CAD and FE software packages were introduced for this project. Nonetheless, load-carrying capacity in rotation was experimentally verified in the most loaded connection, located in a corner arch, to complement the design office's calculations. The moment-rotation capacity of the connection largely satisfied the requirement of the project. This result confirmed that TT connections are an efficient solution for the assembly of timber plate structures.

Finally, this preliminary work proved the feasibility of this construction system at the building scale. With the knowledge gained from this project, building components for standardized applications can now be developed using TT connections.



## 3 Standardized construction system: development and potential

---

This chapter is based on: J. Gamarro, I. Lemaître and Y. Weinand. Mechanical Characterization of Timber Structural Elements using Integral Mechanical Attachments. In *Proceedings of the World Conference on Timber Engineering*. Seoul, South Korea, 2018.

---

### 3.1 Introduction

The preliminary work performed on the Vidy theater described in Chapter 2 has shown the great potential of digitally produced connections for timber plate structures and proven the feasibility of this construction technique at the building scale. However, most research has focused on complex geometries, such as the folded and free-form structures described in Section 1.1.3. With the knowledge gained from research and project implementations, TT connections could be used for more standardized building elements such as roof or slab components with basic geometry. This joining technique offers an alternative to bonding processes and steel fasteners for small and medium-sized timber companies, which generally have the required production tools (CAD, CAM, and CNC), as mentioned in Section 1.1.4.

Therefore, the main objective of this chapter is to develop a standardized construction system for basic building components using only TT connections. Bonding processes or steel fasteners are thus not considered within this work. Based on recent research and new construction paradigms, the construction concept is presented with different connection possibilities depending on fabrication capacities, materials, and assembly insertions. The potential of this new system is then studied through a case-study conducted in collaboration with two industry partners. An FE model is developed for structural investigations, and experimental tests on specific TT configurations are performed to run the model. Subsequently, a comparison with glued and nailed connections, generally used in timber construction, is realized to evaluate the performance of this new construction system.

The chapter is structured as follows:

- Section 3.2 proposes a brief state-of-the-art of recent standardized construction systems using wood-wood connections.
- Section 3.3 presents the development of the new standardized construction system.
- Section 3.4 introduces the case-study.
- Section 3.5 describes the development of the FE model and the experimental study on specific TT connections.
- Section 3.6 discusses the results of the case-study.
- Section 3.7 summarizes the main conclusions.

### 3.2 State-of-the-art

New construction paradigms have emerged with the rise of digital fabrication. A specific approach called “design for manufacture and assembly” (DfMA) [11, 155] has been increasingly applied to the construction industry. The DfMA approach consists in decomposing a construction into different subsystems: an example is the product-based approach used in many other industries (cars, furniture, etc.), as shown in Fig. 3.1. Although buildings cannot be compared to these products for various reasons (unique form and construction site each time), the standardization of components can enhance the efficiency of the construction process to meet ever-increasing normative requirements. The main goal of this approach is to minimize the costs of different stages of construction throughout the life of the building: from manufacturing, assembly, and maintenance to dismantling.

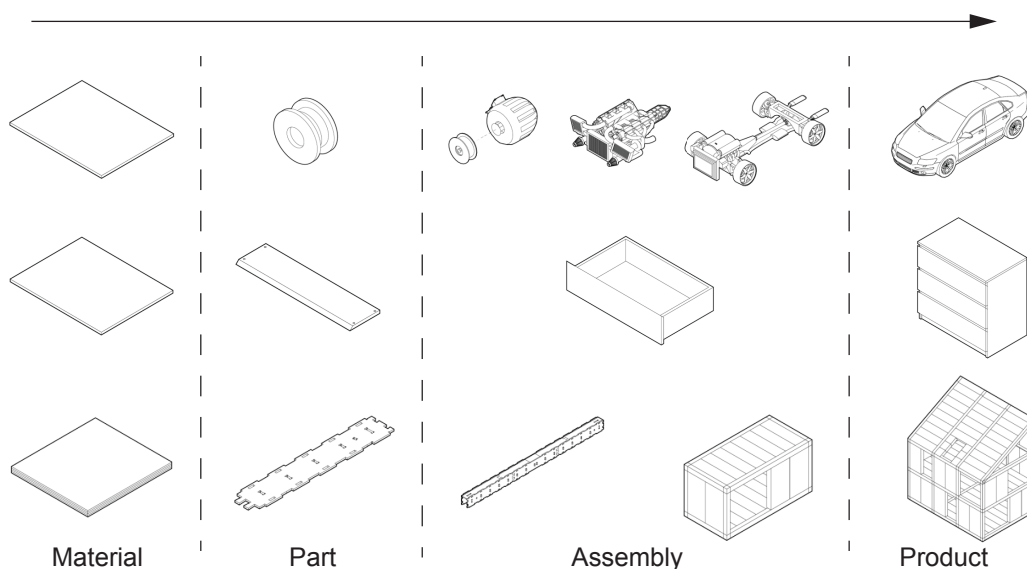


Figure 3.1 – DfMA product-based approach: comparison of the construction with car and furniture industries. Based on [155].



DfMA can be applied to different standardized construction methods, from off-site to flat-pack systems (see Fig. 3.2). However, off-site and mass-construction methods require large-scale centralized factories with large investments, high transportation costs, and products that are not always flexible. Nevertheless, bonding processes generally used in construction require such factories and heavy industrial processes with continuous production controls. On the other hand, flat-pack methods can provide a more distributed and resilient manufacturing process accessible to SMEs, which is beneficial for the local economy and environment. Production flexibility and transport costs are optimized, while efficiency can decrease due to on-site assembly. A combination of flat-pack and prefabricated methods can be considered for SMEs to improve the efficiency of the construction process.

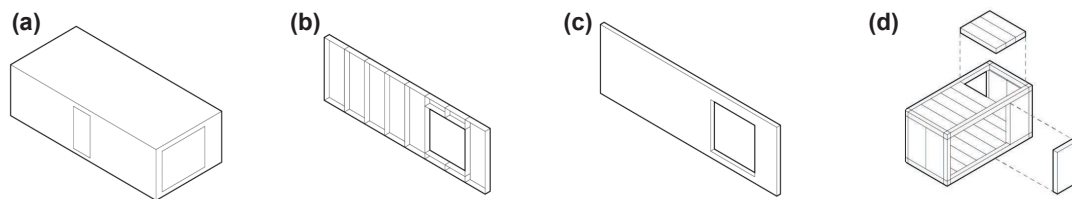


Figure 3.2 – Construction methods: (a) Off-site / (b) Prefabricated panel / (c) Mass panel / (d) Flat-pack. Based on [155].

Based on this idea, the wood grammar frame, presented by Sass [133, 134] in 2006, describes the use of new digital workflows, from design-to-production, for standard housing components using wood-wood connections. It introduces the concept of 2D flat-packs directly delivered on-site, where the different elements of a 3D component (a slab, for example) are assembled on-site to minimize the volume transported (see Fig. 3.3). Only small plates are thus used so as to be manually maneuverable by workers and reconstitute larger spans. Several projects and research studies have been performed using this construction paradigm, such as the WikiHouse developed by the Open Systems Lab (Open Systems Lab<sup>®</sup>, England) [150, 165], the Sim[PLY] construction system (Clemson University School of Architecture, USA) [3, 149], the X-Frame system (X-Frame Limited<sup>®</sup>, New Zealand) [42, 168], and the Facit Homes system

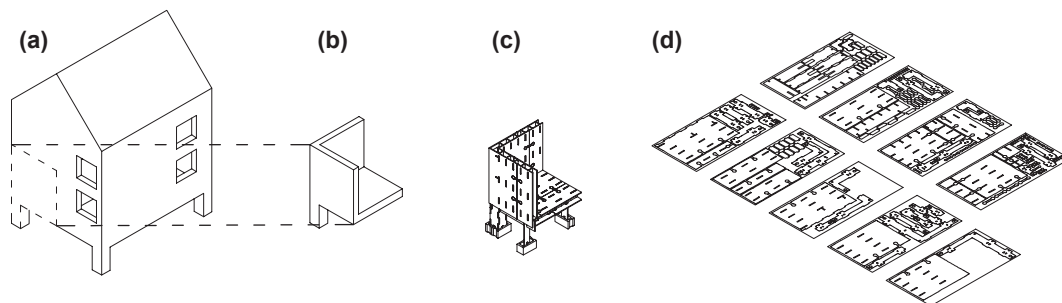


Figure 3.3 – Flat-pack system: (a) 3D structure / (b) Part of the 3D structure / (c) Decomposition of the 3D element into standard panels / (d) Panels and cuts needed to reconstitute the structural element. Based on [133].

### Chapter 3. Standardized construction system: development and potential

(Facit Homes Limited<sup>®</sup>, London, England) [40]. These construction systems are illustrated in Fig. 3.4. They were mainly developed in an academic environment (X-Frame system, Sim[PLY], Wood Frame Grammar) or in non-profit organizations such as the Open Systems Lab (Wiki-House). Only the company Facit Homes Limited<sup>®</sup> in the UK is already business-oriented and available on the construction market. Most of these organizations conduct pilot case-studies to continue their development and address construction challenges. Regarding mechanical performance, no clear guidelines exist for the structural design of such construction systems, as they use different types of wood-wood connections, as well as various types of steel fastener. Nonetheless, recent research on wood-wood connections for timber plate structures, performed at the University of Queensland (St Lucia, Australia), has highlighted the potential structural performance of standardized building elements such as walls with flat or curved geometries [2, 4, 50].



Figure 3.4 – (a) WikiHouse [165] / (b) Wood Frame Grammar system [133] / (c) X-Frame system [168] / (d) Sim[PLY] system [149] / (e) Facit Homes system [40].

### 3.3 Proposal of a standardized construction system

According to recent research and the new construction paradigm introduced above, a standardized construction system made of engineered thin-timber panels using TT connections was developed. The scope of the study and the construction system are presented in this section.

#### 3.3.1 Scope

For the development of a standardized structural system using TT connections, the scope was defined by the fabrication constraints and materials. This research was mainly conducted with the available production tools of the IBOIS laboratory: a five-axis CNC machine (model: MM7S, MAKAS System GmbH, Nersingen, Germany) and a six-axis robot (model: 6400R M2000, ABB, Zurich, Switzerland), as shown in Fig. 3.5. The CNC machine has relatively small dimensions with a cutting capacity of only 2.5 by 1.5 m, which is at least equivalent to machines operating in SMEs. The maximum height is not of major importance, as only engineered timber products in the form of thin panels with a thickness of under 50 mm are considered, such as CLT, LVL, and oriented strand board (OSB). Glued laminated timber (GLT), generally used for beam elements, and fiberboard, rarely employed in structural applications, are not within the scope of this research (see Fig. 3.6). The six-axis robot was installed at IBOIS at the end of 2019 for research into the automatic assembly of prefabricated timber elements. It was not used for the present fabrication research due to constraints imposed by the timeline.

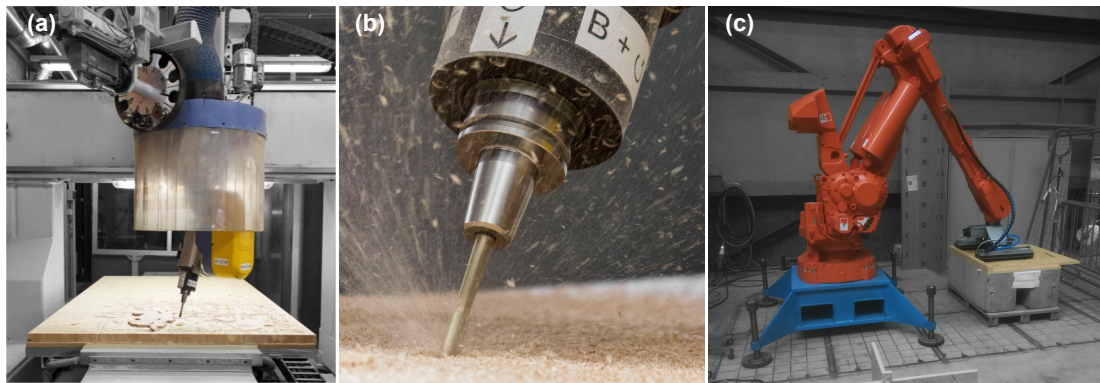


Figure 3.5 – Production tools at IBOIS / (a) five-axis CNC machine / (b) Zoom on the cutting tool during the machining process / (c) six-axis robot when manipulating a panel.

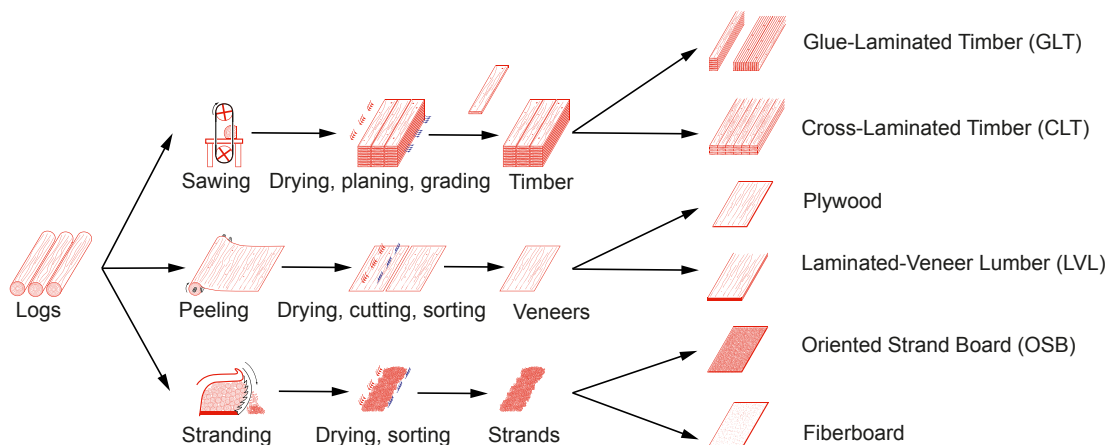


Figure 3.6 – Engineered timber products. Based on [112].

### 3.3.2 The construction system

The main goal of this research was to develop a structural system that can reconstitute elements with a span of 5 to 10 m exclusively with commonly available supplier-sized panels and TT connections. Most standard dimensions of timber panels on the timber construction market range from 2.5 by 1.25 m to 5 by 2.5 m. In addition, the cutting-capacity limitation of production tools for SMEs may also preclude the use of larger panels.

Therefore, the proposed structural element is composed of two rows of parallel beams (webs) connected to two top and bottom panel layers (flanges) through TT connections, with panels arranged in staggered rows to reconstitute the total length of the element with small panels (see Fig. 3.7). This concept can thus achieve spans greater than the length of the panels used without the addition of bonding processes or mechanical fasteners. Due to this specificity, there are discontinuities along the length of elements that can reduce the structural performance (see Fig. 3.7, (10) and (11)). This is not common for interconnected timber elements, which generally show continuity along the element length. Discontinuities along the length of the element are taken up by different connections, which transfers the force flow from one panel to another between the different layers in flanges and webs.

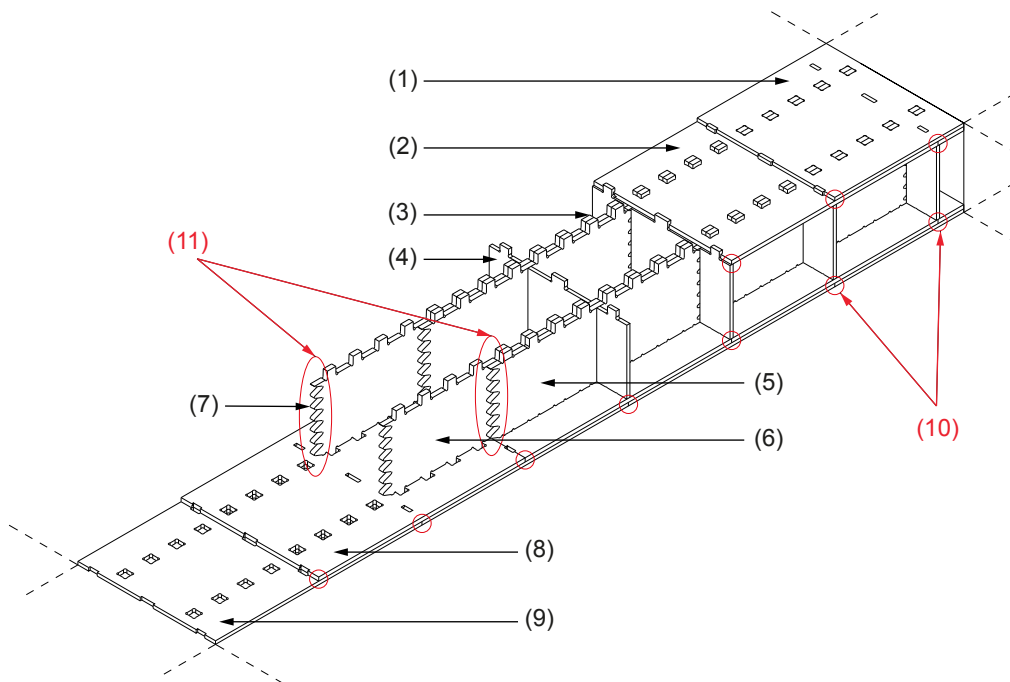


Figure 3.7 – Construction system: (1) top flange exterior layer, (2) top flange interior layer, (3) through-tenon connection, (4) transversal beam, (5) web first layer, (6) web second layer, (7) longitudinal connection for web, (8) bottom flange interior layer, (9) bottom flange exterior layer, (10) discontinuities between flanges, and (11) discontinuities between webs.

### 3.3. Proposal of a standardized construction system

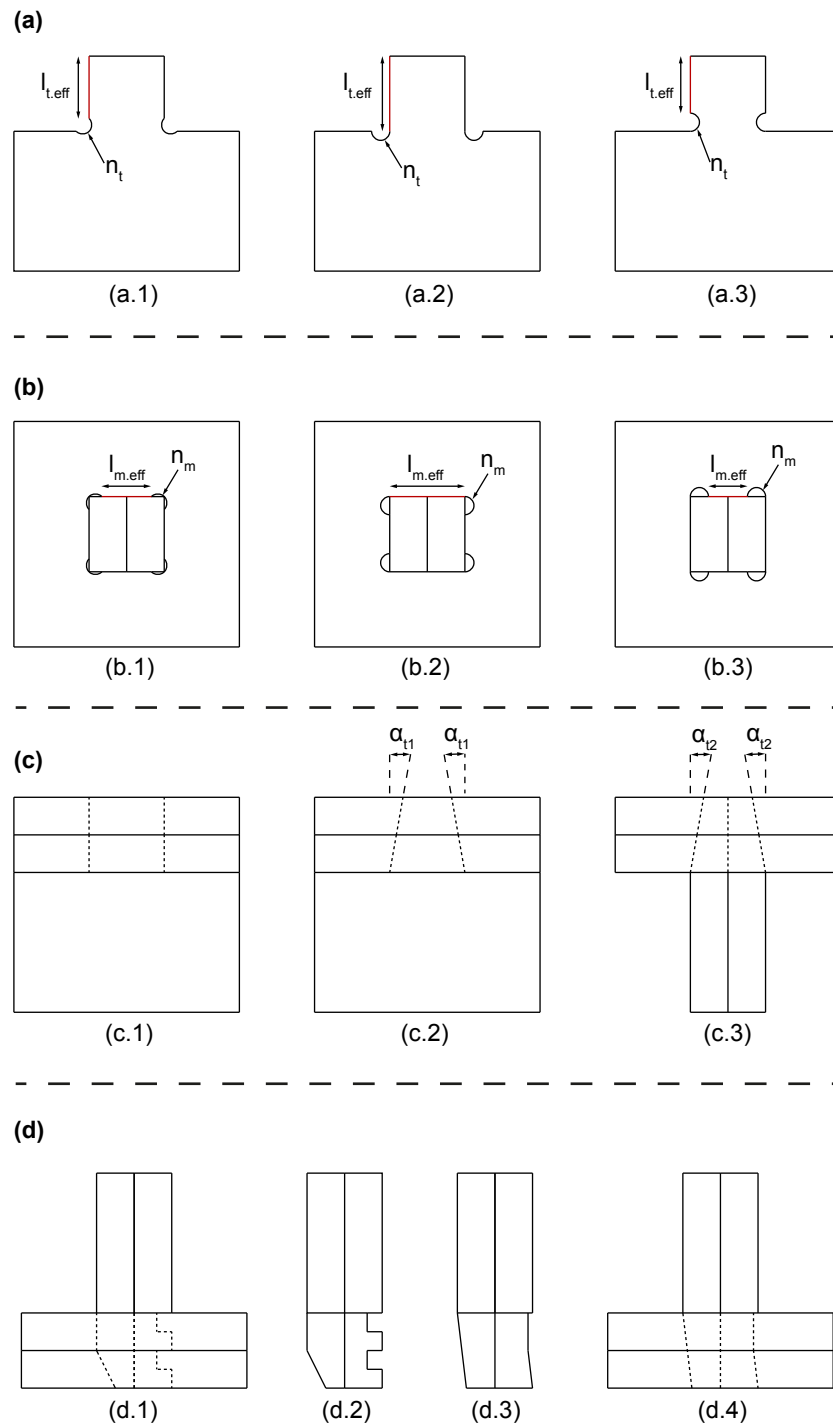


Figure 3.8 – Through-tenon joint parameters: (a) Effective tenon length as function of notch position (front view) / (b) Effective mortise length as function of notch position (top view) / (c) Possible insertion angles (front view and side view for c.3) / (d) Bottom joint for tensile forces (side view).



The main connections between webs and flanges are achieved with TT joints (see Fig. 3.7, (3)). Different TT geometries can be used depending on various parameters, such as the notch position due to the diameter of the cutting tool during CNC manufacturing, as shown in Fig. 3.8a and b. The recommended options for the notch position are (a.2) and (b.2), as the effective tenon and mortise length,  $l_{t,eff}$  and  $l_{m,eff}$ , respectively, are both maximized. Other configurations can be used if needed for a specific application. In addition, two insertion angles  $\alpha_{t1}$  and  $\alpha_{t2}$  can be introduced to facilitate the assembly of the joint (see Fig. 3.8c). These parameters are crucial, as the feasibility of the system depends on the user's ability to assemble several joints in series. The angle  $\alpha_{t1}$  is easier to manufacture, as only three-axis cutting is necessary, compared to five-axis cutting required for the angle  $\alpha_{t2}$ . Thus, the angle  $\alpha_{t1}$  is the preferred option to optimize effort in terms of programming and machining time even if a five-axis operation is still required for the mortise. Nonetheless, both  $\alpha_{t1}$  and  $\alpha_{t2}$  may be required depending on material tolerances.

For the bottom layer, another type of TT joint can be applied to avoid the use of mechanical fasteners to withstand the tensile forces and self-weight of the bottom flange, as shown in Fig. 3.8d. The assembly sequence of such joint geometry follows different insertion vectors that lock the element in its final position (see Fig. 3.9). However, this type of joint also requires additional machining as well as a specific assembly sequence, which can be difficult to follow, depending on whether the element is assembled on-site or prefabricated. Option (d.2) was tested on small-scale prototypes and demonstrated highly fragile behavior during assembly of the different parts. Option (d.3) is preferable if this type of joint is applied in the structure.

Concerning the discontinuities between webs in the same row (see Fig. 3.7, (11)), additional connections to TT joints can be added to transfer the significant shear forces between these elements and improve the mechanical behavior of the structural elements. Finger joints are an appropriate choice since they have a simple and efficient geometry that transfers such stresses (see Fig. 3.10a). In addition, they are easy to assemble and require only three-axis cutting. However, it is necessary to respect a particular assembly sequence if finger joints are used. Webs must be assembled before connecting flanges with TT joints, else the assembly is not feasible. Other alternatives to the finger joint are possible, such as the dovetail joint, the butterfly spline, the round joint, and the dumb-bell spline (see Fig. 3.10b, c, d, and e, respectively). These types of joints demand a longer machining time and are more challenging to assemble. Nonetheless, they can withstand tensile stress in addition to shear stress [68, 170]. This may be of interest in specific applications.

As shown in Fig. 3.7, (4), transversal beams can be distributed along the length of the elements to prevent the lateral buckling of webs and reinforce the lateral behavior of a structural element. These beams are positioned between webs and connected only to flanges with TT joints. They are discontinuous so as not to weaken the cross-section of the longitudinal beams. Nevertheless, if a structural element is used as diaphragm in the structure in order to resist lateral loads, continuous transversal beams can be considered with a special assembly, such as a half-lap joint with longitudinal beams.

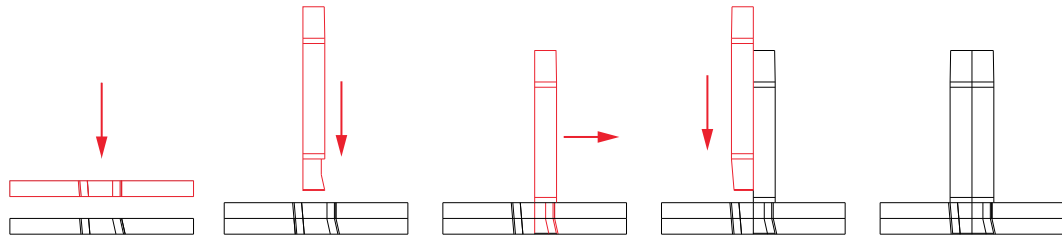


Figure 3.9 – Assembly sequence for bottom TT joints.

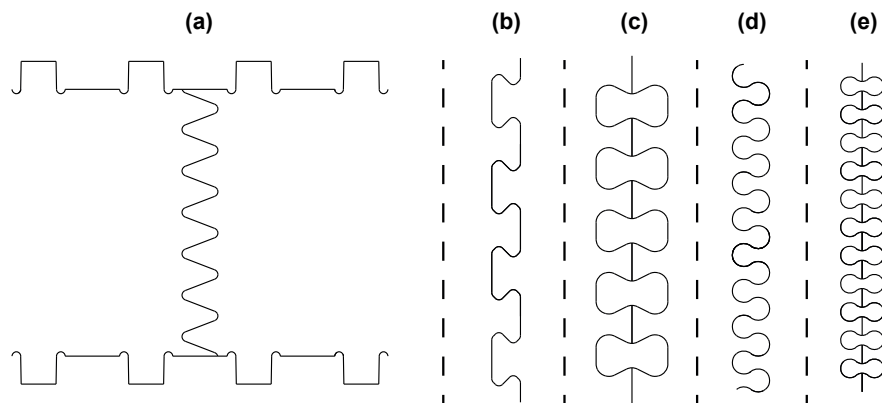


Figure 3.10 – Longitudinal connections for web: (a) Finger joint / (b) Dovetail joint / (c) Butterfly spline / (d) Round joint / (e) Dumb-bell spline.

Finally, this concept of a new structural system using TT connections can be used with different engineered timber products and various geometrical configurations depending on project requirements. The fiber orientation of each panel is preferably positioned in the lengthwise direction of the element.

### 3.4 Case-study

The recent achievements of construction systems using digitally produced wood-wood connections have increased the industry's interest in this low-tech technology. Therefore, a technology transfer has been established with two companies working in the timber industry: MOBIC SA (Harzé, Belgium), specialized in timber construction, and IMAX PRO (Harzé, Belgium), specialized in robotic solutions for timber constructions.

Based on the construction system presented in Section 3.3.2, the aim of this collaboration is to develop prefabricated roof elements for the new industrial hall of the company MOBIC SA (see Fig. 3.11) and more generally, a standardized roof component for housing. The construction of this building of about 7,000 m<sup>2</sup> is planned for 2021 and its design was performed in collaboration with the Bureau d'Etudes Weinand. The structure consists of several building segments assembled in series. Inside these building segments, the roof is divided into elements of approximately 6 m in span, as shown in Fig. 3.11c. This study focuses on these roof elements, which are exclusively made of spruce OSB panels to reduce costs, as OSB is a relatively economical material. Mechanical fasteners are rarely used for OSB edgewise connections compared to bonding joints, which creates the opportunity to use TT joints more frequently with this material.

The overall dimensions of an element are 6.15 m in length, 2.5 m in width, and 0.3 m in height. It is composed of five longitudinal and nine transversal beams, all evenly spaced along their specific directions. For the connections, TT joints were used with a spacing of 50 mm and the configurations (a.2) and (b.1), which are illustrated in Fig. 3.8a and b, respectively. The bottom TT joint with configuration (d.3), displayed in Fig. 3.8d, was chosen to connect the bottom flanges to the webs and prevent the use of mechanical fasteners. An insertion angle  $\alpha_{t1}$  of 1° was introduced to ease the assembly of the top and bottom TT joints. A detailed plan of the roof element with joint geometries can be found in Appendix A.1 (see Fig. A.2 and A.1).

In the particular context of this case-study, a prefabricated approach was preferred instead of a flat-pack system assembled onsite. In fact, the fabrication research was performed at MOBIC SA with a robotic line equipped with special tools for the machining of OSB panels (see Fig. 3.12b). The robotic line can cut panels over a large distance if needed. As a result, it was decided to use continuous panels instead of small size panels (as described in Section 3.3.2) to increase the structural performance of the element and reduce the construction time of the project. The transportation costs were not an issue as the construction site was close to the company factory. Different prototypes with various lengths and geometries were successfully manufactured, as shown in Fig. 3.12. The fabrication process of this new structural element therefore demonstrated the feasibility of its implementation in the production process of a timber company using digital fabrication techniques.



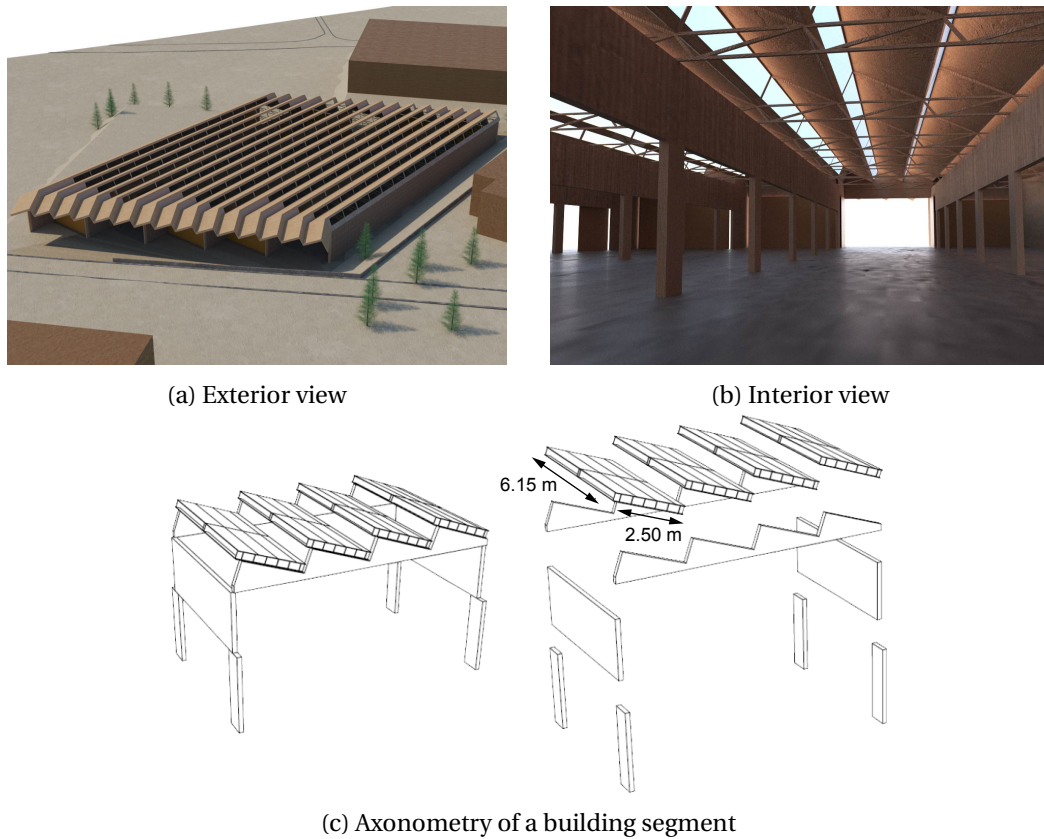


Figure 3.11 – MOBIC SA industrial-hall project.

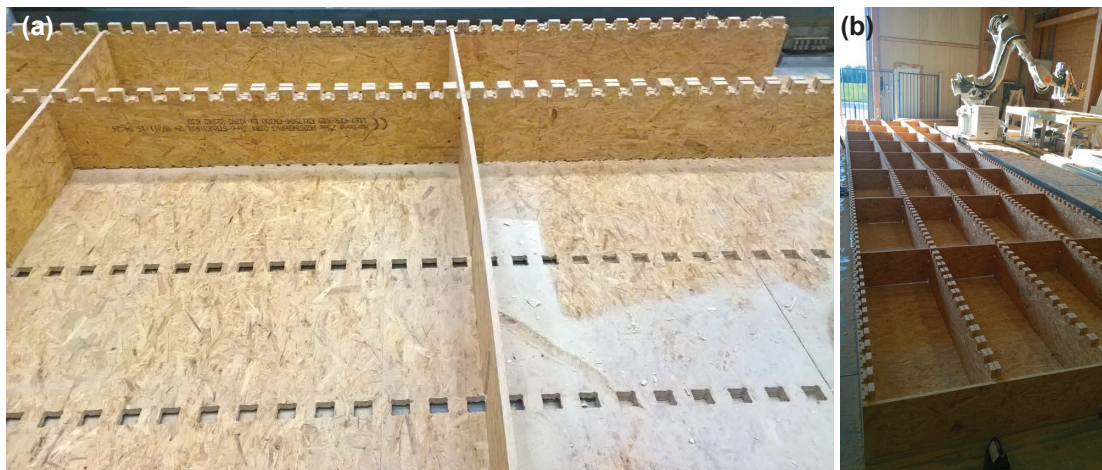


Figure 3.12 – Prefabrication at MOBIC SA: (a) OSB prefabricated element during fabrication / (b) Robotic line equipped with special tools for OSB panels. [Photograph credit: Cedric Moutschen, MOBIC SA]

### 3.5 Numerical model

The structural-performance potential of the roof element presented in Section 3.4 was investigated through the development of an FE model<sup>1</sup>. The design-to-production workflow is an essential aspect of this type of construction system, as highlighted in Chapter 2. Therefore, automated pipelines between CAD and FE software packages were developed for the roof element based on geometrical input parameters, as shown in Fig. 3.13. The software Rhinoceros® (Robert McNeel & Associates, Seattle, USA) and its scripting interface were used for the automatic generation of the geometry, for both the design and calculation model. The geometry was imported automatically to the FE analysis software Abaqus<sup>TM</sup>, version 6.12 (Dassault Systèmes, Vélizy-Villacoublay, France) using custom scripting code. The programming language Python [110] was the coding language common to the different interfaces. In addition, tests were performed to assess the behavior of the TT connections specific to the case-study and implement their mechanical properties in the FE model. Only the load-displacement response of the roof element was of interest in this numerical study as it is generally the main dimensioning criterion for interconnected elements that use semi-rigid connections. The load-carrying capacity and the stress distribution in the joints were not verified by this first approach.

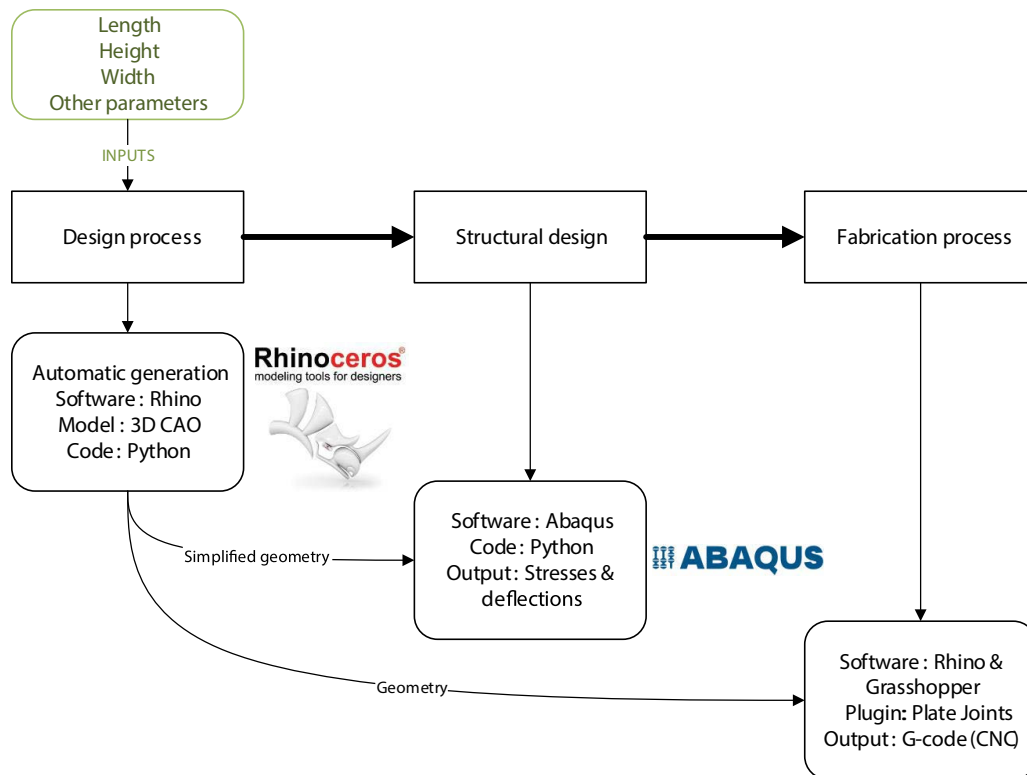


Figure 3.13 – Automatic pipelines from CAD to FE analysis software packages.

<sup>1</sup>The model is based on the work of Stitic [173]. More recent research has since been conducted on this topic [101, 153], and a more detailed review of calculation models is presented in Chapter 4.

### 3.5.1 Modeling approach

#### Geometry

Simplified assumptions were made for the calculation of the roof element, since the use of 3D solid elements is too computationally expensive and complex to model correctly for large-scale structures [173]. Plate theory was thus applied for the mathematical model and panels were represented using conventional shell elements as the panel thickness-to-length ratio was relatively low ( $t/L \leq 0.05$ ) [21]. The conventional shell elements represented the mid-surfaces of the targeted 3D elements with their section properties. Sections were defined according to the geometry displayed in Appendix A.1 (see Fig. A.1). For mesh properties, S4R elements [21] were selected with a uniform size of 50 mm per element, based on a mesh convergence study. S4R elements are defined as four-node, quadrilateral shell elements with large-strain formulation. In addition, the layers composing the flanges and webs were considered as single shell elements (see Fig. 3.14c and d). Transversal beams were represented as small shell elements rigidly connected to longitudinal beams (see Fig. 3.14b), as they had a minor influence on the longitudinal load-displacement response of the element. As a result, a possible half-lap joint between transversal and longitudinal beams was neglected in an initial approach. The inclination of  $20^\circ$  initially planned in the project was not considered in this preliminary investigation. The final shell geometry of the studied element is represented in Fig. 3.16a.

#### Semi-rigid connections

The TT connections were modeled with spring elements to address their semi-rigid behavior. Plate surfaces were partitioned to define the exact location of each connection (see Fig. 3.14, red lines). One TT connection was divided into three springs along the length of the assembly, as shown in Fig. 3.16b. Each spring had three translational and three rotational degrees of freedom (DOF). Only the in-plane shear stiffness of the connection was investigated, which represents the translational DOF in the length direction of the element. The other two translational DOFs were considered to be rigid, while rotational DOFs were considered to be hinged. The in-plane shear stiffness of TT joints as well as nailed connections was defined according to the experimental tests performed in Section 3.5.2. For glued connections, rigid ties were implemented instead of spring elements.

#### Material

Panels of OSB type 4 were defined as a single-layer orthotropic material as described by Zhu et al. [171, 172]. The material properties of the OSB shell-model were considered linear-elastic and were defined by the Lamina type [21]. Only the values of  $E_1$ ,  $E_2$ ,  $\nu_{12}$ ,  $G_{12}$ ,  $G_{13}$ , and  $G_{23}$ , where 1 is the direction parallel to the strand, 2 is the direction perpendicular to the strand, and 3 is the normal to the plane, are required to model an orthotropic shell material. The

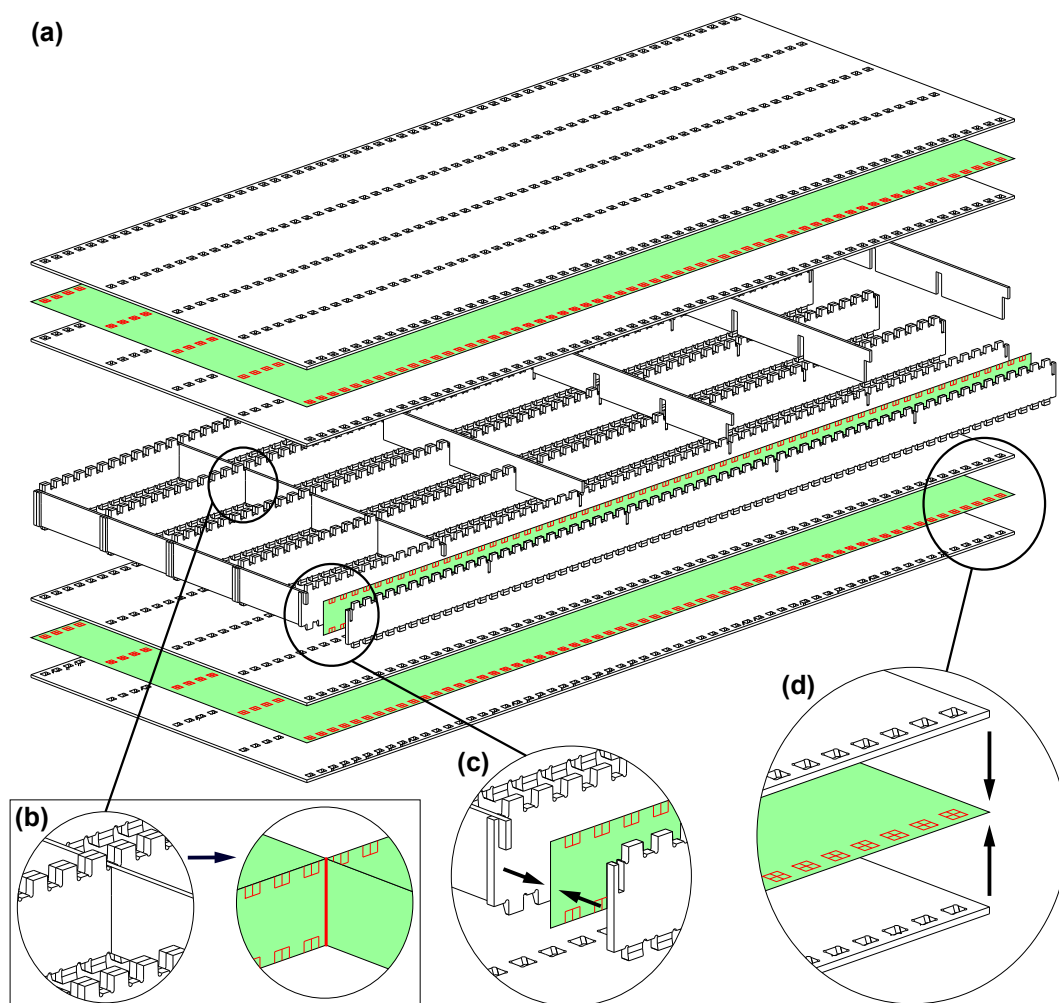


Figure 3.14 – Simplified shell geometry the FE analysis: (a) Exploded view of the studied roof element / (b) Detail of the rigid connection between transversal and longitudinal beams / (c) Model representation of the two longitudinal beam layers as one shell element / (d) Model representation of the two flange layers as one shell element. The red lines represent the shell partition for the connections.

Table 3.1 – Material properties of OSB type 4 for numerical modeling.

Constant	Description	Unit	Value
$\rho$	Density	kg/m <sup>3</sup>	620
$E_1$	Elastic modulus parallel to strand	MPa	4800
$E_2$	Elastic modulus parallel to strand	MPa	1900
$\nu_{12}$	Poisson coefficient	–	0.25
$G_{12}$	Shear moduli	MPa	1090
$G_{13}$		MPa	60
$G_{23}$		MPa	60

shear moduli  $G_{13}$  and  $G_{23}$  are indicated to model the transverse shear deformation. The values of the elastic properties ( $E_i$  and  $G_{ij}$ ) were determined according to the supplier technical document of the industrial partner [102] and the standard EN 12369 [29]. The Poisson ratio coefficient  $\nu_{12}$  was chosen based on literature results [85]. The values of each engineering constant are listed in Table 3.1.

#### **Loading configuration**

The load applied to the studied element was determined according to Eurocode 1 [32] by the Bureau d'Etudes Weinand, considering the location of the case-study. As this preliminary investigation focused on the displacement of the elements, the SLS formulation for the loading configuration was applied. Dead loads were taken into consideration and the SLS loads were distributed uniformly on the top flange of the structural element.

#### **Information transfer from CAD to FE**

A CAD plugin was developed for the automatic generation of the simplified shell geometry, which was imported automatically into the FE analysis software via the Abaqus<sup>TM</sup> scripting interface (see Fig. 3.13). This procedure was accomplished through the following steps:

1. Simplified geometry generation based on a specific indexation system of coordinates for the different elements and joint locations (see Fig. 3.15a and 3.15b).
2. Geometry importation from CAD to FE analysis software packages via the ACIS SAT file format (see Fig. 3.16a).
3. Definition of new coordinates for each element in the FE software.
4. Assignment of section and material properties.
5. Mesh generation.
6. Identification of connection locations via vertices (see Fig. 3.16b).
7. Assignment of spring properties or rigid ties at vertices locations.
8. Implementation of the loading configuration.
9. Calculation start.

Steps 1 and 2 were performed using the CAD plugin while the other steps were performed via the Abaqus<sup>TM</sup> scripting interface. Recently, a new design framework has been developed by Nguyen et al.[101] for the automatic generation of shell FE models for timber structures using a large number of wood-wood connections.

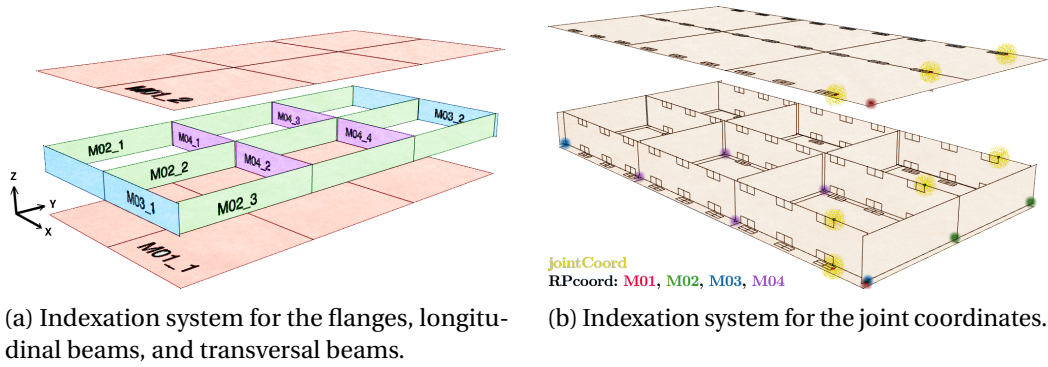


Figure 3.15 – Generation of the simplified geometry for the FE analysis software.

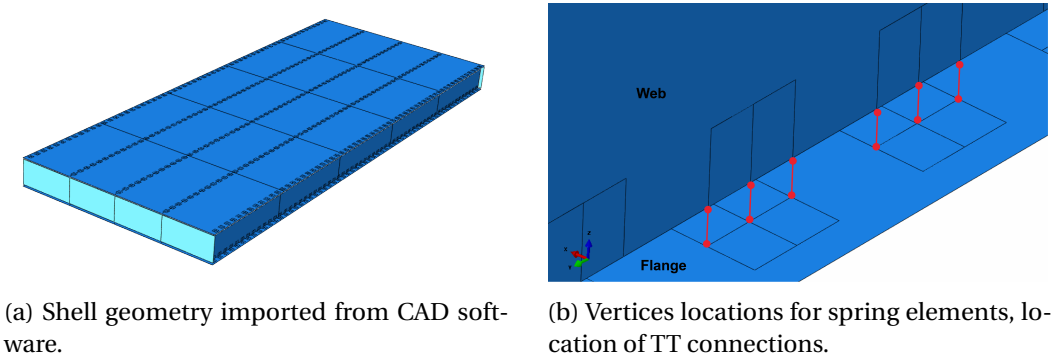


Figure 3.16 – Model representation in the FE analysis software Abaqus™.

### 3.5.2 Connection parameters

Based on the numerical modeling approach described above, the in-plane shear stiffness of the specific TT joint related to the case-study was experimentally studied to define the spring value for the numerical model. Failure modes and load-carrying capacities were not investigated in this experimental work. A more exhaustive study on the behavior of TT connections can be found in Chapter 5.

### Material and methods

For the case-study, several TT configurations were tested to investigate the influence of the top and bottom geometry as well as the different possible longitudinal beam thicknesses (18 or 25 mm). Seven series of different geometries consisting of three replicates were tested. The sample properties are listed in Table 3.2 and illustrated in Fig. 3.17. The top assembly was designed according to the configurations (a.2) and (b.1) in Fig. 3.8a and b, respectively, while the bottom assembly was designed according to (d.3) in Fig. 3.8d. The tensile behavior of the



bottom assembly was not studied during this investigation. The studied TT joint length was 50 mm for each sample and only the spacing between joints was variable (one configuration with a spacing of 100 mm). An insertion angle  $\alpha_{t1}$  of  $1^\circ$  was introduced for all the samples. The fiber orientation (FO) of OSB panels was parallel to the element length, except for the inner layer of flanges (first layer according to Fig. 3.17a). The notch diameter was equal to 13 mm for all samples. Configurations were defined in collaboration with the industrial partner according to manufacturing and supply possibilities.

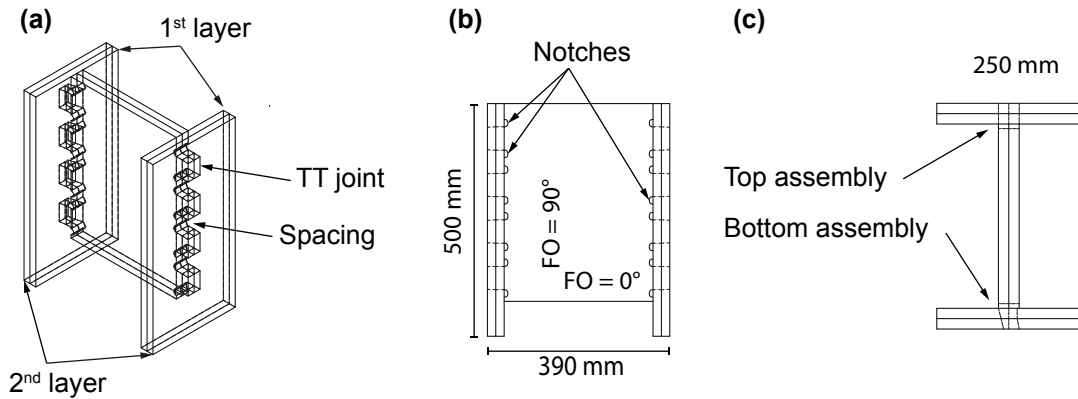


Figure 3.17 – Sample geometry: (a) Axonometry / (b) Side view / (c) Top view.

Table 3.2 – Sample properties.

ID	Nbr	Thickness (mm)			Fiber orientation ( $^\circ$ )			Spacing (mm)	Assembly type
		2nd layer	1st layer	Web	2nd layer	1st layer	Web		
M1	3	18	18	2×18	90	0	90	50	top
M2	3	18	18	2×18	90	0	90	50	bottom
M3	3	18	18	2×25	90	0	90	50	top
M4	3	18	18	2×25	90	0	90	50	bottom
M5	3	18	18	2×25	90	0	90	100	top
M6	3	18	18	2×25	90	0	90	50	top & bottom
M7	3	18	18	2×18	90	0	90	50	top & bottom

Samples were tested using a push-out test configuration as shown in Fig. 3.18a. A 300 kN hydraulic jack (model SEV-16071000, Schalcher Engineering GmbH, Wolfertswil, Switzerland) applied pressure directly to the web, which transmitted the load in the TT joints and the flanges placed on the ground. A beech LVL panel was used to avoid local indentation on the web section. Displacement and loads were recorded by the cylinder sensors. A load-control method was followed with an approximate test duration of 10 minutes per test (partially based on [35]). A total of 19 specimens were tested.

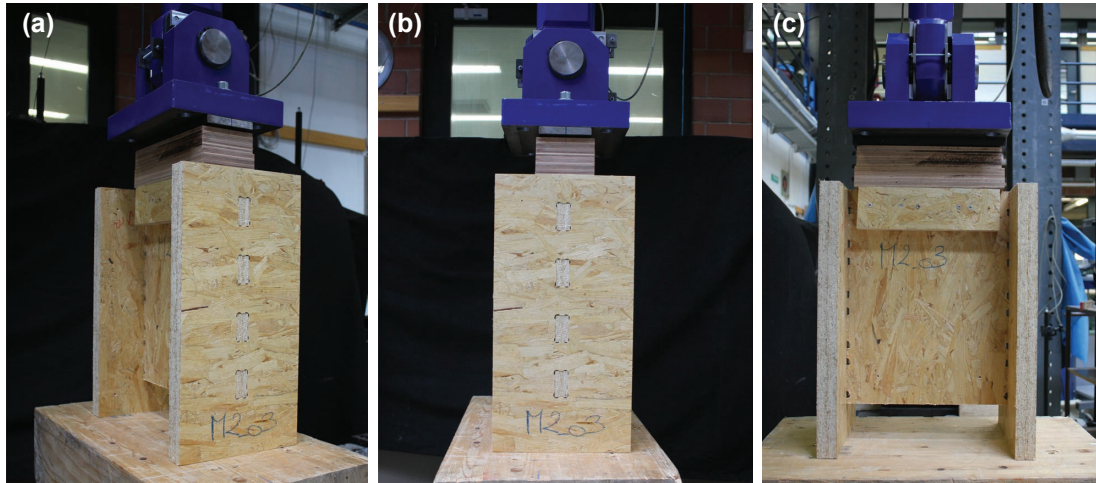


Figure 3.18 – Experimental Setup: (a) Axonometry view / (b) Front view / (c) Side view.

#### Results and discussion

From the test results, two values were obtained: first, the maximum force ( $F_{max}$ ) applied to the sample and second, the shear stiffness ( $K_y$ ) defined by a linear regression from 10 to 40% of  $F_{max}$ . The load distribution in the different joints composing one experimental sample was assumed to be equal in each joint. The stiffness of each joint ( $K_{y,i}$ ) was thus defined according to Equation (3.1), where the total stiffness of the sample ( $K_{y,sample}$ ) is divided by the total number of TT joints ( $n_{joint}$ ). The same principle was applied to  $F_{max}$  with Equation (3.2).

$$K_{y,i} = K_{y,sample} \div n_{joint} \quad (3.1)$$

$$F_{max,i} = F_{max,sample} \div n_{joint} \quad (3.2)$$

The results are summarized in Table 3.3 and represented in Fig. 3.19. The local stiffness curves for all samples are presented in Appendix A.2 (see Fig. A.3).

For the top assembly, the influence of the web thickness was negligible, as the difference between M1 and M3 samples for  $F_{max}$  and  $K_{y,sample}$  was only 1% and 3%, respectively, even though M3 tenon was 14 mm thicker. Similar results were observed for the bottom assembly between the M2 and M4 samples, which emphasizes the negligible influence on the TT joint behavior depending on the use of 18 or 25-mm-thick OSB panels for the web. The particular OSB composition, with a denser surface toward the surface than in the middle of the panel, could explain these results. Increasing the panel thickness by a few millimeters would thus not significantly increase the mechanical properties of the assembly.

For the comparison of the top and bottom assembly, there were differences for the  $K_{y,sample}$  and  $F_{max}$  of 5% and 18%, respectively, between M1 and M2 samples (web of 18 mm) and of 12% and 22%, respectively, between M3 and M4 samples (web of 25 mm). The bottom assembly was 20% less resistant and approximately 10% less stiff for both cases. The reduced



area and the machining of the densest part of the panel in the bottom assembly could be the cause of these differences. These differences should be taken into consideration for the numerical model.

In addition, a spacing of 100 mm between joints was tested. For the same assembly length and web thickness of 25 mm, M5 samples had six joints, while M3 samples had eight joints. For M5 samples,  $K_{ser,i}$  and  $F_{max,i}$  were 25% and 9% higher than M3 samples, respectively. The maximum force difference was similar depending on the number of joints. However, the stiffness was significantly different. The spacing of the joint could influence the mechanical properties of joints in series by reaching a maximal capacity after an optimum spacing length. These results are also based on the assumption that loads were equally distributed in the samples, which is not certain (see Equations (3.1) and (3.2)).

Finally, the two sample types with the top and bottom geometries were tested (M6 and M7). M6 samples showed a behavior similar to M4 samples with a bottom geometry (web with a thickness of 25 mm). Moreover, M7 samples demonstrated an average behavior between M1 and M2 samples (web with a thickness of 18 mm). These samples were tested to ensure that no unexpected negative effects would occur if the two geometries were combined (top and bottom). Accordingly, the behavior was a least equivalent to bottom geometry performance, which was the weakest.

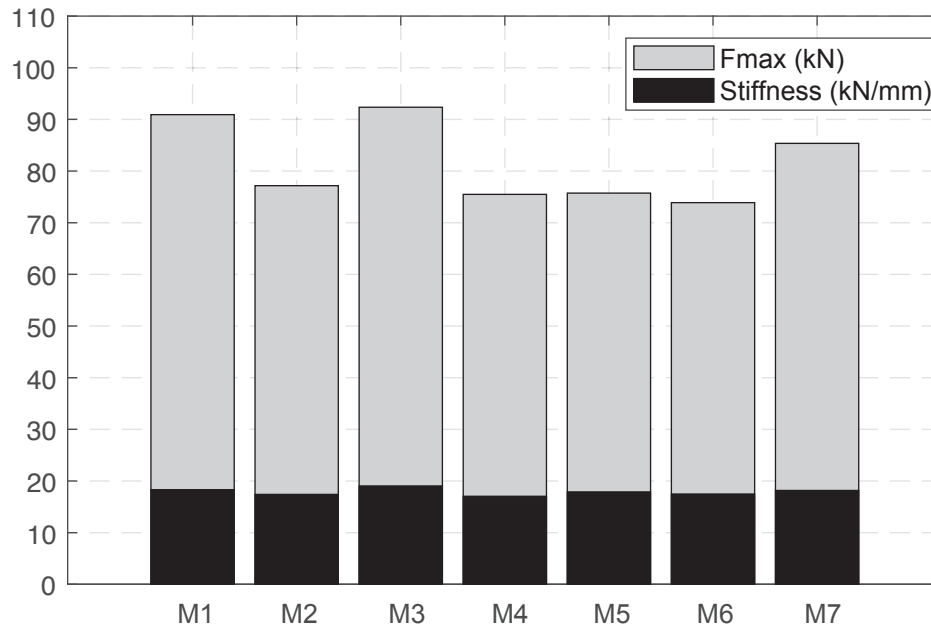


Figure 3.19 – Histogram of the average result per sample for the maximum load ( $F_{max,sample}$ ) and the experimental stiffness ( $K_{y,sample}$ ).

Table 3.3 – Experimental average results per sample.

ID	$n_{tot}$	$K_{y,sample}$ (kN/mm)	$K_{y,i}$ (kN/mm)	$F_{max,exp}$ (kN)	$F_{max,i}$ (kN)
M1	8	18.32	2.29	90.92	11.37
M2	8	17.41	2.18	77.17	9.65
M3	8	19.05	2.38	92.35	11.54
M4	8	17.04	2.13	75.49	9.44
M5	6	17.89	2.98	75.73	12.62
M6	8	17.49	-	73.89	-
M7	8	18.17	-	85.36	-

### Parameter values

Based on the experimental tests, different connection stiffness values  $K_{y,i}$  were used as input parameters for the springs of the numerical model presented in Section 3.5.1:

- M1 value for a top assembly with a web thickness of 18 mm.
- M2 value for a bottom assembly with a web thickness of 18 mm.
- M3 value for a top assembly with a web thickness of 25 mm.
- M4 value for a bottom assembly with a web thickness of 25 mm.

The  $K_{y,i}$  values are listed in Table 3.3. In addition, the connection stiffness value  $K_{nail,i}$  of a nailed connection tested in a previous study [116] was used for comparison. The connection was made of 4-mm diameter nails with a spacing of 50 mm. Glued connections were represented as completely rigid with rigid ties instead of springs.

## 3.6 Results and discussions

Investigations based on the numerical model presented in Section 3.5 were performed to assess whether the use of digitally produced TT connections was a viable alternative to glued and nailed connections for standardized prefabricated elements in the context of a case-study. The most important dimensioning criterion for such interconnected elements is generally the maximum vertical displacement ( $w_{max}$ ) due to the semi-rigid behavior of the connections. Therefore, results were evaluated uniquely according to vertical displacement. A general limit ( $w_{lim}$ ) was defined according to Eurocode 5 [33] and the requirements of the case-study:

$$w_{max} < w_{lim} = L/150 \quad (3.3)$$

where  $L$  is the total length of the structure.

A total of six configurations were computed: two different web thicknesses of 18 and 25 mm, each with the three types of connections described in Section 3.5.2, were considered. Elements

were simply supported for a span of 6.15 m. The results are summarized in Table 3.3 and the configuration with 18-mm-thick webs and TT joints is shown in Fig. 3.20.

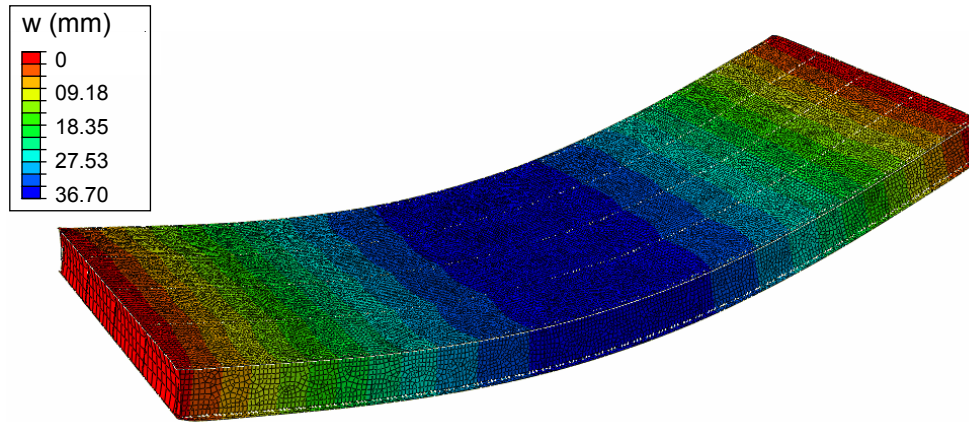


Figure 3.20 – Vertical displacement of the element configuration with a web thickness of 18 mm and TT connections.

Table 3.4 – Maximum vertical displacement for the different element configurations.

Web thickness	Model type	$w_{max}$ (mm)	$w_{lim}$ ratio (%)
2×18 mm	Fully rigid	16.96	41.4
	TT joints	36.70	89.5
	Nailed	60.20	146.8
2×25 mm	Fully rigid	17.32	42.2
	TT joints	38.38	93.6
	Nailed	61.87	150.9

For all the configurations, the maximum vertical displacement was almost two times higher with the TT connections compared to the totally rigid connections. On the other hand, the maximum vertical displacement with TT connections was approximately 39% lower than for nailed connections. In addition, the displacement limit (Equation 3.3) was respected with the use of the TT joints, whereas the displacement with nailed connections was unacceptably large. Overall, TT connections showed a good performance for the load-displacement response of the case-study elements, even if the full rigidity between layers was not reconstituted as in a glued connection. Mechanical fasteners such as nails demonstrated their limitations compared to digitally produced TT joints for thin edgewise connections of OSB panels.

The use of thicker tenons for the configuration with two webs of 25 mm to enhance the mechanical performance was not effective. The maximum vertical displacement was actually slightly superior in the configuration with two 18-mm-thick webs. The experimental results relating to connections showed that the stiffness did not increase with a thicker panel, whereas

### Chapter 3. Standardized construction system: development and potential

self-weight necessarily increased for the roof element. These two phenomena could explain the slightly lower performance of the roof element configuration with two webs of 25-mm in thickness.

In addition, the total computation time for the FE analysis, from the building time to the calculation time of the different models, was investigated with fully and semi-rigid models. A further configuration using three supports with a total span of 12 m was added to assess the impact of larger elements on computation time. The computer used for the numerical simulation was a Dell Precision T5810 Intel® Xeon® CPU E5-1650v3 @ 3.50 GHz with 64 GB of RAM (Dell Technologies, Texas, USA). The results are listed in Table 3.5.

Table 3.5 – Computation times for the different configurations of elements.

Model type	Additional characteristics	Building time (min:s)	Calculation time (min:s)
Fully rigid	12 m span, 3 supports	00:55	00:11.2
	6 m span, 2 supports	00:13	00:06.2
TT joints	12 m span, 3 supports	38:26	02:27
	6 m span, 2 supports	07:05	01:08.5

The rigid model was computed in approximately 1 minute for the longest span, with a computation time five times longer than for the shortest span. The computation time of the rigid models were relatively fast, especially compared to the semi-rigid connection models. The total computation time for the TT-joint models for spans of 6 and 12 m was 8 and 40 minutes, respectively. The computation time for the longest span was also approximately five times longer than for the shortest span, such as the rigid model. The building time for both configurations represented an average of almost almost 90% of the total computation time. The average building and calculation times of the two semi-rigid models were 36 and 10 times longer, respectively, than those of the rigid models. The building time of a semi-rigid model thus drastically increases the total computation time, which is already significant in comparison to rigid models. For a basic roof element and with a relatively computationally efficient computer, the total calculation time can reach 40 minutes.

### **3.7 Conclusions**

Based on the knowledge gained from past research and the DfMA approach, this chapter presents the development of a standardized construction system using only TT connections. Small panels, commonly available on the construction market, are used to reconstitute larger spans for basic housing components, such as slab and roof elements. Different connection types and geometries are introduced to offer a wider range of alternatives for the design, depending on materials and fabrication capacities. Production flexibility and transportation costs are optimized with this standardized system, which makes it accessible to SMEs for more resilient and distributed manufacturing on a local scale.

The feasibility of this system was proven through a case-study conducted in collaboration with two industry partners involved in timber construction. The newly developed construction system, normally composed of small panels, was investigated with continuous elements as a prefabricated approach was selected for the case-study. For economic reasons, the material chosen was spruce OSB type 4. The fabrication process was successfully implemented on a robotic production line at the company's factory. Several prototypes were manufactured with various dimensions and panel sizes.

An FE model was developed, with an automated workflow from CAD to FE software packages, to evaluate the structural potential of the case-study roof element. Only the load-displacement behavior was of interest, as it is the main dimensioning criterion for interconnected elements using semi-rigid connections. A comparison was performed with glued and nailed assemblies, which are widely used connection types in modern timber structures. Although a fully rigid connection was not reconstituted, the roof element with TT connections demonstrated strong structural performance and satisfied the SLS of the project. Moreover, TT joints showed superior performance to that of the nailed assembly, which highlighted the viability of preferring digitally produced wood connections over mechanical fasteners for the edgewise assembly of thin OSB panels. Nonetheless, other engineered timber panels could be considered to improve the structural performance of TT connections and the overall performance of the resulting structure. In addition, the computation time of the FE model was already significant considering the use of this element for basic building components.

Finally, the feasibility and structural potential of this new type of construction system were confirmed. From this first investigation, more convenient calculation models can be developed to reduce engineering costs as well as to give clear guidelines for their structural design.



## 4 Simplified calculation method: development and validation

---

This chapter is based on: J. Gamarro, J. F. Bocquet and Y. Weinand. A Calculation Method for Interconnected Timber Elements Using Wood-Wood Connections. *Buildings*, 10(3):61, 2020. doi:10.3390/buildings10030061.

---

### 4.1 Introduction

The work performed in Chapter 3 has demonstrated the potential of a newly developed standardized construction system using digitally produced TT connections. However, the structural analysis of construction systems using a large number of wood-wood connections has primarily been performed in previous research with sophisticated FE models, such as the one presented in Section 3.5. This type of numerical model is generally complex, computationally expensive, and time-consuming for the design of basic building components. For a wider use of this technology in construction, calculation models must be more convenient to use for engineers in practice compared to the FE models developed so far, as is the case for simple standardized elements. In addition, only the fabrication process was verified on large-scale prototypes with continuous elements, while the flexural performance was evaluated exclusively through numerical investigations.

Therefore, the purpose of this work is to introduce a simplified calculation model that can capture the specifics of the proposed construction system using TT connections in a simple manner. Different calculation models, from analytical theories to numerical modeling approaches, were reviewed to identify the most appropriate method. Based on the manufacturing capabilities and case-study presented in Sections 3.3.1 and 3.4, respectively, three large-scale specimens were assembled with small plates and produced with a CNC machine. Considering the poor mechanical properties of OSB compared to other engineered timber products, a layer of spruce LVL was introduced into the flanges to enhance their overall behav-

ior. Experimental tests on the bending properties of these specimens were conducted to study their mechanical performance and assess the proposed calculation model.

The chapter is structured as follows:

- Section 4.2 introduces the state-of-the-art of calculation models for interconnected timber elements using semi-rigid connections.
- Section 4.3 describes the experimental methods and the large-scale specimens.
- Section 4.4 introduces the simplified calculation method.
- Section 4.5 presents and discusses the different results.
- Section 4.6 summarizes the main conclusions.

### 4.2 State-of-the-art

One of the main parameters of interconnected wooden elements is the mechanical performance of connections between different parts, as a certain continuity between layers is required for structural applications. Glued connections are widely applied to manufactured engineered wood products, such as GLT or CLT, as they are considered fully rigid. Most of the time, the bonding process requires an indoor environment and an rigorous quality control must be executed. As a result, steel fasteners and other types of connections are also extensively used, even if they are not perfectly rigid. The semi-rigidity of the connections between members, also called slip modulus, is an essential parameter that has a large influence on deflection and bending stresses, as shown in Fig. 4.1. For interconnected timber elements with semi-rigid connections, the generally used Euler-Bernoulli beam theory cannot be applied because of the relative displacement between layers caused by the slip modulus of the con-

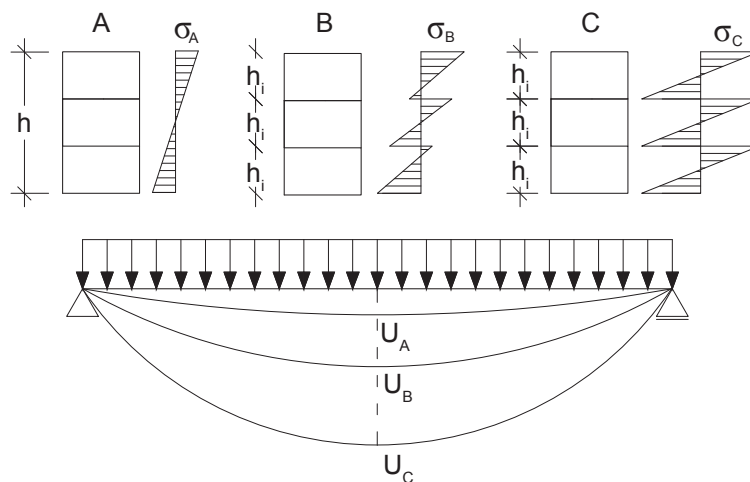


Figure 4.1 – Deflection and bending stress distribution of an interconnected timber element with multiple rectangular cross-sections: (A) using rigid connections, (B) using semi-rigid connections, and (C) without connections. Reproduced from [10].



nections. Consequently, different calculation methods have been developed to characterize the effective bending stiffness ( $EI_{ef}$ ) of interconnected timber elements using semi-rigid connections, as large displacement and stability are generally the most critical criteria for such timber construction systems.

#### 4.2.1 Analytical theories

The theoretical bases for analytical calculation methods appeared with the high demand for large wood cross-sections and the shortage of raw materials during World War I [97]. The first important work was conducted by Möhler [91, 92] in 1955, followed by Schelling [135, 136] in 1968. Based on these works, Heimeshoff [65] formulated the gamma method using a reduction coefficient  $\gamma$ , which takes the relative displacement between layers into consideration. This method is applicable for the following cases: reconstituted elements up to three layers, simply supported beams with a uniform distributed load, and identical spacing and connection types along the length. Deflection due to shear is not considered. According to the gamma method, the effective bending stiffness ( $EI_{ef}$ ) for a reconstituted beam with three elements (see Fig. 4.2) is defined by Equations 4.1 to 4.5:

$$EI_{ef} = \sum_{i=1}^3 (E_i I_i + \gamma_i E_i A_i a_i^2) \quad (4.1)$$

$$\gamma_i = [1 + \pi^2 E_i A_i s_i / (K_i l^2)]^{-1} \text{ for } i = 1 \text{ and } i = 3, \gamma_2 = 1 \quad (4.2)$$

$$a_2 = \frac{\gamma_1 E_1 A_1 (h_1 + h_2) - \gamma_3 E_3 A_3 (h_2 + h_3)}{2 \sum_{i=1}^3 \gamma_i E_i A_i} \quad (4.3)$$

$$a_1 = \frac{h_1 + h_2}{2} - a_2 \quad (4.4)$$

$$a_3 = \frac{h_2 + h_3}{2} + a_2 \quad (4.5)$$

where  $E_i$  is the modulus of elasticity,  $I_i$  is the moment of inertia,  $A_i$  is the cross-sectional area,  $s_i$  is the spacing between connections,  $K_i$  is the slip modulus of connections,  $l$  is the length of the element, and  $h_i$  is the height, according to Fig. 4.2. The gamma method is still relevant and serves as a basis for Eurocode 5 (EC5) Annex B [33] entitled “Mechanically jointed beams”. Girhammar [54] also developed a simplified analysis for different types of support and loading but only for elements of two layers, as a simplified case of the gamma method. Kreuzinger et al. [79, 143, 144] developed another method, called the shear analogy, which can calculate composite beams without limitation in numbers of layers but considering simplified assumptions over two layers. This method considers the composite beam as two beams, one working in flexion and the other in tension or compression. It is used in German standards for timber construction [25] and exists in the form of a report published by the European Organization for Technical Approvals [80]. Although the gamma method presents some limitations, it remains a highly efficient method for calculation by hand compared to the shear analogy method, which is more challenging to implement.

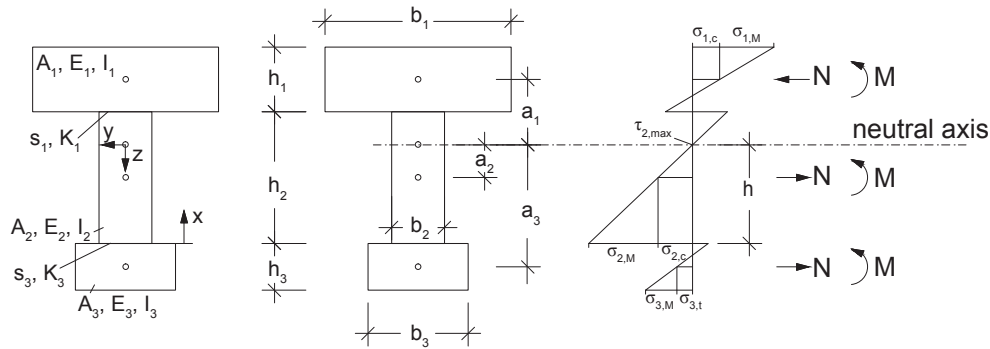


Figure 4.2 – Interconnected beam with three elements according to the gamma method. Reproduced from [10].

#### 4.2.2 Numerical models

From the second half of the 20<sup>th</sup> century, computers allowed the development of numerical calculation methods for reconstituted sections. In 1994, Hoeft [66] developed an FE model for the calculation of multiple-layer beams, which was expanded by Krawczyk [77, 78] with the FE code FELINA (EPFL, Lausanne, Switzerland). At the same time, another FE model for multiple layer beams was developed with SOFiSTiK<sup>®</sup> software (SOFiSTiK AG, Oberschleißheim, Germany) by Gollwitzer [56]. In his thesis, Pirazzi [109] compiled and compared different analytical and numerical approaches, but these mainly applied to steel fastener connections. Concerning wood-wood connections, the mechanical behavior of welding-through wood dowels, which is a specific assembly type used in multi-layer spruce beams, was investigated with 2D FE models [52, 89, 115] as well as a complex 3D FE model [105], with the FE code Cast3M<sup>®</sup> (CEA, Paris-Saclay, France). The development of these 2D FE models was expanded for grooving timber interfaces by Girardon et al. [51, 53]. Roche et al. [130] subsequently studied the semi-rigidity of the dovetail joint for a beam on two supports with a numerical model developed with Matlab<sup>®</sup> (The MathWorks Inc., Natick, USA). For folded free-form timber plate structures using wood-wood connections, similar approaches were developed based on FE shell models with spring and strip elements for the connections [101, 153], as shown in Fig. 4.3.

The recent development of timber-concrete composite structures has also encouraged the development of new semi-rigid connections modeling methods such as strut-and-tie models [74]. For this type of model, basic structural-analysis software packages are commonly used. Composite elements are modeled with 2D beams with adjusted stiffness of for their connections [59, 90]. This method is most likely the preferred option for engineers in practice [23], even though more complex 3D FE models have been developed, mainly for research, such as work on notched wood-wood connections [6, 45, 64].

There are many different analytical and numerical methods for the investigation of the effective bending stiffness of interconnected timber elements due to the semi-rigidity of their

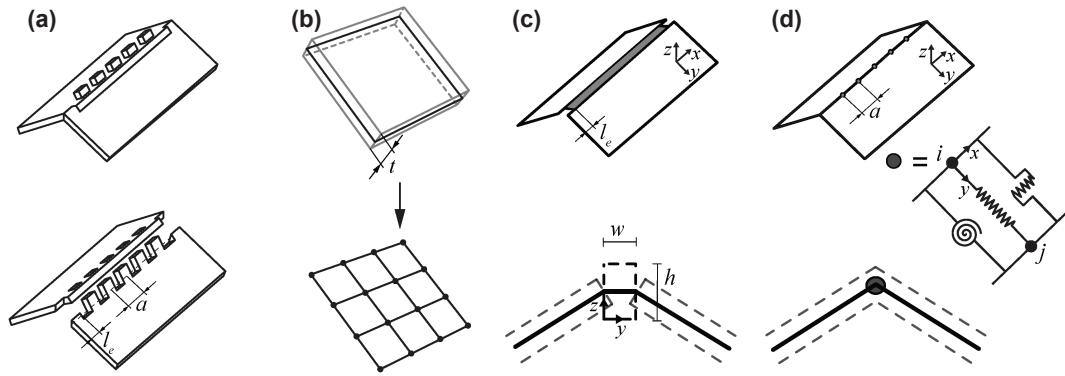


Figure 4.3 – FE model: (a) Timber plates connected by TT joints / (b) Plate as shell element / (c) Connection as strip element / (d) Connection as spring element. Reproduced from [153].

connections. The appropriate method is often chosen according to various parameters, such as the geometry of the element, the type of connection and its mechanical behavior (non-linear or not), and also its structural application. The level of modeling complexity will not be the same if engineers are designing a timber-concrete composite bridge or a 6-m-span slab for housing. It is important to find the right level of complexity for the required structural application.

### 4.3 Materials and experimental methods

Tests were performed on large-scale specimens to study the mechanical behavior of this new type of structural system and to validate the calculation method proposed in Subsection 4.4.1. Bending properties, especially the effective bending stiffness ( $EI_{ef}$ ), were investigated as this is the main area of interest for interconnected timber elements with semi-rigid connections. The specimens were produced with the geometry and materials described in Subsection 4.3.1.

#### 4.3.1 Large-scale specimens

Based on the construction system and the case-study presented in Subsection 3.3.2 and Section 3.4 of the previous chapter, respectively, three large-scale specimens were produced using spruce LVL and OSB, as shown in Fig. 4.4. Spruce LVL was introduced to enhance the overall bending performance of the proposed element. The elements were 8.4 m long ( $L$ ), 0.8 m wide ( $W$ ), and 0.45 m high ( $H$ ). The element length was chosen according to the evolution of the case-study. Only small panels of 1.25 by 2.5 m were used to reconstitute the span, as described in Subsection 3.3.2. As a result, there were several discontinuities along the specimen length (see Fig.4.4, (5) red circles).

The webs were made of OSB type 3 panels with a thickness of 25 mm each (Fig. 4.4, (4)), while the flanges consisted of spruce LVL with a thickness of 21 mm (Fig. 4.4, (2)) and OSB type 3

panels with a thickness of 18 mm (Fig. 4.4, (1)). The webs and flanges were connected using TT connections with a constant spacing of 150 mm. The top and bottom assemblies were similar, both with the configurations (a.2) and (b.1) and an insertion angle  $\alpha_{t1}$  of  $1^\circ$  according to Fig. 3.8. A special bottom TT joint was not implemented to facilitate the assembly process. However, no additional mechanical fasteners, such as screws, were used, and no disassembly between bottom flanges and webs was observed. There were nine transversal beams in OSB 25-mm distributed equally along the length and connected to the flanges using TT joints (Fig. 4.4, (3)). The beams were divided in three parts so as not to weaken the two longitudinal webs.

The fiber orientation of each panel was along their length, and TT joints were directly machined in panels to connect the different part, as no bonding process was used. All parts were cut without gaps with the five-axis CNC machine described in Subsection 3.3.1 and were subsequently assembled by hand. A detailed plan, with the necessary information to reproduce the specimens, can be found in Appendix B.1 (see Fig. B.1 and B.2).

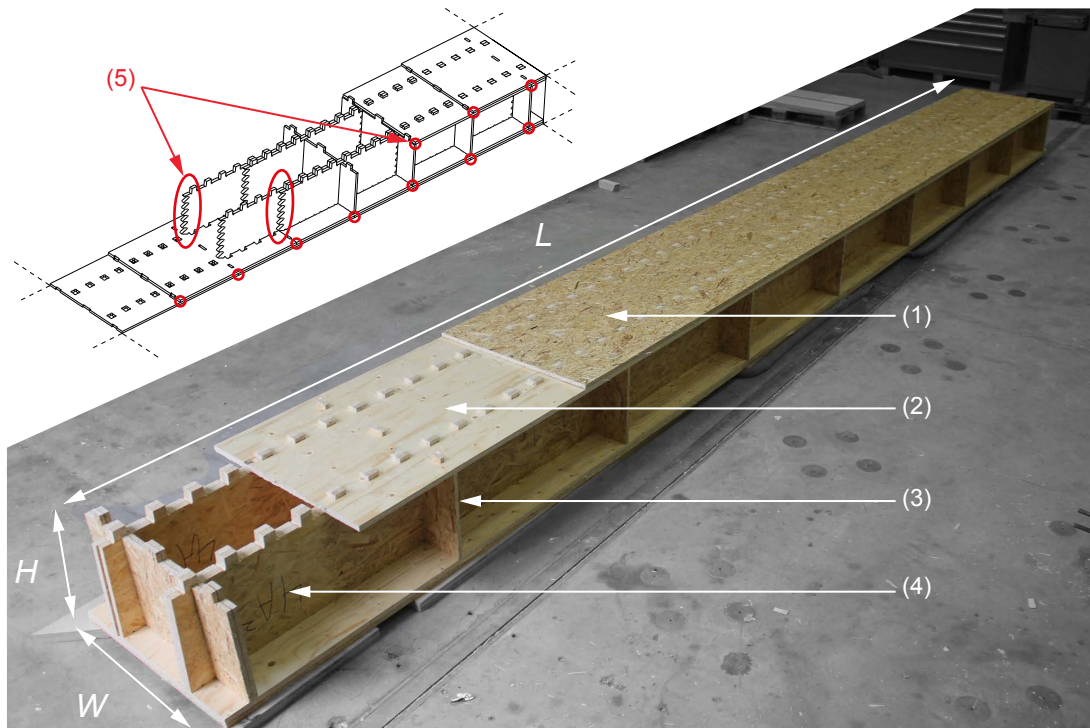


Figure 4.4 – Large-scale specimens produced in the laboratory: (1) top flange exterior layer, (2) top flange interior layer, (3) transversal beam, (4) web double-layered, and (5) discontinuities along the length.

### 4.3.2 Methods

Concerning the panels used for the tests, the density was tested according to EN 323 [36], whereas the other characteristics were obtained from EN 12369 [29] for OSB type 3 (Kronospan,

### 4.3. Materials and experimental methods

Jihlava, Czech Republic) and from the VTT certificate [163] provided by the supplier for spruce LVL Kerto Q® (Metsä Wood, Espoo, Finland). These values are listed in Table 4.1.

Table 4.1 – Material properties.

Designation	Symbol	Units	LVL Q	OSB 3	
Thickness	-	mm	21	18	25
Position	-	-	flatwise	flatwise	edgewise
Density	$\rho_{mean}$	kg/m <sup>3</sup>	481	576	600
Elastic modulus // to grain	$E_{0,mean}$	MPa	10000	4930	3800
Elastic modulus ⊥ to grain	$E_{90,mean}$	MPa	3300	1980	3000
Shear modulus // to grain	$G_{0,mean}$	MPa	60	50	1080
Lay-up	-	-	–     –	– –	– –

Four-point bending tests were performed following the standard EN 408 [37]. The experimental setup is presented in Fig. 4.5. The test length ( $L$ ) was 18 times the depth of the section with a total extra length of 300 mm. Specimens were simply supported with a span of 8.1 m ( $L$ ). LVL beech plates of 40 mm thickness and 225 mm width were used as bearing plates and positioned at the supports and loading heads to minimize local indentation. Two hydraulic jacks symmetrically loaded the structure and no lateral restraints were necessary. Two LVDTs were placed on the top flange at each quarter of the span to report the deflection resulting from bending moments. Furthermore, the digital image correlation (DIC) technique was used to record relative displacement caused by material discontinuities in four areas of the flange sections, as shown in Fig. 4.5 (DIC 1, 2, 3 and 4) and Fig. 4.4 (red circles). The effective bending stiffness  $EI_{ef}$  was calculated according to Equation 4.6 described in EN 408 [37] Section 10.3:

$$w = \frac{23FL^3}{648EI_{ef}} \Rightarrow EI_{ef} = \frac{23L^3}{648} \times \frac{k_{exp}}{2} \quad (4.6)$$

where  $L$  is the span,  $F$  is the load of one hydraulic jack,  $w$  is the deflection at mid-span, and  $k_{exp}$  is the result of the load-deformation regression analysis. As the latter is the result of the total load applied, which is in this case the sum of two hydraulic jacks,  $k_{exp}$  is divided by two.

In addition, 10 impulsive vibration tests per specimen were performed to estimate the initial natural frequency. From this frequency value, an alternative effective bending stiffness,  $EI_{ef.estim}$ , was calculated using Equation 4.7 described in EC5 [33]:

$$EI_{ef.estim} = \frac{2fL^2m}{\pi} \quad (4.7)$$

where  $L$  is the span,  $f$  is the measured natural frequency, and  $m$  is the mass of the specimen. The formulation of Equation 4.7 does not take shear into account. The average specimen mass was 509 kg. Vibrations were triggered using a hammer, and two acceleration transducers (HBM B12/200) were positioned at mid-span with an acquisition speed rate of 200 Hz. The frequency spectrum was computed according to the fast Fourier transform algorithm where the first peak

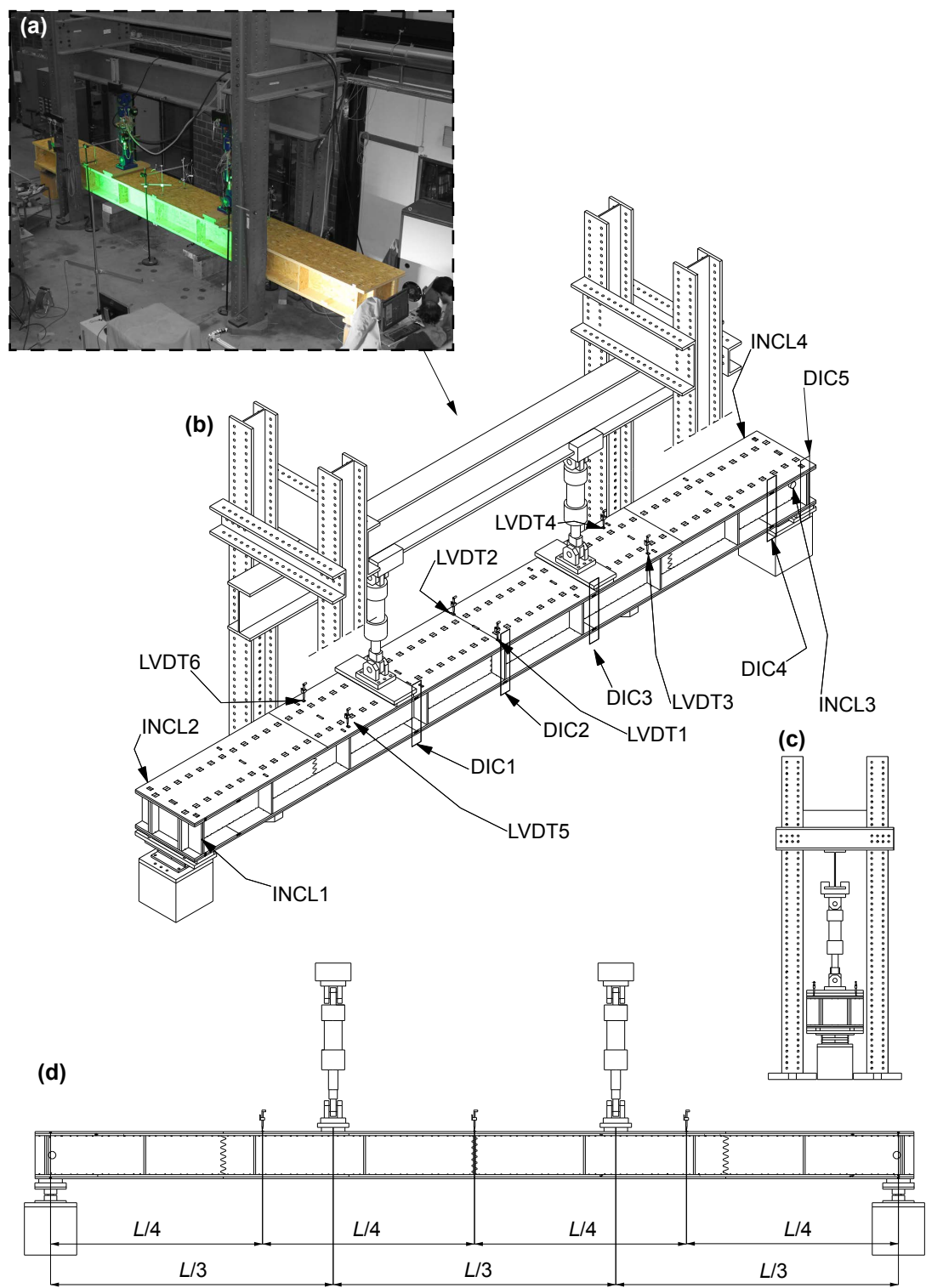


Figure 4.5 – Four-point bending test setup for large-scale specimens: (a) Photograph of the setup during a test / (b) Technical drawing, axonometry / (c) Side view / (d) Front view.

represents the natural frequency  $f$  of the structural element, as shown in Fig. 4.6b. Furthermore, the damping ratio  $\zeta$  was determined using the logarithmic decrement  $\delta$ . This method is suitable to obtain damping ratios of under-damped systems in the time domain [157], and is characterized by Equations 4.8 and 4.9:

$$\delta = \frac{1}{n} \ln \frac{x(t)}{x(t+nT)} \quad (4.8)$$

$$\zeta = \frac{1}{\sqrt{1 + \left(\frac{2\pi}{\delta}\right)^2}} \quad (4.9)$$

where  $x(t)$  is the value of the first studied peak value at time  $t$ ,  $x(t+nT)$  is the peak value at  $n$  periods away. In this case, the first and third peaks of each vibration test were used to compute the damping ratio (see Fig. 4.6a).

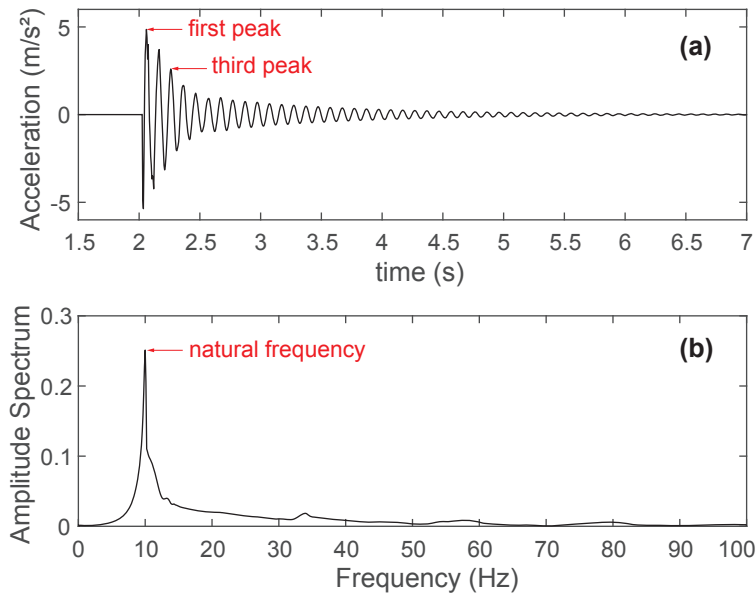


Figure 4.6 – Vibration test on one specimen: (a) acceleration at mid-span over time / (b) Frequency spectrum of the acceleration.

#### 4.4 Simplified calculation model

As described in Section 4.2, there are different types of models for interconnected timber elements, but such models were mainly developed for steel mechanical fasteners such as screws, nails, or bolts. Indeed, fasteners have been one of the most-used connections in recent decades and they remain such. Few models have been created for wood-wood connections. However, those connections that have been produced are markedly different from the TT assembly studied here (primarily wood dowels and surface treatments). In addition, research has been performed on continuous elements that are different from the developed structural elements containing many discontinuities (see Fig. 4.4, red circles). As a result, an analytical

method is difficult to establish for this type of element because of such particularities, which are functions of panel geometries and other characteristics. On the other hand, FE models are often costly and time-consuming as highlighted in Section 4.2, especially for the basic building components developed in this research. In order to represent the complexity of this new structural system in the simplest way as possible, a numerical model made uniquely of beam elements was developed, inspired by modeling approaches described in [23]. The scope of validity of this model remains within the linear elastic range for basic orthogonal geometries of the developed construction system described in Subsection 3.3.2.

### 4.4.1 Modeling approach

The developed construction system as well as the structural element presented in Subsection 4.3.1 have generally symmetrical cross-sections (see Fig. B.2, cutting DD') due to their basic orthogonal geometries. They can thus be considered as a series of parallel I-beams when studying their bending properties, reducing the calculation complexity to a two-dimensional problem. As a result, only one I-beam was modeled to facilitate the calculation for the large-scale specimen. The proposed model is presented in Fig. 4.7 with a complete description of the different parts in Table 4.2. It is composed of elastic beam elements, commonly used in basic structural-analysis software, located at the centroid of each section (see Fig. 4.7a). The beams possess the required information such as the section and material properties used to compute the different results. Beam elements are considered only in the elastic range in view of the behavior observed so far. In addition, they must take into account shear deformation and rotational bending effects, which corresponds to Timoshenko beam theory. Euler-Bernoulli beam theory is not appropriate and should not be used for this modeling approach. The different beam elements are connected together by rigid ties representing the inherent eccentricities between the beams due to their section properties. Rigid ties couple the displacements of two nodes with a rigid connection. The characteristics of rigid ties should have no influence on the global mechanical response (coupling term only).

Connections are usually represented by shear stiffness in models, especially in the cases of mechanical fasteners and continuous elements. Different connectors, such as nails or bolts, are modeled with springs alone without the inclusion of section or material properties. However, a different approach was developed for the TT joints in order to better represent the connections between the different layers of flanges and webs in staggered rows. The tenon component of the TT connection is thus modeled and represented by beam elements with the proper section and material information, such as for webs and flanges. The mortise part is also modeled with beam elements that possess a reduced cross-section in order to consider the hole in the flanges at its location. The semi-rigidity of the connection is taken into consideration with a spring between the contact area of the tenon and the mortise. The assembly gap can be implemented through a unidirectional displacement constraint on each spring. Fig. 4.7c shows the different parts for the modeling of a TT connection with the proposed model: detailed information is listed in Table 4.2 (description and element type).



The friction, whether between contact surfaces or connections, is not considered with this method as in practice it is hard to model and predict for such large-scale elements. The most important parameter to characterize for the proposed model is the spring in the contact area of the TT connection, as displayed in Fig. 4.7c.

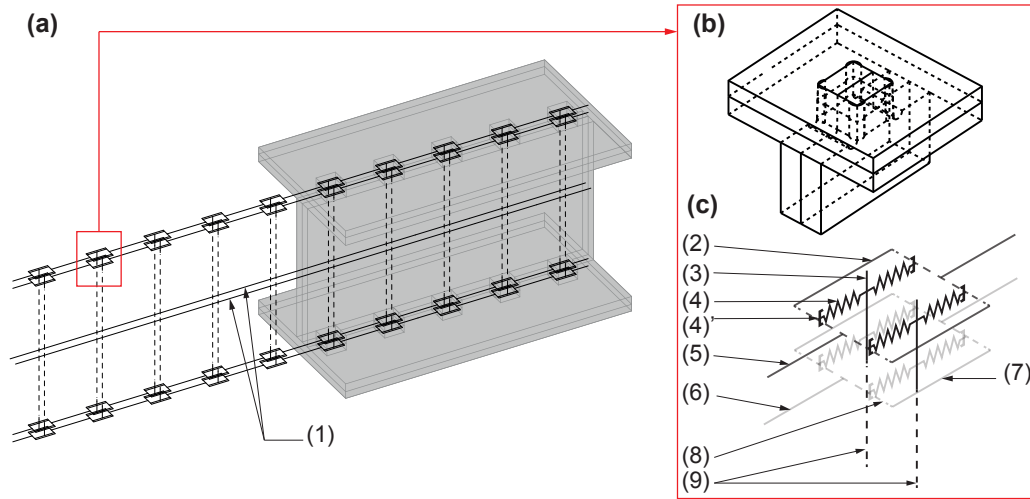


Figure 4.7 – (a) Representation of the proposed calculation model (black lines) for the I-beam using TT connections (3D gray solid) / (b) Axonometry of one TT joint / (c) Modeling of this joint with beam elements and springs.

Table 4.2 – Model properties according to Fig. 4.7.

ID Fig. 4.7 -	Section (mm)	Material -	Description -	Element type -
(1)	372/25	OSB 3	Web	Beam element
(2)	18/175	OSB 3	Top flange ext. with reduced section due to the connection	Beam element
(3)	50/25	OSB 3	Tenon	Beam element
(4)	-	-	Stiffness between the tenon and the flange	Spring element
(4)'	-	-	Unidirectional displacement constraint for assembly gap	Parameter
(5)	18/400	OSB 3	Top flange ext. without reduced section	Beam element
(6)	21/400	LVL Q	Top flange int. without reduced section	Beam element
(7)	21/175	LVL Q	Top flange int. with reduced section due to the connection	Beam element
(8)	-	-	Eccentricities due to the TT connection	Rigid tie
(9)	-	-	Eccentricities between tenon element and web elements	Rigid tie

### 4.4.2 Connection parameters

The mechanical characterization of the TT joint in the contact zone is essential. Such characterization allows to determine the stiffness value of the spring element in the calculation model presented in Fig. 4.7c. Therefore, tests were conducted on the specific TT connection of the studied specimens in order to perform the calculation. A more exhaustive study of the behavior of TT connections is presented in Chapter 5.

### Material and methods

This experimental protocol is described more precisely in Subsection 5.4.1. A total of 10 identical samples were produced with the same CNC machine used for the structural element to obtain a surface condition similar to the real application. The properties and geometry were chosen according to the structural system presented in Subsection 4.3.1. The panels used for these tests belonged to the same batch as those used for the fabrication of the three large-scale specimens. The material and samples were conditioned in a normalized environment at a temperature of 20°C and relative humidity of 65% [72]. Tests were realized using a static universal testing machine (model LFV-200, Walter+Bai AG, Löhningen, Switzerland [164]) and a displacement control method with a speed of 0.01 mm/s for an approximate duration of 3 to 4 minutes per test. Fig. 4.8 shows the configuration of the experimental setup. The hydraulic jack applied pressure on the contact zone of 50 by 39 mm composed of OSB and LVL, while two LVDTs measured the deformation  $d$  within the range of the distance  $L_d$  of 75 mm. The average of the two LVDTs was used to determine the final deformation and extract the contact stiffness. Finally, the grain orientation of the different panels was perpendicular to the contact zone as is the case for the structural element configuration.

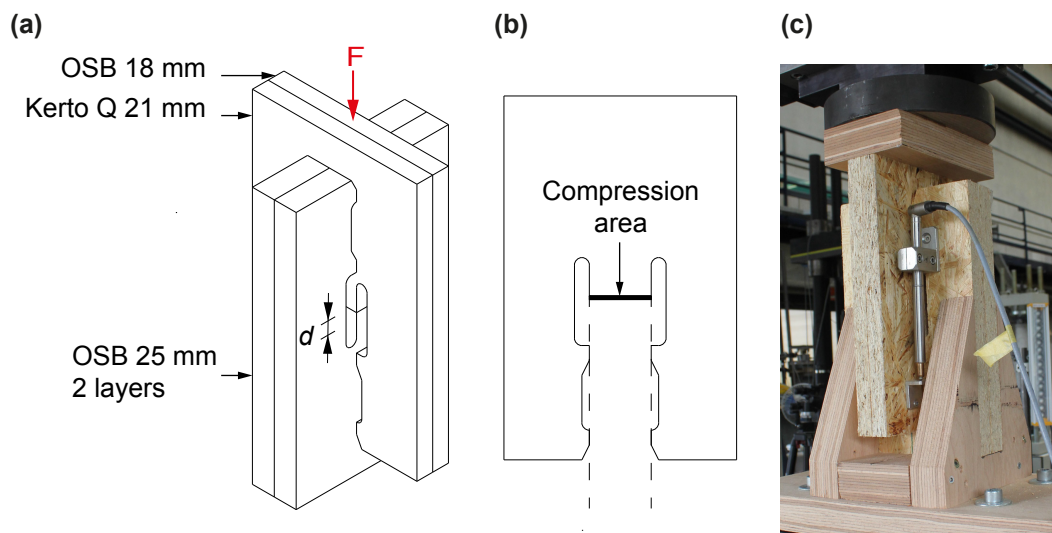


Figure 4.8 – (a) Axonometry of the experimental setup for TT joints / (b) Side view / (c) Photograph of the experimental setup with LVDTs.

## Results

The experimental stiffness,  $K_{y,exp}$ , was defined by a linear regression analysis of the load-deformation response between 10 to 40% of the maximum load applied [35]. The experimental curves are presented in Fig. 4.9. The average value for  $K_{y,exp}$  was 31.09 kN/mm, with a relative standard deviation of only 6%. Such relative standard deviation represents an acceptable homogeneity considering these materials. Equation (4.10) defines the stiffness value for one spring element,  $K_{y,i}$ , of the calculation model, as one connection is divided into several spring elements (Fig. 4.7c):

$$K_{y,i} = K_{y,exp} \div n_{spring} \quad (4.10)$$

As a result, the  $K_{y,i}$  value of 3.89 kN/mm was used to compute the semi-rigid (SR) calculation model. The geometry and precision of CNC cutting for the joint were chosen so as to assemble the different parts of the structural element without gaps. The initial stiffness shown in Fig. 4.9 was higher than the  $K_{y,i}$  value. However, this initial stiffness phenomenon was not taken into consideration as it occurred for very low load values and may be due to several factors, such as material characteristics, manufacturing parameters, assembly gaps, and moisture content. Alternatively, the value may have resulted from a unique effect that was confined to the first loading of the connection and did not persist over time. This phenomenon occurred for very low displacement, from 0 to 0.1 mm, and is thus complicated to assess considering the parameters influencing it. Consequently,  $K_{y,i}$  was used directly in the calculation model and no unidirectional displacement constraint was implemented. The failure mode and maximum resistance capacity were not studied as the local behavior of the connection was not the primary interest in this chapter.

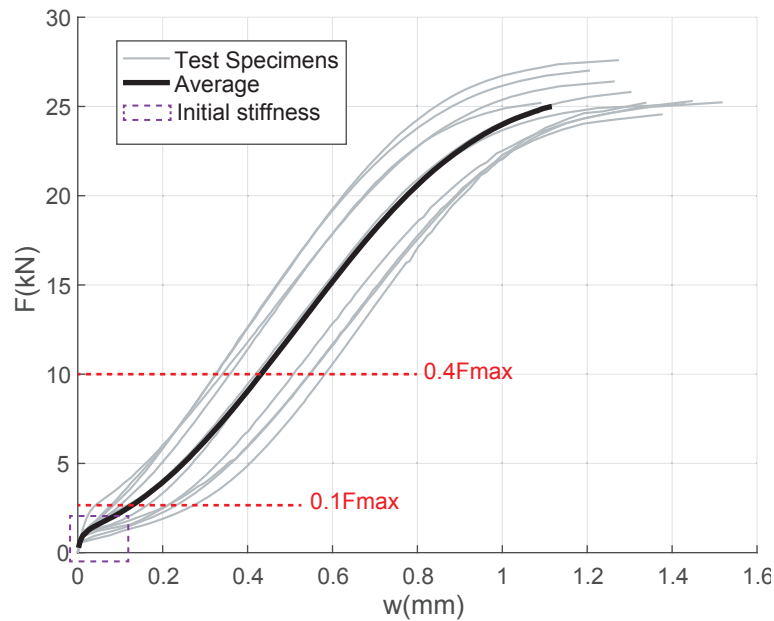


Figure 4.9 – Experimental curves for the specific TT connections made of spruce LVL and OSB.

### Parameter values

The input parameter for the TT connection is based on experimental results (SR model) described in the previous Subsection 4.4.2. However, two other values were used to assess the calculation model and study the influence of the semi-rigidity. One was a completely rigid model, named R, with infinite stiffness in the contact area that imitated a glued connection. Another one, referred to as Optim., was based on a curve fit from the large-scale bending test results presented in Subsection 4.5.1. The goal was to obtain the exact same mechanical response as the bending tests by adjusting the contact stiffness value of the Optim. model and compare it to the value used in the SR model. This Optim. model was only used for comparison and not to develop a reliable calculation methodology. To summarize, three different models were computed:

1. The SR model, using the value from connection tests (proposed calculation method of this study)
2. The R model, not taking into consideration the semi-rigid behavior of connections (rigid model)
3. The Optim. model, to determine the influence of different stiffness values

The input parameter,  $K_{y,i}$ , of each case is listed in Table 4.3.

In addition, the gamma method, described in Subsection 4.2.1 with Equations 4.1 to 4.5, was used to compare the model with the most commonly employed analytical method in practice. All calculations and assumptions can be found in Appendix B.2.

## 4.5 Results and discussion

The results are presented in three parts: first, the effective bending stiffness  $EI_{ef}$ , which is the main interest of this study; second, the effects of panel discontinuities as this is a challenging part of the construction system; and finally, the failure mode is briefly described to investigate potential areas of interest for future research.

### 4.5.1 Effective bending stiffness

Fig. 4.10 shows the deflection at mid-span as a function of the total applied load. The specimens had an elastic linear behavior until failure. An average of the three replicates was determined by linear regression up to the maximum force before failure to compare the  $EI_{ef}$  of the tests and the different calculation models presented in Subsection 4.4.2. The results are listed in Table 4.3.

For the  $EI_{ef}$ , the SR model was the closest calculation to the tests with a difference of  $-11.98\%$ , whereas the R model was  $41.75\%$  more rigid. Considering a simple rigid model is thus not appropriate according to the large overestimation for the serviceability of this type of struc-

Table 4.3 – Results of effective bending stiffness ( $EI_{ef}$ ) and natural frequency ( $f$ ).

ID	$K_{y,i}$ (kN/mm)	$EI_{ef}$ (N·mm <sup>2</sup> )	$\delta_{EI}^*$ (%)	$f$ (Hz)	$\delta_f^*$ (%)
-					
Tests	-	$7.76 \times 10^{12}$	0	9.89	0
Model SR	3.89	$6.83 \times 10^{12}$	-11.98	8.39	-15.17
Model Optim.	6.16	$7.76 \times 10^{12}$	0	8.95	-9.50
Model R	$\infty$	$1.10 \times 10^{13}$	41.75	10.65	7.68
Gamma method	-	$9,80 \times 10^{12}$	26.29	-	-

\* Differences compared to the tests.

ture. This difference highlights the importance of considering the stiffness of wood-wood connections. The gamma method also had an  $EI_{ef}$  that was 26.29% higher than that of the tests. Even though the analytical method considers the semi-rigidity of connections, the bending properties were significantly overestimated. The discontinuities along the element length and the element's different layers are not captured accurately with the gamma method. The SR model is thus better adapted for estimating the bending stiffness and, therefore, the displacement of the element.

Nevertheless, the SR model had a connection stiffness approximately 37% lower than the Optim. model that perfectly represents the tests. The slip modulus difference in the most loaded connection for a load of 30 kN (approximate failure load) between the SR and Optim. models was about 0.027 mm, which demonstrates the high sensitivity of this criteria for the model. The precision of the experimental characterization of the TT connection is therefore crucial in obtaining an accurate prediction. Experimental protocols are investigated and developed to obtain the most accurate behavior of this type of wood-wood connections in Chapter 5.

For the vibration tests, the detailed results of the 30 replicates for the natural frequency and the damping ratio can be examined in an open-access data repository [47]. Concerning the natural frequency  $f$ , the average value for the three slabs was 9.89 Hz with a coefficient of variation of 2.18%. The alternative effective bending stiffness  $EI_{ef.estim}$ , obtained from this result and from Equation 4.7, was equal to  $1.07 \times 10^{13}$  N·mm<sup>2</sup> while the  $EI_{ef}$ , from the bending test, was  $7.76 \times 10^{12}$  N·mm<sup>2</sup>. As a result, the bending stiffness estimated from the vibration tests was 37.89% higher than the one estimated from the bending tests. The low amplitude of the vibration tests, triggered only by a hammer, can explain this difference. Loads in connections were thus markedly low compared to those of the bending tests, and as a consequence, the initial stiffness described in Subsection 4.4.2 (see Fig. 4.9) was activated. The connections were thus stiffer with the low intensity loads of the vibration tests. The rigid model was the closest to the natural frequency tested whereas the SR and Optim. models were respectively -15.17% and -9.50% lower, respectively. The manufacturing parameters are not only important for the assembly process but also for the prediction of the structural behavior as they influence the initial stiffness of the connection.

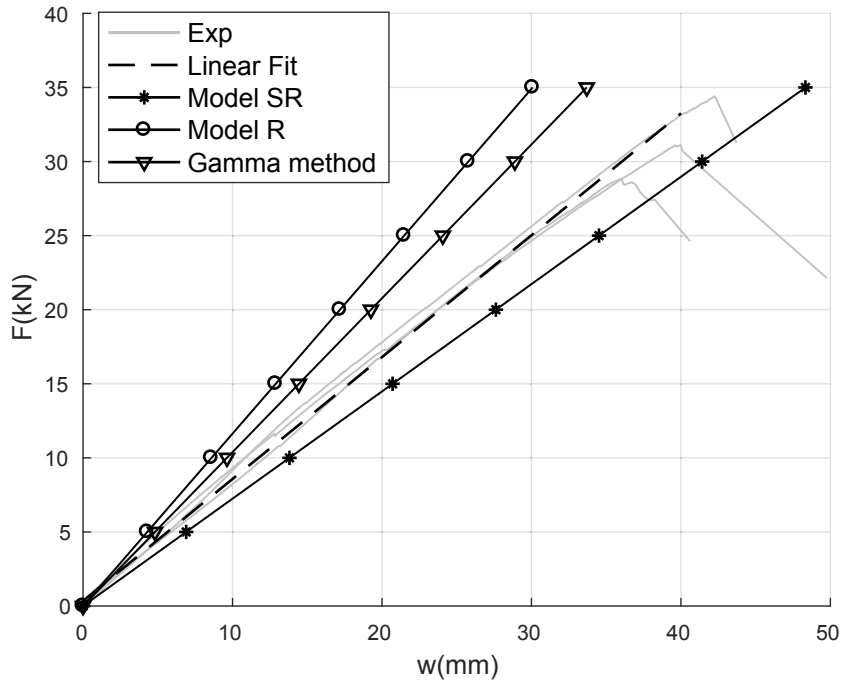


Figure 4.10 – Deflection-load curves at mid-span for tests and calculation models.

In addition, the average damping ratio  $\zeta$  of the three specimens was 2.05% with a coefficient of variation of 4.39%. The highly conservative damping ratio value defined in EC5 [33] for timber floors is 1%. Nevertheless, several European national application documents give values of around 2% [169], such as the UK document [15]. In Annex B of the ISO standard 10137 [71], the recommended value for bare timber floor is 2% and the typical range is between 1.5 and 4%. The value  $\zeta$  determined during the tests corresponds to typical timber floor damping ratios. Therefore, there is no more exceptional friction in this type of construction system than in traditional timber floors, which confirms the choice not to model friction in the calculation model.

Overall, the difference between the tests and the proposed SR model can be explained primarily by the sensitivity of the contact stiffness criteria, which is influenced by the intensity of loads in connections, material characteristics, manufacturing parameters, assembly gaps, and moisture content. However, the SR model remains conservative by being slightly lower compared to the tests. The model could be enhanced with a more accurate prediction of TT connection behavior and an exploration of the effect of manufacturing parameters on structural performance.

#### 4.5.2 Panel discontinuities

Fig. 4.11 illustrates the displacement caused by flange discontinuities for the tests and the SR model at the specific positions on the specimens as described in Fig. 4.5. Negative dis-

placement represent flanges in compression as they move closer, while positive displacement represent flanges in tension as they move apart. The highest displacement reached 2 mm in the tension flange located under the hydraulic jack (see Fig. 4.11c) where the SR model had the highest error with a drift of 0.5 mm. For flanges in tension, the calculation model remained within a maximum error range of 0.2 mm with a good correlation for displacement in the middle of the specimens (see Fig. 4.11b). A contact can occur between flanges in compression, from 0.5 to 1.5 mm displacement, as observed twice during the tests (see Fig. 4.11b and c). Assembly tolerances, shrinkage and swelling spacing, material variability, and other parameters have an influence on this phenomenon and are complicated to estimate in advance. As a result, no displacement limitation was considered for the SR model. The absence of displacement limitation can explain these differences when contact occurs. Based on experience and fabrication knowledge, a limit for this parameter could be considered as input to improve the SR model. Finally, the SR model provided a reliable approximation of displacement between panel discontinuities considering the small range of displacement.

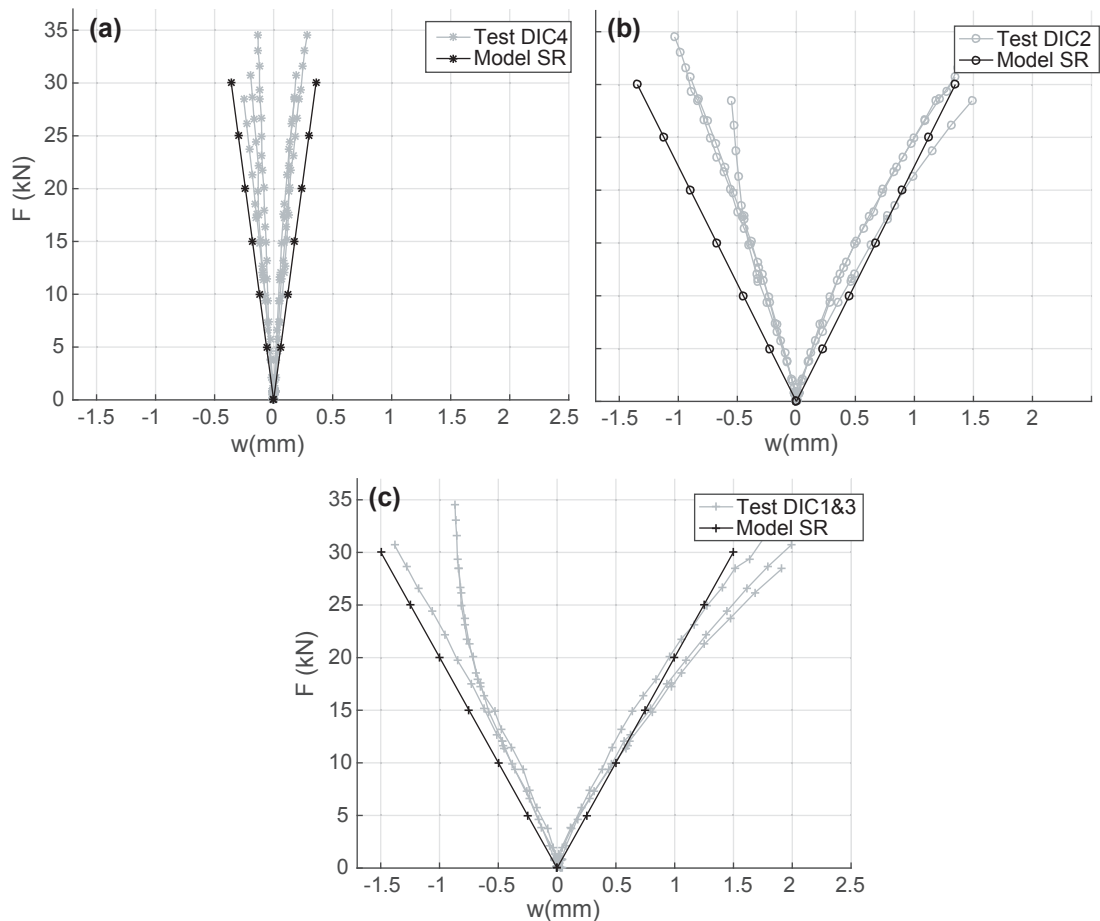


Figure 4.11 – Displacement comparison between the tests and SR model caused by flange discontinuities: (a) DIC 4 area, near support of the element / (b) DIC 2 area, middle of the element / (c) Average of DIC 1 and 3 areas, under hydraulic jacks.

**4.5.3 Failure mode in tension**

Although it was not the main objective of this chapter, several remarks can be made concerning the failure mode of this type of element. A brittle failure in tension was observed in the middle of all specimens and was located in the OSB bottom flange. It is well known that a low width-to-thickness ratio in flanges has a substantial influence on the resistance of long-span elements and on the failure mode of this type of construction system. Such a ratio causes a non-uniform stress distribution along flange elements, called shear lag. This phenomenon is influenced by several factors, such as material shear properties, boundary conditions, type of loading, and width-to-span ratio of flanges. However, European timber standards [33, 146] deal with shear lag by changing the physical cross-section dimensions with an effective width defined only by a constant ratio of the span, regardless of the other factors. Equation 4.11 defines the effective width for our case, following the EC5 guideline:

$$b_{eff} \leq 0.15L = 0.15 \times 8100 = 1215 \text{ mm} \quad (4.11)$$

where  $b_{eff}$  is the effective width and  $L$  is the span.

The estimated failure profiles were not respected in the different cases, which was probably caused by the higher variability of OSB panels compared to other engineered timber panels. The exact length of the failure profile ( $l_{rupt}$ ) was determined to better interpret the results, as shown in Fig. 4.12.

The average tensile strength parallel to the fiber direction of OSB 3 was calculated using Equation 4.12, according to Subsection 7.2.7 of the Swiss standard for timber structures [146]. In addition, the maximum tensile strength ( $\sigma_t$ ) and the shear lag coefficient ( $U$ ) of each specimen were calculated according to Equations (4.13) and (4.14), respectively:

$$f_{t,mean} = \frac{f_{t,k0.05}}{0.85} = \frac{9.4}{0.85} = 11.06 \text{ MPa} \quad (4.12)$$

$$\sigma_t = \frac{F_{t,max}}{l_{rupt} \times t_{OSB3,flatwise}} \quad (4.13)$$

$$U = \frac{f_{t,mean}}{\sigma_t} \quad (4.14)$$

where  $f_{t,mean}$  is the average material tensile strength parallel to the fiber direction,  $f_{t,k0.05}$  is its characteristic 5<sup>th</sup> percentile value,  $F_{t,max}$  is the maximum tensile load in the OSB bottom flange obtained from the calculation model when the failure occurred,  $l_{rupt}$  is the exact failure length, and  $t_{OSB3,flatwise}$  is the panel thickness of the OSB bottom flange (constant value of 18 mm).

The results for each specimen, as well as the average results, are listed in Table 4.4. Although the failure length was lower than the effective width calculated, the tensile strength was approximately two times less resistant than expected. It is thus difficult to establish that Equation 4.11 is sufficient to approximate the shear lag coefficient for this type of structural



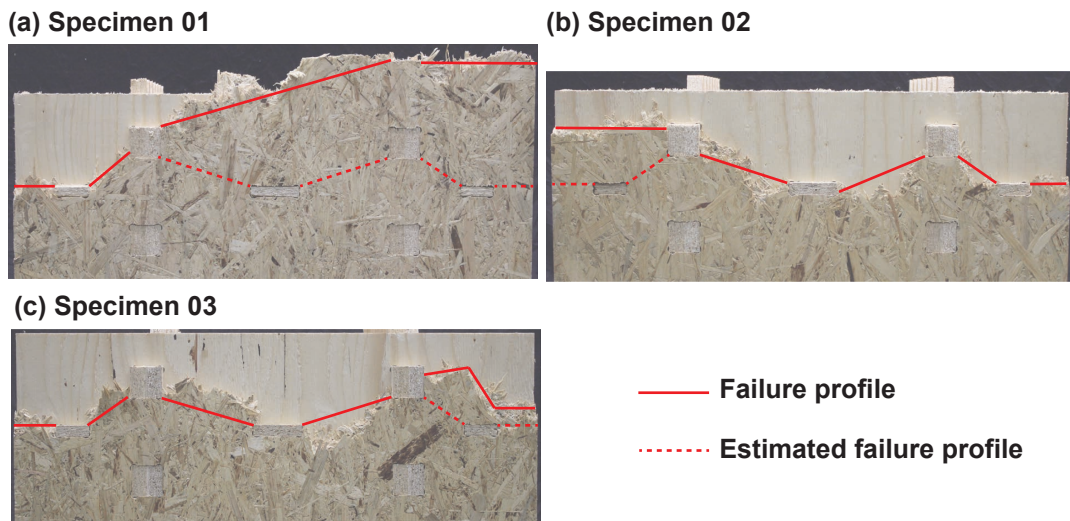


Figure 4.12 – Tensile failure profile of OSB bottom flange panels.

Table 4.4 – Results for tensile failure in the OSB bottom flange for each specimen.

ID	$F_{t,max}$	$l_{rupt}$	$\sigma_t$	$U$
-	(kN)	(mm)	(MPa)	-
Spec.01	66.44	627.5	5.88	1.88
Spec.02	55.70	585	5.29	2.09
Spec.03	60.10	680	4.91	2.25
Av.	60.75	630.08	5.36	2.07

system. In addition to the inherent complexity of this phenomenon, parts of panels cut into flanges for the TT connections (mortise parts) can change the expected behavior and, as a consequence, complicate the calculation. As the tensile properties were not characterized by tests and considering the variability of OSB, the above results should be treated with caution. These results simply give an initial overview of a possible failure mode due to shear lag and highlight the importance of further research. Finally, other material types could be used to avoid a brittle failure in the lower flange and enhance the overall structural performance. OSB panels were chosen according to the case-study for several specific reasons as mentioned in Section 3.4.

### 4.6 Conclusions

Analytical theories, such as the gamma method, are widely implemented in practice to evaluate the performance of timber elements interconnected by semi-rigid connections. However, such theories cannot take into consideration discontinuities along the length of the new construction system in a simple manner. In this chapter, a convenient numerical calculation method, compared to complex FE models, is presented to address this issue through the application of beam elements in the elastic range. The semi-rigidity of TT connections is defined with spring elements characterized through experimental tests.

Bending tests were performed on large-scale specimens to validate the proposed calculation model and investigate the effective bending properties as they are generally the most critical criteria. The specimens were manufactured in a laboratory using spruce LVL and OSB panels. According to commonly available dimensions from suppliers, small panels were used to reconstitute a span of 8.1 m. The reproducibility of the CNC manufacturing and assembly processes, performed by hand, were validated by the small variation between the three specimens observed during the tests.

The results demonstrated that the proposed methodology is effective to predict the mechanical behavior of this new type of element. The model captured accurately the different discontinuities along the length of the elements. In addition, input parameters such as displacement limitations for flanges in compression could improve the model's response. The effective bending stiffness predicted by the model was slightly lower compared to the average value obtained from the tests. The large overestimation of the rigid model and the gamma method, as well as the displacement difference in the most loaded connection with the Optim. model, emphasized the importance of taking the semi-rigidity of TT connections into consideration. This stiffness value can be characterized by elementary tests on the studied connections.

Moreover, the estimated bending stiffness based on the natural frequency value was different from that obtained from the bending tests. The initial contact stiffness value, which is stiffer than the slip modulus, can explain this variation because of the low intensity of loads during the vibration tests. This phenomenon occurred for very low displacement from 0 to 0.1 mm and is thus difficult to estimate. However, the long-term effect of this phenomenon and its persistence through time are unknown, categorizing the model as conservative in the context of the design. The damping ratio was in the range of typical timber floor values and proved that the effect of friction between the elements could be neglected. As a result, friction was not considered in the model, as is usually the case in practice for timber structural elements.

Considering the failure modes, tensile failures in the bottom flanges due to the brittle characteristics of OSB were observed. Differences in expected maximum strength were pointed out and could be due to stress concentrations in the flanges. Furthermore, the shear lag phenomenon should be investigated in greater depth in future research. However, the tensile properties were not characterized by these tests and the preliminary results should thus be treated with caution.

Finally, through simple experimental tests on connections, the proposed calculation model provides a practical methodology for obtaining the stress distribution and the global displacement of interconnected elements using TT joints. Nevertheless, complementary work remains necessary to properly design these elements for the construction market according to building codes. The load-carrying capacity, failure modes, and slip modulus of connections should be established for different engineered timber panels ordinarily used in industry in order to give clear guidelines for the design of TT joints and stiffness values for calculation models.

In addition, a first investigation on the creep behavior of this newly developed construction system can be found in Appendix B.3, based on the case-study presented in this chapter. It is an important preliminary work, as creep greatly influences the SLS of timber structures.



## 5 Mechanical characterization of through-tenon joints

---

This chapter is based on:

J. Gamero, J. F. Bocquet and Y. Weinand. Experimental investigations on the load-carrying capacity of digitally produced wood-wood connections. *Engineering Structures*, 213:110576, 2020. doi:10.1016/j.engstruct.2020.110576.

&

A. C. Nguyen, J. Gamero, J. F. Bocquet and Y. Weinand, Numerical investigations on the shear behavior of digitally produced wood-wood connections, manuscript in preparation for publication.

---

### 5.1 Introduction

Since the development of timber structures using a large number of digitally produced wood-wood connections, numerous calculation models have been developed, from complex FE to simplified methods, as presented in Chapter 4. All these models rely on the mechanical behavior of connections, which is an essential parameter in the prediction of the structural response of timber structures. The stiffness and load-carrying capacity of connections greatly influence displacement, stress distribution, and failure modes of global structures. However, few studies have been performed on the local behavior of wood-wood connections, as steel fasteners and glue have replaced them in timber structures during recent decades. Most research has focused on experimental investigations for specific case-studies, as mentioned in Section 1.1.3. The mechanical behavior of TT connections has thus primarily been studied in rotation because of the particular origami or free-form shapes of these structures, such as the Vidy theater presented in Chapter 2. However, with the development of standardized timber elements interconnected by TT joints for basic housing systems, the load-carrying capacity for in-plane loads is crucial for sound structural design.

Therefore, this chapter investigates the local behavior of TT connections for in-plane loading.

The construction system for interconnected timber elements using multiple TT joints in series presented in Chapter 3 is used as reference for this study. The different element members can be single- or double-layered, as presented in Fig. 5.1a and b, respectively, depending on design choices and manufacturing possibilities. The grain orientation of the different panels composing one element is always in the length direction and, as a result, parallel to the tenon length (Fig. 5.1c). The notches  $n_t$  and  $n_m$ , resulting from the cutting tool diameter, are positioned so as to maximize the contact surface for in-plane loads (see Fig. 3.8, configurations (a.2) and (b.2)). In addition to notches, TT joints are characterized by several geometrical parameters in this investigation: the tenon length  $l_t$ , the tenon thickness  $t_t$ , the tenon height or mortise thickness  $t_m$ , the tenon spacing  $s_t$ , and a possible angle  $\alpha_t$  to ease the assembly process.

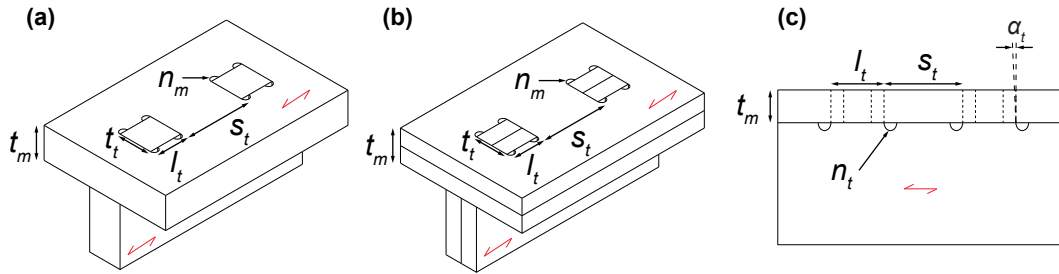


Figure 5.1 – Geometry and parameters of a TT connection: (a) Axonometry of a single-layered connection / (b) Axonometry of a double-layered connection / (c) Side view of a connection.

Concerning the load-carrying capacity of TT connections, different failure modes can be expected depending on the connection parameters when the connection is loaded in the length direction as shown in Fig. 5.2: (b) shear failure in the tenon, (c) compression failure in the tenon, (d) shear failure in the mortise, and (e) compression failure in the mortise. Only shear and compression failures are of interest, since only tenons with a width-to-length ratio ( $t_m/l_t$ ) less than or equal to 1 are studied here. If the slenderness of the tenon is greater than 1, the failure modes could differ from those mentioned. This research investigates shear failure in the tenon component (b) and compression failure in both the tenon (c) and mortise (e) components. Mortise shear failure (d) is not studied here as it can be easily avoided with the basic geometrical considerations described in Equation 5.1:

$$f_{vk,mortise} \times 2 \times s_t \times t_m > f_{vk,tenon} \times l_t \times t_t \quad (5.1)$$

$$2s_t > l_t \quad (5.2)$$

where  $f_{vk}$  is the characteristic shear strength of the material. Equation 5.1 can be simplified to Equation 5.2 if the mortise and tenon parts have the same thickness and material properties. In most cases, the spacing between the tenons ( $s_t$ ) is longer than the tenon length ( $l_t$ ) and a shear failure of the mortise rarely occurs.

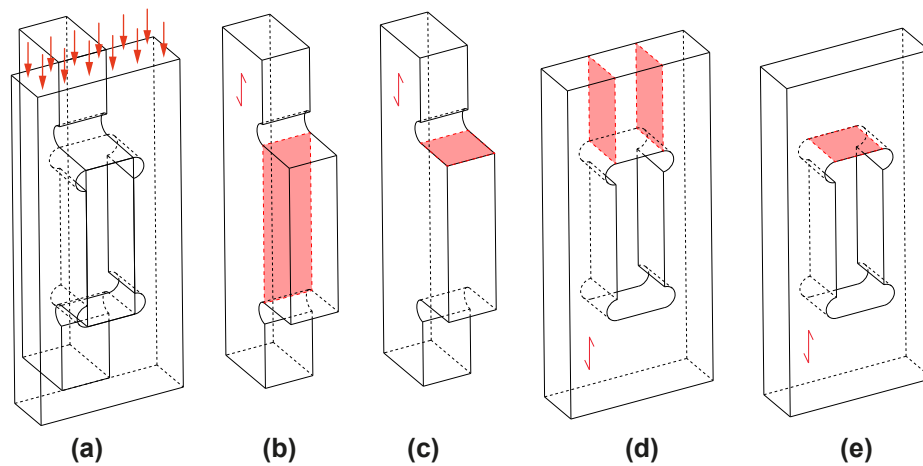


Figure 5.2 – Possible failure modes of a TT connection: (a) Axonometry of a TT joint loaded in its length direction / (b) Shear failure area in tenon part / (c) Compression failure area in tenon part / (d) Shear failure area in mortise part / (e) Compression failure area in mortise part.

Both the contact stiffness for the proposed calculation model, defined in the previous Subsection 4.4.2, and the shear stiffness, more widely used in calculation models such as the analytical gamma method and other numerical models [101, 153], were studied.

Based on these considerations, there are several objectives in this chapter: (i) determine the mechanical behavior of TT joints for different commonly available engineered timber panels and tenon lengths ( $l_t$ ), (ii) estimate the stiffness and load-carrying capacity of TT joints for both compression and shear, (iii) estimate the load-carrying capacity of TT joints according to existing European building standards (Eurocode 5 [33]) with the characteristic values given by the panel manufacturer's product specifications, and (iv) compare these design guidelines to the tests. For this purpose, an extensive experimental campaign comprising more than 400 tests was conducted, and two different experimental setups were developed to study both the compression and shear behaviors of TT connections. The results were compared to existing design criteria for load-carrying capacity. In addition, a numerical model based on continuum damage mechanics developed by Nguyen[100] and presented in Appendix C.4 was implemented to investigate the shear behavior of TT connections, in particular the wood-wood connection stiffness obtained exclusively from tests.

The chapter is structured as follows:

- Section 5.2 introduces the state-of-the-art of design guidelines and experimental setups.
- Section 5.3 shows the engineered timber panels used in the study.
- Section 5.4 describes the experimental setups developed and the loading procedure.
- Sections 5.5 and 5.6 present the results for compression and shear, respectively.
- Section 5.7 gives guidelines on the load-carrying capacity of the connections studied.
- Section 5.8 summarizes the main conclusions.

## 5.2 State-of-the-art

### 5.2.1 Design guidelines for wood-wood connections

Connections have a large influence on the structural performance of timber structures. Their mechanical behavior is an important parameter, both for the SLS determined by their rigidity and for the ultimate limit state determined by their load-carrying capacity. The introduction of the connection stiffness, called slip modulus  $K_{ser}$ , was a major advance in EC5 [33] for solving problems of stability and large displacement, but it was only defined for steel fasteners such as nails, dowels, bolts, or screws. For the load-carrying capacity of wood-wood connections, few guidelines are proposed in the Swiss standard [146] or in the national application document of German standard [25]. However, such standards apply exclusively to traditional carpentry joints. Several pieces of research have also been performed on traditional joints, as it is an area of interest in the field of built heritage restoration for the assessment and restoration of old timber constructions. Research into both the strengthening of traditional carpentry joints [13, 14] as well as on traditional tenon-mortise connections [41, 75, 107] has been performed. Unfortunately, these traditional joints are mainly used for beam and post connections, and they are different from modern ones used for engineered timber panels. Although a multiple tenon joint produced by CNC machining was studied by Claus et al. [20], it was only applied to beam and post assemblies. For timber plate products, new timber-to-timber contact joints have been developed to reconstitute the diaphragm effect of CLT in modern structures [19, 138, 139, 140]. Based on EC5 and these works, the connection failures are generally verified with design equations, which can serve as a basis for the structural design of TT connections.

Regarding shear failure of the tenon component (presented in more detail in Fig. 5.3a) a non-uniform stress distribution called the hammock-shape shear-stress distribution (HSSSD) can be expected according to two studies [147, 159]. The design Equations 5.3 and 5.4 can then be used:

$$\tau_d \leq k_{v,red} \times f_{v,k} \frac{k_{mod}}{\gamma_M} \quad (5.3)$$

$$\tau_d = \frac{F}{l_t \times t_t} \quad (5.4)$$

where  $\tau_d$  is the design shear stress,  $k_{v,red}$  is the coefficient for considering the non-uniform shear-stress distribution HSSSD,  $f_{v,k}$  is the characteristic shear strength,  $k_{mod}$  is the modification factor for load duration and moisture content, and  $\gamma_M$  is the partial factor according to material properties.

For the compression failure, the different parameters are shown in Fig. 5.3b, c, and d. A spreading of the compression strength can be expected according to EC5 and Verbist et al. [159]. It is taken into consideration with the coefficient  $k_{c,\alpha}$ . The angle  $\alpha$  is equal to  $0^\circ$  for the studied configuration, as the grain orientation is always parallel to the joint length. The



design Equations 5.5, 5.6 and 5.7 can therefore be used as reference:

$$\sigma_{c,d} \leq k_{c,\alpha} \times f_{c,0,k} \frac{k_{mod}}{\gamma_M} \quad (5.5)$$

$$\sigma_{c,d} = \frac{F}{t_t \times t_m} \quad (5.6)$$

$$k_{c,\alpha} = 1 + \sin \alpha \times (k_{c,90} - 1) \quad (5.7)$$

where  $\sigma_{c,d}$  is the design compression stress,  $f_{c,0,k}$  is the characteristic compression strength parallel to the grain,  $k_{c,\alpha}$  represents the spreading of compression stress, and  $k_{c,90}$  represents the spreading of compression stress perpendicular to the grain. Compression spreading in the mortise area is expected to be higher than in the tenon, as stress can propagate on both sides of the tenon, as shown in Fig. 5.3b. With the same material properties, the compression failure should therefore occur in the tenon component.

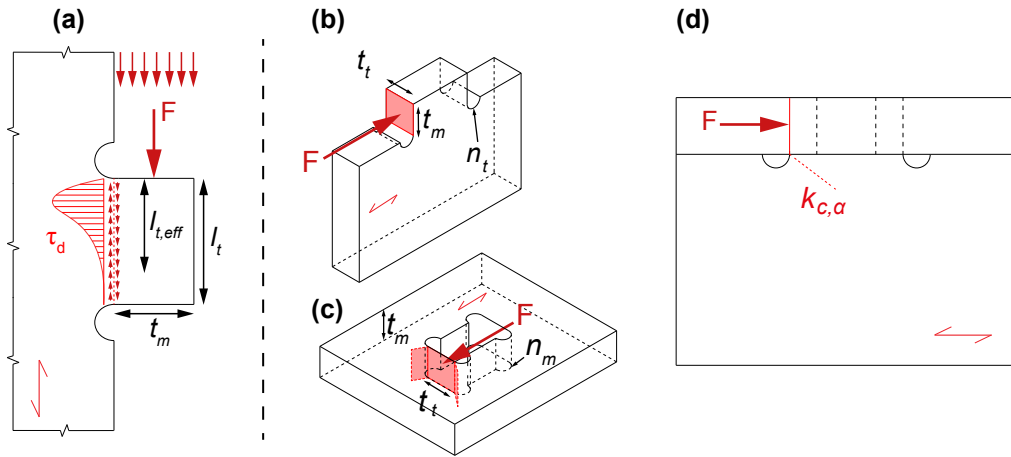


Figure 5.3 – Failure modes studied: (a) Shear failure in tenon part / (b) Compression failure in tenon part / (c) Compression failure in mortise part / (d) Expected compression spreading in tenon part.

### 5.2.2 Experimental protocols for the shear behavior of timber

Several methods exist in the literature to characterize the shear properties of wood material, whereas the same method is generally used to evaluate compression properties. Furthermore, these approaches were mostly developed for the characterization of glued products such as GLT and CLT. For structural timber and GLT, the standard EN 408 [37] proposes determining the shear strength parallel to the grain with an inclined setup as shown in Fig. 5.4a. Schmidt et al. [138, 139] have used this type of test setup for shear-key timber connectors. It is a simple and efficient method to avoid expensive and time-consuming steel setups but is difficult to apply with the geometry of TT. For CLT, the standard EN 16351 [30] introduces three methods: a basic method for determining the shear strength in Annex D (Fig. 5.4c), an alternative method for determining the rolling shear strength and stiffness in Annex F.3.3 (Fig. 5.4b), and a method

inspired by an inclined setup for determining shear values within a layer (net cross-section) in Section E4.2. For wood-based panels, the standard EN 789 [38] gives a method for determining panel shear properties with a particular loading arrangement as presented in Fig. 5.4d. For planar shear properties, a similar setup as the one shown in Fig. 5.4d is also presented but with glued steel plates on the side of panels. Finally, the old French standard NF B51-032 [99], published in 1981, presents a method for compressive shear tests (Fig. 5.4e). Although these different methodologies cannot be transposed directly to wood-wood connections, as they are generally used for material specifications, they can inspire new experimental protocols. Push-out tests are also commonly used to study the shear behavior of timber joints [19]. Recently, specific research into TT joints related to a case-study was performed with push-out tests [111], in addition to those presented in Subsection 3.5.2. These tests are convenient to use because they do not require any additional steel members for the setup. However, this method cannot be performed on a single joint to obtain a precise value. In 2016, a steel-based setup was developed by Mira et al. [22] to investigate the shear behavior of digitally produced wood-wood connections, although the assembly geometry was different. Based on this work and the standard EN 789 [38], a new experimental setup was developed for investigating the shear behavior of TT in the present study.

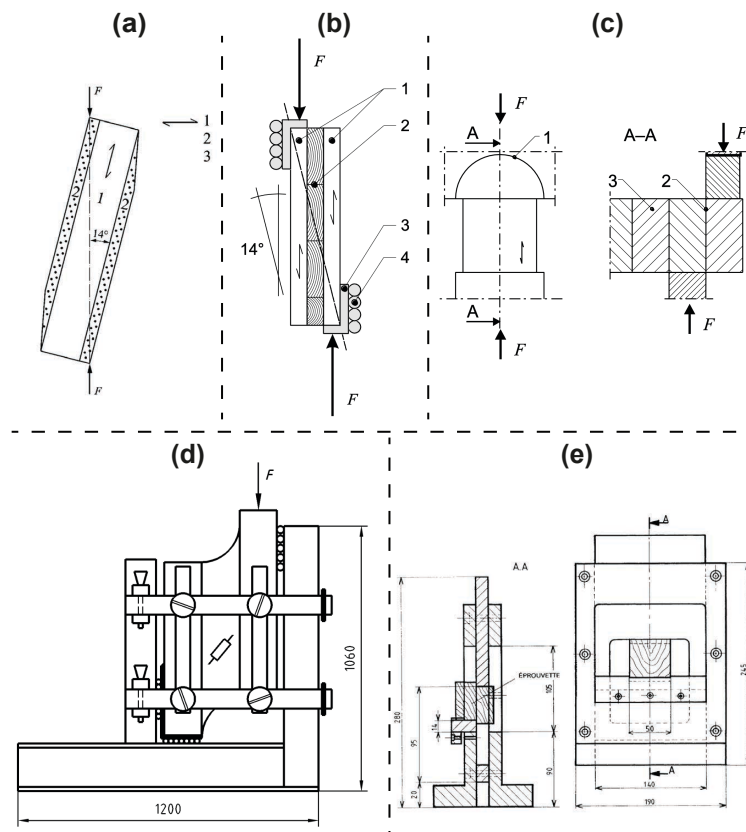


Figure 5.4 – Shear experimental setup for timber: (a) EN 408 [37] / (b) EN 16351 Annex E3.3 [30] / (c) EN 16351 Annex D [30] / (d) EN 789 [38] / (e) NF B51-032 [99].

## 5.3 Materials

### 5.3.1 General

This study was conducted on different types of engineered timber panels. The panels were chosen because of their wide distribution among wood suppliers on the European market and their standardized mechanical properties. Spruce oriented strand board type 3 (OSB 3), spruce and beech laminated veneer lumber (LVL), and spruce multiply solid wood (MSW) panels were investigated. A thin thickness of less than 40 mm was preferred considering the type of construction system developed using TT. Ongoing research on specific case-studies [49, 120] has also influenced the choice of materials. The different panels are shown in Fig. 5.5 and their characteristics are listed in Table 5.1. Material properties and characteristics were obtained from the following sources: the standard EN 12369 [29] for OSB type 3 (Kronospan, Jihlava, Czech Republic), the VTT certificate [163] for spruce LVL Kerto Q<sup>®</sup> (Metsä Wood, Espoo, Finland), and the supplier technical certificates for beech LVL Baubuche Q<sup>®</sup> (Pollmeier, Creuzburg, Germany) [9] and spruce MSW (Dold<sup>®</sup>, Buchenbach, Germany) [26].

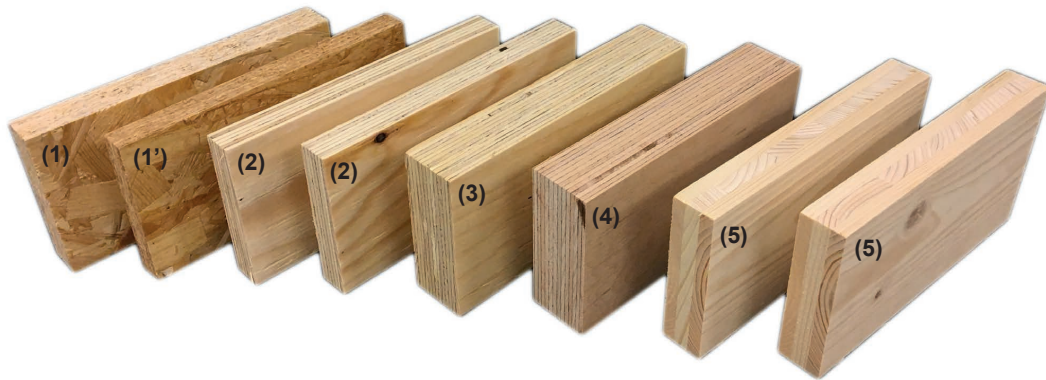


Figure 5.5 – Materials used for the experimental investigation on TT connections: (1) OSB type 3 25 mm / (1') OSB type 3 18 mm / (2) Spruce LVL 21 mm / (3) Spruce LVL 39 mm / (4) Beech LVL 40 mm / (5) Spruce MSW 27 mm.

Table 5.1 – Material properties for the experimental investigation of TT connections.

ID	Type	Species	Thickness (mm)	Ply number	Lay-up	Lay-up thickness (mm)	Thickness tolerance (mm)
(1)	OSB 3	Spruce	25	3	-	-	+ - 0.8
(1')	OSB 3	Spruce	18	3	-	-	+ - 0.8
(2)	LVL	Spruce	21	7	-     -	3 each	-1.03 +1.43
(3)	LVL	Spruce	39	13	-     -     -	3 each	-1.57 +1.97
(4)	LVL	Beech	40	14	-       -	3 each*	+ - 1
(5)	MSW	Spruce	27	3	-	6.9/13.2/6.9	+ - 1

\* 2 mm on the two outer layers because of the finishing process.

### 5.3.2 Moisture content and properties

The characteristic strength and material property values, determined by the manufacturers, are given for an equilibrium moisture content resulting from a temperature of 20°C and a relative humidity of 65% for OSB and LVL panels [9, 29, 163]. For the MSW panel, such values are determined for a moisture content near 12%, where the average density ( $\rho_{mean}$ ) is 480 kg/m<sup>3</sup> [26]. As a result, samples were conditioned in a climate chamber at a relative humidity of 65 ± 5% and a temperature of 20 ± 2°C until reaching a constant mass. The mass was considered constant when the results of two successive weighing operations, conducted 24 hours apart, did not differ from the mass of the test piece by more than 0.1% . Specimens were stored in the climate chamber for several weeks before testing. The density ( $\rho_{mean,test}$ ) was then determined according to EN 323 [36]: the results are listed in Table 5.2.

Table 5.2 – Tested material densities compared to the manufacturer's values.

ID	$\rho_{mean,test}$ (kg/m <sup>3</sup> )	$\rho_{mean}$ (kg/m <sup>3</sup> )	$\delta_\rho$ (%)
(1)	605.29	600	0.88
(1')	595.92	600	-0.68
(2)	485.37	510	-4.83
(3)	483.18	510	-5.26
(4)	799.35	800	-0.08
(5)	462.03	480	-3.74

The tested material densities were approximately similar to the manufacturer's values, with a maximum difference of only 5.26%. It was therefore not necessary to specifically measure the moisture content, which was considered to have stabilized at 12% for all materials. The characteristic strength and material property values specified for the different materials were thus considered in the analysis. In addition, the specimen types in this study were produced from different panels randomly selected from a batch of 10 panels per material to have a good statistical representation.

### 5.3.3 Compression strength characterization

Although the mechanical properties of all materials used in this study were standardized, the characteristic compression strength was tested for each panel in order to determine a precise value on the one hand and to assess the discrepancy between manufacturer's and test values on the other hand. Compression tests were chosen because they are relatively quick and straightforward to perform. Therefore, not all properties were re-characterized by tests, such as for the characteristic shear strength. All experimental data presented in this section are available in an open-access data repository [48].

### Method

Material compression tests were performed according to the standard EN 789 [38], which is used for the determination of mechanical properties for wood-based panels. In Appendix C.1.1, the dimensions of each specimen type are listed in Table C.1, and the test setup is presented in Fig. C.1. A static universal testing machine (model LFV-200, Walter+Bai AG, Löhningen, Switzerland [164]), with a maximum loading capacity of 200 kN, was used for the material specimens (1) (1') (2) (5) while another static machine (model PL 2.5K, Schenck) with a maximum capacity of 2500 kN was used for (3) and (4). The load was directly applied to the axis of the specimens' upper faces with a constant rate of 0.19 kN/s for (1), 0.24 kN/s for (1'), 0.27 kN/s for (2), 0.7 kN/s for (3), 0.15 kN/s for (4), and 0.3 kN/s for (5). A total of 10 replicates per material were tested and two linear variable differential transformers (LVDT) were positioned on each side of the specimens.

### Results

The average ultimate load ( $F_{max}$ ) was determined from the tests. The 5% fractile value ( $F_{max,0.05}$ ) was then calculated in order to compare the tested characteristic compression strength ( $f_{c,0,k,test}$ ) with the characteristic strength given by panel manufacturers ( $f_{c,0,k}$ ). The methodology for calculating the 5% fractile values ( $F_{max,0.05}$ ) is presented in Appendix C.1.2. All results are listed in Table 5.3. For OSB 25 and 18 mm,  $f_{c,0,k,test}$  was significantly lower than  $f_{c,0,k}$  with differences of -34.49% and -37.92%, respectively. In contrast,  $f_{c,0,k,test}$  for spruce LVL 21 mm and spruce MSW 27 mm was significantly higher than  $f_{c,0,k}$  with differences of 41.67% and 74.59%, respectively. Concerning spruce LVL 39 mm and beech LVL 40 mm, the values of  $f_{c,0,k,test}$  were the closest to  $f_{c,0,k}$  with differences of only 11.83% and 3.55%, respectively. These significant differences, whether negative or positive, emphasize the discrepancy between standard and test values depending on the panel type. OSB and MSW panels have a particular lay-up with a large cross-layer in the middle, which may have increased these differences although these values should be more accurate. For spruce LVL 21 mm, the difference is due to the gap in performance as function of the panel thickness [163] but remains relatively close to the value of spruce LVL 39 mm. LVL panels are thus more reliable than OSB and MSW panels.

Table 5.3 – Results of compression tests per material according to EN 789 [38].

ID	$F_{max}$ (kN)	$c_{v,F_{max}}$ (%)	$F_{max,0.05}$ (kN)	Section (mm <sup>2</sup> )	$f_{c,0,k,test}$ (MPa)	$f_{c,0,k}$ (MPa)	$\delta$ (%)
(1)	41.82	7.02	36.50	3618	10.09	15.40	-34.49
(1')	53.78	7.81	45.94	5000	9.19	14.80	-37.92
(2)	120.10	3.15	113.05	4200	26.92	19.00	41.67
(3)	237.24	2.36	226.80	7800	29.08	26.00	11.83
(4)	460.84	2.28	441.55	8000	55.19	53.30	3.55
(5)	118.75	4.78	108.42	5400	20.08	11.50	74.59

## 5.4 Experimental methods

The load-carrying capacity of the connections in compression and the contact stiffness, necessary for the simplified model presented in Chapter 4, were investigated with the experimental setup described in Subsection 5.4.1. In contrast, their load-carrying capacity in shear and the stiffness required for commonly used calculation models were studied with the shear experimental setup presented in Subsection 5.4.2. In addition, the loading procedure for both setups is introduced in Subsection 5.4.3.

### 5.4.1 Compression tests

#### Experimental setup

The experimental setup developed for the shear behavior could also have been used to test the compression behavior. However, the shear setup, composed of numerous steel elements, is time-consuming to prepare for a single test. In view of the large number of tests, this compression setup was therefore designed for an efficient experimental campaign, as it does not require a long preparation time prior to testing. The compression behavior of the TT joints was investigated with the experimental setup presented in Fig. 5.6. The static universal testing machine [164], presented in Subsection 5.3.3, with a maximum loading capacity of 200 kN was used. Loads were applied in the joint axis and two 10-mm-thick steel plates (6)(9) were used to avoid local indentation at the top and bottom faces of the specimens. Lateral restraints (3) were positioned to prevent a lateral shift of the sample with respect to the loading axis. A support plate (4) was bolted to the testing machine. Beech LVL was chosen to compose the setup for its high mechanical characteristics. Two LVDTs were placed on each side of the samples to record the relative displacement at the contact area ( $d$ ).

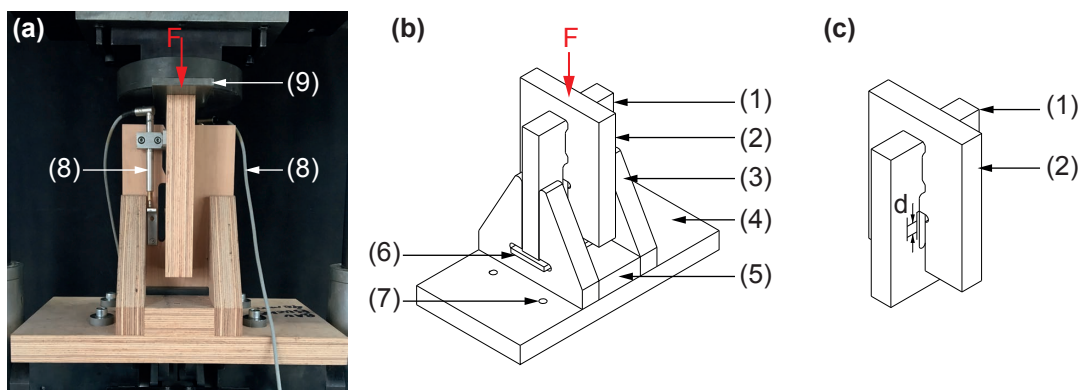


Figure 5.6 – Compression experimental setup for TT connections: (a) Side view: (8) two LVDTs sensors and (9) steel plate 10 mm / (b) Technical axonometry: (1) tenon part of the specimen, (2) mortise part of the specimen, (3) lateral restraints, (4) support plate, (5) support plate, (6) steel plate 10 mm, and (7) bolt  $\varnothing 24$  mm / (c) Specimen:  $d$  is the measured area.

### Specimens

The specimen geometries are described in Fig. 5.7 and their properties are listed in Table 5.4. According to the possibilities of the construction system, single- and double-layered (SL and DL, respectively) TT joints were studied. The materials described in Section 5.3 were assembled as follows: OSB 3 18 and 25 mm (DL), spruce LVL 21 mm (DL), spruce LVL 39 mm (SL), beech LVL 40 mm (SL) and spruce MSW 27 mm (DL). Only TT joints made of the same material were studied. However, the influence of different material combinations could be investigated in future research. The design objective was to reach the compression limit of the TT assembly for one connection. The geometry was thus carefully designed to prevent shear failures by considering the tenon length  $l_t$  as infinite (see Fig. 5.7b). The gray part of the specimen, illustrated in Fig. 5.7b, represents the TT connection, while the other part was only manufactured to prevent a lateral displacement of the mortise. The parameter  $e_t$  was kept as small as possible to avoid additional friction in the experimental setup, and  $l_{t,2}$  was reduced to the minimum distance necessary to ensure the overall stability of the test setup. The mortise part, shown in Fig. 5.7d, was a basic mortise geometry cut in its cross-sectional plane. With this configuration, the load was applied directly on the top face of the mortise part to study the compression behavior. All tests were performed with the grain orientation parallel to the joint length. For each specimen type, 15 replicates were produced with the five-axis CNC machine, described in Subsection 3.3.1, for a total of 75 tests. A spiral router cutter Marathon (ID 240502, Leitz<sup>®</sup>, Oberkochen, Germany [86]) was used with a diameter of 12 mm, a rotational speed of 18,000 r/min, and a feed speed of 4.5 m/min. The notch diameters  $n_t$  and  $n_m$  were set at 13 mm as fixed parameters for all specimens due to the cutting tool diameter of 12 mm. Such a tool diameter was found to be a good compromise between minimizing the loss of material in the assembly area and having a tool that was sufficiently strong for an efficient production (and thus optimized for number of machining cycles, tool wear, etc.). It was already a relatively small tool compared to those used in timber construction. No additional gaps were added during the contouring of the TT joints.

Table 5.4 – Specimen properties for compression tests on TT as described in Fig. 5.7.

ID	Units	EM1	EM2	EM3	EM4	EM5
Materials	-	OSB3	Kerto Q	Kerto Q	Baubuche	MSW
Layers	-	2	2	1	1	2
$h_t$	mm	260	260	260	260	260
$w_t$	mm	180	180	180	180	180
$t_t$	mm	50	42	39	40	54
$l_t$	mm	50	50	50	50	50
$l_{t,2}$	mm	117	117	117	117	117
$e_t$	mm	10	10	10	10	10
$h_m$	mm	260	260	260	260	260
$w_m$	mm	190	190	190	190	190
$t_m$	mm	36	42	39	40	54
$l_m$	mm	87	87	87	87	87

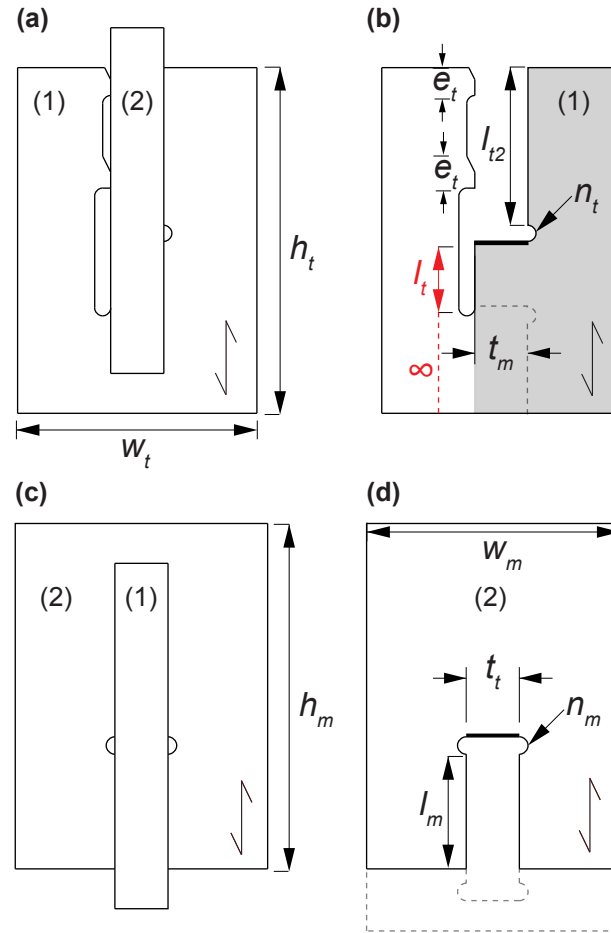


Figure 5.7 – TT compression specimens: (a) Front view: (1) tenon part and (2) mortise part / (b) Front view with only (1), the gray part represents the TT connection / (c) Side view / (d) Side view with only (2).

#### 5.4.2 Shear tests

##### Experimental setup

An experimental setup was developed to perform shear tests on single TT joints, as shown in Fig. 5.8a. Details are presented in technical and schematic drawings in Fig. 5.8b and c. Specimens were positioned in a rigid steel frame anchored inside the same static universal testing machine [164] presented in the previous subsection with a maximum loading capacity of 200 kN. The hydraulic jack applied pressure on the axis of the mortise specimen (4) through a steel plate of 40 mm thickness (1) possessing the same dimensions as the mortise specimen to avoid local indentation. The tenon specimen (5) was rigidly fixed on its top by a steel plate of 15 mm thickness (3) and four bolts of 24 mm diameter (2): two on each side. A 5-mm-thick steel plate (6) was welded to the lower part of the bolts to maintain them in their initial position and avoid lateral displacement. In addition, a 40-mm-thick beech LVL plate (7) was bolted to



the setup to maintain the tenon component in position and prevent the rotation of its lower part. The mortise component was kept in position thanks to a 20-mm-thick steel plate (8) and a steel bracket (11). They were fastened with eight bolts of 12 mm diameter. Two other bolts of 12 mm diameter (9) linking the steel plates (8) and (3) were inserted on each side of the mortise part to stiffen the lateral displacement of the setup. Two Teflon plates (10) were positioned between the steel plate (8) and the mortise component to remove friction between these parts. Two LVDTs were mounted on each side of the specimens on the axis of the TT (12). The lateral displacement of the setup was controlled with four LVDTs positioned on the plates (3) and (8), which resulted in negligible movement.

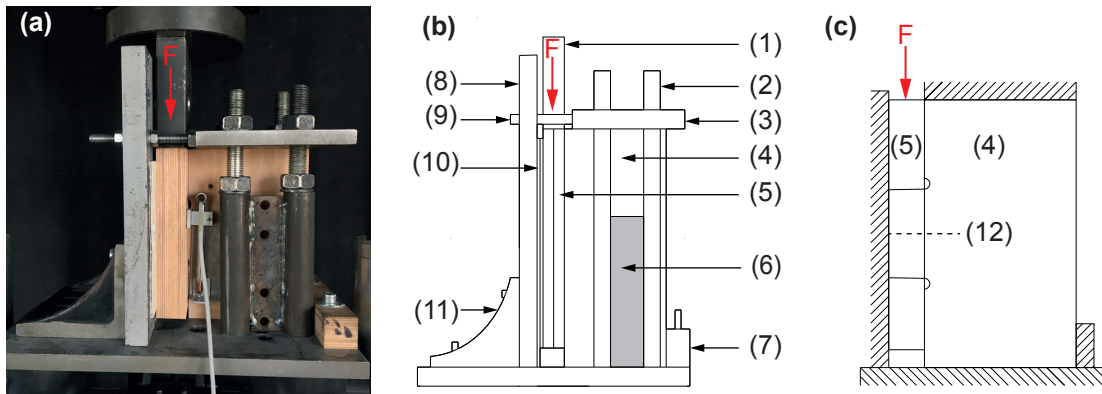


Figure 5.8 – Side view of the shear experimental setup for TT connections: (a) Photograph / (b) Technical drawing: (1) steel plate 40 mm, (2) bolt Ø24 mm, (3) steel plate 15 mm, (4) tenon part, (5) mortise part, (6) steel plate 5 mm, (7) beech LVL 40 mm, (8) steel plate 20 mm, (9) bolt Ø12 mm, (10) two Teflon plates, and (11) steel bracket 20 mm with 8 bolts Ø12 mm / (c) Schematic drawing: (12) two LVDTs sensors.

### Specimens

The specimen geometry parameters are displayed in Fig. 5.9 and all properties are listed in Table 5.5. The same material and layer configurations as those described for compression in Subsection 5.4.1 were used. For all materials, tenon lengths  $l_t$  of 50, 100, and 150 mm were considered, except for OSB 3 for which the lengths were equal to 50, 65, and 80 mm due to the material's low compression strength. Equation 5.2 was verified for each specimen to determine the height of the mortise part  $h_m$  and avoid shear failure in it. The height of the tenon part  $h_t$  was then established by adding 20 mm to  $h_m$  to allow for displacement during the tests. The widths of the mortise  $w_m$  and tenon  $w_t$  were calculated to be at least three times larger than the tenon thickness  $t_t$  and mortise thickness  $t_m$ , respectively. An insertion angle  $\alpha_t$  of  $1^\circ$  was defined to ease the insertion of the tenon in the mortise, as each panel has a thickness tolerance (see Table 5.1) that can make the assembly process difficult. All tests were performed with the grain orientation parallel to the joint length. For each specimen type, 20 replicates were produced for a total of 300 tests. The same CNC machine and manufacturing parameters described in Subsection 5.4.1 were used.

Table 5.5 – Specimen properties for shear tests on TT as described in Fig. 5.9.

ID	Materials	Layers	$l_t$ (mm)	$h_t$ (mm)	$h_m$ (mm)	$w_t$ (mm)	$w_m$ (mm)	$t_t$ (mm)	$t_m$ (mm)
T1-50	OSB 3	2	50	250	230	163	156	50	36
T1-65	OSB 3	2	65	250	230	163	156	50	36
T1-80	OSB 3	2	80	250	230	163	156	50	36
T2-50	Kerto Q	2	50	250	230	169	160	42	42
T2-100	Kerto Q	2	100	300	280	169	160	42	42
T2-150	Kerto Q	2	150	350	330	169	160	42	42
T3-50	Kerto Q	1	50	250	230	169	160	39	39
T3-100	Kerto Q	1	100	300	280	169	160	39	39
T3-150	Kerto Q	1	150	350	330	169	160	39	39
T4-50	Baubuche	1	50	250	230	169	160	40	40
T4-100	Baubuche	1	100	300	280	169	160	40	40
T4-150	Baubuche	1	150	350	330	169	160	40	40
T5-50	MSW	2	50	250	230	169	160	54	54
T5-100	MSW	2	100	300	280	169	160	54	54
T5-150	MSW	2	150	350	330	169	160	54	54

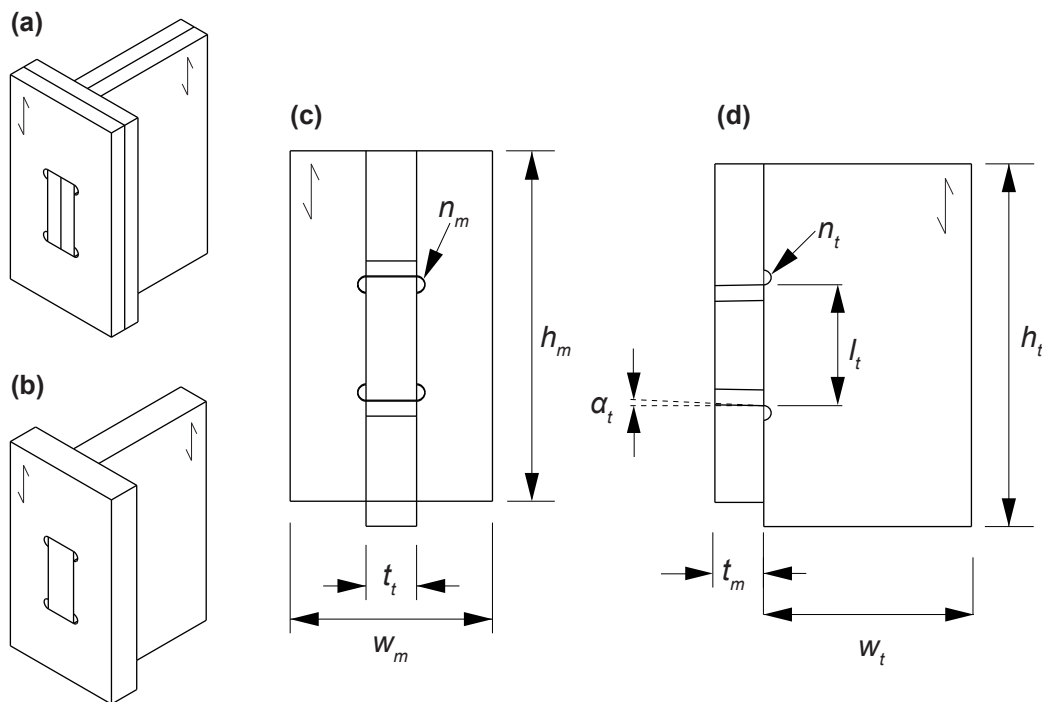


Figure 5.9 – TT shear specimens: (a) Axonometry of single-layered type / (b) Axonometry of double-layered type / (c) Front view / (d) Side view.

### 5.4.3 Loading procedure

An experimental protocol dedicated to wood-wood connections does not exist in the current standards. However, the standard EN 26891 gives general principles for the determination of strength and deformation characteristics for joints made with mechanical fasteners [35]. Because of the similarities between these joints and the studied wood-wood connections, this standard was thus used for this experimental campaign. The protocol was divided into seven steps of loading as shown in Fig. 5.10. First, a load-control method was applied with different loading levels in relation to the estimated maximum force  $F_{est}$ . This force was determined with a preliminary test on a non-used replicate for each specimen configuration. From 70% of  $F_{est}$ , a displacement-control method was applied with a constant slip rate of 0.01 mm/s to obtain a total testing time between 10 and 15 minutes. The maximum slip limit  $v_{i,max}$  of 1.5 mm described in the standard was not considered so as to explore the entire connection behavior.

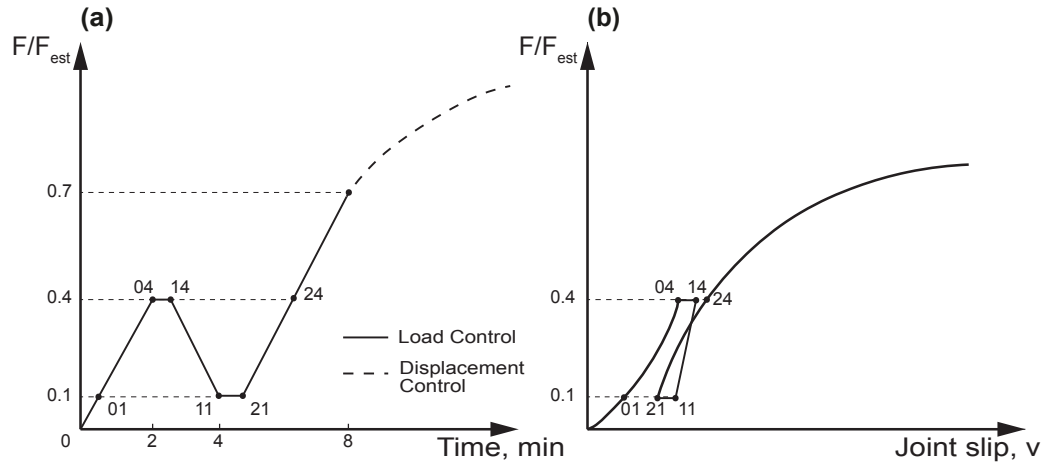


Figure 5.10 – (a) Loading procedure / (b) Idealized load-deformation curve and measurements according to EN 26891 [35].

According to the standard EN 26891, several values were defined: the initial slip  $v_i$  (Equation 5.8), the modified initial slip  $v_{i,mod}$  (Equation 5.9), the initial slip modulus  $k_i$  (Equation 5.10), and the slip modulus  $k_s$  (Equation 5.11). The slip modulus after first loading  $k_{s,mod}$  (Equation 5.12) was also calculated for the numerical study on shear behavior.

$$\text{Initial slip} = v_i = v_{04} \quad (5.8)$$

$$\text{Modified initial slip} = v_{i,mod} = 4/3(v_{04} - v_{01}) \quad (5.9)$$

$$\text{Initial slip modulus} = k_i = 0.4F_{max}/v_i \quad (5.10)$$

$$\text{Slip modulus} = k_s = 0.4F_{max}/v_{i,mod} \quad (5.11)$$

$$\text{Slip modulus after first loading} = k_{s,mod} = (0.4F_{max} - 0.1F_{max})/(v_{24} - v_{21}) \quad (5.12)$$

where  $F_{max}$  is the average ultimate load per specimen type

## 5.5 Compression tests

The characteristic and test values ( $f_{c,0,k}$  and  $f_{c,0,k,test}$ ), determined in Subsection 5.3.3, were used to investigate the compression behavior of the TT connections. The results on the compression behavior of TT connections are discussed in this section. In addition, all experimental data presented in this section are available in an open-access data repository [48].

### Results

The results of the compression tests for TT joints are listed in Table 5.6, and the failures per specimen type are shown in Fig 5.12. The full load-displacement curves per specimen type are displayed in Fig. 5.11. The statistical distribution of the maximum load ( $F_{max}$ ) and slip modulus ( $k_s$ ) can be found in Appendix C.2 (see Fig C.2 and C.3). The average coefficient of variation for the maximum load ( $F_{max}$ ) and slip modulus ( $k_s$ ) were quite low, with values of approximately 5% and 15%, respectively. The experimental procedure is thus consistent for this type of tests.

For the load-carrying capacity, the 5% fractile values of the maximum load ( $F_{max,0.05}$ ) were used to directly compare the compression strength ( $\sigma_{c,k,TT}$ ) with the characteristic compression strengths ( $f_{c,0,k}$  and  $f_{c,0,k,test}$ ) according to Equations 5.13 and 5.14:

$$\sigma_{c,k,TT} = \frac{F_{max,0.05}}{A_c} ; A_c = t_t \times t_m \quad (5.13)$$

$$\sigma_{c,k,TT} \leq k_{c,\alpha} \times f_{c,0,k} \quad (5.14)$$

with the compression spreading coefficient ( $k_{c,\alpha}$ ) always equal to 1 as the grain orientation is parallel to the joint length. Equation 5.14 is derived from Equation 5.5 where the modification factor ( $k_{mod}$ ) and partial factor ( $\gamma_M$ ) were removed, as only 5% fractile characteristic values were directly compared.

Due to the discrepancy in the characteristic compression properties and real performance of materials emphasized in Subsection 5.3.3, significant differences were observed between the compression strengths  $\sigma_{c,k,TT}$  and  $f_{c,0,k}$ . For OSB TT joints (EM1),  $\sigma_{c,k,TT}$  was 22.09% lower than  $f_{c,0,k}$ , while it was 47.79% and 82.70% higher for spruce LVL (EM2) and MSW (EM5), respectively. Therefore, the EC5 guidelines defined in Equation 5.14 were either underestimating or overestimating the actual load-carrying capacity to a great extent, placing EM1 on the unsafe side of design. For the single-layered joints EM3 and EM4, the differences were less pronounced as their compression properties were more precisely determined. The material characterization announced by panel manufacturers  $f_{c,0,k}$  plays a major role in correctly calculating the compression strength of TT.

In contrast,  $\sigma_{c,k,TT}$  was an average of 10.84% higher among all materials than the real compression performance  $f_{c,0,k,test}$ , with differences ranging from 4.32% to 25.50%. The value of EM1 was approximately 25% higher while the values of the specimens EM2, EM3, EM4,

and EM5 were only 7% higher on average. The internal panel lay-up and material variability influence this phenomenon. Thus, these results highlight compression spreading uniquely in OSB TT joints (EM1). The spreading coefficient  $k_{c,\alpha}$  equal to 1 with the grain orientation parallel to the joint (Equation 5.14) is thus consistent with the results obtained for the other materials. However, considering the high discrepancy between  $f_{c,0,k}$  and  $f_{c,0,k,test}$  for several panels (EM1, EM2 and EM5), it is difficult to establish a general rule for the compression spreading coefficient for TT connections made of engineered timber panels. A recommended spreading coefficient  $k_{c,\alpha}$  could be defined according to the material type and joint geometry if the specifications of the material are accurate. Otherwise, it is conservative to not consider the spreading.

Concerning joint stiffness, the initial stiffness highlighted in Subsection 4.4.2 and Fig. 4.9 for very low displacement from 0 to 0.1 mm was also observed for all materials. This could be a unique effect due to several factors, such as material characteristics, manufacturing parameters, assembly gaps, and wood swelling. As a result, the initial slip modulus  $k_i$  was stiffer than the slip modulus  $k_s$  for all materials except T1, for which  $k_i$  was almost equal to  $k_s$ , and T4 for which  $k_s$  was stiffer than  $k_i$  by 15%. The slip modulus  $k_s$  can thus be used directly in the simplified calculation model to be on the safe side of design, as presented in Chapter 4. It is recommended to use the initial slip modulus  $k_i$  to remain conservative in the prediction of displacement for T4 specimens only. Overall, sawn timber products, such as LVL and MSW, demonstrated superior performance over panels composed of wood strands, such as OSB, in terms of both their connection stiffness and load-carrying capacity.

Table 5.6 – Experimental results for compression tests on TT connections.

Designation	Symbol	Units	EM1	EM2	EM3	EM4	EM5
Initial slip	$v_i$	mm	0.59	0.64	0.62	0.50	0.67
Modified initial slip	$v_{i,mod}$	mm	0.57	0.75	0.71	0.43	0.74
Maximum slip	$v_{i,max}$	mm	1.89	2.30	2.09	2.36	3.11
Initial slip modulus	$k_i$	kN/mm	15.71	36.62	33.68	87.14	41.13
Slip modulus	$k_s$	kN/mm	16.07	31.95	29.30	101.03	37.13
Coefficient of variation of $k_i$	$c_{v,i}$	%	13.35	33.48	19.80	8.58	14.58
Coefficient of variation of $k_s$	$c_{v,s}$	%	9.29	32.74	17.59	8.60	10.75
Maximim load	$F_{max}$	kN	22.72	54.84	51.14	106.83	67.70
Coefficient of variation of $F_{max}$	$c_{v,F_{max}}$	%	6.55	5.47	5.11	3.89	6.75
5% fractile of $F_{max}$	$F_{0,05}$	kN	20.77	49.55	47.48	99.28	61.24
Section	$A_c$	mm <sup>2</sup>	1800	1764	1521	1600	2916
Tested strength	$\sigma_{c,k,TT}$	MPa	11.53	28.08	31.21	62.05	21.01
Relative error 01	$\delta_{\sigma_{c,k,TT}/f_{c,0,k}}$	%	-22.09*	47.79	20.04	16.36	82.70
Relative error 02	$\delta_{\sigma_{c,k,TT}/f_{c,0,k,test}}$	%	25.50*	4.32	7.34	12.42	4.64

\* Reference: OSB 18 mm as it has the lowest  $f_{c,0,k,test}$ .

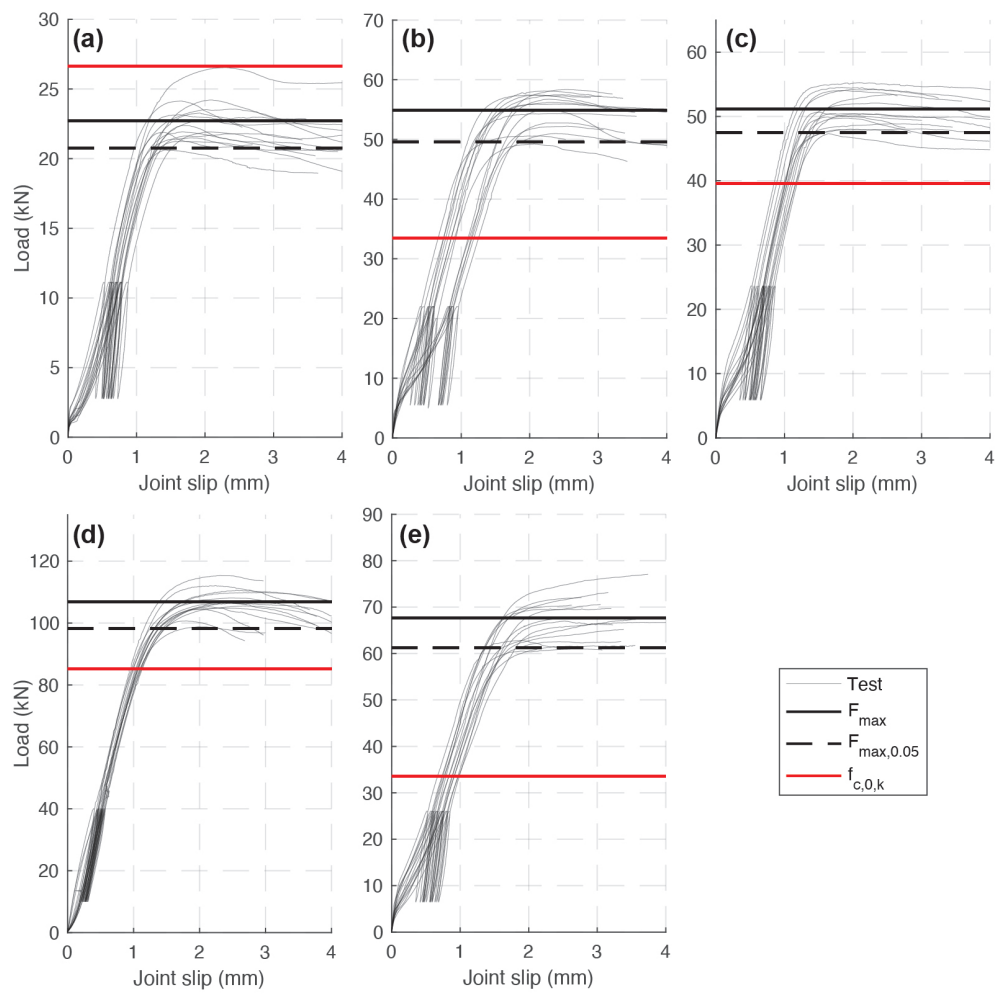


Figure 5.11 – Load-displacement curves of all specimens for compression tests: (a) EM1 / (b) EM2 / (c) EM3 / (d) EM4 / (e) EM5.

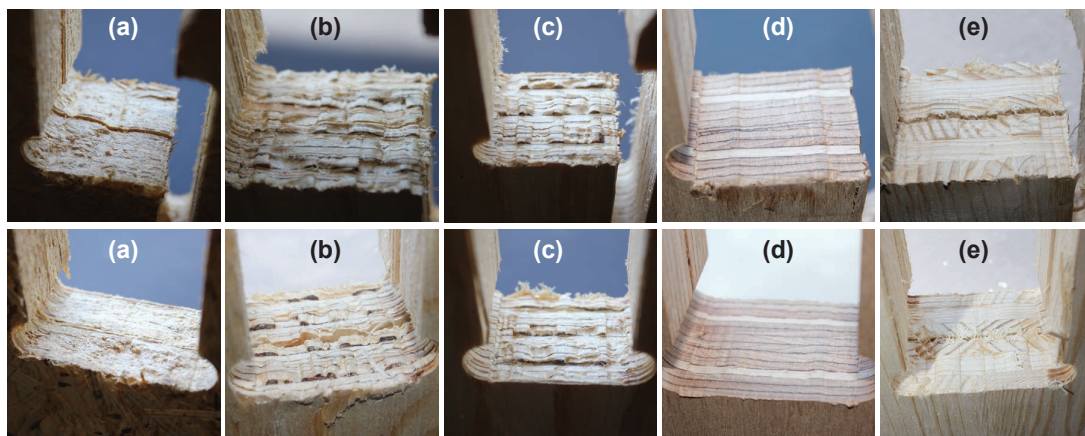


Figure 5.12 – Failure pictures of all TT specimens in compression: (a) EM1 / (b) EM2 / (c) EM3 / (d) EM4 / (e) EM5.

## 5.6 Shear tests

The shear results section is divided into two parts. The first subsection presents the experimental results with a comparison with existing guidelines for the load-carrying capacity. The numerical model presented in Appendix C.4 is then compared to the experimental results in terms of both the load-carrying capacity and stiffness of the connections. For the shear behavior of TT connections, the characteristic shear strength ( $f_{v,k}$ ) of each material was not tested, as the discrepancy between product specifications and real performance was already highlighted by material compression tests (see Subsection 5.3.3). Manufacturer's values were used directly for this investigation. All experimental data are available in an open-access data repository [48].

### 5.6.1 Results

The experimental results are presented by material type in this section. The statistical distribution of the different slip modulus ( $k_s$ ) and maximum loads ( $F_{max}$ ) per specimen type can be found in Appendix C.3 (see Fig. C.4 and Fig. C.6). The average coefficients of variation for the maximum load ( $F_{max}$ ) and slip modulus ( $k_s$ ) were approximately 7% and 16%, respectively for all tests. The experimental procedure is thus consistent for this type of test. The shear strength of TT ( $\tau_{v,k,TT}$ ) was defined according to Equation 5.15 with the 5% fractile values ( $F_{max,0.05}$ ) extracted from the tests. The EC5 guidelines based on Equation 5.3 and defined by Equation 5.16 were used for comparison:

$$\tau_{v,k,TT} = \frac{F_{max,0.05}}{A_v} ; A_v = l_t \times t_t \quad (5.15)$$

$$\tau_{v,k,TT} \leq k_{v,red} \times f_{v,k} \quad (5.16)$$

In an initial approach, the reduction coefficient ( $k_{v,red}$ ) was considered equal to 1, and the modification factor ( $k_{mod}$ ) and partial factor ( $\gamma_M$ ) were removed as only 5% fractile characteristic values were directly compared.

#### T1 - Spruce OSB 18/25 mm, double-layered

For the OSB connections (T1), all results are listed in Table 5.7. The load-displacement curves per tenon length are displayed in Fig. 5.13 and the failures are shown in Fig. 5.14. A compression failure occurred in the specimens with the maximum tenon length (T1-80) instead of a shear failure because of the significant difference between  $f_{c,0,k}$  and  $f_{c,0,k,test}$  (see Fig. 5.14c and d). The T1-80 specimens were thus excluded from this analysis. In contrast, a shear failure occurred for the specimens T1-50 and T1-65 as expected (see Fig. 5.14a and b). The shear strength values  $\tau_{v,k,TT}$  for T1-50 and T1-65 were 27.08% and 21.84% lower than  $f_{v,k}$ , respectively. The load-carrying capacity of OSB TT connections was thus overestimated by approximately 25% for this configuration. This difference could be explained by the discrep-

ancy between the announced characteristic strength and the real performance of the material. However, if the reduction coefficient  $k_{v,red}$  is applied with a value of 0.8, as described in national application documents of EC5 [159],  $\tau_{v,k,TT}$  is only an average of 5.62% lower than  $f_{v,k}$  for the two tenon lengths.

The initial slip modulus  $k_i$  was stiffer than the slip modulus  $k_s$  by an average of 15% for all specimens. This is due to the initial stiffness of the assembly for very small displacement, such as those observed for the compression contact stiffness in Subsection 5.5. Therefore, the slip modulus  $k_s$  can be used directly in calculation models while remaining conservative in the design. The slip modulus increased by 15% between T1-50 and T1-65 while remaining constant between T1-65 and T1-80. It was thus relatively constant with the different tenon lengths.

Table 5.7 – Results for T1 specimens.

Designation	Symbol	Units	T1-50	T1-65	T1-80
Initial slip	$v_i$	mm	0.24	0.29	0.30
Modified initial slip	$v_{i,mod}$	mm	0.28	0.33	0.36
Maximum slip	$v_{i,max}$	mm	1.08	1.34	2.68
Initial slip modulus	$k_i$	kN/mm	24.95	28.28	28.31
Slip modulus	$k_s$	kN/mm	21.12	24.16	24.22
Coefficient of variation of $k_i$	$c_{v,i}$	%	20.60	25.20	15.62
Coefficient of variation of $k_s$	$c_{v,s}$	%	18.77	23.50	14.26
Maximum load	$F_{max}$	kN	14.30	19.09	21.13
Coefficient of variation of $F_{max}$	$c_{v,F_{max}}$	%	7.16	5.52	6.06
5% fractile of $F_{max}$	$F_{0,05}$	kN	12.58	17.53	19.01
Section	$A_v$	mm <sup>2</sup>	2500	3250	4000
Tested strength	$\tau_{v,k,TT}$	MPa	5.03	5.39	4.75
Characteristic strength	$f_{v,k}$	MPa	6.90	6.90	6.90
Relative error	$\delta_{\tau_{v,k,TT}/f_{v,k}}$	%	-27.08	-21.84	-31.12

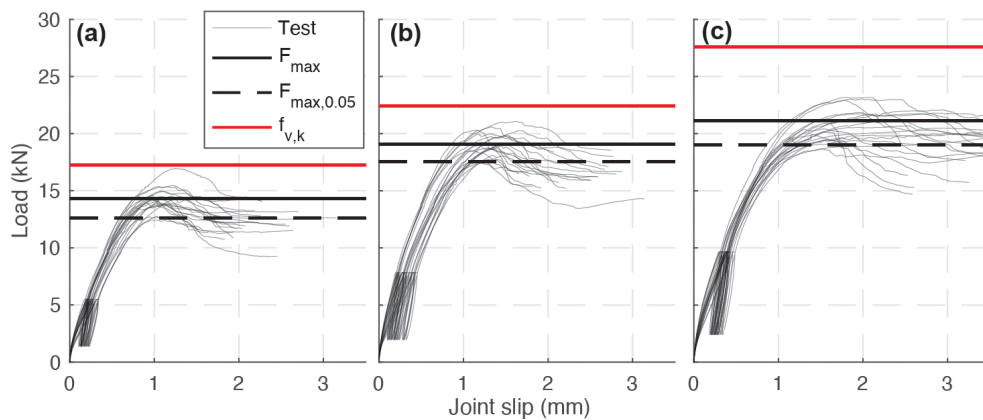


Figure 5.13 – Load-displacement curves: (a) T1-50 / (b) T1-65 / (c) T1-80.



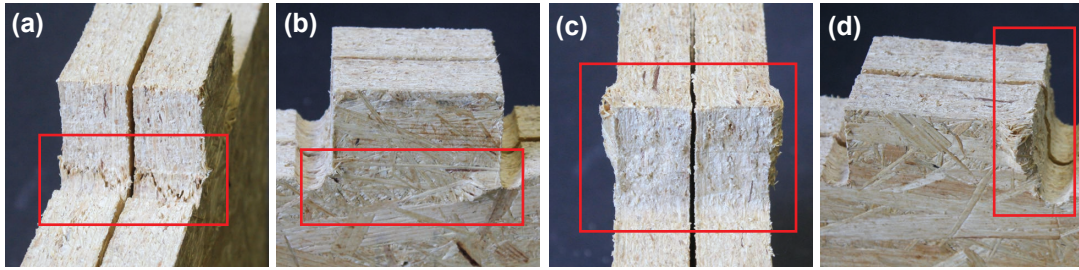


Figure 5.14 – Failure pictures of T1 specimens: (a) Front view of T1-50 / (b) Side view of T1-50 / (c) Front view of T1-80 / (d) Side view of T1-80.

### T2 - Spruce LVL 21 mm, double-layered

For the double-layered spruce LVL connections (T2), all results are listed in Table 5.8. The load-displacement curves per tenon length are displayed in Fig. 5.16, and the failures are shown in Fig. 5.15.

A distinct shear failure occurred in the expected area of the joints for all tenon lengths, as shown in Fig. 5.15. The shear strength values  $\tau_{v,k,TT}$  for T2-50, T2-100, and T2-150 were 23.68%, 26.06%, and 31.14% higher than  $f_{v,k}$ , respectively. The load-carrying capacity of T2 was underestimated by approximately 27% by the current guidelines and had a reduction coefficient  $k_{v,red}$  equal to 1. The difference could partially be explained by the variability of the material, as the compression strength was 40% higher than expected (see Table 5.3). Nevertheless, the shear strength is generally assumed to be constant with the panel thickness for spruce LVL, as opposed to the compression strength, and the variability should therefore be less significant. In addition, the shear strength  $\tau_{v,k,TT}$  increased marginally with the tenon length: by about 6% between 50 and 150 mm.

For the connection stiffness, the same phenomenon found for T1 was observed for T2. The initial slip modulus  $k_i$  was also stiffer than the slip modulus  $k_s$  by an average of 10%, due to the initial stiffness of the assembly. Furthermore, the slip modulus  $k_s$  was not constant along the tenon length and increased linearly by 8% every 50 mm.

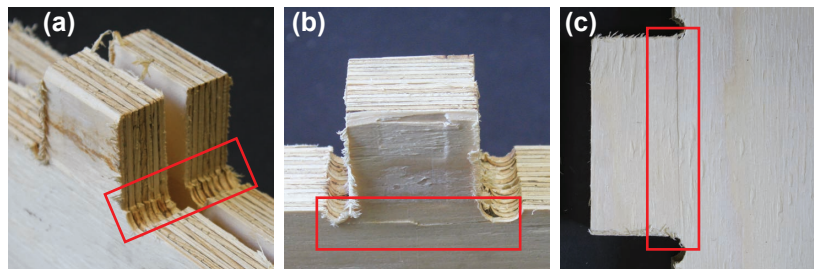


Figure 5.15 – Failure pictures of T2 specimens: (a) Axonometry / (b) Front view T2-50 / (c) Front view T2-100.

Table 5.8 – Results for T2 specimens.

Designation	Symbol	Units	T2-50	T2-100	T2-150
Initial slip	$v_i$	mm	0.14	0.27	0.34
Modified initial slip	$v_{i,mod}$	mm	0.16	0.30	0.38
Maximum slip	$v_{i,max}$	mm	0.74	1.11	1.45
Initial slip modulus	$k_i$	kN/mm	41.14	44.85	49.09
Slip modulus	$k_s$	kN/mm	37.39	40.31	43.67
Coefficient of variation of $k_i$	$c_{v,i}$	%	24.37	30.14	20.13
Coefficient of variation of $k_s$	$c_{v,s}$	%	24.84	30.75	16.71
Maximum load	$F_{max}$	kN	13.52	27.58	40.77
Coefficient of variation of $F_{max}$	$c_{v,F_{max}}$	%	8.12	7.17	5.16
5% fractile of $F_{max}$	$F_{0,05}$	kN	11.69	23.83	37.18
Section	$A_v$	mm <sup>2</sup>	2100	4200	6300
Tested strength	$\tau_{v,k,TT}$	MPa	5.57	5.67	5.90
Characteristic strength	$f_{v,k}$	MPa	4.50	4.50	4.50
Relative error	$\delta_{\tau_{v,k,TT}/f_{v,k}}$	%	23.68	26.06	31.14

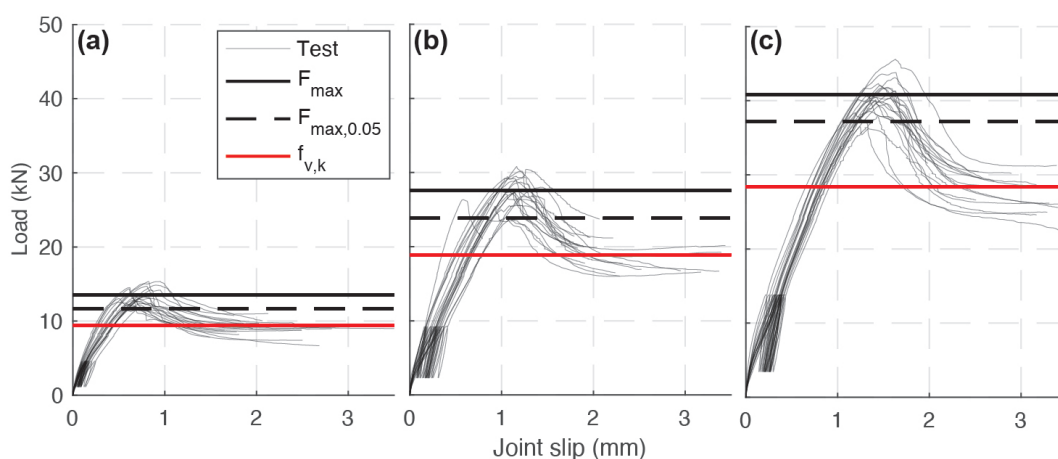


Figure 5.16 – Load-displacement curves: (a) T2-50 / (b) T2-100 / (c) T2-150.

### T3 - Spruce LVL 39 mm, single-layered

For the single-layered spruce LVL connections (T3), all results are listed in Table 5.9. The load-displacement curves per tenon length are displayed in Fig. 5.17, and the failures are shown in Fig. 5.18.

For all tenon lengths, a clear shear failure was observed, similar to the T2 double-layered spruce LVL specimens. The shear strength values  $\tau_{v,k,TT}$  for T3-50, T3-100, and T3-150 were 14.73%, 13.80%, and 17.34% higher than  $f_{v,k}$ , respectively. The difference between  $\tau_{v,k,TT}$  and  $f_{v,k}$  was reduced compared to T2, with more accurate material characteristics. Nonetheless,

the load-carrying capacity of T3 was still underestimated by approximately 15% by the current guidelines, even if the reduction coefficient  $k_{v,red}$  was considered equal to 1. Moreover, the shear strength  $\tau_{v,k,TT}$  did not increase with tenon length, even marginally, in contrast to T2 specimens.

The initial slip modulus  $k_i$  was stiffer than the slip modulus  $k_s$  by an average of 10%, such as in the case of T2. In addition, the slip modulus  $k_s$  also increased with the tenon length of the specimens but in a non-linear manner, as observed for T2. The slip modulus  $k_s$  increased by approximately 40% between T3-50 and T3-100 and by only 10% between T3-100 and T3-150. No clear trend was thus observed between  $k_s$  and the tenon length for LVL spruce specimens.

Table 5.9 – Results for T3 specimens.

Designation	Symbol	Units	T3-50	T3-100	T3-150
Initial slip	$v_i$	mm	0.16	0.22	0.30
Modified initial slip	$v_{i,mod}$	mm	0.18	0.24	0.33
Maximum slip	$v_{i,max}$	mm	0.66	0.85	1.17
Initial slip modulus	$k_i$	kN/mm	30.09	41.60	47.69
Slip modulus	$k_s$	kN/mm	26.96	38.09	42.74
Coefficient of variation of $k_i$	$c_{v,i}$	%	15.10	12.89	15.12
Coefficient of variation of $k_s$	$c_{v,s}$	%	15.58	12.36	14.98
Maximum load	$F_{max}$	kN	11.57	22.90	34.43
Coefficient of variation of $F_{max}$	$c_{v,F_{max}}$	%	8.52	7.18	5.31
5% fractile of $F_{max}$	$F_{0,05}$	kN	10.07	19.97	30.89
Section	$A_v$	mm <sup>2</sup>	1950	3900	5850
Tested strength	$\tau_{v,k,TT}$	MPa	5.16	5.12	5.28
Characteristic strength	$f_{v,k}$	MPa	4.50	4.50	4.50
Relative error	$\delta_{\tau_{v,k,TT}/f_{v,k}}$	%	14.73	13.80	17.34

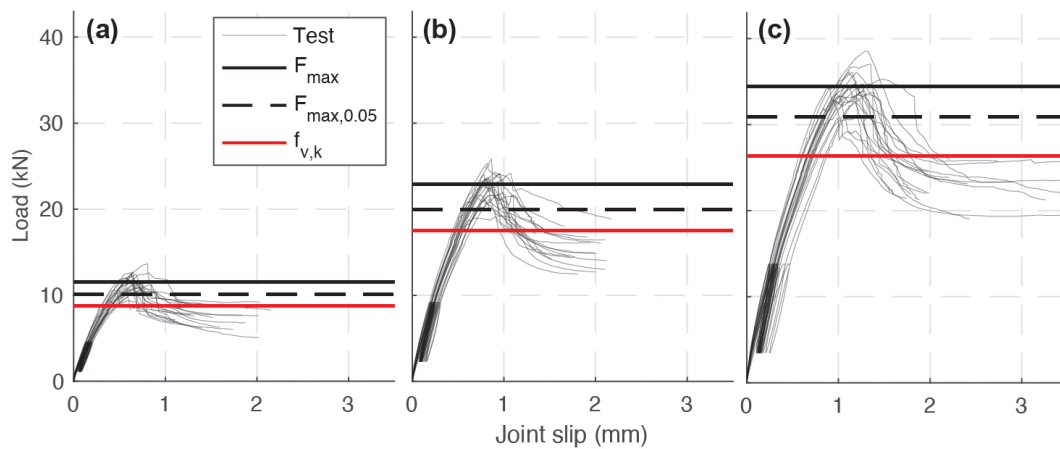


Figure 5.17 – Load-displacement curves: (a) T3-50 / (b) T3-100 / (c) T3-150.

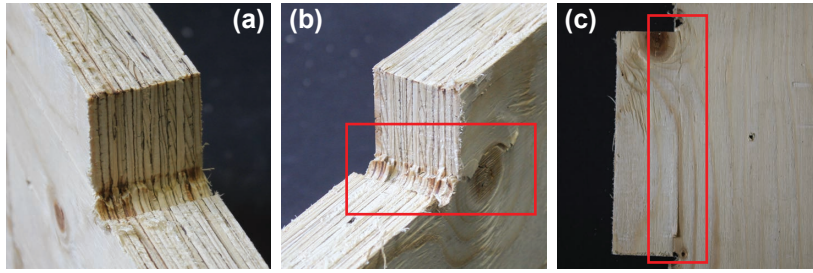


Figure 5.18 – Failure pictures of T3 specimens: (a) Axonometry side 1 / (b) Axonometry side 2 / (c) Front view.

#### T4 - Beech LVL 40 mm, single-layered

For the single-layered beech LVL connections (T4), all results are listed in Table 5.10. The load-displacement curves per tenon length are displayed in Fig. 5.19, and the failures are shown in Fig. 5.20, with net shear failures in the expected joint areas.

For the load-carrying capacity, the shear strength values  $\tau_{v,k,TT}$  of the connection for T4-50, T4-100, and T4-150 were 42.23%, 33.96%, and 26.81% higher than  $f_{v,k}$ , respectively. The load-carrying capacity of T4 was underestimated by an average of approximately 35% by the current guidelines, which corresponds to the trends for T2 and T3. In addition, the material characteristics for T4 can be considered more accurate, as the difference from the compression strength was only of 3.55%. The reduction coefficient  $k_{v,red}$  therefore seems irrelevant for this configuration. In contrast to T2, the shear strength  $\tau_{v,k,TT}$  decreased by approximately 5% while the tenon length increased by 50 mm.

For the connection stiffness, the initial slip modulus  $k_i$  was stiffer than the slip modulus  $k_s$  by an average of 7%, as observed for all other test configurations. The slip modulus  $k_s$  increased by 71% between T4-50 and T4-100 while it decreased by 9% between T4-100 and T4-150. This trend is not similar to the trends of either T2 or T3.

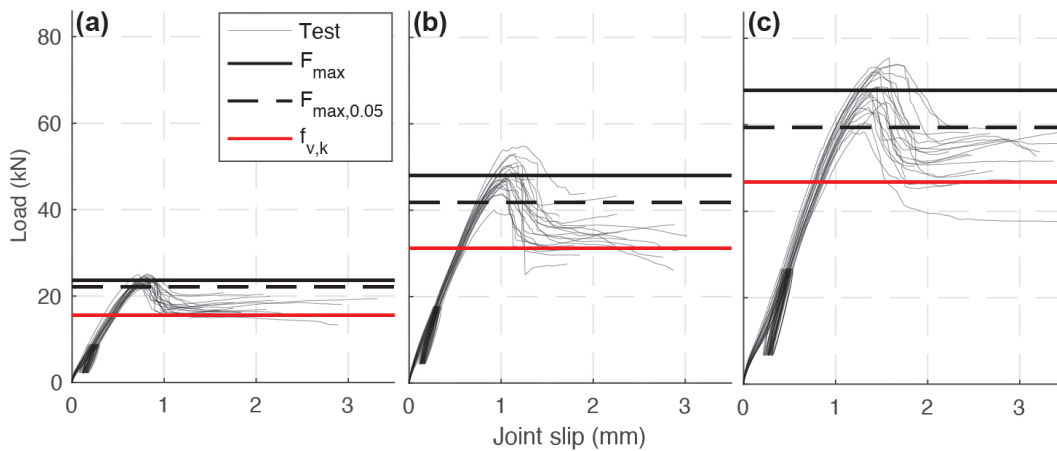


Figure 5.19 – Load-displacement curves: (a) T4-50 / (b) T4-100 / (c) T4-150.

Table 5.10 – Results for T4 specimens.

Designation	Symbol	Units	T4-50	T4-100	T4-150
Initial slip	$v_i$	mm	0.24	0.30	0.47
Modified initial slip	$v_{i,mod}$	mm	0.27	0.32	0.49
Maximum slip	$v_{i,max}$	mm	0.81	1.08	1.44
Initial slip modulus	$k_i$	kN/mm	39.82	64.88	58.40
Slip modulus	$k_s$	kN/mm	35.71	61.10	55.44
Coefficient of variation of $k_i$	$c_{v,i}$	%	16.49	7.20	8.03
Coefficient of variation of $k_s$	$c_{v,s}$	%	15.60	4.39	7.09
Maximum load	$F_{max}$	kN	23.66	47.99	68.03
Coefficient of variation of $F_{max}$	$c_{v,F_{max}}$	%	3.67	7.38	6.98
5% fractile of $F_{max}$	$F_{0,05}$	kN	22.19	41.79	59.35
Section	$A_v$	mm <sup>2</sup>	2000	4000	6000
Tested strength	$\tau_{v,k,TT}$	MPa	11.09	10.45	9.89
Characteristic strength	$f_{v,k}$	MPa	7.80	7.80	7.80
Relative error	$\delta_{\tau_{v,k,TT}/f_{v,k}}$	%	42.23	33.96	26.81

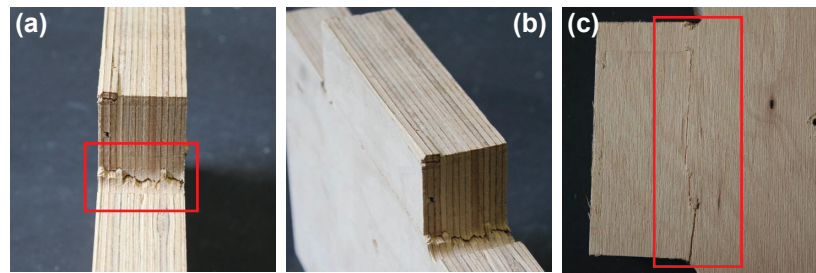


Figure 5.20 – Failure pictures of T4 specimens: (a) Side view / (b) Axonometry / (c) Front view.

#### T5 - Spruce MSW 27 mm, double-layered

For the double-layered spruce MSW connections (T5), all results are listed in Table 5.11. The load-displacement curves per tenon length are displayed in Fig. 5.21, and the failures are shown in Fig. 5.22.

A shear failure occurred in the joints in the expected area and can be observed on both external sides of the panels (see Fig. 5.15). The T5 specimens showed the most significant differences between the tests and manufacturer's values. The shear strength values  $\tau_{v,k,TT}$  of the connection for T5-50, T5-100, and T5-150 were 124.42%, 111.52%, and 120.53% higher than  $f_{v,k}$ , respectively. As a result, the load-carrying capacity of T5 was underestimated by approximately half. The large difference of 75% between the product specification and tests highlighted in the material characterization subsection (see Table 5.3) could partially explained this substantial underestimation by the existing guidelines. Nonetheless, the load-carrying capacity was relatively constant along the tenon length, as observed for T1 and T3.

## Chapter 5. Mechanical characterization of through-tenon joints

For the connection stiffness, the initial slip modulus  $k_i$  was on average 7% stiffer than the slip modulus  $k_s$ , as observed for T4. The slip modulus also increased non-linearly with the tenon length, following the same trend observed for T3. It increased by 35% between T5-50 and T5-100 and by 18% between T5-100 and T5-150.

Table 5.11 – Results for T5 specimens.

Designation	Symbol	Units	T5-50	T5-100	T5-150
Initial slip	$v_i$	mm	0.20	0.27	0.36
Modified initial slip	$v_{i,mod}$	mm	0.22	0.29	0.38
Maximum slip	$v_{i,max}$	mm	0.78	1.00	1.72
Initial slip modulus	$k_i$	kN/mm	39.22	53.22	61.04
Slip modulus	$k_s$	kN/mm	36.25	48.81	57.44
Coefficient of variation of $k_i$	$c_{v,i}$	%	17.41	17.86	17.07
Coefficient of variation of $k_s$	$c_{v,s}$	%	16.27	16.91	13.56
Maximum load	$F_{max}$	kN	19.14	35.11	53.61
Coefficient of variation of $F_{max}$	$c_{v,F_{max}}$	%	9.89	6.27	6.49
5% fractile of $F_{max}$	$F_{0,05}$	kN	16.36	30.84	48.23
Section	$A_v$	mm <sup>2</sup>	2700	5400	8100
Tested strength	$\tau_{v,k,TT}$	MPa	6.06	5.71	5.95
Characteristic strength	$f_{v,k}$	MPa	2.70	2.70	2.70
Relative error	$\delta_{\tau_{v,k,TT}/f_{v,k}}$	%	124.42	111.52	120.53

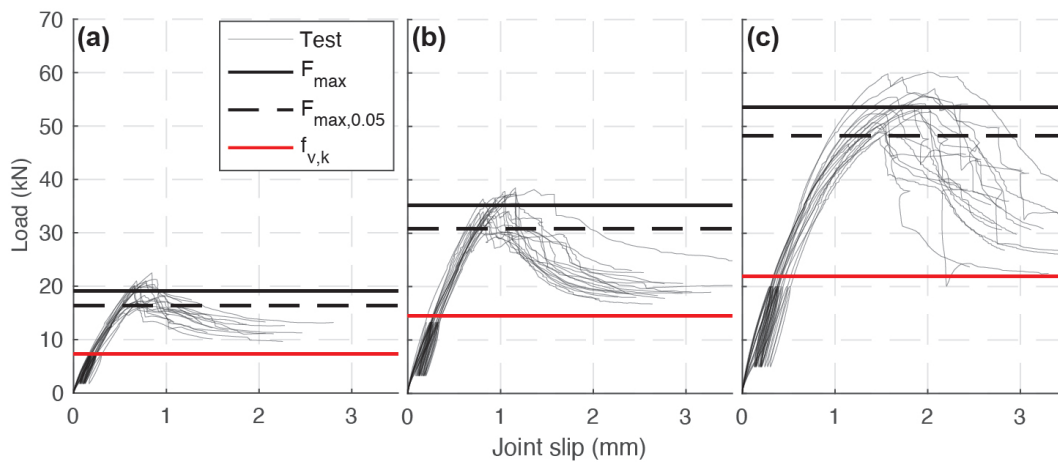


Figure 5.21 – Load-displacement curves: (a) T5-50 / (b) T5-100 / (c) T5-150.



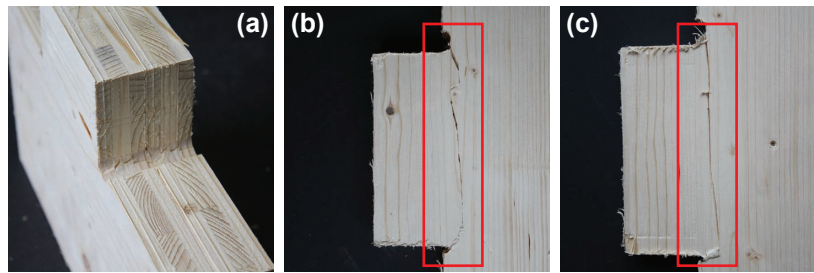


Figure 5.22 – Failure pictures of T5 specimens: (a) Axonometry / (b) Side view 1 / (c) Side view 2.

### Summary

With respect to load-carrying capacity, all materials showed a clear shear failure in the expected connection area of the tenon. The only exception was the OSB assembly with the longest tenon, which was discarded from the results analysis. The OSB samples were also the only assemblies that overestimated the current guidelines: by approximately 25%. In contrast, the MSW assemblies underestimated them by more than 100%. The material characterization showed large differences between tested and manufacturer-provided values for compression strength, which could partially explain the differences for OSB and MSW assemblies. Furthermore, these two materials have a particular lay-up, described in Table 5.1, with a large cross-layer in the middle, which could also contribute to such differences between announced material characteristics and their real performance. For the LVL specimens, the connection shear strength was 25% higher than in the EC5 guidelines defined by Equation 5.16, without taking the reduction coefficient  $k_{v,red}$  into consideration. Therefore, it seems that for the particular TT geometry, considering accurate material characteristics, the reduction coefficient  $k_{v,red}$  is not relevant. Moreover, a stress spreading could be inferred, as the assembly strength is higher than expected. Additional tests on the shear properties of each panel should be performed to verify this possible phenomenon, since no material characterization of the shear properties was conducted in this study.

With regard to the slip modulus of the connections, all materials showed an initial slip modulus  $k_i$  that was more rigid than the slip modulus  $k_s$  due to the initial contact stiffness. The slip modulus  $k_s$  can thus be used directly in calculation models while remaining conservative in the design. The stiffer initial stiffness was attributed to high internal friction forces in the connections, as no assembly gaps were implemented in the connection design. Furthermore, specimens were conditioned in a standardized environment, and the wood swelling could have increased this phenomenon. Nonetheless, if gaps are introduced to the assembly, they should be taken into consideration by implementing unidirectional displacement constraints in numerical models or by using a secant stiffness [146] for analytical models.

In a first approach, an elastic-brittle behavior of the assembly was investigated with the current guidelines criteria for shear (see Fig. 5.23a). However, the TT connection can be classified in

the low-ductility class of assembly according to Eurocode 8 guidelines [34] and the test results (see Fig. 5.23b). As a result, a numerical model was developed to more accurately capture the connection behavior and optimize the load-carrying capacity value. In addition, the slip modulus of the connection was also investigated, as simplified analytical models do not exist. In fact, the slip modulus is generally obtained from tests for wood-wood connections, as simplified analytical models are cumbersome to establish. The results of the numerical model are presented in the next section.

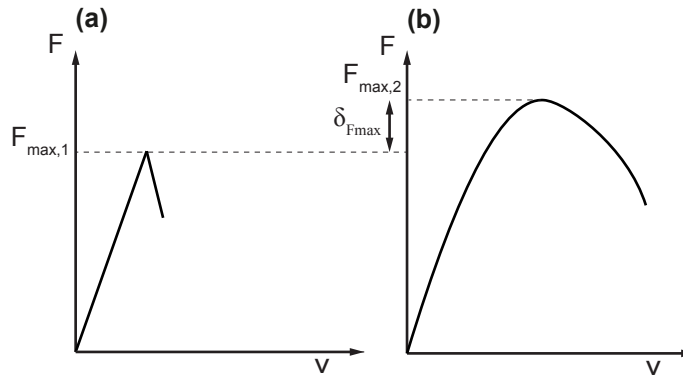


Figure 5.23 – (a) Elastic-brittle behavior / (b) low-ductility behavior.

### 5.6.2 Results vs. numerical model<sup>1</sup>

In this section, a numerical model based on continuum damage mechanics, initially developed by Sandhaas [131] for dowel type connections and subsequently adapted by Roche et al. [129] for wood-wood connections, is compared to the shear tests. The numerical model developed by Nguyen [100] is fully described in Appendix C.4.

For the comparison of experimental and numerical investigations, the slip modulus after the first loading  $k_{s,mod}$  was considered in addition to the slip modulus  $k_s$ , as defined by Equation 5.12 in Subsection 5.4.3. When the samples are loaded for the first time, the contact between the faces of the connections is accompanied by the crushing of tiny asperities on their surface, represented in Fig. 5.24b, which influences the slip modulus  $k_s$ . As a result, the slip modulus after the first loading  $k_{s,mod}$  was also computed so as to consider the linear range between 10 and 40% of the load-displacement curves after the first loading (see Fig. 5.24a). The statistical distribution of the slip modulus  $k_s$  vs.  $k_{s,mod}$  per specimen type for a tenon length of 50 mm can be found in Appendix C.3 (see Fig. C.5). For each test configuration, the lower and upper bounds defined by the 5% fractile factor were computed in addition to the mean value for direct comparison of the load-carrying capacity with Equation 5.16.

Moreover, the shear stress distribution was analyzed to assess the non-uniform HSSSD shape generally expected, as described in Subsection 5.2.1. The stress profile of each material was

<sup>1</sup>The numerical model was developed by A. C. Nguyen.



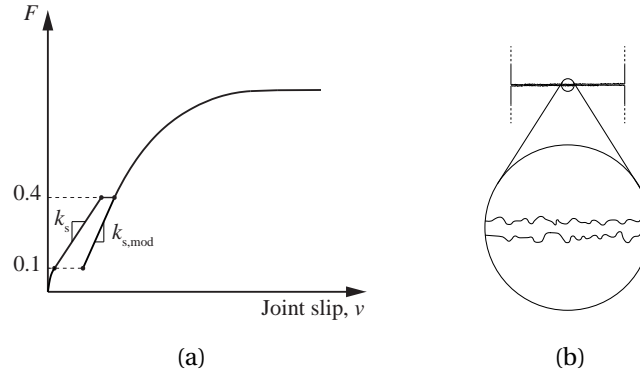


Figure 5.24 – (a) General shape of the load-displacement curves / (b) Tiny asperities at the surface of the faces in contact that are crushed during the first loading.

plotted from nodal stress values along the longest tenon length on the expected failure path. The longest tenon length was chosen because it has the higher number of nodal values due to having the highest number of mesh elements. A concentration factor  $K_t$  was calculated to evaluate the concentration of stress, such as performed by Villar-García et al. [161]:

$$K_t = \frac{\tau_{peak}}{\tau_{ref}} = \frac{\approx f_{v,mean}}{F_{ref} / l_t \cdot l_t} \quad (5.17)$$

where  $\tau_{peak}$  represents the time at which the model stress peak is close to the mean shear strength value of the material  $f_{v,mean}$  (depending on time and mesh increments of the model), and  $\tau_{ref}$  is the considered uniform distribution stress value under the load  $F_{ref}$  obtained when the model reaches the model stress peak  $\tau_{peak}$ .

### T1 - Spruce OSB 18/25 mm, double-layered

The numerical model and experimental curves of double-layered OSB specimens T1 are compared in Fig. 5.25, and the results are listed in Table 5.12.

For the load-carrying capacity of the joint, the model shear strength  $\tau_{v,k,model}$  was about 35% higher than the tested strength  $\tau_{v,k,TT}$  while almost equal to the characteristic strength  $f_{v,k}$ , with a difference of only 1%. The model is coherent with the input material values  $f_{v,k}$  and the difference between product specifications and real performance explains the differences with respect to  $\tau_{v,k,TT}$ . The model for the OSB is thus similar to the design criteria defined by Equation 5.16. The shear stress distribution along the tenon length obtained with the numerical model is illustrated in Fig. 5.26 for the T1-80 specimen. The distribution was obtained when the mean shear strength  $f_{v,mean} = 8.0$  MPa was reached, which corresponded to a load of 18.3 kN. The shear stress profile along the tenon was similar to the expected HSSSD shape with a stress concentration close to the loaded surface of the tenon. A lower stress increase was also observed in the vicinity of the opposite notch. The stress concentration factor  $K_t$  was equal to 1.79. However, the stress concentration did not devalue the ultimate

strength, as the ultimate strength corresponds to the  $f_{v,k}$  criteria. Stress diffusion around the notches could partially explain this phenomenon. In addition, the model showed lower ductile behavior compared to the tests. A more brittle behavior of the connection was expected, which could be due to the specifics of OSB material with a particular lay-up composed of wood fibers.

Concerning the connection stiffness, the model slip modulus  $k_{model}$  largely overestimated the slip modulus  $k_s$  by an average of 87% for all tenon lengths. On the other hand, the model slip modulus  $k_{model}$  was similar to the slip modulus after first loading  $k_{s,model}$  with an average difference of only 6%. The model can thus accurately capture the slip modulus after the first loading but not the global slip modulus of the connection for T1.

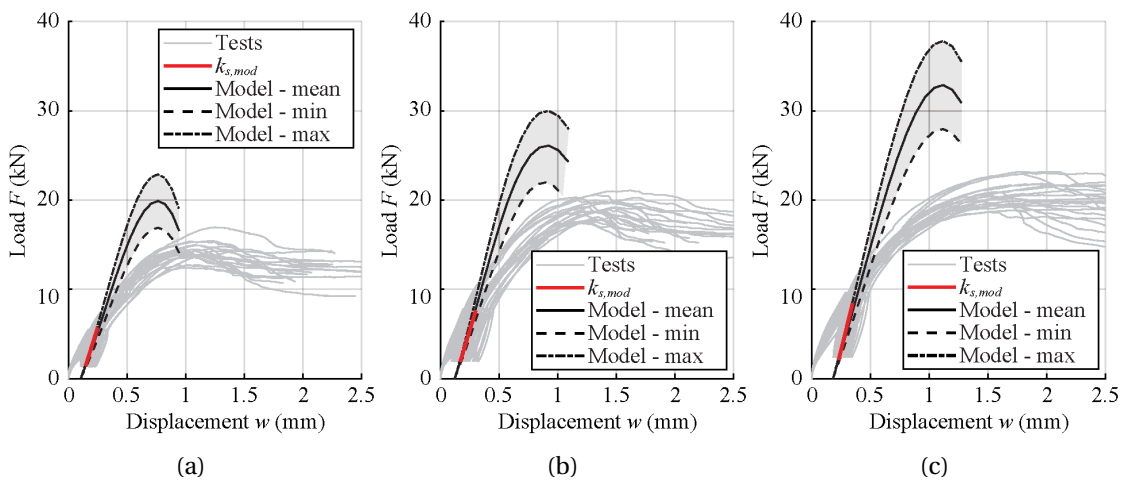


Figure 5.25 – Load-displacement curves vs. model: (a) T1-50 / (b) T1-65 / (c) T1-80.

Table 5.12 – Results for T1 specimens vs. model.

Designation	Symbol	Units	T1-50	T1-65	T1-80
Model slip modulus	$k_{model}$	kN/mm	38.22	44.14	47.85
Slip modulus	$k_s$	kN/mm	21.12	24.16	24.22
Slip modulus after first loading	$k_{s,model}$	kN/mm	41.67	43.22	53.39
Model error on $k_s$	$\delta_{k_s}$	%	80.94	82.69	97.56
Model error on $k_{s,model}$	$\delta_{k_{s,model}}$	%	-8.29	2.13	-10.38
Model maximum load	$F_{max,model}$	kN	19.96	26.10	32.88
5% fractile of $F_{max,model}$	$F_{max,model,0.05}$	kN	16.97	22.18	27.95
Model strength	$\tau_{v,k,model}$	MPa	6.79	6.83	6.99
Characteristic strength	$f_{v,k}$	MPa	6.90	6.90	6.90
Tested strength	$\tau_{v,k,TT}$	MPa	5.03	5.39	4.75
Model error vs. $f_{v,k}$	$\delta_{\tau_{v,k,model} // f_{v,k}}$	%	-1.63	-1.09	1.26
Model error vs. $\tau_{v,k,TT}$	$\delta_{\tau_{v,k,model} // \tau_{v,k,TT}}$	%	34.90	26.55	47.01

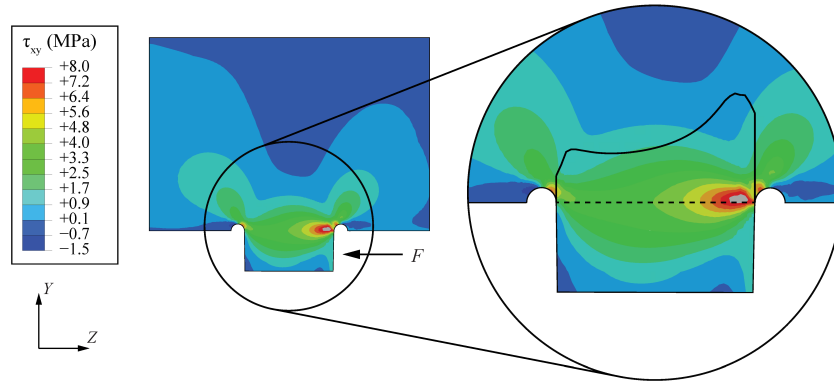


Figure 5.26 – Shear stress distribution along the tenon for T1 specimens.

### T2 - Spruce LVL 21 mm, double-layered

The numerical model and experimental curves of double-layered spruce LVL specimens T2 are compared in Fig. 5.27, and the results are listed in Table 5.13.

The model shear strength  $\tau_{v,k,model}$  was close to the tested strength  $\tau_{v,k,TT}$ , with differences of only -4.73%, -7.85%, and -12.92% for T2-50, T2-100, and T2-150, respectively. The model was more accurate for a smaller tenon length for this joint configuration and slightly conservative. As a result, the model shear strength  $\tau_{v,k,model}$  was an average of 16% higher than the characteristic shear strength  $f_{v,k}$  for the different tenon lengths. The model is thus more accurate than the existing design criteria for optimizing the load-carrying capacity of this assembly. The shear stress distribution along the tenon length is illustrated in Fig. 5.28 for the T2-150 specimen. It was obtained when the mean shear strength  $f_{v,mean} = 5.4$  MPa was reached, which corresponded to a load of 19.7 kN. As observed for T1 specimens, the same stress profile (HSSSD) was observed with a concentration factor of  $K_t$  of 1.86. However, the stress concentration did not devalue the ultimate strength, as  $\tau_{v,k,model}$  was higher than  $f_{v,k}$ . Nonetheless, for the load of 19.7 kN, the joint was still in the linear range, as shown in Fig. 5.27c. Further research should thus be conducted to identify the causes of the modeling shortcomings, which can be attributed to increment times, mesh refinement at the stress concentration areas, or failure modes defining the onset of failure. In addition, the low-ductility shape of the assembly was coherent, even if the model underestimated the displacement for all T2 configurations.

The model slip modulus  $k_{model}$  for the specimen T2-50 with a tenon length of 50 mm was reasonably close to both the slip modulus  $k_s$  and the slip modulus after first loading  $k_{s,model}$ , with differences of -11.43% and -12.09%, respectively. However for the two other tenon lengths of 100 and 150 mm,  $k_s$  remained relatively constant compared to the increases in  $k_{model}$  and  $k_{s,model}$ . The difference between  $k_s$  and  $k_{model}$  was thus more important, with differences of 17.99% and 30.88% for T2-100 and T2-150, respectively. For the T1 configuration, therefore, the model can more accurately capture the slip modulus after the first loading than the slip modulus of the connection.

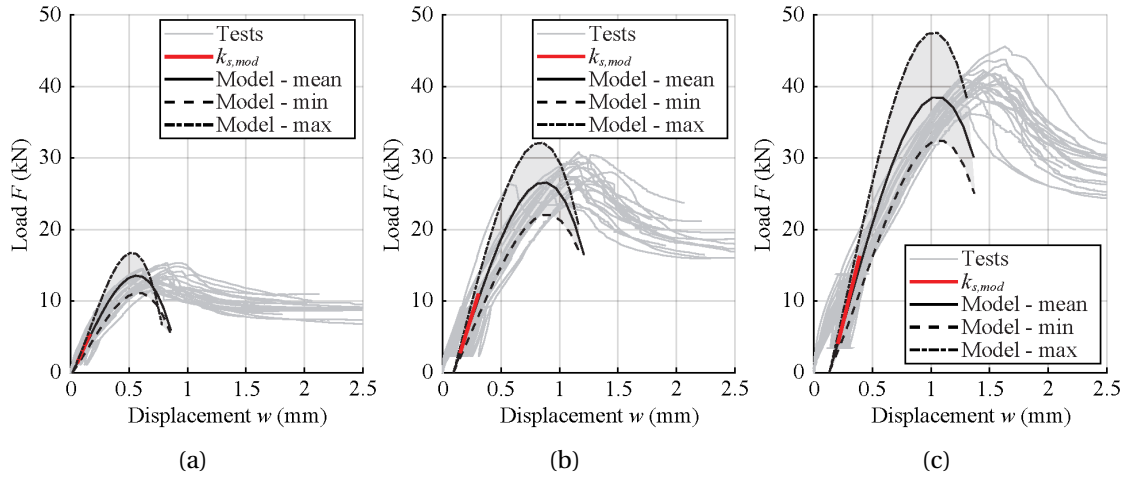


Figure 5.27 – Load-displacement curves vs. model: (a) T2-50 / (b) T2-100 / (c) T2-150.

Table 5.13 – Results for T2 specimens vs. model.

Designation	Symbol	Units	T2-50	T2-100	T2-150
Model slip modulus	$k_{model}$	kN/mm	33.11	47.56	57.15
Slip modulus	$k_s$	kN/mm	37.39	40.31	43.67
Slip modulus after first loading	$k_{s,mod}$	kN/mm	37.67	52.33	65.66
Model error on $k_s$	$\delta_{k_s}$	%	-11.43	17.99	30.88
Model error on $k_{s,mod}$	$\delta_{k_{s,mod}}$	%	-12.09	-9.12	-12.96
Model maximum load	$F_{max,model}$	kN	13.49	26.26	38.08
5% fractile of $F_{max,model}$	$F_{max,model,0.05}$	kN	11.13	21.96	32.38
Model strength	$\tau_{v,k,model}$	MPa	5.30	5.23	5.14
Characteristic strength	$f_{v,k}$	MPa	4.50	4.50	4.50
Tested strength	$\tau_{v,k,TT}$	MPa	5.57	5.67	5.90
Model error vs. $f_{v,k}$	$\delta_{\tau_{v,k,model}/f_{v,k}}$	%	17.83	16.17	14.20
Model error vs. $\tau_{v,k,TT}$	$\delta_{\tau_{v,k,model}/\tau_{v,k,TT}}$	%	-4.73	-7.85	-12.92

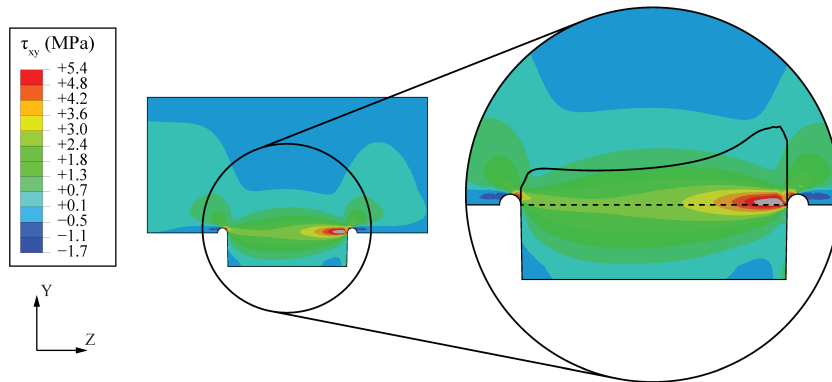


Figure 5.28 – Shear stress distribution along the tenon for T2-150 specimens.

### T3 - Spruce LVL 39 mm, single-layered

The numerical model and experimental curves of single-layered spruce LVL specimens T3 are compared in Fig. 5.29, and the results are listed in Table 5.14.

For the double-layered specimens T2, the model shear strength  $\tau_{v,k,model}$  was close to the tested strength  $\tau_{v,k,TT}$ , with differences of only 2.32%, -2.28%, and -4.65% for T2-50, T2-100, and T2-150, respectively. As a result, the model shear strength  $\tau_{v,k,model}$  was an average of 13% higher than the characteristic shear strength  $f_{v,k}$  for the different tenon lengths. The model is thus more accurate than the existing design criteria for the optimization of the load-carrying capacity of this assembly. The shear stress distribution along the tenon length is illustrated in Fig. 5.30 for the T3-150 specimen. It was obtained when the mean shear strength  $f_{v,mean} = 5.4$  MPa was reached, which corresponded to a load of 15.4 kN. The expected non-uniform distribution HSSSD was observed, such as for T1 and T2, with a concentration factor of  $K_t$  of 2.18. The same conclusions as those reached for T2 can be deduced with the stress concentration of T3. The stress concentration also did not devalue the ultimate strength, as  $\tau_{v,k,model}$  was higher than  $f_{v,k}$ . However, the load of 15.4 kN was still in the linear range, as shown in Fig. 5.29c, and further research should thus be conducted to identify the modeling issues. In addition, the low-ductility shape of the assembly was coherent, even if the model slightly underestimated the displacement, as observed on T2.

Concerning the connection stiffness, the model slip modulus  $k_{model}$  overestimated the slip modulus  $k_s$  by an average of 23% for all tenon lengths. In contrast, the model slip modulus  $k_{model}$  was very close to the slip modulus after first loading  $k_{s,mod}$ , with an average difference of only -4%. The model can thus capture accurately the slip modulus after the first loading but not the global slip modulus of the connection. As for T2, the same trend for  $k_{model}$  and  $k_{s,mod}$  can be observed with an increase corresponding to the tenon length of specimens.

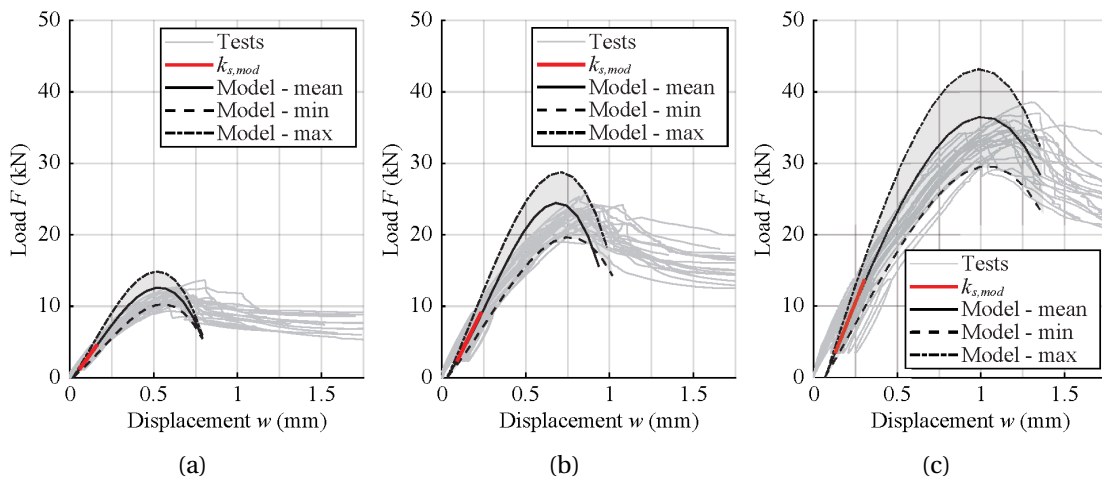


Figure 5.29 – Load-displacement curves vs. model: (a) T3-50 / (b) T3-100 / (c) T3-150.

Table 5.14 – Results for T3 specimens vs. model.

Designation	Symbol	Units	T3-50	T3-100	T3-150
Model slip modulus	$k_{model}$	kN/mm	31.61	45.79	55.52
Slip modulus	$k_s$	kN/mm	26.96	38.09	42.74
Slip modulus after first loading	$k_{s,model}$	kN/mm	32.50	47.62	58.53
Model error on $k_s$	$\delta_{k_s}$	%	17.38	20.24	29.89
Model error on $k_{s,model}$	$\delta_{k_{s,model}}$	%	-2.74	-3.83	-5.13
Model maximum load	$F_{max,model}$	kN	12.54	24.28	36.43
5% fractile of $F_{max,model}$	$F_{max,model,0.05}$	kN	10.30	19.52	29.45
Model strength	$\tau_{v,k,model}$	MPa	5.28	5.00	5.03
Characteristic strength	$f_{v,k}$	MPa	4.50	4.50	4.50
Tested strength	$\tau_{v,k,TT}$	MPa	5.16	5.12	5.28
Model error vs. $f_{v,k}$	$\delta_{\tau_{v,k,model}/f_{v,k}}$	%	17.39	11.21	11.89
Model error vs. $\tau_{v,k,TT}$	$\delta_{\tau_{v,k,model}/\tau_{v,k,TT}}$	%	2.32	-2.28	-4.65

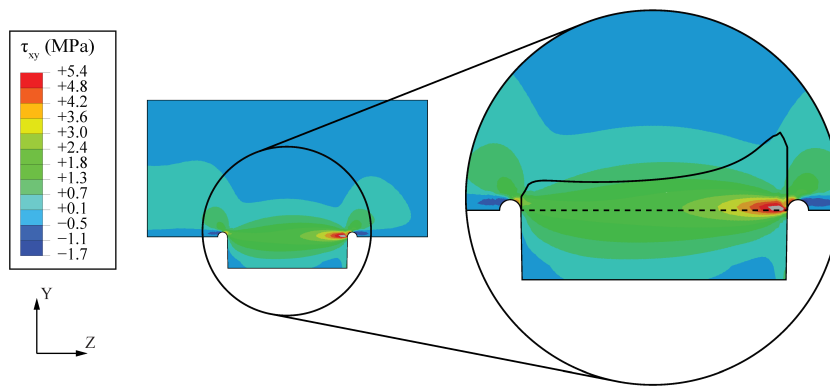


Figure 5.30 – Shear stress distribution along the tenon for T3-150 specimens.

#### T4 - Beech LVL 40 mm, single-layered

The numerical model and experimental curves of single-layered beech LVL specimens T4 are compared in Fig. 5.31, and the results are listed in Table 5.15.

With respect to the load-carrying capacity of the joint, the model shear strength  $\tau_{v,k,model}$  underestimated the tested strength  $\tau_{v,k,TT}$  by 20%, while it overestimated the characteristic strength  $f_{v,k}$  by 8%. The model is thus close to the existing design criteria defined by Equation 5.16 with a slight improvement of 8% for the prediction of the load-carrying capacity. The shear stress distribution along the tenon length is illustrated in Fig. 5.32 for the T4-150 specimen. It was obtained when the mean shear strength  $f_{v,mean} = 9.3$  MPa was reached, which corresponded to a load of 26.7 kN. The distribution profile was similar to those observed for OSB and spruce LVL, with a concentration factor  $K_t$  of 2.26. As observed for the other materials, the stress concentration did not devalue the ultimate strength, as the ultimate strength

corresponds approximately to the  $f_{v,k}$  criteria. However, the load of 26.7 kN was still in the linear range, as shown in Fig. 5.31c, and further research should thus be conducted to identify shortcomings in the modeling. The displacement of the joints were also underestimated by the model for this configuration.

Concerning the connection stiffness, the model slip modulus  $k_{model}$  overestimated the slip modulus  $k_s$  by an average of 26% for all tenon lengths while it underestimated the slip modulus after first loading  $k_{s,model}$  by an average of 12%. Nonetheless, the trend for  $k_{model}$  and  $k_{s,model}$  can be observed with an increase corresponding to the tenon length of specimens, as was the case for T2 and T3.

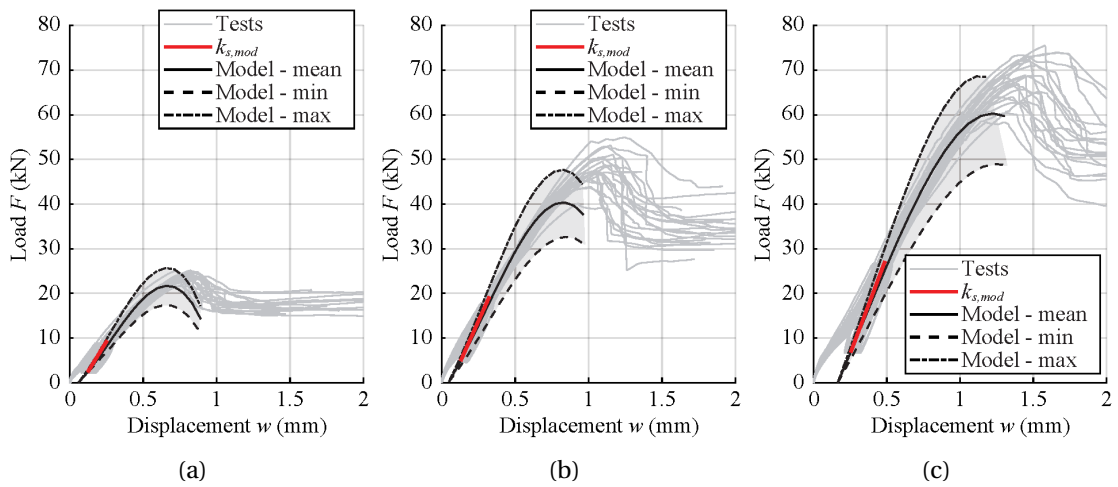


Figure 5.31 – Load-displacement curves vs. model: (a) T4-50 / (b) T4-100 / (c) T4-150.

Table 5.15 – Results for T4 specimens vs. model.

Designation	Symbol	Units	T4-50	T4-100	T4-150
Model slip modulus	$k_{model}$	kN/mm	45.72	65.35	78.94
Slip modulus	$k_s$	kN/mm	35.71	61.10	55.44
Slip modulus after first loading	$k_{s,model}$	kN/mm	53.52	73.54	86.98
Model error on $k_s$	$\delta_{k_s}$	%	28.03	6.96	42.40
Model error on $k_{s,model}$	$\delta_{k_{s,model}}$	%	-14.57	-11.13	-9.24
Model maximum load	$F_{max,model}$	kN	21.74	41.16	59.70
5% fractile of $F_{max,model}$	$F_{max,model,0.05}$	kN	17.55	33.52	48.63
Model strength	$\tau_{v,k,model}$	MPa	8.78	8.38	8.10
Characteristic strength	$f_{v,k}$	MPa	7.80	7.80	7.80
Tested strength	$\tau_{v,k,TT}$	MPa	11.09	10.45	9.89
Model error vs. $f_{v,k}$	$\delta_{\tau_{v,k,model}/f_{v,k}}$	%	12.51	7.44	3.91
Model error vs. $\tau_{v,k,TT}$	$\delta_{\tau_{v,k,model}/\tau_{v,k,TT}}$	%	-20.89	-19.79	-18.06

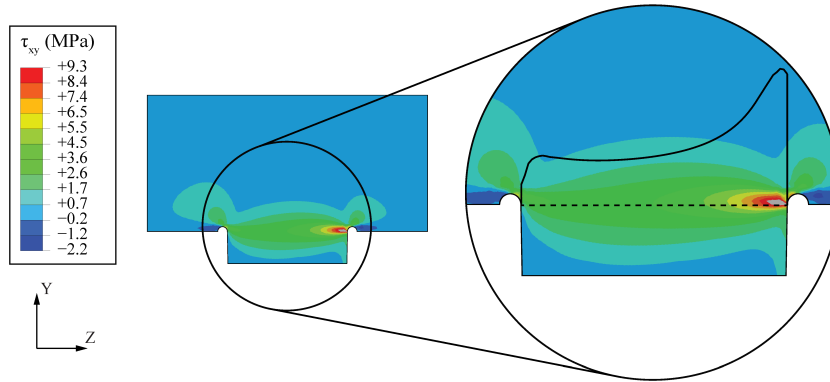


Figure 5.32 – Shear stress distribution along the tenon for T4-150 specimens.

### T5 - Spruce MSW 27 mm, double-layered

The numerical model and experimental curves of double-layered spruce MSW specimens T5 are compared in Fig. 5.33, and the results are listed in Table 5.16.

The model shear strength  $\tau_{v,k,model}$  was relatively similar to the tested strength  $\tau_{v,k,TT}$ , with differences of only -3.46%, -9.51%, and -11.06% for T5-50, T5-100, and T5-150, respectively. As for T2, the model for this joint configuration was more accurate for a smaller tenon length and was slightly conservative. Moreover, the model shear strength  $\tau_{v,k,model}$  was an average of 100% higher than the characteristic shear strength  $f_{v,k}$  for the different tenon lengths. The model is thus not consistent compared to the product specifications, in contrast to the T1 model results. On the other hand, the model is more precise than the existing design criteria at optimizing the load-carrying capacity of this assembly. The shear stress distribution is illustrated in Fig. 5.34 for the T5-150 specimen. It was obtained when the mean shear strength  $f_{v,mean} = 3.2$  MPa was reached, which corresponded to a load of 11.6 kN. The distribution profile was similar to those observed for OSB and LVL with a concentration factor  $K_t$  of 2.26. As observed for the other materials, the stress concentration did not devalue the ultimate strength, as  $\tau_{v,k,model}$  was higher than  $f_{v,k}$ . However, the load of 11.6 kN was still in the linear range, as shown in Fig. 5.33c, and further investigations should thus be conducted to identify the modeling issues. The displacement of the joints were also underestimated by the model for this configuration.

Concerning the connection stiffness, the model slip modulus  $k_{model}$  overestimated the slip modulus  $k_s$  by an average of 16% for all tenon lengths while it underestimated the slip modulus after first loading  $k_{s,mod}$  by an average of 9%. Nonetheless, the trend for  $k_{model}$  and  $k_{s,mod}$  can be observed with an increase corresponding to the tenon length of specimens, such as for all LVL specimens.



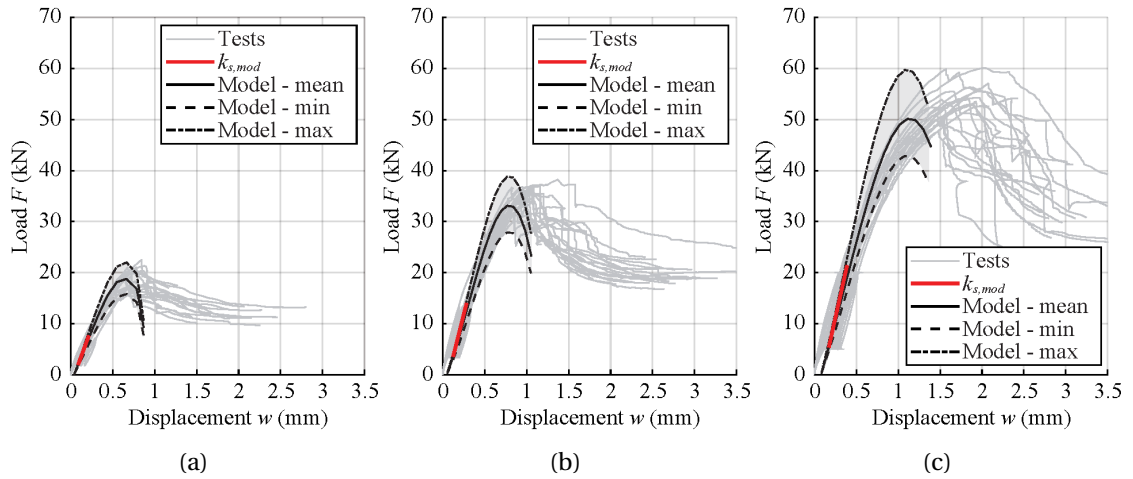


Figure 5.33 – Load-displacement curves vs. model: (a) T5-50 / (b) T5-100 / (c) T5-150.

Table 5.16 – Results for T5 specimens vs. model.

Designation	Symbol	Units	T5-50	T5-100	T5-150
Model lip modulus	$k_{model}$	kN/mm	41.13	56.62	68.75
Slip modulus	$k_s$	kN/mm	36.25	48.81	57.44
Slip modulus after first loading	$k_{s,mod}$	kN/mm	44.55	65.18	73.58
Model error on $k_s$	$\delta k_s$	%	13.45	15.86	19.69
Model error on $k_{s,mod}$	$\delta k_{s,mod}$	%	-7.68	-13.14	-6.57
Model maximum load	$F_{max,model}$	kN	18.77	33.00	50.13
5% fractile of $F_{max,model}$	$F_{max,model,0.05}$	kN	15.79	27.91	42.90
Model strength	$\tau_{v,k,model}$	MPa	5.85	5.17	5.30
Characteristic strength	$f_{v,k}$	MPa	2.70	2.70	2.70
Tested strength	$\tau_{v,k,TT}$	MPa	6.06	5.71	5.95
Model error vs. $f_{v,k}$	$\delta \tau_{v,k,model} / f_{v,k}$	%	116.66	91.40	96.15
Model error vs. $\tau_{v,k,TT}$	$\delta \tau_{v,k,model} / \tau_{v,k,TT}$	%	-3.46	-9.51	-11.06

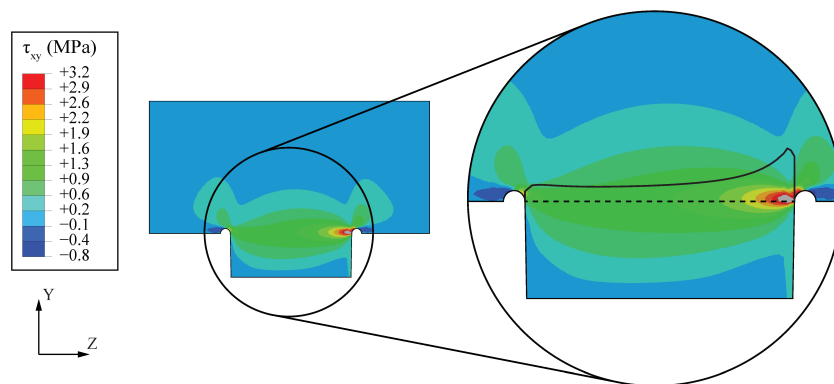


Figure 5.34 – Shear stress distribution along the tenon for T5-150 specimens.

### Summary

A comparison of the shear strength between characteristic, tested, and model values is presented in Fig. 5.35 for all materials. The model shear strength was in relatively good agreement with the tests for MSW and spruce LVL panels (T2, T3, and T5) and showed less variability in results compared to the characteristic values for beech LVL (T4). Only the model results for OSB (T1) were similar to the characteristic values and, as a result, overestimated the load-carrying capacity of the assembly. The model demonstrated superior accuracy in estimating the load-carrying capacity of the TT assembly compared to existing guidelines. The model can thus be used in future research to optimize the load-carrying capacity of TT connections depending on the materials.

However, inconsistencies were highlighted for the shear stress distribution concerning the level of loading, and further research should be performed on the mesh and time increments of the model. In addition, no clear trend was evident from either the model or the tests in the load-carrying capacity as function of the tenon length.

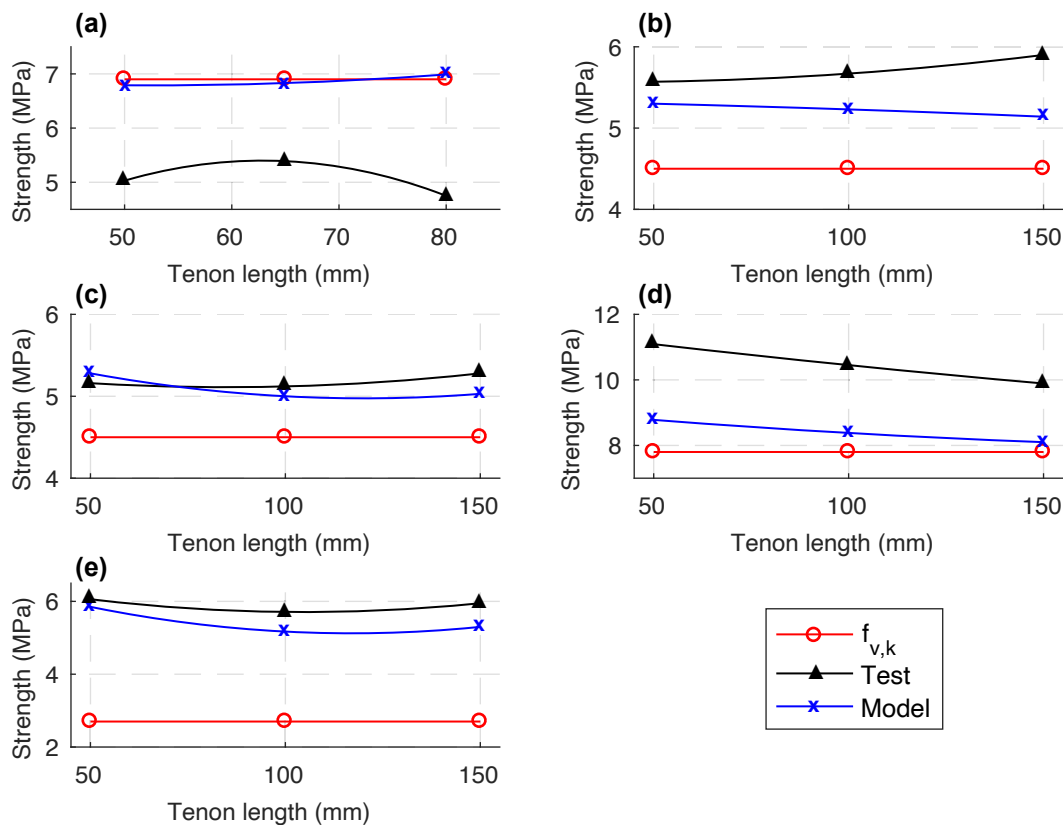


Figure 5.35 – Shear strength comparison between characteristic values ( $f_{v,k}$ ), tested values ( $\tau_{v,k,TT}$ ), and FE model values ( $\tau_{v,k,model}$ ): (a) T1 / (b) T2 / (c) T3 / (d) T4 / (e) T5.

A comparison of the connection stiffness between tested slip modulus, tested slip modulus after first loading, and model slip modulus values is also presented in Fig. 5.36. The model was in good agreement with the tested slip modulus after first loading with an underestimation of approximately 8% for all configurations. However, the model significantly overestimated the tested slip modulus by 32.8% for the different configurations and by 19.25% if the OSB configuration was excluded from the analysis. There were also large variations depending on the tenon length and material. As a result, the model slip modulus is not appropriate to be implemented in calculations models, as the overall displacement of an interconnected structure would be largely underestimated. The model could be improved for the prediction of TT joint slip modulus with the introduction of deformable contact elements in comparison with the surface-to-surface interaction with a hard contact used in this work. Element deletion could also be introduced to alleviate mesh dependency and element distortion, as performed by Sandhaas et al. [132]. Nonetheless, the model was consistent regarding the increase of the slip modulus as function of the tenon length, as observed on the slip modulus after first loading and for the slip modulus of T2, T3, and T5. This trend could be investigated in future research.

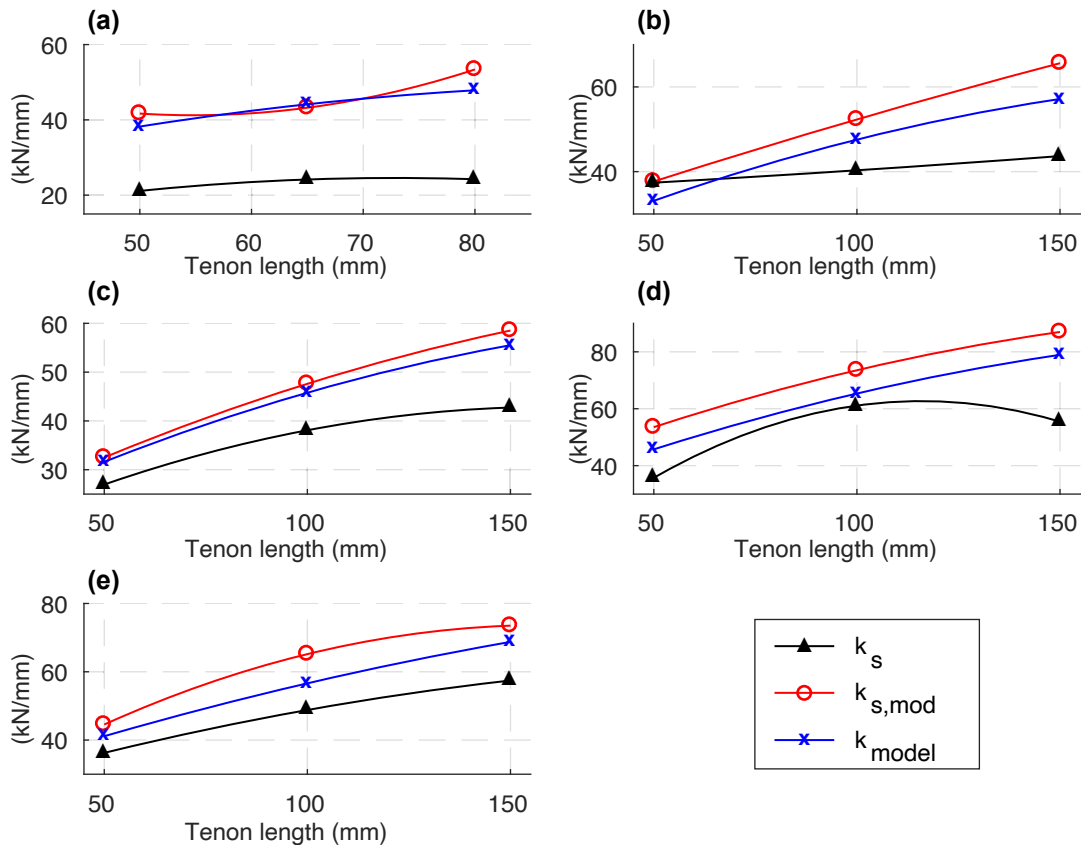


Figure 5.36 – Connection stiffness comparison between slip modulus ( $k_s$ ), slip modulus after first loading ( $k_{s,mod}$ ), and FE model slip modulus values ( $k_{model}$ ): (a) T1 / (b) T2 / (c) T3 / (d) T4 / (e) T5.

## 5.7 Design guidelines

A summary of the results on the load-carrying capacity is presented in this section. The load-carrying capacity of TT connections is defined by several failure modes, as described in Fig. 5.2. Shear and compression failures, illustrated in Fig. 5.3, were investigated and are compared to the EC5 guidelines in Section 5.5 and Subsection 5.6.1. The results are summarized in Table 5.17. In addition, the results for each specimen type are presented in a graph in which the characteristic load ( $F_{max,0.05}$ ) is a function of the tenon length ( $l_t$ ), as shown in Fig. 5.37. The area of interest is defined as ranging from a tenon length of 50 mm to the optimum tenon length determined when the resistant shear capacity reaches the compression capacity of the joint. The optimum tenon length was defined for both the tests ( $l_{t,optim,test}$ ) and the EC5 guidelines ( $l_{t,optim,EC5}$ ). The optimum length derived from EC5 can be calculated according to these equations (if  $k_{v,red}$  and  $k_{c,\alpha}$  are considered equal to 1):

$$f_{v,k} \times l_t \times t_t > f_{c,0,k} \times t_m \times t_t \quad (5.18)$$

$$l_{t,optim,EC5} > \frac{f_{c,0,k} \times t_m}{f_{v,k}} \quad (5.19)$$

The differences between  $l_{t,optim,EC5}$  and  $l_{t,optim,test}$  were between approximately 2 and 15%. Although these values were relatively close for the different panels, the load-carrying capacities for these different tenon lengths were different depending on the panel type. In the analysis, only the shear load-carrying capacity was considered before the compression load-carrying capacity was reached. Strength coupling was not investigated in the first approach.

Table 5.17 – Summary of the test results for TT connections.

Designation	Units	T1&EM1	T2&EM2	T3&EM3	T4&EM4	T5&EM5
Materials	-	spruce	spruce	spruce	beech	spruce
Type	-	OSB 3	LVL	LVL	LVL	MSW
TT layers	-	2	2	1	1	2
$f_{v,k}$	(MPa)	6.9	4.5	4.5	7.8	2.7
$\tau_{v,k,TT}$	(MPa)	5.21	5.71	5.19	10.48	5.91
$\delta_{\tau_{v,k,TT}/f_{v,k}}$	(%)	-24.46	26.96	15.29	34.33	118.82
$\sigma_{c,k,TT}$	(MPa)	11.53	28.08	31.21	62.05	21.01
$\delta_{\sigma_{c,k,TT}/f_{c,0,k}}$	(%)	-22.09	47.79	20.04	16.36	82.70
$\delta_{\sigma_{c,k,TT}/f_{c,0,k,test}}$	(%)	25.50	4.32	7.34	12.42	4.64
$l_{t,optim,EC5}$	(mm)	77.22	177.33	225.33	273.33	230.00
$l_{t,optim,test}$	(mm)	78.82	201.84	232.20	248.15	192.43
$\delta_{EC5/Test}$	(%)	2.07	13.82	3.05	-9.21	-16.33

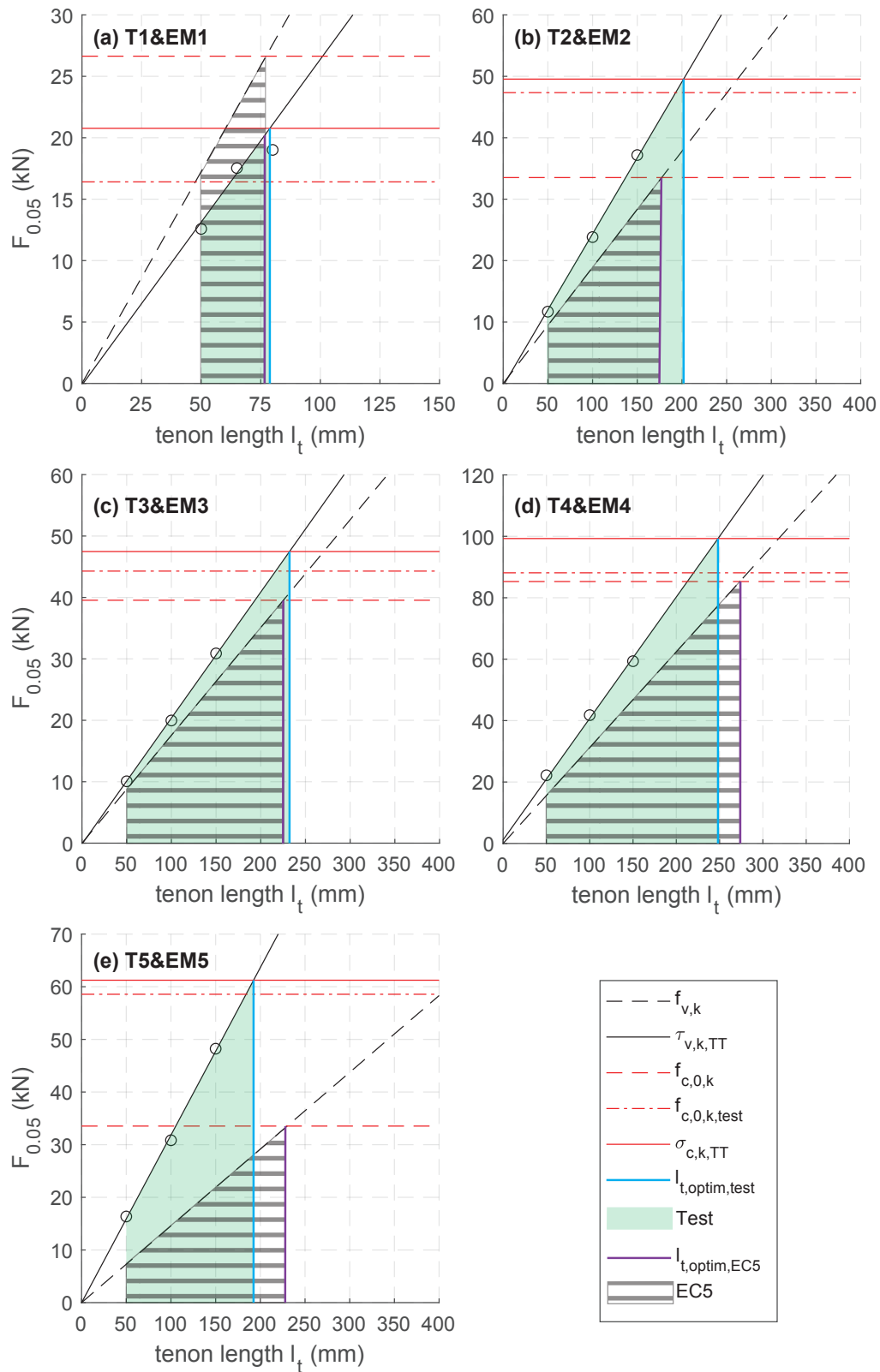


Figure 5.37 – Load-carrying capacity of TT connections as a function of tenon length.

To summarize, only the load-carrying capacity of OSB TT joints (T1 and EM1) was overestimated (by 25%) according to EC5 (Fig. 5.37a). On the contrary, the load-carrying capacity of spruce MSW joints (T5 and EM5) was greatly underestimated by half (Fig. 5.37e). Both of these materials showed significant differences between the characteristic values announced by the manufacturer (or the material standard) and those tested. It is thus complicated to structurally design such connections without experiments because of their large material variability. In contrast, TT joints made of LVL panels were underestimated by approximately 25% with more precise material properties (Fig. 5.37b,c and d). The closest to the EC5 guidelines was the single-layered spruce LVL connection (T3 and EM3) with a difference of approximately 15%. Moreover, as the characteristic compression strength ( $f_{c,0,k,test}$ ) was tested for all materials, compression spreading (of 25%) was highlighted only for the OSB TT joints. The same value was observed for the shear strength of LVL panels, which could also demonstrate a spreading phenomenon in the context of shear behavior.

Among the developments toward a more comprehensive code on timber structures, Dietsch et al. [24] stated that the determination of shear properties of wood-based panels used in structural design could be improved. They also mentioned three methods for developing standards for structural design: tabulated data or design diagrams, simplified design methods, and scientifically based design methods. They also highlighted that design diagrams are useful methods for standard applications — such applications corresponds to the structural elements developed with TT connections presented in Chapter 3. Based on materials composing a TT assembly, different approaches could be used. LVL panels could be designed with EC5 equations with research on spreading coefficients to optimize the TT connection, as they already show a close alignment of product specifications and characteristic values. Otherwise, design diagrams could be used for materials such as OSB and spruce MSW that show a higher discrepancy between manufacturer specifications and characteristic values. These diagrams can be based on experimental tests following the procedures developed in Section 5.4 for shear and compression. They can be inspired by Fig. 5.37 and use different parameters such as material, tenon length, panel thickness, material lay-up, and others, as such parameters were shown to influence the TT behavior.

## 5.8 Conclusions

The in-plane behavior of digitally produced TT joints was investigated in this chapter, as such joints are increasingly applied in standard construction systems. Shear and compression failure modes were considered and two test setups were developed for this purpose. An experimental campaign was performed on commonly available timber panels to expand the knowledge of several materials. The scope of the study was limited to a grain orientation parallel to the joint and three different tenon lengths. The experimental results were compared to the EC5 guidelines for traditional carpentry assemblies to assess the existing state-of-the-art for the structural design of such joints. A numerical model based on continuum damage mechanics, presented in Appendix C.4, was also compared to the tests.

Significant differences were observed between the announced characteristic strength values and real performance of the materials, especially for OSB and MSW panels. The material characteristics are of high importance in accurately determining the load-carrying capacity through design criteria derived from EC5. This discrepancy is thus problematic for performing a safe design with, for example, the overestimation of the OSB compression strength (and probably shear strength). This discrepancy is less critical when the properties are overestimated, as was the case for all other materials, but it is not relevant for an optimized and coherent design. As stated by Dietsch et al. [24], the correspondence between product specifications and EC5 could be improved.

Concerning the load-carrying capacity of TT joints, existing EC5 guidelines were mainly found to be conservative. Only the capacity of OSB TT joints was overestimated while all others were underestimated. The highest difference was for the spruce MSW with twice the load-carrying capacity expected. These two materials (OSB and MSW) are characterized by a particular lay-up with a large cross-layer in the middle of the panels, which may have increased these differences. The specimen type that led to the conformance to the EC5 guidelines was the single-layered spruce LVL connection with a difference of only 15%, while the LVL specimens were underestimated by an average of approximately 25%. The EC5 spreading coefficient for compression  $k_{c,\alpha}$ , equal to 1 when the grain orientation is parallel to the joint, was found to be consistent, while the reduction factor coefficient due to the non-uniform stress distribution of shear  $k_{v,red}$  was not relevant according to the test results. Existing criteria can therefore be safely used for LVL materials in the first approach, while design diagrams based on the experimental procedures developed in this work can be implemented if the product specifications are considered uncertain, such as for OSB and MSW. Moreover, the numerical model was in good agreement with the load-carrying capacity test results, even if inconsistencies were highlighted for the shear stress distribution with regards to the level of loading. The model could be used as a complement to tests in future research with an optimization of the time increment and mesh near stress concentrations.

For both the contact and the shear connection stiffness, the initial slip modulus  $k_i$  was stiffer than the slip modulus  $k_s$  for almost all materials. In fact, a very high initial stiffness was

observed for very low displacement from 0 to 0.1 mm. It is difficult to predict behavior for such low displacement, as such behavior can be caused by several parameters, including manufacturing parameters assembly gaps, and wood swelling. Nonetheless, the slip modulus  $k_s$  of the different tested configurations can thus be used directly in the different calculation models while remaining conservative in the displacement predictions. Assembly gaps can be implemented as function of the chosen manufacturing parameters. However, the numerical model largely overestimated the slip modulus  $k_s$  for all materials, and the introduction of deformable contact elements should be investigated to improve the model response. As a result, experimental tests remain necessary for defining the slip modulus for TT connections. With additional tests on both TT connections and shear properties of timber products, an analytical model could be established based on the experimental protocol developed in this work.

To conclude, the behavior of TT connections for commonly used timber panels was characterized, and newly developed experimental protocols were found to be consistent. Design guidelines were evaluated to safely use TT connections in standardized structural elements. Therefore, this work is a sound basis for optimizing the existing guidelines and developing analytical models for digitally produced TT connections. Further research could also investigate the notch-size effect, the effective number of connections, and creep behavior. The long-term objective is to create an extensive database on digitally produced connections for timber products in order to propose general guidelines for building codes.



## 6 Conclusions and outlook

### 6.1 Conclusions

The use of wood as a building material can help mitigate the construction industry's impact on natural resources and global warming to create a more sustainable built environment. The increasing demand for sustainable products has led to the development of new engineered wood-based materials and their wider adoption in modern construction. In the meantime, traditional hand-crafted assemblies have been progressively replaced by steel fasteners and bonding processes with the standardization of the timber industry. However, recent advances in digital fabrication through CAD and CAM have offered new design possibilities for wood-wood connections, particularly for timber plate structures. With new design-to-production workflows, digitally produced wood-wood connections have become a cost-competitive alternative for the edgewise assembly of thin timber panels, as a large number of connections with different geometries can now be easily manufactured. Therefore, this thesis presents research aiming to broaden the use of this specific joining technique into common timber construction practice, with the main conclusions summarized as follows:

#### **Building implementation**

The first building implementation of a double-layered timber folded-plate structure using digitally produced wood-wood connections, the Vidy theater, was presented. Approximately 300 different plate shapes, 450 different joint angles, and over 3,000 TT connections were applied to the design of this building. The inherent complexity was managed with a design-to-production workflow, linking the fabrication process and its capabilities to the architectural design and planning process. Specific computational tools for the design of a large number of digitally produced TT connections were efficiently used in a project environment with multiple stakeholders. In addition to LVL panels generally employed in previous research, CLT panels were investigated for the first time and showed superior rotational performance for this specific TT geometry. The potential of other engineered timber products for such assembly was thus demonstrated. The moment-rotation capacity of the connection largely satisfied

the requirements of the project, showing the efficiency of TT connections for the assembly of timber plate structures. Furthermore, the applicability of this construction system was demonstrated at the building scale.

### **Development of standardized construction systems**

Based on past research and DfMA approach, a novel standardized construction system uniquely using TT connections was introduced. The feasibility of this construction system was confirmed through a case-study both for continuous elements with an industrial partner's robotic line and for small panels with a CNC machine in the laboratory. The prefabricated approach reduces on-site construction time and increases structural performance using continuous elements. On the contrary, the flat-pack approach optimizes transportation costs and production flexibility, thereby making it accessible to SMEs for more resilient and distributed manufacturing on a local scale. Different connection types and geometries were proposed depending on materials and fabrication capacities to offer a wider range of alternatives for the design and to ease the assembly process. For this research, assembly was performed by hand. The reliability of the fabrication and assembly processes was validated by the low variability observed among different specimens in the large-scale experiments.

### **Calculation methodology and structural performance**

The SLS is generally the most critical criterion for interconnected elements using semi-rigid connections. As a result, the load-displacement response of the developed construction system was first investigated using an FE model to compare TT joints with glued and nailed assemblies, widely used in timber construction. TT joints demonstrated a superior performance to that of the nailed assemblies, which highlighted the viability of digitally produced wood connections as an alternative to mechanical fasteners for the edgewise assembly of thin panels. Nonetheless, the structural analysis of such construction systems has been mainly achieved with sophisticated, computationally expensive, and time-consuming FE models, which contrasts with the simplicity of basic housing elements. On the other hand, analytical theories, widely implemented in practice to evaluate the performance of mechanically jointed beams, cannot accurately capture their specific characteristics.

A practical numerical model was thus introduced using beam elements in the elastic range and spring elements to represent semi-rigid connections. Large-scale experimental bending and vibration tests were performed to validate the proposed calculation model. The model was in good agreement with the experimental results for the effective bending properties, being slightly conservative compared to rigid model and existing analytical approach. In addition, the model accurately captured the various discontinuities along the length of the elements. Friction was not considered in the model, as the damping ratio was similar to typical timber floor values without any exceptional effects due to the connections. Therefore, the proposed calculation model, with simple tests on connections, offers a convenient calculation

methodology to obtain the stress distribution and global displacement of interconnected elements using multiple TT joints.

### Creep behavior

In addition to the semi-rigid behavior of connections, creep also has a significant influence on the SLS of timber elements. Moreover, the EC5 guidelines require  $k_{def}$ , the reduction factor for the evaluation of creep deformation, to be doubled when applied to timber connections. An experimental test conducted under outdoor conditions was thus performed on a large-scale specimen and compared to the proposed calculation model to verify the existing guidelines. The contribution of connection creep to the final displacement was found to be approximately 25%. Nonetheless, the EC5 guidelines largely overestimated the final displacement by 30% while the final displacement was underestimated by 14% if creep was not considered. When the reduction factor  $k_{def}$  was not doubled, the most accurate prediction of the final displacement was observed, with a difference of only 9%. Therefore, the existing guidelines are conservative and structural design could be optimized by not doubling the reduction factor  $k_{def}$  for timber connections. This first quantitative study presents reassuring results for the long-term behavior of such construction systems.

### Connection behavior

The in-plane behavior of digitally produced TT joints was investigated, as it is an essential parameter for the prediction of the structural response of such timber structures. The load-carrying capacity and slip modulus of commonly available engineered timber panels were determined through an experimental campaign. Existing guidelines for traditional carpentry assemblies were compared to the test results, and an FE model was developed to approximate their performance. Significant differences were observed between the announced characteristic strength values and real performance of the materials, especially for materials characterized by a specific lay-up with a large cross-layer in the middle, such as OSB and MSW. The correspondence between product specifications and standard values could be improved for an optimized and coherent design.

Concerning the load-carrying capacity of TT joints, existing guidelines were mainly found to be conservative, except for OSB panels. Existing criteria can therefore be safely applied to LVL materials in an initial approach, while design diagrams based on the experimental procedures developed in this work can be established if the product specifications are considered uncertain, such as for OSB and MSW. The spreading coefficient for compression  $k_{c,\alpha}$  was found to be consistent, while the reduction-factor coefficient due to the non-uniform stress distribution of shear  $k_{v,red}$  was not relevant according to the test results. The numerical model was in good agreement with the load-carrying capacity test results. The initial connection stiffness was stiffer than the slip modulus for all materials and for very low displacement, which are difficult to predict accurately. The tested connection stiffness for the different TT configurations can

## Chapter 6. Conclusions and outlook

---

thus be directly applied in calculation models with conservative displacement predictions. However, the numerical model significantly overestimated connection stiffness for all configurations. As a result, tests remain necessary if other geometries or materials are to be employed in TT connections. This work constitutes a solid foundation for the optimization of design guidelines and for the creation of an extensive database on digitally produced wood-wood connections.

### General

To conclude, different investigations were performed at large-scale element and connection levels. Practical design methodologies, covering both geometrical and structural considerations, were thus established. Based on this research, the novel standardized construction system using digitally produced TT connections proposed in the present thesis can be applied reliably in a project environment for basic roof and slab elements with convenient design methods for practitioners.

## 6.2 Outlook

Research and development on digitally fabricated wood-wood connections applied to novel timber construction systems is a very broad topic and the scope of this thesis therefore had to be limited. As a result, several challenges remain to be addressed and the following topics could be explored:

### **Modeling and optimization of connections**

Based on the work performed in Chapter 5, analytical models for the prediction of the slip modulus and the optimization of existing design guidelines for the load-carrying capacity of digitally produced TT connections could be investigated. Additional tests, both of the shear properties of timber panels and of TT connections, would be necessary. Moreover, the FE model could be improved in terms of its mesh and time increments as well as by introducing deformable contact elements to reduce the number of experimental tests and study local effects. Finally, the influence of different grain orientations, notch sizes, and number of connections could be taken into consideration in future studies.

### **Creep of connections**

Based on the first quantitative study presented in Appendix B.3, a more in-depth analysis of the creep behavior of wood-wood connections could be conducted. Additional experimental tests and more advanced calculation models would be necessary. The preliminary assessment of existing guidelines regarding the evaluation of the creep behavior of timber connections in EC5 could thus potentially be confirmed.

### **Enhancement of connections**

Connection stiffness is an essential parameter for the load-displacement response and, as a result, for the SLS. New digital fabrication processes could be developed to harden contact surfaces of the assembly. The slip modulus would thus be larger, enhancing the load-displacement response of the structural element. In addition, reinforcements could also be studied to improve their low-ductility behavior and increase their load-carrying capacity.

### **Diaphragm effect**

The diaphragm effect of floor and wall elements is important for transferring lateral loads, such as wind or earthquake, into timber structures. The study of the diaphragm effect of such novel construction system would require additional experimental tests on the out-of-plane behavior of TT connections and in-plane behavior of large-scale elements. Additionally, the proposed model should be adapted and assessed for this loading configuration.

### Shear lag phenomenon

The low width-to-thickness ratio of flanges causes a non-uniform stress distribution along the flange width, referred to as shear lag. Shear lag generally reduces the load-carrying capacity of flanges in compression and tension. The current EC5 standards take shear lag into consideration by changing the physical cross-sectional dimensions with an effective width defined only by a constant ratio of the span. However, shear lag is influenced by other parameters, such as material shear properties, boundary conditions, type of loading, and width-to-span ratio of flanges. The local shear lag effect could be studied for different engineered timber products and configurations in order to assess the existing guidelines. In addition, the local effect of wood-wood connections on this phenomenon could also be evaluated.

### Design automation

Existing CAD plugins already exist for the automatic generation of geometry and fabrication files for TT connections. The specific geometry of this novel construction system composed of small panels could be incorporated in a new specific CAD plugin based on different input parameters, such as panel size, span, width, height, and joint parameters. The automatic generation of the proposed calculation model could also be added to directly transfer the geometry into commonly used structural-analysis software packages.

### Robotic assembly

Until the present, the assembly of timber plates with multiple wood-wood connections has been performed exclusively by hand. In a prefabricated approach, automation of the assembly process using robots could optimize costs and lead to an evolution of connection geometries and performance. A current doctoral study, entitled “Robotic Assembly of Integrally Attached Timber Plate Structures”, is currently being conducted on this topic within in the Laboratory of Timber Construction at EPFL.

### Digitally produced connections and sawn timber

In contrast to the engineered timber products used in this research, digitally produced connections applied to sawn lumber products, which are completely adhesive-free, could result in even more sustainable construction systems. A current doctoral study, entitled “Woodworking Joints and Assembly Methods for Locally Sawn Solid Timber Elements in Free-form Structures”, is currently being performed on this topic in the Laboratory of Timber Construction at EPFL [160].



## Funding

This research was supported by the NCCR Digital Fabrication, funded by the Swiss National Science Foundation (NCCR Digital Fabrication Agreement #51NF40-141853).

The National Centre of Competence in Research for Digital Fabrication is Switzerland's initiative to lead the development and integration of digital technologies within the field of architecture.





## **A Appendix of Chapter 3**

A.1 Detailed geometry of roof element for the case-study

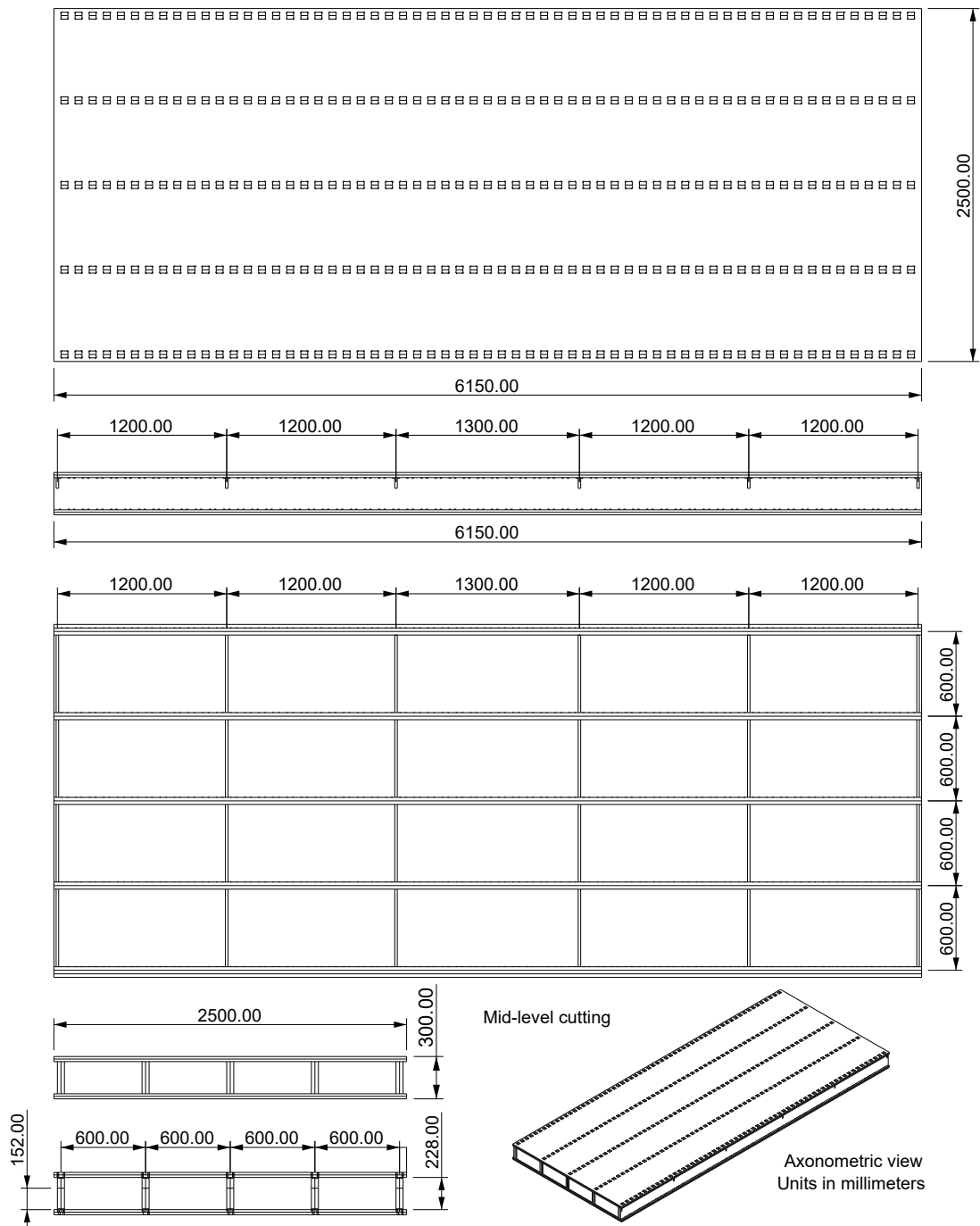


Figure A.1 – Detailed plan of the case-study roof element.

## A.2. Experimental curves of the push-out tests performed on OSB TT joints for the specific case-study

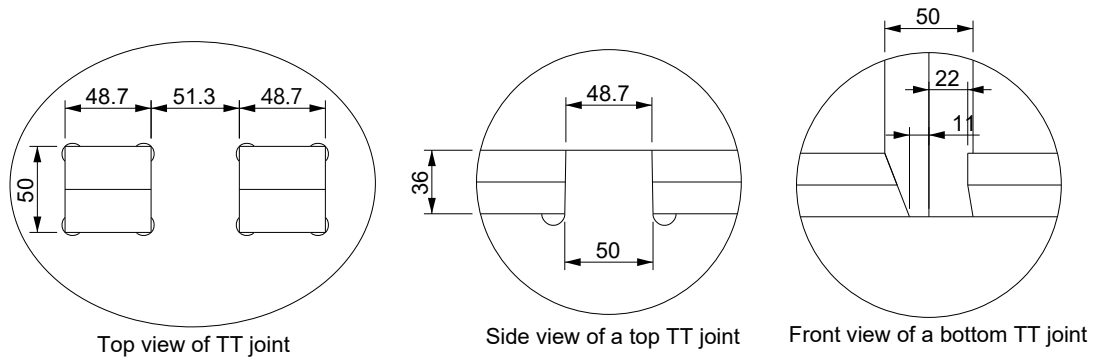


Figure A.2 – Detailed plan of the top and bottom TT geometry of the case-study roof element.

## A.2 Experimental curves of the push-out tests performed on OSB TT joints for the specific case-study

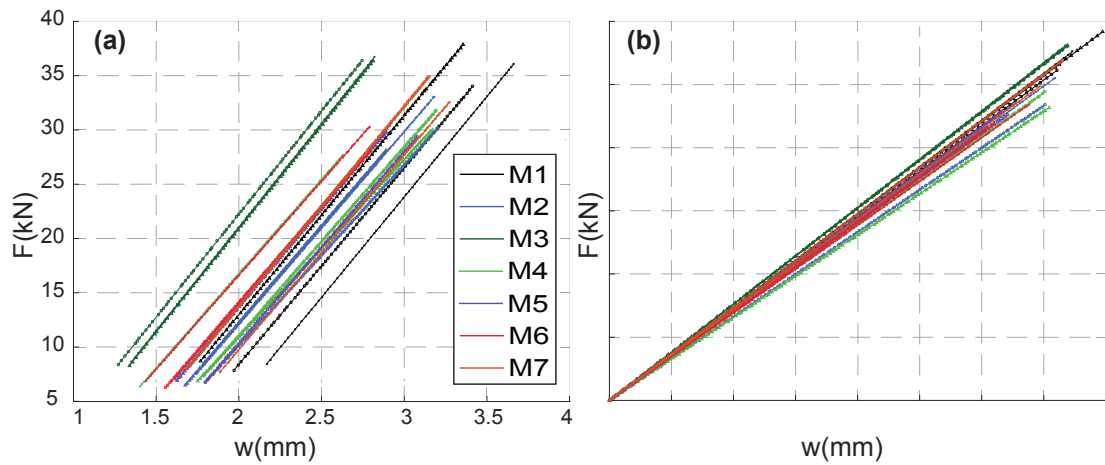


Figure A.3 – Experimental curves of the push-out tests performed on OSB TT joints: (a) Stiffness curves  $K_{y,sample}$  / (b) Comparison of the stiffness curves  $K_{y,sample}$ .



## **B Appendix of Chapter 4**

B.1 Detailed plans of large-scale specimens

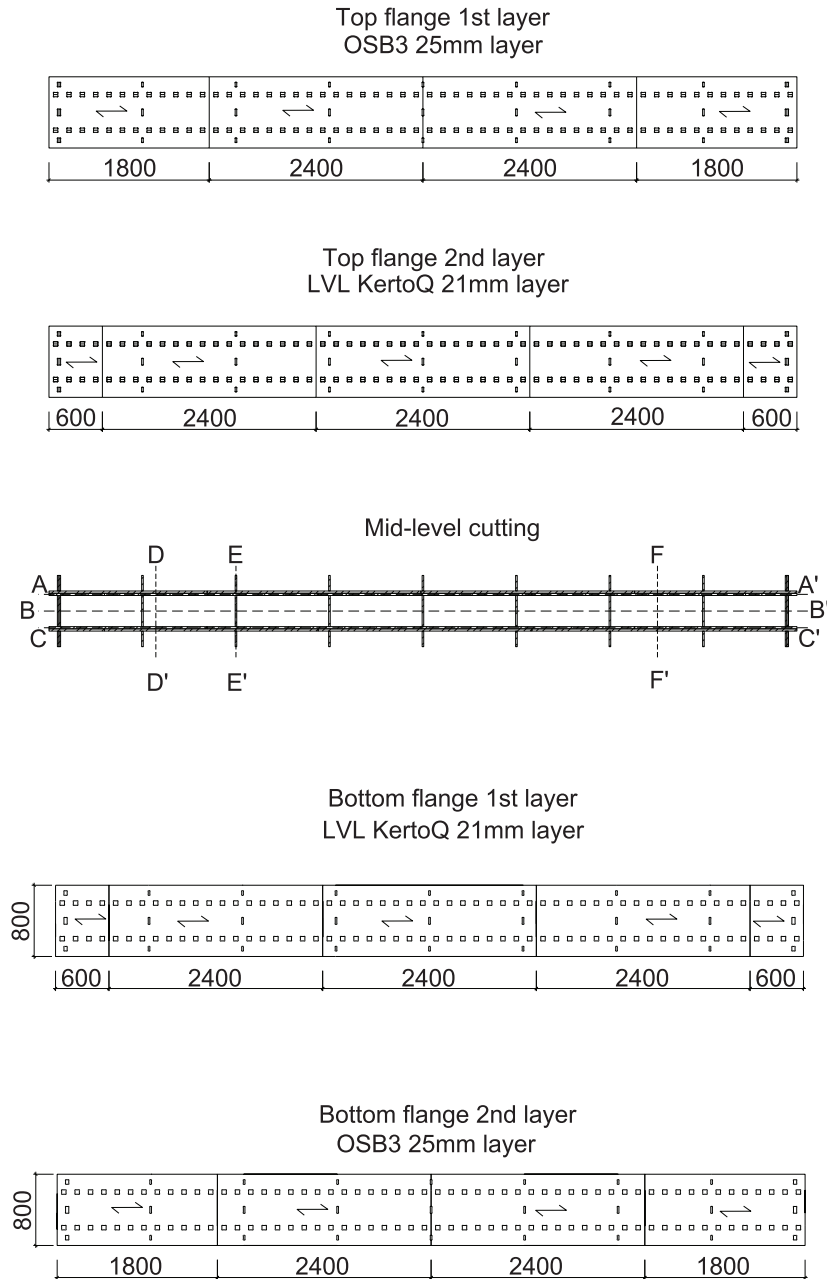


Figure B.1 – Detailed plan of large-scale specimens: part 1.

## B.1. Detailed plans of large-scale specimens

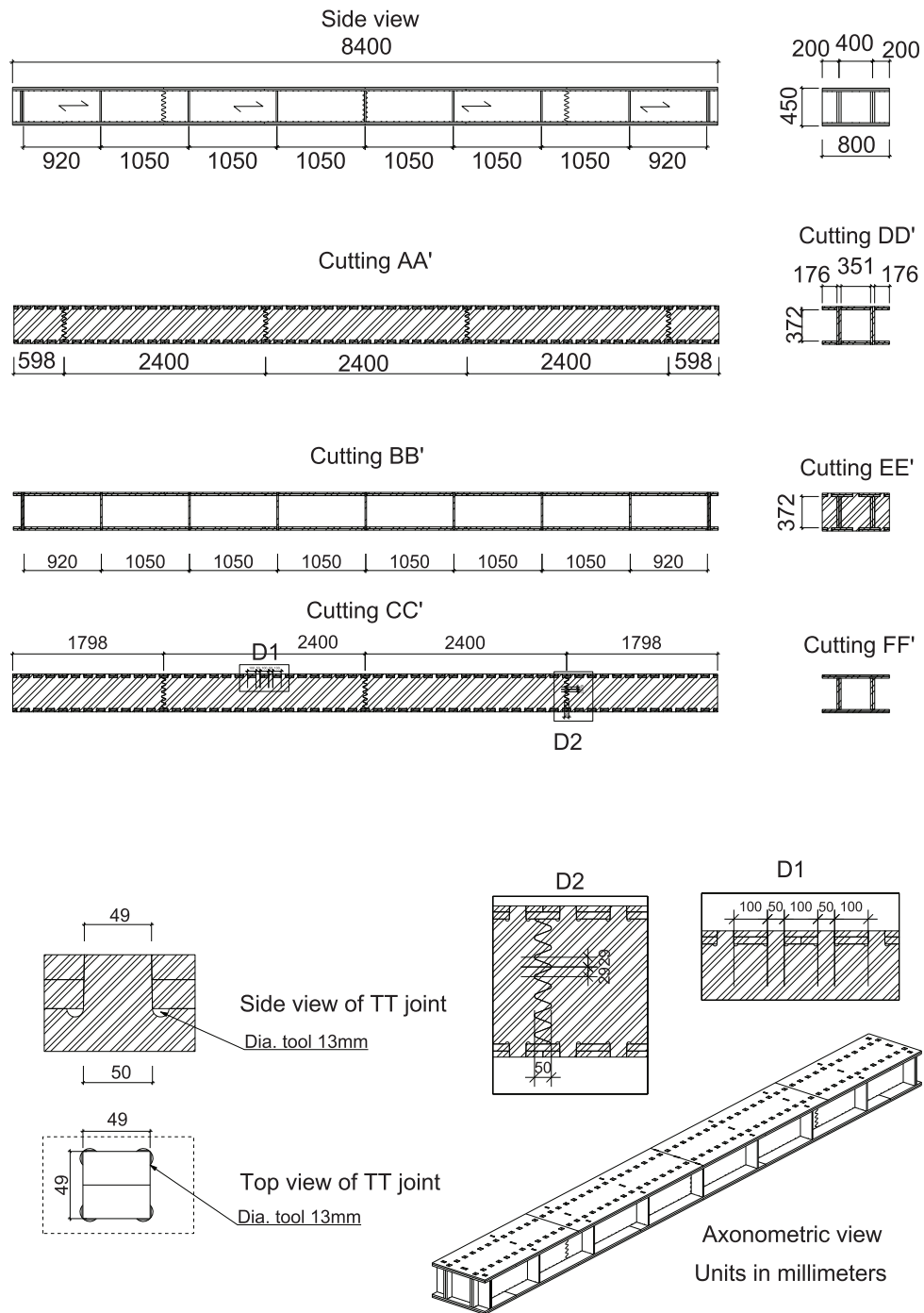


Figure B.2 – Detailed plan of large-scale specimens: part 2.

## B.2 Gamma method calculations

The gamma method, defined by equations 4.1 to 4.5, was used to calculate the effective bending stiffness ( $El_{ef}$ ) of the large-scale specimens. However, as described in chapter 4, all discontinuities along the element cannot be addressed with this method. Several assumptions were thus applied in order to perform the calculation:

- All elements of the large-scale specimen were considered continuous.
- The different layers of flanges and webs were merged into one element each, as the method can only calculate jointed beams of up to three elements.
- The elastic modulus of the flanges was defined by a thickness-dependent ratio of the two materials used (OSB and LVL).
- The stiffness value of the connections  $K_1$  and  $K_3$  was taken from the shear-test results of TT OSB connections performed in chapter 5, section 5.6.1 (specimens T1-50). The LVL was not considered for the stiffness of the connection as no shear tests were performed on this specific configuration.

The different parameter values used for the calculation are listed below (refer to Fig. 4.2 for the geometrical parameters):

$$\begin{array}{lll}
 E_{0,mean,OSB3,flat} = 4930 \text{ MPa} & h_1 = h_3 = 36 \text{ mm} & b_1 = b_3 = 400 \text{ mm} \\
 E_{0,mean,OSB3,edge} = 3800 \text{ MPa} & h_2 = 372 \text{ mm} & b_2 = 50 \text{ mm} \\
 E_{0,mean,LVL,flat} = 10000 \text{ MPa} & h_{OSB,flat} = 18 \text{ mm} & s_1 = s_3 = 150 \text{ mm} \\
 & h_{LVL,flat} = 21 \text{ mm} & K_1 = K_3 = 21120 \text{ N.mm}^{-1}
 \end{array}$$

The elastic modulus of each member was calculated as follows:

$$\begin{aligned}
 E_1 = E_3 &= \frac{(E_{0,mean,OSB3,flat} \times h_{OSB,flat} + E_{0,mean,LVL,flat} \times h_{LVL,flat})}{h_{OSB,flat} + h_{LVL,flat}} = 7660 \text{ MPa} \\
 E_2 &= E_{0,mean,OSB3,edge} = 3800 \text{ MPa}
 \end{aligned}$$

The moment of inertia and the cross-sectional area were calculated according to formulas for rectangular cross-sections:

$$\begin{aligned}
 I_1 = I_3 &= \frac{b_1 \times h_1^3}{12} = 1977300 \text{ mm}^4 & I_2 &= \frac{b_2 \times h_2^3}{12} = 214495200 \text{ mm}^4 \\
 A_1 = A_3 &= b_1 \times h_1 = 15600 \text{ mm}^2 & A_2 &= b_2 \times h_2 = 18600 \text{ mm}^2
 \end{aligned}$$



Finally, the effective bending stiffness ( $EI_{ef}$ ) was determined according to the gamma method described below:

$$\begin{aligned}\gamma_1 &= [1 + \pi^2 E_1 A_1 s_1 / (K_1 l^2)]^{-1} = 0,89 \\ \gamma_2 &= [1 + \pi^2 E_2 A_2 s_2 / (K_2 l^2)]^{-1} = 1 \\ \gamma_3 &= [1 + \pi^2 E_3 A_3 s_3 / (K_3 l^2)]^{-1} = 0,89 \\ a_2 &= \frac{\gamma_1 E_1 A_1 (h_1 + h_2) - \gamma_3 E_3 A_3 (h_2 + h_3)}{2 \sum_{i=1}^3 \gamma_i E_i A_i} = 0 \text{ mm} \\ a_1 &= \frac{h_1 + h_2}{2} - a_2 = 205,5 \text{ mm} \\ a_3 &= \frac{h_2 + h_3}{2} + a_2 = 205,5 \text{ mm} \\ EI_{ef} &= \sum_{i=1}^3 (E_i I_i + \gamma_i E_i A_i a_i^2) = 9,80 \times 10^{12} \text{ N}\cdot\text{mm}^2\end{aligned}$$

According to the gamma method and the simplified assumptions listed above, the effective bending stiffness of the large-scale element was  $9,80 \times 10^{12} \text{ N}\cdot\text{mm}^2$ .

## B.3 Creep behavior

This appendix is based on: J. Gamero, M. Nakad, J. F. Bocquet and Y. Weinand. Case-study on the creep behavior of interconnected elements using wood-wood connections. In *Proceedings of the World Conference on Timber Engineering*. Santiago, Chile, 2020. Abstract submitted.

### B.3.1 Introduction

Wood and engineered timber products are considered as viscoelastic materials with a time-dependent strain-stress behavior [141, 142]. The increasing deformation of these types of materials over time under permanent loads is commonly referred to as creep. The creep behavior of timber products depends on several factors. The load direction with respect to grain orientation is an important parameter, since deformations are higher when loads are applied perpendicularly than when applied parallel to the grain [46, 93]. The type of stress is also a parameter influencing creep due to the anisotropic behavior of wood, as shown in several studies [58, 142]. In addition, environmental conditions, such as temperature and relative humidity, influence creep behavior. The temperature itself influences creep deformation, but effects are only notable above 35°C [67, 93]. However, changes in both temperature and relative humidity impact the moisture content of wood and significantly accelerate the creep effect. This specific phenomenon is generally called mechano-sorptive creep [5, 106, 113]. Therefore, creep of wood materials is a very complex phenomenon that has been investigated since the 1960s and remains an ongoing research topic in wood material science. Nonetheless, the general creep behavior of a timber element can be described as occurring in three stages [43, 114], as shown in Fig. B.3a: (1) the deformation is first characterized by a rapid increase followed by a decreasing creep velocity, (2) the deformation is then constant over time, and finally (3) the deformation shows a rapid increase until failure with non-linear viscoelasticity.

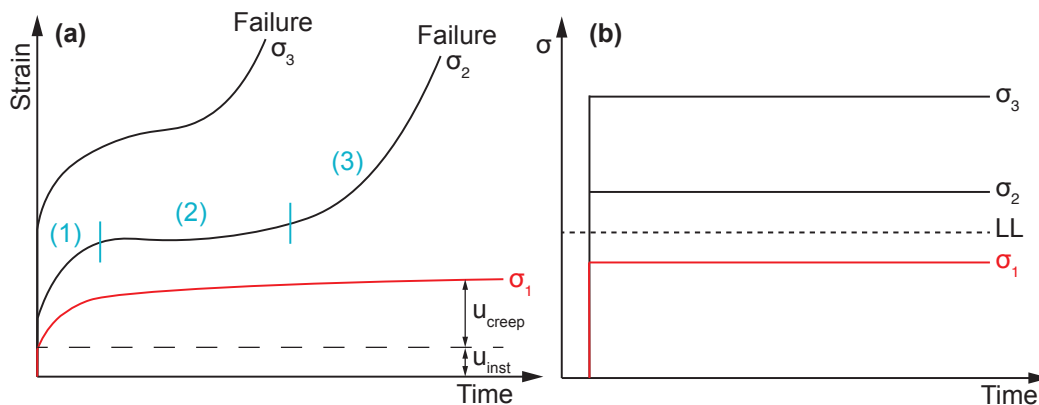


Figure B.3 – (a) Creep strain curve for different stress levels / (b) Different stress levels compared to the limit of linearity (LL).

The structural design of interconnected timber elements is mainly governed by the SLS, as discussed in Chapter 4. Therefore, it is important to properly consider creep as it largely influences the general displacement of timber structures. Within current timber construction standards, such as EC5 [33], creep is considered with different modification factors depending on the service class. There are three service classes that describe the environmental conditions (temperature and relative humidity) to which the construction element may be subjected. Based on the service class and the type of wood material, different values are assigned to two modification factors, namely  $k_{mod}$  and  $k_{def}$ . The first modification factor  $k_{mod}$  for load duration and moisture content is applied to the load-carrying capacity of members according to Equation B.1:

$$R_d = k_{mod} \frac{R_k}{\gamma_M} \quad (B.1)$$

where  $R_k$  is the characteristic load-carrying capacity value and  $\gamma_M$  is the partial factor for material properties. The strength-reduction factor  $k_{mod}$  limits the stress level to remain in the limit of linearity (LL) and avoid a creep failure, as shown with the red curve  $\sigma_1$  in Fig. B.3a and b. If this first condition is respected, wood can be considered as linear viscoelastic, and the deformation is thus considered as a ratio of the elastic deformation under permanent loads. As a result, the second modification factor  $k_{def}$  reduces the elastic properties of timber according to the following equations:

$$E_{mean,fin} = \frac{E_{mean}}{1 + k_{def}} \quad (B.2) \quad K_{ser,fin} = \frac{K_{ser}}{1 + k_{def}} \quad (B.4)$$

$$G_{mean,fin} = \frac{G_{mean}}{1 + k_{def}} \quad (B.3) \quad k_{def} = \frac{u_{creep}}{u_{inst}} \quad (B.5)$$

where  $E_{mean}$  is the mean value of modulus of elasticity,  $G_{mean}$  is the mean value of shear modulus,  $K_{ser}$  is the slip modulus of connections,  $k_{def}$  is the reduction factor for the evaluation of creep deformation,  $u_{creep}$  is the deformation due to creep and  $u_{inst}$  is the instantaneous elastic deformation, as shown in Fig. B.3a. The final deformations of timber elements are calculated with these modified properties. However, the reduction coefficient  $k_{def}$  is calculated differently for connections constituted of timber elements. It is stated in Subsection 2.3.2.2 of EC5 [33] that the value of  $k_{def}$  should be doubled for a connection constituted of timber elements with the same time-dependent behavior. If the connection is constituted of two wood materials with different time-dependent behavior, the factor  $k_{def}$  is calculated according to Equation B.6:

$$k_{def} = 2\sqrt{k_{def,1} \cdot k_{def,2}} \quad (B.6)$$

where  $k_{def,1}$  and  $k_{def,2}$  are the reduction factors for the two timber elements composing the assembly. In both cases, the value of  $k_{def}$  for wood-wood connections largely increases the global displacement.

Therefore, the goal of this work was to compare the existing guidelines concerning the creep-reduction factor  $k_{def}$  for wood-wood connections with the case-study presented in Chapter 4. As a result, an experimental test was conducted in outdoor conditions on the newly developed structural element, as shown in Fig. B.4. The deformation factor  $k_{def}$  for OSB panels was also tested, as high variability was observed for this material.



Figure B.4 – Photograph of the experimental setup in outdoor conditions.

### B.3.2 Material and methods

The same large-scale specimen (LSS) as the one presented in Section 4.3.1 of Chapter 4 was experimentally tested in outdoor conditions. The detailed plan can be found in Appendix B.1 (see Fig. B.1 and B.2). The LSS, with a span of 8.1 m, was placed on two supports under a ventilated shelter and exposed to natural variations of humidity and temperature, which corresponds to a service class 2 according to EC5. The test setup is presented in Fig. B.5. The LSS was loaded with eight small OSB control panels (CP) of 18 mm thickness weighted with lead to create a distributed loading configuration (see Fig. B.5a, b and c). The CPs were used to estimate the creep factor  $k_{def}$  of OSB under these specific environmental conditions because of the high material variability of OSB. These CPs had a length of 900 mm and a width of 290 mm. The panels were loaded with a punctual load of 180 N at their centers (see Fig. B.5d). All displacement were recorded using a theodolite Leica TCR 705 (Leica Geosystems, Wetzlar, Germany) with 26 targets positioned along the LSS and 24 targets along the CPs, as shown in Fig. B.5d, e, f, and g. Displacement measurements were performed every day for the first week, then every 3 days for 1 month, then every week for 6 months, and finally every 2 weeks. All measurements were conducted over a total period of approximately 400 days. Humidity and temperature variations were monitored every hour with three sensors (Data logger EL-USB-2+, Thermolab SARL, Préverenges, Switzerland) placed under the ventilated shelter.

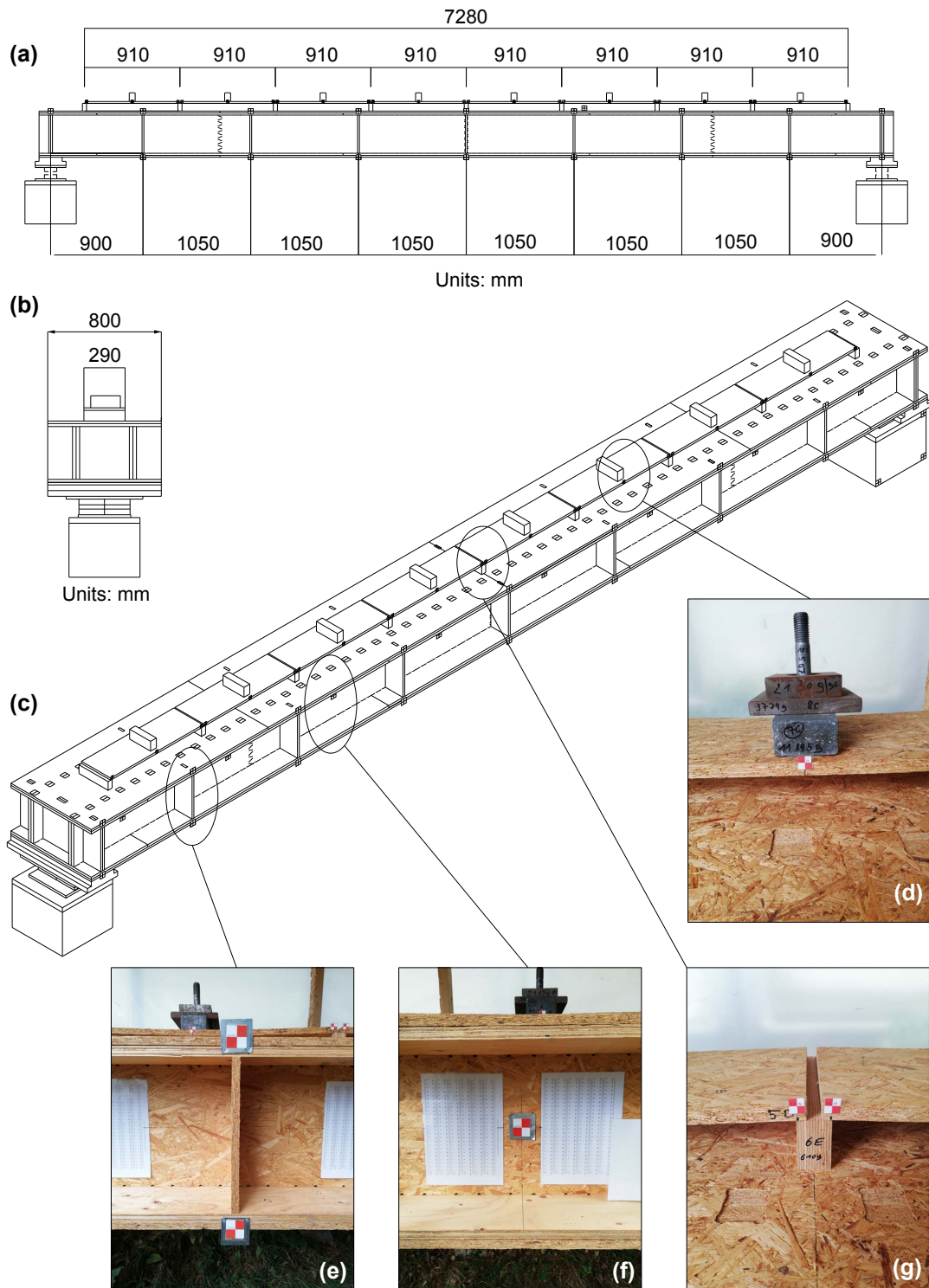


Figure B.5 – Experimental setup details: (a) Front view / (b) Side view / (c) Axonometry / (d) Punctual load on OSB panel / (e) Displacement targets on top and bottom flanges / (f) Displacement target on web / (g) Displacement targets on support conditions of OSB panels.

### B.3.3 Loading procedure

The loading configurations of the LSS and CPs were calculated based on the static test results in Chapter 4 as follows:

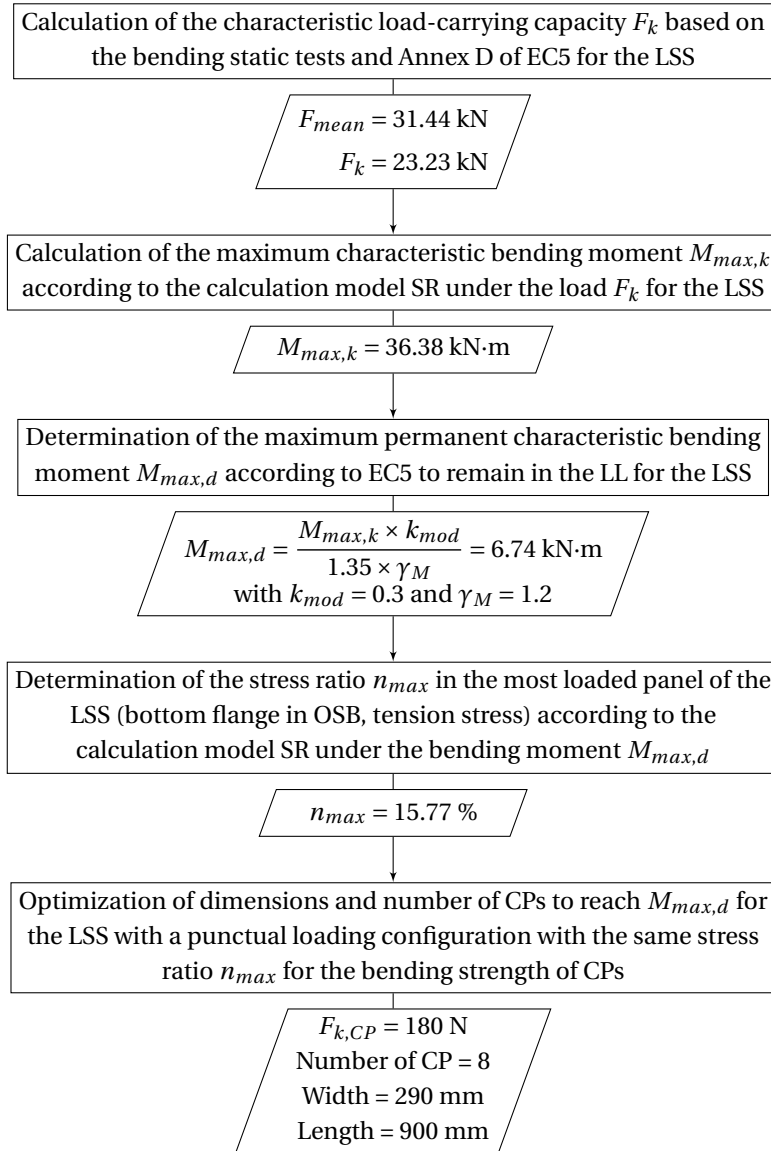


Figure B.6 – Loading calculation method for the creep test.

The maximum permanent characteristic bending moment  $M_{max,d}$  derived from the static bending test and the calculation model SR presented in Section 4.4 of Chapter 4 was thus applied on the LSS in the form of a distributed load with the CPs. The stress ratio  $n_{max}$  in the most loaded panel of the LSS, retrieved with the calculation model SR, was then applied to the bending strength of the CPs with punctual loads. The number and dimensions of CPs along the LSS were optimized to reach the  $M_{max,d}$ . This specific loading configuration allows the

creep behavior of LSS and OSB type 3 panels to be retrieved from a single test setup. However, several assumptions were adopted for the calculation of the loading configurations. For the calculation of  $M_{max,d}$  only the OSB reduction-strength factor  $k_{mod}$ , equal to 0.3, was used instead of a ratio between LVL and OSB factors, as OSB panels comprised the major part of the LSS. The stress level in the most loaded panel of the LSS was located in the bottom flange in tension while the CPs were tested in bending. There is no differentiation of the factor  $k_{def}$  according to the type of stress in EC5, but creep deformations due to tension are generally lower than creep due to bending, as specified in the New Zealand timber structures standard [57, 103]. This difference was not considered in this calculation. Finally, only the creep deformation factor  $k_{def}$  of OSB was tested, as OSB is usually the material with the highest variability. For LVL,  $k_{def}$  was considered equal to be equal to 0.8 according to a service class 2 in EC5.

#### B.3.4 Calculation models

From the SR calculation model, three different configurations were implemented to study the influence of the connections on creep behavior:

- Model 01: the creep deformation  $k_{def}$  was not applied to the connections.
- Model 02: the creep deformation  $k_{def}$  was applied to the connections according to the existing guidelines described by Equation B.6 but without factor 2. The creep factor was not doubled, as specified in EC5.
- Model 03: the creep deformation  $k_{def}$  was applied to the connections according to the existing guidelines described by Equation B.6, as specified in EC5.

All material properties were defined according to Equations B.2, B.3 and B.4. The reduced material properties used in all the models are listed in Table B.1.

Table B.1 – Material properties with the reduction coefficient  $k_{def}$  applied.

Designation	Symbol	Units	LVL Q	OSB 3
Elastic modulus // to grain	$E_{0,mean,fin}$	MPa	5556	1467
Elastic modulus $\perp$ to grain	$E_{90,mean,fin}$	MPa	1833	589
Shear modulus // to grain	$G_{0,mean,fin}$	MPa	33	15

#### B.3.5 Results

The curves of the maximum displacement  $w_{max}$  over time for the LSS and CPs are shown in Fig. B.7, and the temperature and humidity over time are displayed in Fig. B.8. All results are listed in Table B.2, and a comparison between the test and the calculation for the LSS is presented in Table B.3. The LSS and CPs stabilized after a period of 200 days, as shown in Fig. B.7. The same stabilization was highlighted in other studies on OSB and LVL materials [94, 167]. As a result, the 400-day period was considered sufficiently representative to study the

creep behavior of the LSS and CPs.

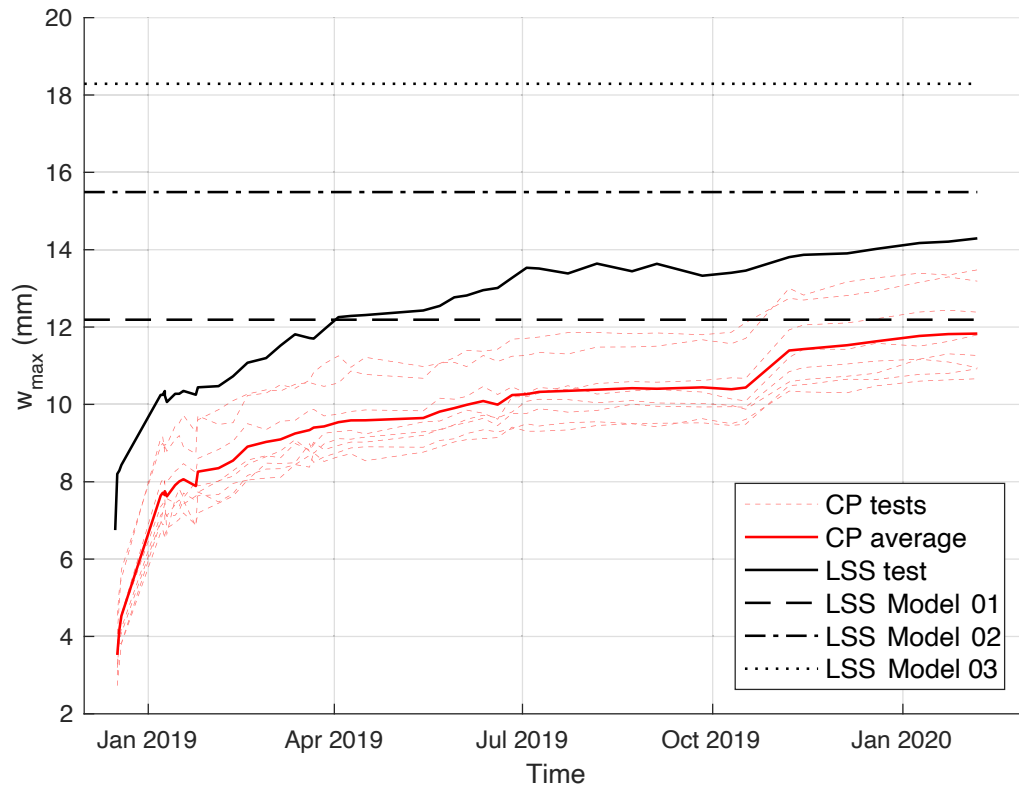


Figure B.7 – Maximum displacement  $w_{max}$  over time for the LSS and CPs.

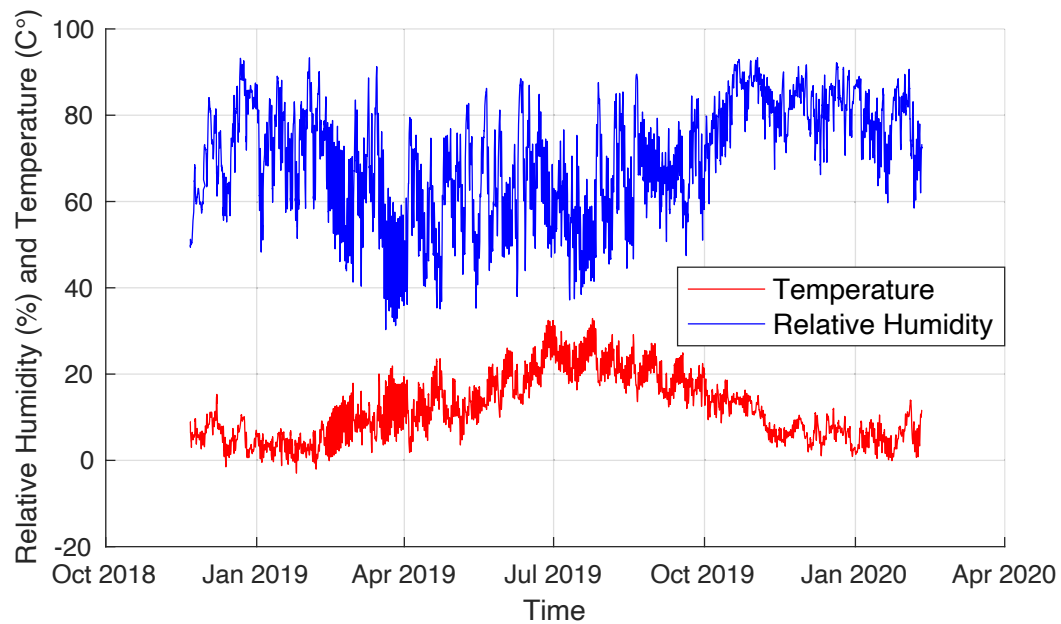


Figure B.8 – Humidity and temperature measured under the ventilated shelter.



Table B.2 – Maximum displacement  $w_{max}$  over time for the LSS test and CP average.

Time (days)	LSS test		CP average	
	$w_{max}$ (mm)	Ratio (-)	$w_{max}$ (mm)	Ratio (-)
0	6.75	1.00	3.52	1.00
2	8.43	1.25	4.53	1.29
21	10.25	1.52	7.64	2.17
32	10.35	1.53	8.06	2.29
49	10.47	1.55	8.35	2.37
100	11.94	1.77	9.43	2.68
148	12.43	1.84	9.64	2.74
198	13.53	2.00	10.26	2.91
249	13.44	1.99	10.41	2.96
304	13.46	1.99	10.43	2.96
353	13.9	2.06	11.53	3.28
402	14.21	2.11	11.82	3.36

For the CPs, the ratio between the initial and final maximum displacement, at  $t = 0$  and 402 days, respectively, was equal to 3.36 (see Table B.2), which corresponds to a reduction factor  $k_{def}$  equal to 2.36 according to Equation B.5. Based on EC5, the  $k_{def}$  value for OSB material in environmental conditions corresponding to a service class 2 is equal to 2.25. The difference between the tested and standard  $k_{def}$  values was only 5%. The tested  $k_{def}$  value of 2.36 was thus used in the different calculation models for the LSS, both for the material properties presented in Table B.1 and for the connection stiffness listed in Table B.3. In addition, the small variation between the tested and standard values showed that the CPs were stabilized close to the final state, which supports the assumption that the 400-day period was sufficiently representative to study the creep behavior.

Table B.3 – Comparison between test and calculation models for the maximum displacement  $w_{max}$  of the LSS.

ID (-)	$k_{def}$ (-)	$K_{ser,fin}$ (kN/mm)	$w_{max}$ (mm)	$\delta w_{max,test}$ (%)
LSS test	-	-	14.21	-
LSS Model 01	0	3.89	12.19	-14
LSS Model 02	1.37	1.64	15.49	9
LSS Model 03	2.74	1.04	18.29	29

According to the comparison presented in Table B.3, the maximum displacement obtained

with the LSS Model 01, which did not account for creep in the connections, was lower than the maximum displacement measured during the test, with an underestimation of 14%. Creep effect should thus be taken into consideration to ensure a safe design for the SLS. On the other hand, the maximum displacement predicted by the LSS Model 02 was found to be the closest to the test result with an overestimation of the final displacement of only 9%. Finally, the LSS Model 03 demonstrated the highest difference with respect to the test result with a 29% overestimation of the final displacement. Therefore, the current guidelines for the consideration of creep in timber connections, described by Equation B.6 and implemented in the LSS Model 03, appear to be overly conservative. However, the application of the same guidelines without factor 2 described in Equation B.7 was more appropriate for the prediction of the final displacement of the LSS, as shown with the LSS Model 02.

$$k_{def} = \sqrt{k_{def,1} \cdot k_{def,2}} \quad (B.7)$$

As a result, Equation B.7 provided a more accurate assessment of the connection creep-reduction factor  $k_{def}$  for this specific case-study. Finally, the contribution of connection creep to the final displacement of the LSS was approximately 25%.

### **B.3.6 Conclusions**

The creep behavior of timber has a significant influence on the SLS, which generally governs the design of interconnected elements with semi-rigid connections. The reduction factor  $k_{def}$  is used in the current timber construction standard (EC5) to reduce the elastic properties of timber and calculate the final displacement of structures while accounting for creep. Nonetheless, this reduction factor  $k_{def}$  is doubled according to Equation B.6 when applied to timber connections, such as digitally produced TT connections. Therefore, a first quantitative approach based on the case-study presented in Chapter 4 was conducted to assess these existing guidelines. An experimental test under outdoor conditions was performed on the same large-scale specimen as the one presented in Section 4.3.1 to investigate its creep behavior. The results of this first quantitative study demonstrated that the existing guidelines overestimated the final displacement by approximately 30% when the  $k_{def}$  factor was doubled. On the contrary, without considering creep in the connections, results showed that the final displacement was underestimated by 14%, highlighting the importance of taking creep into account. Finally, the most accurate prediction of the final displacement, with a difference of only 9% compared to the test, was achieved without doubling the  $k_{def}$  factor, as described in Equation B.7. Therefore, this first experimental test is reassuring for the long-term behavior of the type of construction system using wood-wood connections proposed in this thesis. The existing guidelines are highly conservative and structural design could be optimized without doubling the  $k_{def}$  factor of the connections while remaining on the safe side of design. Nonetheless, future research should confirm this preliminary work with more advanced analytical or numerical rheological models [27] and additional tests.

## **C Appendix of Chapter 5**

## C.1 Material compression tests

### C.1.1 Method and specimens

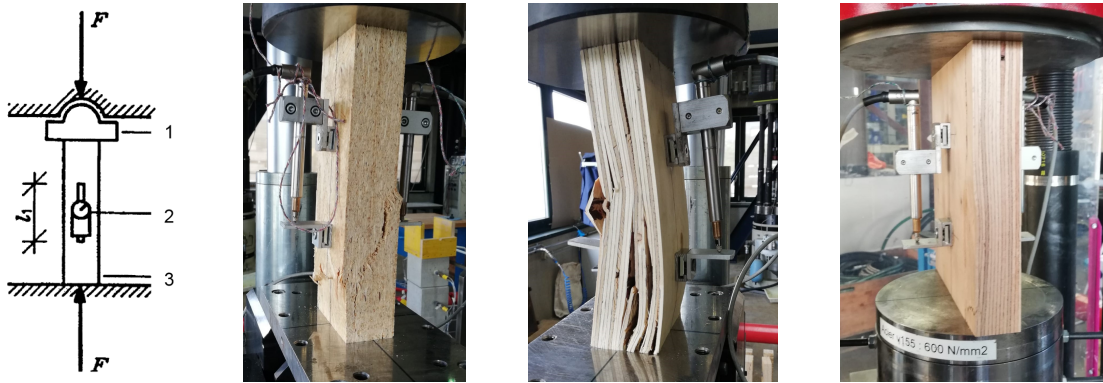


Figure C.1 – Compression setup: (a) EN789 [38]: (1) spherical seated, (2) transducer, and (3) test piece / (b) OSB specimen / (c) Spruce LVL specimen / (d) Beech LVL specimen.

Table C.1 – Specimen properties for compression tests according to EN 789 [38].

ID	Material thickness (mm)	Number of layer (mm)	Total thickness (mm)	Width (mm)	Length (mm)
(1)	18	3	54	67	300
(1')	25	2	50	100	300
(2)	21	2	42	100	240
(3)	39	2	78	100	430
(4)	40	1	40	200	240
(5)	27	2	54	100	290

### C.1.2 Methodology for calculating the 5% fractile values

The 5% fractile value ( $F_{max,0.05}$ ) was determined according to the methodology defined in Annex D of Eurocode 0 [31]. The coefficient of variation ( $c_{v,F_{max}}$ ) for each material was under 10%. As a result, a small sample size of 10 replicates is sufficient to determine the characteristic strength according Hunt et al. [69]. A log-normal distribution was assumed, which is generally the case for compression strength parallel to the grain for timber properties [82]. Equations C.1 to C.3 from Eurocode 0 were used:

$$F_{max,0.05} = \exp[m_y - k_n s_y] \quad (C.1)$$

$$m_y = \frac{1}{n} \sum_{i=1}^n \ln(F_{max,i}) \quad (C.2)$$

$$s_y = \sqrt{\frac{1}{n-1} \sum_{i=1}^n (\ln(F_{max,i}) - m_y)^2} \quad (C.3)$$

where  $F_{max}$  is the maximum load,  $n$  is the number of specimens,  $k_n$  is the characteristic fractile factor for a sample size of 10 replicates (constant value of 1.92),  $m_y$  is the average of the natural logarithm values, and  $s_y$  is the standard deviation of the natural logarithm values. All results are listed in Table C.2.

Table C.2 – Test results of the maximum load ( $F_{max}$ ) for the material compression tests.

Material ID	(1)	(1')	(2)	(3)	(4)	(5)
Units	(kN)	(kN)	(kN)	(kN)	(kN)	(kN)
Specimen 01	44.12	58.28	124.00	234.75	457.42	116.50
Specimen 02	41.72	55.42	127.32	233.30	475.03	114.62
Specimen 03	43.78	49.50	121.41	237.35	465.74	126.55
Specimen 04	39.01	51.78	117.13	248.66	444.48	123.90
Specimen 05	44.99	45.28	116.07	232.20	467.95	113.26
Specimen 06	38.57	55.75	120.17	234.17	473.37	116.71
Specimen 07	41.31	58.63	115.40	245.42	457.61	114.79
Specimen 08	39.72	57.17	119.93	232.79	450.49	129.19
Specimen 09	38.37	52.22	117.32	238.97	451.53	117.72
Specimen 10	46.65	53.81	122.23	234.83	467.97	114.29
Average	41.82	53.78	120.10	237.24	461.16	118.75
$c_{v,F_{max}}$	7.02%	7.81%	3.15%	2.36%	2.25%	4.78%
$m_y$	3.73	3.98	4.79	5.47	6.13	4.78
$s_y$	0.07	0.08	0.03	0.02	0.02	0.05
$F_{max,0.05}$	36.50	45.94	113.05	226.80	441.55	108.42

## C.2 Statistical distribution of compression tests of TT connections

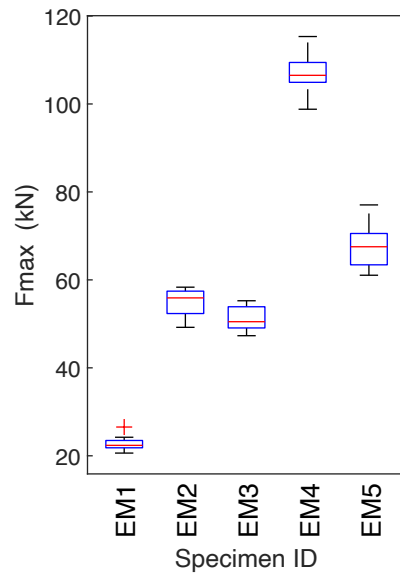


Figure C.2 – Boxplot of  $F_{max}$  values per specimen type for the compression tests of TT connections. The box-plot represents the median with the red central mark and the 25<sup>th</sup> and 75<sup>th</sup> percentiles with the bottom and top edges of the box, respectively.

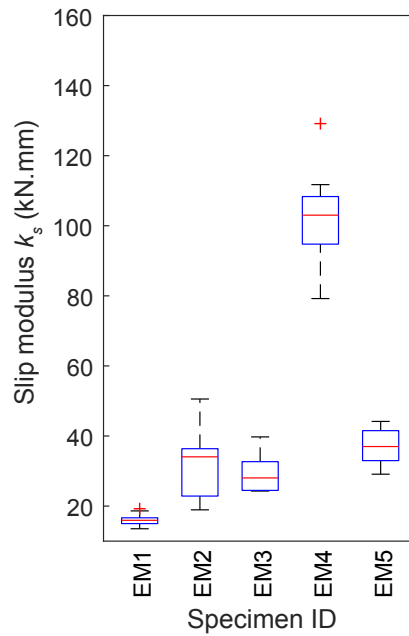


Figure C.3 – Boxplot of  $k_s$  values per specimen type for the compression tests of TT connections.

### C.3 Statistical distribution of shear tests of TT connections

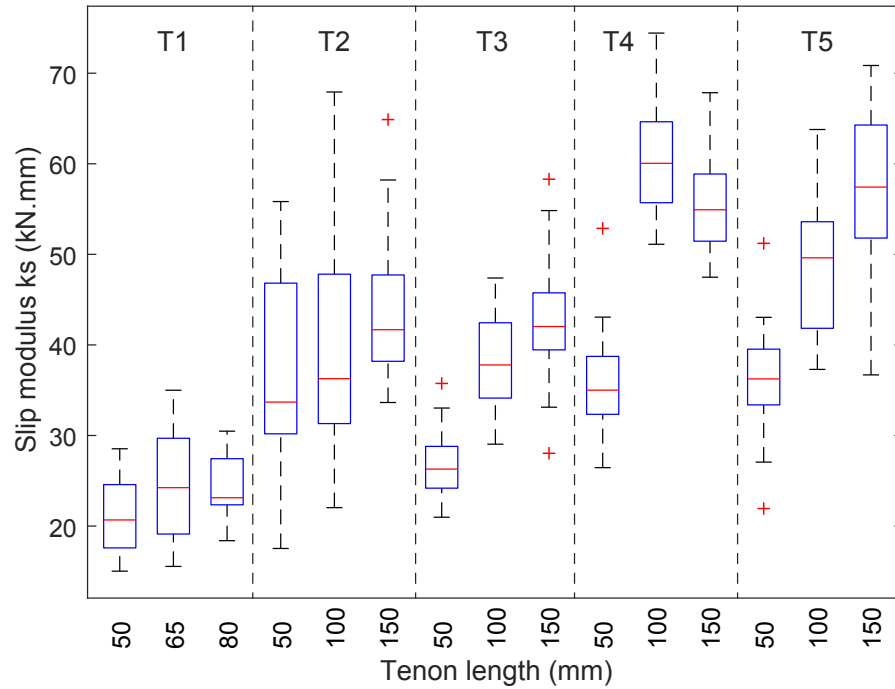


Figure C.4 – Boxplot of  $k_s$  values per specimen type for the shear tests of TT connections.

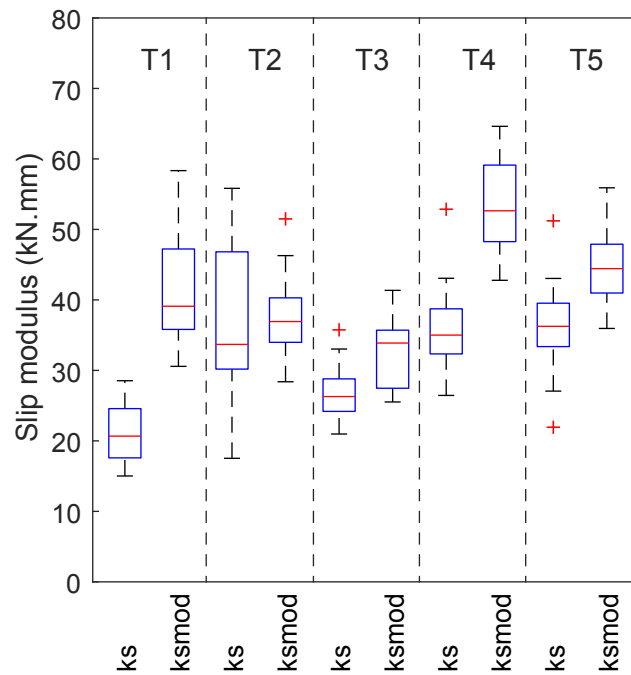


Figure C.5 – Boxplot of  $k_s$  and  $k_{smod}$  values per specimen type for the shear tests of TT connections with a tenon length of 50 mm.

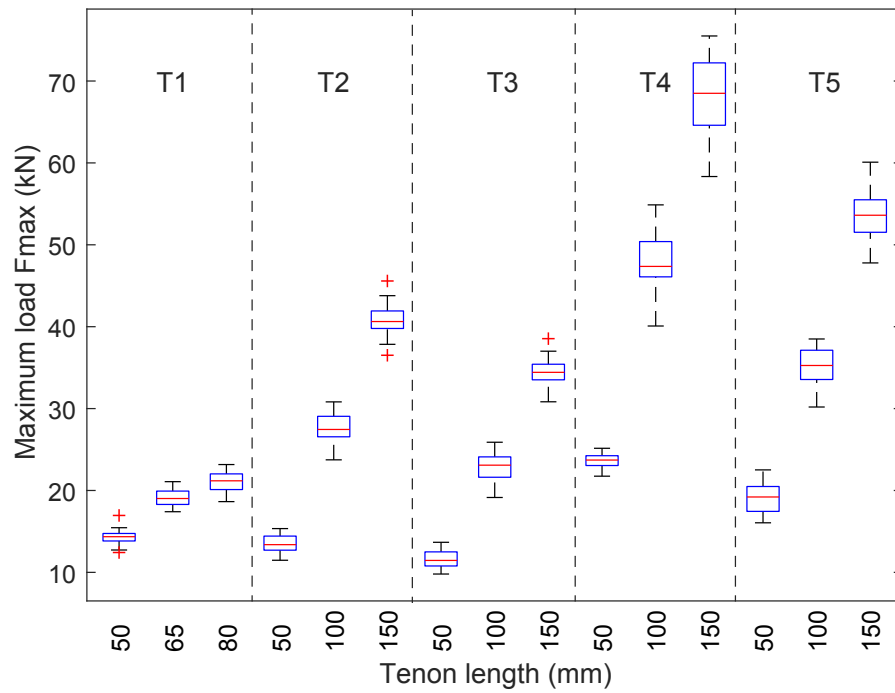


Figure C.6 – Boxplot of  $F_{max}$  values per specimen type for the shear tests of TT connections.



## C.4 Numerical model for TT connections<sup>1</sup>

The numerical model proposed by Sandhaas [131] and based on continuum damage mechanics (CDM) was used to model the non-linear behavior of wood-wood connections, whose results are presented in Section 5.6. The CDM approach consists in modifying the stiffness matrix or its inverse, namely the compliance matrix, through specific damage parameters. The model was built in the finite element analysis software (FEA) Abaqus<sup>TM</sup>, version 6.12 (Dassault Systèmes, Vélizy-Villacoublay, France). The model generation was programmed using the Abaqus Scripting Interface in the Python programming language. However, instead of generating the wood-wood connection geometry using a plugin built in the FEA software, the geometry was imported from the Rhinoceros<sup>®</sup> (Robert McNeel & Associates, Seattle, USA) CAD software.

### C.4.1 Material model

Timber was modeled as a single orthotropic layer, in contrast to the multi-layered model applied by Roche et al. [129] in which each veneer layer was represented with its orientation (longitudinal layers at 0° and crosswise layers at 90°) with interfaces considered rigid. Material directions used in this study are indicated in Figure C.7. The main direction (1) is the longitudinal direction of the fibers, parallel to the grain; the second (2) and third (3) directions, both perpendicular to the grain, are tangential and radial to the rings, respectively.

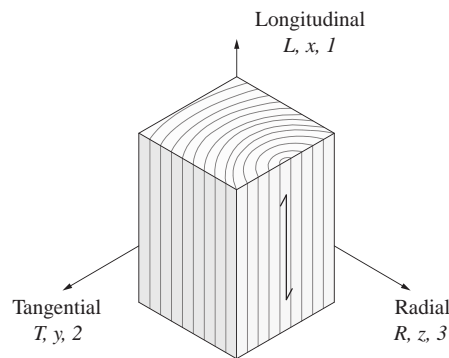


Figure C.7 – Definition of the material directions 1, 2, and 3.

### C.4.2 Continuum damage model

Principles of continuum damage mechanics can be explained according to the stiffness matrix or its inverse, namely the compliance matrix. Before damage occurs and for the remaining undamaged material, the material behavior is described based on Hooke's law with strains  $\epsilon$  expressed as a function of the effective stresses  $\sigma^{\text{ef}}$ , which are the stresses acting on the

<sup>1</sup>This part was performed by A. C. Nguyen.

## Appendix C. Appendix of Chapter 5

non-damaged material, and the elastic compliance matrix  $\mathbf{C}^{\text{el}}$ :

$$\boldsymbol{\varepsilon} = \mathbf{C}^{\text{el}} \boldsymbol{\sigma}^{\text{ef}} \quad (\text{C.4})$$

The relationship defined in Equation C.4 can be expressed as follows:

$$\begin{bmatrix} \varepsilon_{11} \\ \varepsilon_{22} \\ \varepsilon_{33} \\ 2\varepsilon_{12} \\ 2\varepsilon_{13} \\ 2\varepsilon_{23} \end{bmatrix} = \begin{bmatrix} \frac{1}{E_{11}} & \frac{-\nu_{12}}{E_{22}} & \frac{-\nu_{31}}{E_{33}} & 0 & 0 & 0 \\ \frac{-\nu_{12}}{E_{11}} & \frac{1}{E_{22}} & \frac{-\nu_{32}}{E_{33}} & 0 & 0 & 0 \\ \frac{-\nu_{13}}{E_{11}} & \frac{-\nu_{23}}{E_{22}} & \frac{1}{E_{33}} & 0 & 0 & 0 \\ 0 & 0 & 0 & \frac{1}{G_{12}} & 0 & 0 \\ 0 & 0 & 0 & 0 & \frac{1}{G_{13}} & 0 \\ 0 & 0 & 0 & 0 & 0 & \frac{1}{G_{23}} \end{bmatrix} \begin{bmatrix} \sigma_{11} \\ \sigma_{22} \\ \sigma_{33} \\ \sigma_{12} \\ \sigma_{13} \\ \sigma_{23} \end{bmatrix} \quad (\text{C.5})$$

In FEA software packages, the inverse on the compliance matrix has to be implemented, namely the elastic stiffness matrix  $\mathbf{D}^{\text{el}}$ , which is defined as:

$$\mathbf{D}^{\text{el}} = \begin{bmatrix} (1 - \nu_{23}\nu_{32})\Delta E_{11} & (\nu_{21} + \nu_{31}\nu_{23})\Delta E_{11} & (\nu_{31} + \nu_{21}\nu_{32})\Delta E_{11} & 0 & 0 & 0 \\ (\nu_{12} + \nu_{13}\nu_{32})\Delta E_{22} & (1 - \nu_{13}\nu_{31})\Delta E_{22} & (\nu_{32} + \nu_{31}\nu_{12})\Delta E_{22} & 0 & 0 & 0 \\ (\nu_{13} + \nu_{12}\nu_{23})\Delta E_{33} & (\nu_{23} + \nu_{21}\nu_{13})\Delta E_{33} & (1 - \nu_{12}\nu_{21})\Delta E_{33} & 0 & 0 & 0 \\ 0 & 0 & 0 & G_{12} & 0 & 0 \\ 0 & 0 & 0 & 0 & G_{13} & 0 \\ 0 & 0 & 0 & 0 & 0 & G_{23} \end{bmatrix} \quad (\text{C.6})$$

with

$$\Delta = \frac{1}{(1 - \nu_{12}\nu_{21} - \nu_{13}\nu_{31} - \nu_{23}\nu_{32} - 2\nu_{12}\nu_{23}\nu_{31})} \quad (\text{C.7})$$

As orthotropic material properties were considered, both stiffness and compliance matrices are symmetric and the following equation can therefore be defined:

$$\frac{\nu_{ij}}{E_{ii}} = \frac{\nu_{ji}}{E_{jj}} \quad \text{for } i = 1, 2, 3 \text{ and } i \neq j \quad (\text{C.8})$$

The constitutive orthotropic damage model involves nine independent damage parameters, namely  $d_{c,11}$ ,  $d_{t,11}$ ,  $d_{c,22}$ ,  $d_{t,22}$ ,  $d_{c,33}$ ,  $d_{t,33}$ ,  $d_{12}$ ,  $d_{13}$ , and  $d_{23}$ , with the indices t and c corresponding to damage occurring in tension and compression, respectively. Since compression and tension are triggered by the same normal stress components  $\sigma_{ii}$ , damage variables in tension

and compression can be combined using the Macaulay operator defined by Equation C.9:

$$\langle a \rangle = \frac{a + |a|}{2} \quad (\text{C.9})$$

such that the damage parameters  $d_{11}$ ,  $d_{22}$  and  $d_{33}$  can be defined as follows:

$$d_{ii} = d_{t,ii} \frac{\langle \sigma_{ii} \rangle}{|\sigma_{ii}|} + d_{c,ii} \frac{\langle -\sigma_{ii} \rangle}{|\sigma_{ii}|} \quad \text{for } i = 1, 2, 3 \quad (\text{C.10})$$

The number of damage parameters introduced in the damage compliance matrix  $\mathbf{C}^{\text{dam}}$  is then reduced to six, namely  $d_{11}$ ,  $d_{22}$ ,  $d_{33}$ ,  $d_{12}$ ,  $d_{13}$ , and  $d_{23}$ . When the material is damaged, strains  $\boldsymbol{\varepsilon}$  are expressed as function of the nominal stresses  $\boldsymbol{\sigma}$  and the damaged compliance matrix  $\mathbf{C}^{\text{dam}}$ :

$$\boldsymbol{\varepsilon} = \mathbf{C}^{\text{dam}} \boldsymbol{\sigma} \quad (\text{C.11})$$

with

$$\mathbf{C}^{\text{dam}} = \begin{bmatrix} \frac{1}{(1-d_{11})E_{11}} & \frac{-\nu_{21}}{E_{22}} & \frac{-\nu_{31}}{E_{33}} & 0 & 0 & 0 \\ \frac{-\nu_{12}}{E_{11}} & \frac{1}{(1-d_{22})E_{22}} & \frac{-\nu_{32}}{E_{33}} & 0 & 0 & 0 \\ \frac{-\nu_{13}}{E_{11}} & \frac{-\nu_{23}}{E_{22}} & \frac{1}{(1-d_{33})E_{33}} & 0 & 0 & 0 \\ 0 & 0 & 0 & \frac{1}{(1-d_{12})G_{12}} & 0 & 0 \\ 0 & 0 & 0 & 0 & \frac{1}{(1-d_{13})G_{13}} & 0 \\ 0 & 0 & 0 & 0 & 0 & \frac{1}{(1-d_{23})G_{23}} \end{bmatrix} \quad (\text{C.12})$$

When the material is undamaged, damage parameters are equal to zero. The parameters start increasing when damage is initiated such that components of the compliance matrix  $C_{ijkl}$  are reduced. When complete damage occurs, damage parameters are equal to 1. However, to avoid numerical instabilities, a maximum value of 0.999995 was implemented in the numerical model.

### C.4.3 Failure modes

Sandhaas [131] defined eight failure criteria to determine when material damage occurs, with eight corresponding failure modes  $F_M$  expressed according to stresses  $\sigma_{ij}$  and strengths  $f_{ij}$ . Among them, three are ductile (in compression) and five are brittle (in tension and shear). For all failure modes, damage is initiated when  $F_M > 1$ .

### Ductile failure modes

- Failure criterion I -  $F_{c,1}$ :

For  $\sigma_{11} < 0$ , corresponding to failure in compression parallel-to-grain and associated with the damage variable  $d_{c,11}$ ,

$$F_{c,1} = \frac{-\sigma_{11}}{f_{c,11}} \leq 1 \quad (C.13)$$

- Failure mode II -  $F_{c,2}$ :

For  $\sigma_{22} < 0$ , corresponding to failure in compression perpendicular-to-grain in the tangential direction and associated with the damage variable  $d_{c,22}$ ,

$$F_{c,2} = \frac{-\sigma_{22}}{f_{c,22}} \leq 1 \quad (C.14)$$

- Failure mode III -  $F_{c,33}$ :

For  $\sigma_{33} < 0$ , corresponding to failure in compression perpendicular-to-grain in the radial direction and associated with the damage variable  $d_{c,33}$ ,

$$F_{c,3} = \frac{-\sigma_{33}}{f_{c,33}} \leq 1 \quad (C.15)$$

### Brittle failure modes

- Failure mode IV -  $F_{t,1}$ :

For  $\sigma_{11} \geq 0$ , corresponding to failure in tension parallel-to-grain and associated with damage variable  $d_{t,11}$ ,

$$F_{t,1} = \frac{\sigma_{11}}{f_{t,11}} \leq 1 \quad (C.16)$$

- Failure mode V -  $F_{t,2}$ :

For  $\sigma_{22} \geq 0$ , corresponding to failure in tension perpendicular-to-grain in the tangential direction and associated with damage variables  $d_{t,22}$ ,  $d_{12}$ ,  $d_{23}$ ,

$$F_{t,2} = \frac{(\sigma_{22})^2}{(f_{t,22})^2} + \frac{(\sigma_{12})^2}{(f_{12})^2} + \frac{(\sigma_{23})^2}{(f_{23})^2} \leq 1 \quad (C.17)$$

- Failure mode VI -  $F_{t,33}$ :

For  $\sigma_{33} \geq 0$ , corresponding to failure in tension perpendicular-to-grain in the radial direction and associated with damage variables  $d_{t,33}$ ,  $d_{13}$ ,  $d_{23}$ ,

$$F_{t,3} = \frac{(\sigma_{33})^2}{(f_{t,33})^2} + \frac{(\sigma_{13})^2}{(f_{13})^2} + \frac{(\sigma_{23})^2}{(f_{23})^2} \leq 1 \quad (C.18)$$

- Failure mode VII:  $F_{v,2}$

Shear failure, tangential if  $\sigma_{22} < 0$  (brittle), associated with damage variables  $d_{12}$  and  $d_{23}$ ,

$$F_{v,2} = \frac{(\sigma_{12})^2}{(f_{12})^2} + \frac{(\sigma_{23})^2}{(f_{23})^2} \leq 1 \quad (\text{C.19})$$

- Failure mode VIII:  $F_{v,3}$

Shear failure, radial if  $\sigma_{33} < 0$  (brittle), associated with damage variables  $d_{13}$  and  $d_{23}$ ,

$$F_{v,3} = \frac{(\sigma_{13})^2}{(f_{13})^2} + \frac{(\sigma_{23})^2}{(f_{23})^2} \leq 1 \quad (\text{C.20})$$

#### C.4.4 Damage evolution

Each of the eight failure modes  $F_M$  was associated with one or several damage parameters. Since different failure modes can trigger shear damage variables, the latter need to be superposed according to Equations C.21, C.22, and C.23 for longitudinal and rolling shear:

$$d_{12} = 1 - (1 - d_{12,V}) \cdot (1 - d_{12,VII}) \quad (\text{C.21})$$

$$d_{13} = 1 - (1 - d_{13,VI}) \cdot (1 - d_{13,VIII}) \quad (\text{C.22})$$

$$d_{23} = 1 - (1 - d_{23,V}) \cdot (1 - d_{23,VI}) \cdot (1 - d_{23,VII}) \cdot (1 - d_{23,VIII}) \quad (\text{C.23})$$

Damage parameters and failure criteria were linked through a history parameter  $\kappa_M$ , tracking the loading history and defined as follows:

$$\kappa_M = \max\{F_M, 1\} \quad (\text{C.24})$$

Two linear damage evolution laws, functions of the history parameter  $\kappa_M$ , were used by Sandhaas [131]: an elastic perfectly plastic behavior was considered for ductile failure modes (see Figure C.8a) and a fracture-energy-based tension softening was defined for brittle failure modes (see Figure C.8b). The softening behavior was characterized according to the fracture energy, which is the energy required to form a crack and is used in fracture mechanics. Damage parameters, defined according to these laws, were expressed as Equations C.25 and C.26 for ductile and brittle failure modes, respectively:

$$d_M = 1 - \frac{1}{\kappa_M} \quad (\text{C.25})$$

$$d_M = 1 - \frac{f_M^2 - \frac{2g_{f,ij}E_{ij}}{\kappa_M}}{f_M^2 - 2g_{f,ij}E_{ij}} \quad (\text{C.26})$$

where  $g_f$  is the characteristic fracture energy used to reduce mesh dependency and defined as the ratio between the fracture energy  $G_f$  and the characteristic element length  $h$ , referred to

as CELENT in Abaqus<sup>TM</sup>:

$$g_f = \frac{G_f}{h} \quad (C.27)$$

In this study, a square root was added to the history parameter associated with brittle failure modes V to VIII to prevent an overly slow increase of the damage variable, since the corresponding failure functions were defined by the sum of the squares of stresses (see Equations C.17 to C.20). This modification has already been performed by Roche et al. [129]; however, in their study, the modification was applied to all damage parameters associated with brittle failure modes. The damage parameters associated with failure modes V to VIII exclusively were thus:

$$d_M = 1 - \frac{f_M^2 - \frac{2g_{f,ij}E_{ij}}{\sqrt{\kappa_M}}}{f_M^2 - 2g_{f,ij}E_{ij}} \quad (C.28)$$

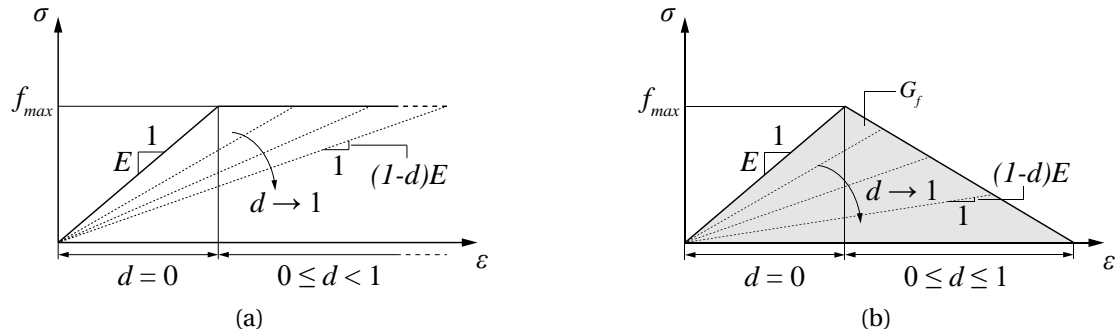


Figure C.8 – Damage evolution laws: (a) Elastic perfectly plastic for damage parameters associated with ductile failure modes (b) Fracture-energy-based tension softening for damage parameters associated with brittle failure modes.

#### C.4.5 Subroutine algorithm

As for the model developed by Roche et al. [129] for the semi-rigid moment-resisting behavior of MTSJ, the continuum damage model was implemented using a user defined field USDFLD subroutine. Its algorithm for the continuum damage model is summarized in Fig. C.9.

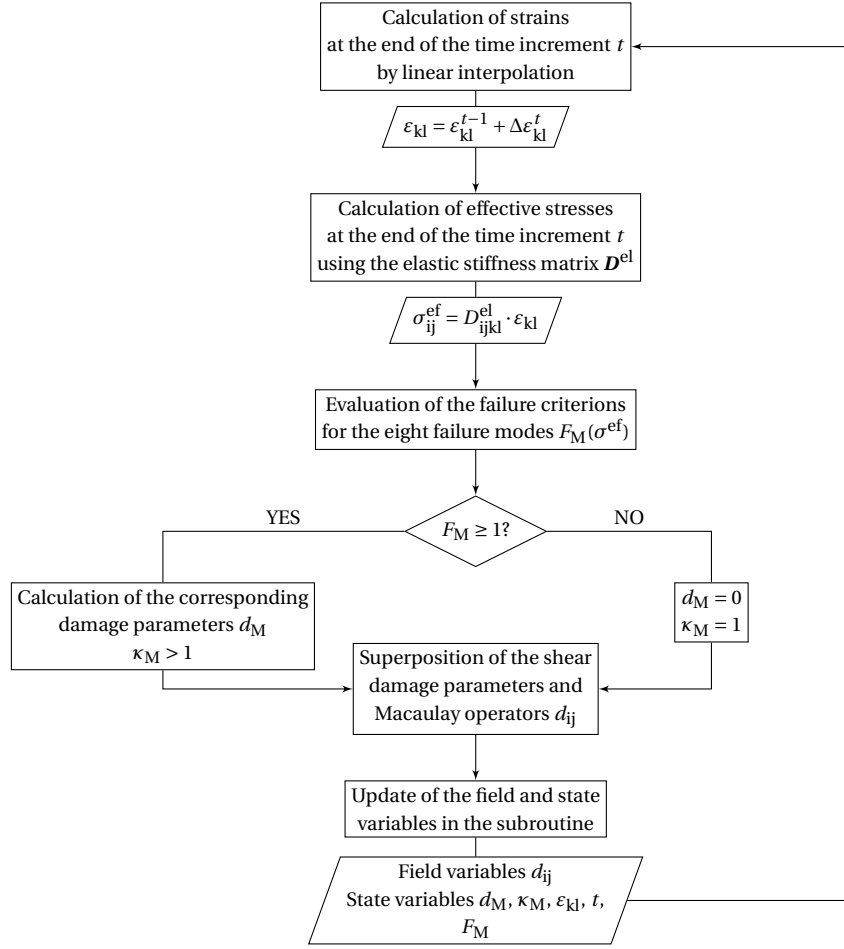


Figure C.9 – Flow chart illustrating the algorithm of the USDFLD subroutine for the continuum damage model.

Orthotropic material properties  $E_{ii}$ ,  $G_{ij}$  and  $\nu_{ij}$  were defined as field-dependent with the six damage parameters  $d_{ij}$  corresponding to the six field variables  $f_1$ ,  $f_2$ ,  $f_3$ ,  $f_4$ ,  $f_5$ , and  $f_6$ , such that:

$$E_{ii,t} = E_{ii,t-1} \cdot (1 - f_i) \quad \text{with} \quad f_i = d_{ii} \quad \text{for} \quad i = 1, 2, 3 \quad (\text{C.29})$$

$$G_{12,t} = G_{12,t-1} \cdot (1 - f_4) \quad \text{with} \quad f_4 = d_{12} \quad (\text{C.30})$$

$$G_{13,t} = G_{13,t-1} \cdot (1 - f_5) \quad \text{with} \quad f_5 = d_{13} \quad (\text{C.31})$$

$$G_{23,t} = G_{23,t-1} \cdot (1 - f_6) \quad \text{with} \quad f_6 = d_{23} \quad (\text{C.32})$$

$$\nu_{12,t} = \nu_{12,t-1} \cdot (1 - f_1) \quad \text{with} \quad f_1 = d_{11} \quad (\text{C.33})$$

$$\nu_{13,t} = \nu_{13,t-1} \cdot (1 - f_1) \quad \text{with} \quad f_1 = d_{11} \quad (\text{C.34})$$

$$\nu_{23,t} = \nu_{23,t-1} \cdot (1 - f_2) \quad \text{with} \quad f_3 = d_{33} \quad (\text{C.35})$$

Non-linear geometric analysis was performed with initial and maximum time increments

of 0.001 and 0.1, respectively. The load was applied with displacement-control, imposing a displacement of 1.5 times the maximum slip  $v_{i,\max}$  for all numerical simulations.

### C.4.6 Contact modeling

Contacts between the different parts of the specimen were modeled by defining surface-to-surface interactions in Abaqus<sup>TM</sup>. A Coulomb friction model was considered for the tangential behavior, while the normal behavior was implemented with a "hard" contact relationship, which implies that no transfer of tensile forces occurs between the two surfaces and the penetration of the slave surface into the master surface is minimized. Friction coefficient values of  $\mu_{\text{edge}} = 0.26$  edgewise and  $\mu_{\text{flat}} = 0.40$  flatwise, provided by the manufacturer of Kerto<sup>®</sup> Q panels [163], were considered for all materials: it was found that variations of the friction coefficient have a minor influence. In fact, variations of  $\mu_{\text{edge}}$  between values of 0.1 and 0.4 were found to have an influence below 2% and 1% on the displacement and stresses, respectively. Contacts implemented in the model are illustrated in Figure C.10 for the specimen T2-50. Contacts ① between the faces of the tenon and the internal faces of the mortise in the  $YZ$  plane, ② between the long edge of the tenon part and the closest larger face of the mortise part, and ③ between the bottom face of the tenon in the  $XY$  plane and the corresponding internal face of the mortise (see Figure C.10a) were modeled considering a friction coefficient  $\mu_{\text{edge}} = 0.26$  and with separation allowed after contact. A surface-to-surface interaction with a friction coefficient of  $\mu_{\text{edge}} = 0.26$  with no separation allowed after contact was implemented ④ between the loaded surface of the tenon part in the plane  $XY$  and the corresponding internal face of the mortise in contact (see Figure C.10b). For two-layered specimens, a surface-to-surface interaction was also defined considering a friction coefficient  $\mu_{\text{flat}} = 0.40$  and allowing separation after contact between the surfaces of the mortise panels and the tenon panels in contact: ⑤ and ⑥, respectively, in Figure C.10c.

Contacts implemented in the model are illustrated in Figure C.10 for the specimen T2-50. Contacts ① between the faces of the tenon and the internal faces of the mortise in the  $YZ$  plane, ② between the long edge of the tenon part and the closest larger face of the mortise part, and ③ between the bottom face of the tenon in the  $XY$  plane and the corresponding internal face of the mortise (see Figure C.10a) were modeled considering a friction coefficient  $\mu_{\text{edge}} = 0.26$  and with separation allowed after contact. A surface-to-surface interaction with a friction coefficient of  $\mu_{\text{edge}} = 0.26$  with no separation allowed after contact was implemented ④ between the loaded surface of the tenon part in the plane  $XY$  and the corresponding internal face of the mortise in contact (see Figure C.10b). For two-layered specimens, a surface-to-surface interaction was also defined considering a friction coefficient  $\mu_{\text{flat}} = 0.40$  and allowing separation after contact between the surfaces of the mortise panels and the tenon panels in contact: ⑤ and ⑥, respectively, in Figure C.10c.



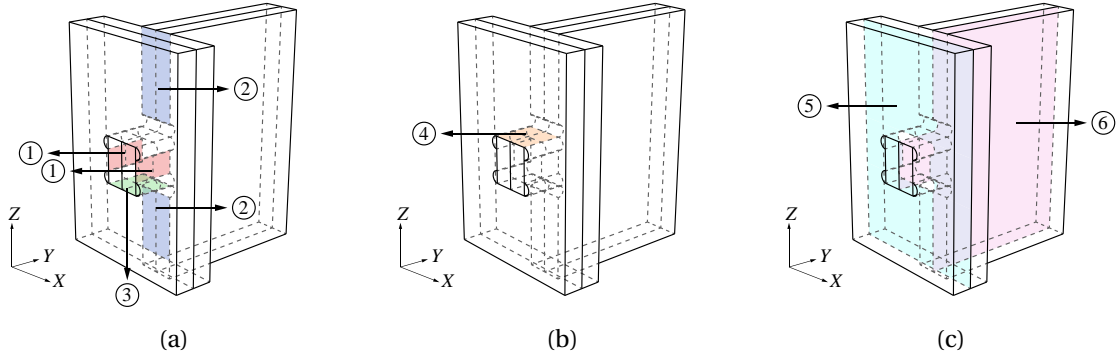


Figure C.10 – Contact modeling using surface-to-surface interactions illustrated for specimen T2-50: (a) Friction coefficient  $\mu_{\text{edge}} = 0.26$  with separation allowed after contact for the surfaces of the tenon and mortise parts ①, ②, and ③ (b) Friction coefficient  $\mu_{\text{edge}} = 0.26$  with no separation allowed after contact between the loaded face of the tenon part and the corresponding face of the mortise part ④ (c) For two-layered specimens, friction coefficient  $\mu_{\text{flat}} = 0.40$  with separation allowed between the panels of the mortise part ⑤ and the tenon part ⑥.

#### C.4.7 Mesh

Linear hexahedral elements with reduced integration C3D8R were used. A mesh convergence study was conducted on the T3-50 specimen with mesh sizes ranging from 10 to 2 mm in steps of 1 mm, considering the middle of the linear range between 10 and 40% of  $F_{\text{max}}$  to be 25% of  $F_{\text{max}}$ . Results of the mesh convergence study are presented in Figure C.11, in which the total CPU time indicated corresponds to the time obtained using a Lenovo Intel® Core™ i7-4800MQ CPU @ 2.7GHz with 16 GB of RAM 1600 MHz (Lenovo Group Limited, Beijing, China). Vertical displacement was shown to converge (see Figure C.11a), whereas increasing maximum shear stress values were obtained for decreasing mesh element sizes (see Figure C.11b).

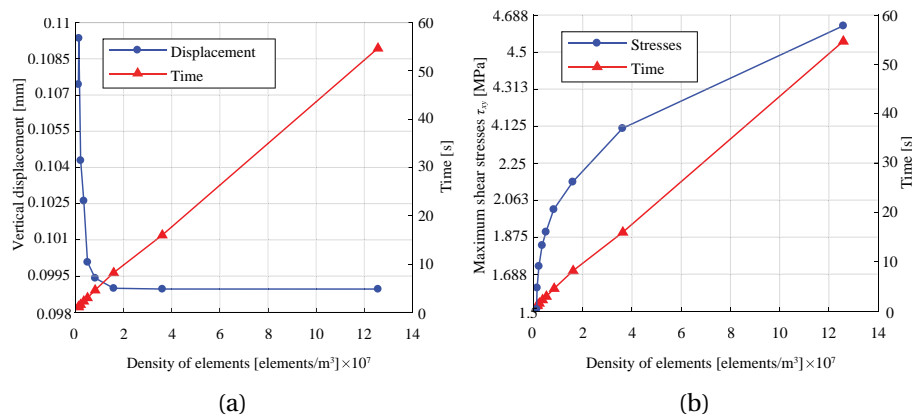


Figure C.11 – Mesh convergence study performed for specimen T3-50 under a load of 25%  $F_{\text{max}}$ : (a) Vertical displacement converge (b) Maximum shear stresses do not converge.

The non-convergence of stresses is explained by the presence of singularity points with theoretically infinite stresses at the notches of the connections. Indeed, both normal and shear stresses present increasingly high values at the position of the notches when the mesh element size is reduced. This can be observed in Figure C.12, which represents the stresses over the height of the sample along a line passing through the notches (dotted line). These areas were thus avoided for the interpretation of numerical results, and the smallest mesh was thus chosen in adopting a refined-mesh strategy to reduce the computational time. It was found that a refined-mesh element size of 2 mm in the vicinity of the tenon and a coarse-mesh element size of 16 mm away from this region of interest were leading to a difference of vertical displacement of 1% while reducing total CPU time by 85%. The resulting mesh is illustrated in Figure C.13 for the T3-50 specimen.

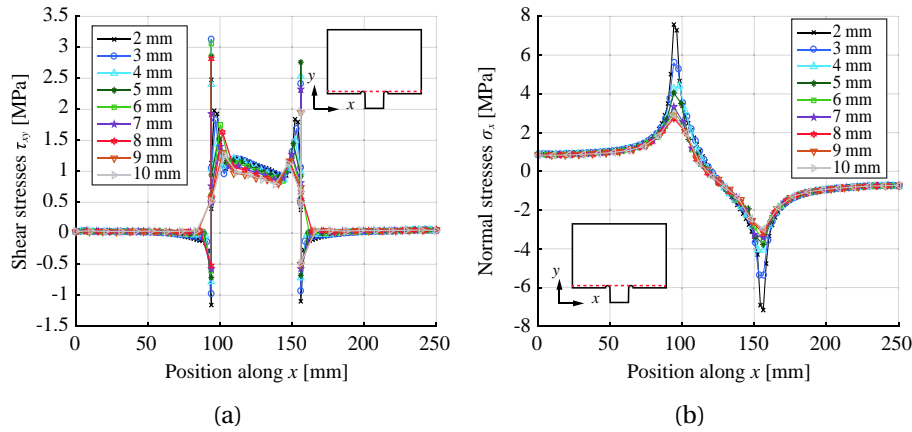


Figure C.12 – Stresses along a path passing through the notches (dotted line), which represent singularity points with theoretically infinite stresses, for mesh sizes varying from 10 to 2 mm in steps of 1 mm: (a) Shear stresses (b) Normal stresses.

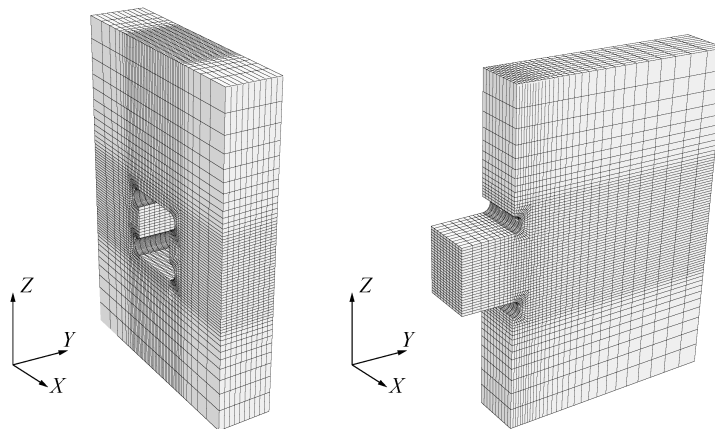


Figure C.13 – Mesh for the sample T3-50 - Refined-mesh element size of 2 mm in the vicinity of the tenon and coarse-mesh element size of 16 mm away from this region of interest.

### C.4.8 Material properties

Mean values of material properties were implemented in the model, such that a direct comparison between experimental tests and numerical simulations could be made. Material properties with parameters  $X$  were considered as following a normal distribution characterized by a mean  $\mu$  and a standard deviation  $\sigma$  (see Figure C.14). Based on the coefficient of variation  $c_v$ , defined by Equation C.36, and considering the 5 % characteristic fractile factor  $k_\infty = 1.64$  for a infinite number of experiments, the mean values were defined from the characteristic values  $X_{k,\text{inf}}$  using Equation C.37. Similarly, the upper bounds  $X_{k,\text{sup}}$  were derived from the characteristic values  $X_{k,\text{inf}}$  using Equation C.38.

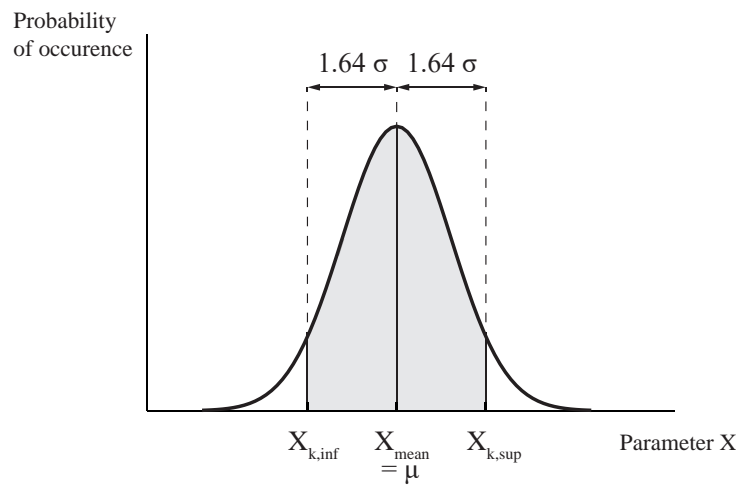


Figure C.14 – Normal distribution with mean  $\mu$  and a standard deviation  $\sigma$  for material property parameters  $X$ .

$$c_v = \frac{\sigma}{\mu} = \frac{\sigma}{X_{\text{mean}}} \quad (\text{C.36})$$

$$X_{\text{mean}} = \frac{X_{k,\text{inf}}}{1 - 1.64c_v} \quad (\text{C.37})$$

$$X_{k,\text{sup}} = \frac{1 + 1.64c_v}{1 - 1.64c_v} \cdot X_{k,\text{inf}} \quad (\text{C.38})$$

The coefficient of variation was determined to be approximately equal to  $c_v = 0.1$  for spruce LVL by comparing characteristic and mean values of elastic modulus from the Kerto® Q panel certificate [163]. A coefficient of variation  $c_v = 0.1$  was therefore considered for LVL and MSW materials. For OSB, the characteristic 5 % fractile factor defined in the standard EN 12369 as equal to 0.85 times the mean value was considered [29].

In this model, the material was represented by a single layer, in contrast to the multilayer approach used by Roche et al. [129] for the different veneer layers of spruce LVL. The goal of this model was to predict the behavior of wood-wood connections with a design approach, using

the values from the manufacturer instead of calibrating the numerical model with material parameters. Material properties were therefore retrieved directly from the panels certificates for LVL and MSW [9, 26, 163], while material properties from the standard EN 12369 [29] were considered for OSB 3.

### Elastic properties

Mean values of elastic material properties for each material studied are presented in Table C.3. Poisson's ratio values for OSB, beech LVL, and spruce MSW, not provided by the manufacturers, were taken from the literature for OSB [49], beech [60], and spruce [44].

Table C.3 – Elastic properties (mean values).

Property	Symbols	Material					Units
		(1), (1')	(2)	(3)	(4)	(5)	
Density	$\rho_k$	550	480	480	730	480	kg/m <sup>3</sup>
Elastic modulus // to grain	$E_{0,\text{mean}}, E_{11}$	3800	10 000	10 500	13 200	5800	MPa
Elastic modulus $\perp$ to grain, edgewise	$E_{90,\text{edge,mean}}, E_{22}$	3000	2400	2400	2200	5500	MPa
Elastic modulus $\perp$ to grain, flatwise	$E_{90,\text{flat,mean}}, E_{33}$	1980	130	130	2200	1600	MPa
Shear modulus edgewise	$G_{0,\text{edge,mean}}, G_{12}$	1080	600	600	820	600	MPa
Shear modulus flatwise, // to grain	$G_{0,\text{flat,mean}}, G_{13}$	50	60	120	430	60	MPa
Shear modulus flatwise, $\perp$ to grain	$G_{90,\text{flat,mean}}, G_{23}$	50	22	22	430	60	MPa
Poisson's ratio 12	$\nu_{12}$	0.25	0.09	0.09	0.365	0.467	-
Poisson's ratio 13	$\nu_{13}$	0.25	0.85	0.85	0.464	0.372	-
Poisson's ratio 23	$\nu_{23}$	0.25	0.68	0.68	0.726	0.245	-

The influence of Poisson's ratio values  $\nu_{12}$ ,  $\nu_{13}$ , and  $\nu_{23}$  was investigated for the T3-50 specimen by comparing simulations using different sets of Poisson's ratios values found in the literature on spruce and spruce LVL with the results obtained with values provided by the supplier for Kerto<sup>®</sup> Q panels [163]. The values considered, their references, most of which were listed in Sandhaas' thesis [131], and their influence on the stiffness of the connection are presented in Table C.4. They were found to have no significant influence on the results with average variations on the stiffness of  $+0.37\% \pm 0.51\%$ .

Table C.4 – Poisson's ratio values from the literature on spruce and spruce LVL.

Reference	$\nu_{12}$	$\nu_{13}$	$\nu_{23}$	$\Delta k$
	[-]	[-]	[-]	[%]
Kerto <sup>®</sup> Q [163]	0.09	0.85	0.68	-
Kerto <sup>®</sup> S [163], as used by Roche et al. [129]	0.61	0.6	0.5	+0.33
Kollmann and Côté [76] ( <i>Picea abies</i> )	0.53	0.43	0.24	+0.24
Neuhaus [98] ( <i>Picea abies</i> )	0.554	0.41	0.311	+0.05
Wood Handbook [44] ( <i>Picea sitchensis</i> )	0.467	0.372	0.245	+1.25
Blaß and Bejtka [8]	0.511	0.511	0.203	-0.03

### Strength properties

Characteristic values of strength properties are presented in Table C.5 for each material studied. Since the value for tensile strength perpendicular-to-grain flatwise, corresponding to the interlaminar resistance, was not provided in most panel certificates, transversal isotropy was considered for this property such that  $f_{t,33} = f_{t,22}$ . This assumption is frequently made for timber modeling considering only the directions parallel- and perpendicular-to-grain since differences between values in both radial and tangential directions are small compared to the longitudinal direction [161, 108].

Table C.5 – Mechanical properties (characteristic values) in MPa [163].

Property	Symbols	Material					
		(1)	(1')	(2)	(3)	(4)	(5)
Tensile strength // to grain	$f_{t,0,k}, f_{t,11}$	9.4	9	19	26	51	8.4
Compressive strength // to grain	$f_{c,0,k}, f_{c,11}$	15.4	14.8	19	26	53.3	11.5
Tensile strength $\perp$ to grain	$f_{t,90,edge,k}, f_{t,22}$	7	6.8	6	6	8	8
Compressive strength $\perp$ to grain	$f_{c,90,edge,k}, f_{c,22}$	12.7	12.4	9	9	19	11.1
Tensile strength $\perp$ to grain	$f_{t,90,flat,k}, f_{t,33}$	7	6.8	-	-	-	-
Compressive strength $\perp$ to grain	$f_{c,90,flat,k}, f_{c,33}$	10	10	2.2	2.2	13	11.1
Longitudinal shear strength	$f_{v,0,edge,k}, f_{12}$	6.8	6.8	4.5	4.5	7.8	2.7
Longitudinal shear strength	$f_{v,0,flat,k}, f_{13}$	1	1	1.3	1.3	3.8	2.7
Rolling shear strength	$f_{v,90,flat,k}, f_{23}$	1	1	0.6	0.6	3.8	2.7

Fracture energy values implemented in the model were retrieved from Sandhaas [131] and are presented in Table C.6. These values influence the softening behavior, as illustrated in Figure C.8b.

Table C.6 – Fracture energy values in N/mm for spruce and beech [131].

Property	Mnemo	Spruce	Beech
Fracture energy tension // to grain	$G_{f,11}$	6.0	10.0
Fracture energy tension $\perp$ to grain	$G_{f,22}$	0.5	0.71
Fracture energy tension $\perp$ to grain	$G_{f,33}$	0.5	0.71
Fracture energy longitudinal shear	$G_{f,12}$	1.2	1.2
Fracture energy longitudinal shear	$G_{f,13}$	1.2	1.2
Fracture energy rolling shear	$G_{f,23}$	0.6	0.6

The influence of mechanical properties were assessed similarly to the study performed by Sandhaas [131] by modifying the strength and fracture energy values perpendicular-to-grain to the maximum values, parallel-to-grain. Values in compression and tension perpendicular-to-grain for strength and fracture energy were found to have a minor influence on the results with the same behavior and maximum load variations of under 1%. The properties in longitudinal shear lead to an increase of 39.38%.



# Bibliography

- [1] A. Adel, A. Thoma, M. Helmreich, F. Gramazio, and M. Kohler. Design of robotically fabricated timber frame structures. In P. Anzalone, M. Del Signore, and A. J. Wit, editors, *ACADIA 2018 Recalibration: On Imprecision and Infidelity. Proceedings of the 38th Annual Conference of the Association for Computer Aided Design in Architecture*, pages 394 – 403, 2018. Available online: [http://papers.cumincad.org/data/works/att/acadia18\\_394.pdf](http://papers.cumincad.org/data/works/att/acadia18_394.pdf) (accessed on January 2020).
- [2] Y. Al-Qaryouti, K. Baber, and J. M. Gattas. Computational design and digital fabrication of folded timber sandwich structures. *Automation in Construction*, 102:27 – 44, 2019. doi:10.1016/j.autcon.2019.01.008.
- [3] D. Albright, V. Blouin, D. Harding, U. Heine, N. Huette, and D. Pastre. Sim[ply]: Sustainable construction with prefabricated plywood componentry. *Procedia Environmental Sciences*, 38:760 – 764, 2017. doi:10.1016/j.proenv.2017.03.159.
- [4] Y. Alqaryouti, D. Fernando, and J. Gattas. Structural behavior of digitally fabricated thin-walled timber columns. *International Journal of Structural Stability and Dynamics*, 19(10):1950126, 2019. doi:10.1142/S0219455419501268.
- [5] L. D. Armstrong and R. S. T. Kingston. Effect of Moisture Changes on Creep in Wood. *Nature*, 185(4716):862–863, Mar. 1960. doi:10.1038/185862c0.
- [6] C. Bedon and M. Fragiaco. Three-dimensional modelling of notched connections for timber-concrete composite beams. *Structural Engineering International: Journal of the International Association for Bridge and Structural Engineering (IABSE)*, 27(2):184–196, 2017. doi:10.2749/101686617X14881932435295.
- [7] F. Bianconi and M. Filippucci. *Digital Wood Design: Innovative Techniques of Representation in Architectural Design.*, volume 24 of *Lecture Notes in Civil Engineering*. Springer International Publishing, 2019. doi:10.1007/978-3-030-03676-8.
- [8] H. J. Blaß and I. Bejtka. Numerische Berechnung der Tragfähigkeit und der Steifigkeit von querzugverstärkten Verbindungen mit stiftförmigen Verbindungsmitteln. *Karlsruher berichte zum ingenieurholzbau band 10*, Universitätsverlag Karlsruhe, 2008. Available online: <https://publikationen.bibliothek.kit.edu/1000008463/388493> (accessed on January 2020).

## Bibliography

---

- [9] H. J. Blaß and J. Streib. Baubuche beech laminated veneer lumber - design assistance for drafting and calculation in accordance with eurocode 5, 2017. Available online: <http://pollmeier.com/en/downloads/design-manual.html> (accessed on January 2020).
- [10] H. J. Blaß and C. Sandhaas. *Timber Engineering - Principles for Design*. KIT Scientific Publishing, Karlsruhe, 2017. doi:10.5445/KSP/1000069616.
- [11] G. Boothroyd. Product design for manufacture and assembly. *Computer-Aided Design*, 26(7):505 – 520, 1994. doi:10.1016/0010-4485(94)90082-5.
- [12] P. Börjesson and L. Gustavsson. Greenhouse gas balances in building construction: wood versus concrete from life-cycle and forest land-use perspectives. *Energy Policy*, 28(9):575 – 588, 2000. doi:10.1016/S0301-4215(00)00049-5.
- [13] J. M. Branco and T. Descamps. Analysis and strengthening of carpentry joints. *Construction and Building Materials*, 97:34 – 47, 2015. doi:10.1016/j.conbuildmat.2015.05.089. Special Issue: Reinforcement of Timber Structures.
- [14] J. M. Branco, M. Piazza, and P. J. Cruz. Experimental evaluation of different strengthening techniques of traditional timber connections. *Engineering Structures*, 33(8):2259 – 2270, 2011. doi:10.1016/j.engstruct.2011.04.002.
- [15] BS EN 1995-1-1:2004. UK National annex to Eurocode 5: design of timber structures - Part 1-1: General - Common rules and rules for buildings. British Standards Institution.
- [16] A. Bukauskas, P. Mayencourt, P. Shepherd, B. Sharma, C. Mueller, P. Walker, and J. Bregulla. Whole timber construction: A state of the art review. *Construction and Building Materials*, 213:748 – 769, 2019. doi:10.1016/j.conbuildmat.2019.03.043.
- [17] H. Buri and Y. Weinand. Origami - folded plate structures, architecture. In *Proceedings of the World Conference of Timber Engineering WCTE*, 2008. Available online: <http://infoscience.epfl.ch/record/118687> (accessed on January 2020).
- [18] H. U. Buri. *Origami - Folded Plate Structures*. PhD thesis, ENAC, Lausanne, 2010. doi:10.5075/epfl-thesis-4714.
- [19] T. Claus, T. Riehle, W. Seim, and T. Gotz. Interlocking shear wall connections. In *World Conference on Timber Engineering*, Seoul, Republic of Korea, 2018. Available online: [https://www.uni-kassel.de/fb14bau/uploads/media/CLAUS\\_\\_RIEHLE\\_\\_SEIM\\_\\_GÖTZ\\_\\_INTERLOCKING\\_SHEAR\\_WALL\\_CONNECTIONS.pdf](https://www.uni-kassel.de/fb14bau/uploads/media/CLAUS__RIEHLE__SEIM__GÖTZ__INTERLOCKING_SHEAR_WALL_CONNECTIONS.pdf) (accessed on January 2020).
- [20] T. Claus, W. Seim, and B. Schröder. Multiple Tenons – Experimental Study on Load-Bearing Capacity and Deformation Characteristics. In *World Conference on Timber Engineering*, pages 701–707, Vienna, Austria, 2016. Available online: [https://www.researchgate.net/publication/324220990\\_MULTIPLE\\_TENONS-EXPERIMENTAL\\_STUDY\\_ON\\_LOAD-BEARING\\_CAPACITY\\_AND\\_DEFORMATION\\_CHARACTERISTICS](https://www.researchgate.net/publication/324220990_MULTIPLE_TENONS-EXPERIMENTAL_STUDY_ON_LOAD-BEARING_CAPACITY_AND_DEFORMATION_CHARACTERISTICS) (accessed on January 2020).



- [21] Dassault Systèmes Simulia. *Abaqus 6.12 Online Documentation*, 2012. Available online: <http://abaqus.software.polimi.it/v6.12/index.html> (accessed on February 2020).
- [22] M. Dedijer, S. Roche, and Y. Weinand. Shear resistance and failure modes of edgewise multiple tab-and-slot joint (MTSJ) connection with dovetail design for thin LVL spruce plywood Kerto-Q panels. In J. Eberhardsteiner, W. Winter, A. Fadaï, and M. Pöll, editors, *World Conference on Timber Engineering*, pages 1516–1523. TU Verlag, Vienna, 2016. doi:20.500.11850/333997. Available online: <https://infoscience.epfl.ch/record/221015> (accessed on January 2020).
- [23] A. Dias, J. Schänzlin, and P. Dietsch. *Design of timber-concrete composite structures A state-of-the-art report by COST Action FP1402/ WG 4*. Shaker Verlag GmbH, 2018. Available online: <https://www.costfp1402.tum.de/en/publications/> (accessed on January 2020).
- [24] P. Dietsch and S. Winter. Eurocode 5—Future Developments towards a More Comprehensive Code on Timber Structures. *Structural Engineering International*, 22(2):223–231, May 2012. doi:10.2749/101686612X13291382991001.
- [25] DIN 1052. Design of timber structures - General rules and rules for buildings. German Institute for Standardization.
- [26] Dold Holzwerke GmbH. Panneaux 3-plis et 5-plis, 2008. Available online: <http://doldholz.homepage.t-online.de/doldweb/images/stories/dold/franz.%20-%203-s%20prospekt%20mehrseiter.pdf> (accessed on January 2020).
- [27] F. Dubois, J.-M. Husson, N. Sauvat, and N. Manfoumbi. Modeling of the viscoelastic mechano-sorptive behavior in wood. *Mechanics of Time-Dependent Materials*, 16(4):439–460, Nov. 2012. doi:10.1007/s11043-012-9171-3.
- [28] C. Eastman. The use of computers instead of drawings in building design. *American Institute of Architects Journal*, 63:46–50, 01 1975. Available online: [https://www.researchgate.net/publication/234643558\\_The\\_Use\\_of\\_Computers\\_Instead\\_of\\_Drawings\\_in\\_Building\\_Design](https://www.researchgate.net/publication/234643558_The_Use_of_Computers_Instead_of_Drawings_in_Building_Design) (accessed on January 2020).
- [29] EN 12369-1:2001. Wood-based panels - Characteristic values for structural design - Part 1 : OSB, particleboards and fiberboards. European Committee for Standardization.
- [30] EN 16351:2015. Timber structures - Cross laminated timber - Requirements. European Committee for Standardization.
- [31] EN 1990:2003-03. Eurocode 0: Basis of structural design - Annex D - Design assisted by testing. European Committee for Standardization.
- [32] EN 1991-1-1:2003-03. Eurocode 1: Actions on structures - Part 1-1: Densities, self weight, imposed loads for buildings . European Committee for Standardization.

## Bibliography

---

- [33] EN 1995-1-1:2005. Eurocode 5: Design of timber structures - Part 1-1: General - Common rules and rules for buildings. European Committee for Standardization.
- [34] EN 1998-1:2005. Eurocode 8: Design of structures for earthquake resistance - Part 1: General rules, seismic actions and rules for buildings. European Committee for Standardization.
- [35] EN 26891:1991. Timber structures - Joints made with mechanical fasteners - General principles for the determination of strength and deformation characteristics. European Committee for Standardization.
- [36] EN 323:1993. Wood-based panels. Determination of density. European Committee for Standardization.
- [37] EN 408:2010. Timber structures - Structural timber and glued laminated timber - Determination of some physical and mechanical properties. European Committee for Standardization.
- [38] EN 789:2004. Timber structures - Test methods - Determination of mechanical properties of wood based panels. European Committee for Standardization.
- [39] ETA-08/0238. Solid wood slab element to be used as a structural element in buildings. Schilliger Holz-Industrie AG. European Technical Approval, 2018. Available online: <https://www.schilliger.ch/wp-content/uploads/2019/05/ETA-CLT-Schilliger-Holz-2018.pdf> (accessed on January 2020).
- [40] Facit Homes Limited<sup>®</sup>, London, England. Available online: <http://facit-homes.com> (accessed on January 2020).
- [41] A. O. Feio, P. B. Lourenço, and J. S. Machado. Testing and modeling of a traditional timber mortise and tenon joint. *Materials and Structures*, 47(1):213–225, Jan 2014. doi:10.1617/s11527-013-0056-y.
- [42] G. Finch, G. Marriage, M. Gjerde, and A. Pelosi. Experiments in timber space frame design: Fabrication, construction and structural performance. In *The 24th International Conference on Computer-aided Architectural Design Research in Asia (Caadria 2019)*, pages 153–162, 2019. Available online: [https://www.researchgate.net/publication/332567655\\_Experiments\\_in\\_Timber\\_Space\\_Frame\\_Design\\_Fabrication\\_Construction\\_and\\_Structural\\_Performance](https://www.researchgate.net/publication/332567655_Experiments_in_Timber_Space_Frame_Design_Fabrication_Construction_and_Structural_Performance) (accessed on January 2020).
- [43] W. Findley and F. Davis. *Creep and Relaxation of Nonlinear Viscoelastic Materials*. Dover Civil and Mechanical Engineering. Courier Corporation, 2013.
- [44] Forest Products Laboratory. *Wood handbook : wood as an engineering material*. U.S. Department of Agriculture, Forest Service, Forest Products Laboratory, 1999. doi:10.2737/FPL-GTR-113.

- 
- [45] M. Fragiaco. A finite element model for long-term analysis of timber-concrete composite beams. *Structural Engineering and Mechanics*, 20(2):173–189, 2005. doi:10.12989/sem.2005.20.2.173.
- [46] Fragiaco Massimo and Batchelar Mark. Timber Frame Moment Joints with Glued-In Steel Rods. II: Experimental Investigation of Long-Term Performance. *Journal of Structural Engineering*, 138(6):802–811, June 2012. doi:10.1061/(ASCE)ST.1943-541X.0000517.
- [47] J. Gamarro, J. F. Bocquet, and Y. Weinand. Vibration tests on interconnected timber elements using wood-wood connections. *Mendeley Data*, v1, 2019. doi:10.17632/hmc3bpwyw2.1.
- [48] J. Gamarro, J. F. Bocquet, and Y. Weinand. Dataset of the paper: Experimental investigations on the load-carrying capacity of digitally produced wood-wood connections. *Mendeley Data*, v1, 2020. doi:10.17632/trpf7c56cb.1.
- [49] J. Gamarro, I. Lemaître, and Y. Weinand. Mechanical Characterization of Timber Structural Elements using Integral Mechanical Attachments. In *World Conference on Timber Engineering*, Seoul, Republic of Korea, 2018.
- [50] J. Gattas and Z. You. Design and digital fabrication of folded sandwich structures. *Automation in Construction*, 63:79 – 87, 2016. doi:10.1016/j.autcon.2015.12.002.
- [51] S. Girardon. *Amélioration des performances mécaniques des assemblages bois sur bois vissés par préparation des interfaces : application à la réalisation d’éléments de structure*. PhD thesis, École Nationale Supérieure des Technologies et Industries du Bois, 2014. Available online: <http://www.theses.fr/2014LORR0188/document> (accessed on January 2020).
- [52] S. Girardon, C. Barthram, L. Resch, J.-F. Bocquet, and P. Triboulot. Determination of shearing stiffness parameters to design multi-layer spruce beams using welding-through wood dowels. *European Journal of Wood and Wood Products*, 72(6):721–733, Nov 2014. doi:10.1007/s00107-014-0834-4.
- [53] S. Girardon and J.-F. Bocquet. Mechanical behaviour of pre-stressed spruce timber–timber 2.5-mm-step grooved connections under shearing tests. *European Journal of Wood and Wood Products*, 75(5):719–727, Sep 2017. doi:10.1007/s00107-016-1135-x.
- [54] U. A. Girhammar. A simplified analysis method for composite beams with interlayer slip. *International Journal of Mechanical Sciences*, 51(7):515 – 530, 2009. doi:10.1016/j.ijmecsci.2009.05.003.
- [55] J. Glover, D. White, and T. Langrish. Wood versus Concrete and Steel in House Construction: A Life Cycle Assessment. *Journal of Forestry*, 100(8):34–41, 2002. doi:10.1093/jof/100.8.34.

## Bibliography

---

- [56] T. Gollwitzer and N. Gebbeken. A new Beam-Finite-Element for flexible bond in composite sections [Ein neues FEM-Stabelement für nachgiebige Verbundquerschnitte]. *Bautechnik*, 81(7):549–554, 2004. doi:10.1002/bate.200490126.
- [57] G. Granello and A. Palermo. Creep in timber: Research overview and comparison between code provisions. *New Zealand Timber Design Journal*, 27(2):6–22, 2019.
- [58] P. Gressel. Zur Vorhersage des langfristigen Formänderungsverhaltens aus Kurz-Kriechversuchen. *Holz als Roh- und Werkstoff*, 42(8):293–301, Aug. 1984. doi:10.1007/BF02608938.
- [59] M. Grosse, R. Hartnack, S. Lehmann, and K. Rautenstrauch. Modellierung von diskontinuierlich verbundenen Holz-Beton-Verbundkonstruktionen / Teil 1: Kurzzeittragverhalten. *Bautechnik*, 80(8):534–541, Aug. 2003. doi:10.1002/bate.200304120.
- [60] D. Guitard. *Mécanique Du Matériau Bois et Composites*. Cepadue Editions, Toulouse, 1987. ISBN: 2-85428-152-7.
- [61] L. Gustavsson, R. Madlener, H.-F. Hoen, G. Jungmeier, T. Karjalainen, S. Klöhn, K. Mahapatra, J. Pohjola, B. Solberg, and H. Spelter. The Role of Wood Material for Greenhouse Gas Mitigation. *Mitigation and Adaptation Strategies for Global Change*, 11(5):1097–1127, Sept. 2006. doi:10.1007/s11027-006-9035-8.
- [62] L. Gustavsson, K. Pingoud, and R. Sathre. Carbon Dioxide Balance of Wood Substitution: Comparing Concrete- and Wood-Framed Buildings. *Mitigation and Adaptation Strategies for Global Change*, 11(3):667–691, May 2006. doi:10.1007/s11027-006-7207-1.
- [63] L. Gustavsson and R. Sathre. Variability in energy and carbon dioxide balances of wood and concrete building materials. *Building and Environment*, 41(7):940–951, July 2006. doi:10.1016/j.buildenv.2005.04.008.
- [64] S. Hehl, T. Tannert, R. Meena, and T. Vallee. Experimental and Numerical Investigations of Groove Connections for a Novel Timber-Concrete-Composite System. *Journal of Performance of Constructed Facilities*, 28(6):A4014010, 2014. doi:10.1061/(ASCE)CF.1943-5509.0000549.
- [65] B. Heimeshoff. Zur berechnung von biegeträgern aus nachgiebig miteinander verbundenen querschnittsteilen im ingenieurholzbau. *Holz als Roh- und Werkstoff*, 45(6):237–241, Jun 1987. doi:10.1007/BF02616416.
- [66] M. Hoefft. *Zur Berechnung von Verbundträgern mit beliebig gefügtem Querschnitt*. PhD thesis, École Polytechnique Fédérale de Lausanne, Lausanne, 1994. doi:10.5075/epfl-thesis-1213.
- [67] C. Huet, D. Gittard, and P. Morlier. Le bois en structure, son comportement différé. *Annales de l'Institut Technique du Batiment et des Travaux Publics*, 1988.

- [68] W. Hufenbach, F. Adam, T. Heber, N. Weckend, F.-W. Bach, T. Hassel, and D. Zaremba. Novel Repair Concept for Composite Materials by Repetitive Geometrical Interlock Elements. *Materials*, 4(12):2219–2230, 2011. doi:10.3390/ma4122219.
- [69] R. D. Hunt and A. H. Bryant. Statistical implications of methods of finding characteristic strengths. *Journal of Structural Engineering*, 122(2):202–209, 1996. doi:10.1061/(ASCE)0733-9445(1996)122:2(202).
- [70] IPCC. 2018: Summary for Policymakers. In: *Global Warming of 1.5° C. An IPCC Special Report on the impacts of global warming of 1.5° above pre-industrial levels and related global greenhouse gas emission pathways, in the context of strengthening the global response to the threat of climate change, sustainable development, and efforts to eradicate poverty*. [Masson-Delmotte, V., P. Zhai, H.-O. Pörtner, D. Roberts, J. Skea, P.R. Shukla, A. Pirani, W. Moufouma-Okia, C. Péan, R. Pidcock, S. Connors, J.B.R. Matthews, Y. Chen, X. Zhou, M.I. Gomis, E. Lonnoy, T. Maycock, M. Tignor, and T. Waterfield (eds.)]. World Meteorological Organization, Geneva, Switzerland, 32 pp.
- [71] ISO 10137:2007. Bases for design of structures – serviceability of buildings and walkways against vibration. International Organization for Standardization.
- [72] ISO 554:1976. Standard atmospheres for conditioning and, or testing - Specifications. International Organization for Standardization.
- [73] ISO 6983-1:20092. Automation systems and integration - Numerical control of machines - Program format and definitions of address words - Part 1 : data format for positioning, line motion and contouring control systems. International Organization for Standardization.
- [74] A. Kenel. *Zur Berechnung von Holz/Beton-Verbundkonstruktionen : entwicklung und Vergleich verschiedener Berechnungsmethoden*, volume 115/42 of *Forschungs- und Arbeitsberichte / Abteilung 115, Holz, EMPA*. EMPA, Dübendorf, 2000.
- [75] H. Koch, L. Eisenhut, and W. Seim. Multi-mode failure of form-fitting timber connections – Experimental and numerical studies on the tapered tenon joint. *Engineering Structures*, 48:727–738, Mar. 2013. doi:10.1016/j.engstruct.2012.12.002.
- [76] F. F. P. Kollmann and W. A. Côté. *Principles of wood science and technology - I Solid Wood*, volume 1. Springer, 1968. doi:10.1007/978-3-642-87928-9.
- [77] P. Krawczyk. *Nonlinear analysis of layered structures with weak interfaces*. PhD thesis, École Polytechnique Fédérale de Lausanne, 2006. doi:10.5075/epfl-thesis-3554.
- [78] P. Krawczyk, F. Frey, and A. Zielinski. Large deflections of laminated beams with interlayer slips. *Engineering Computations*, 24(1):17–32., 2007. doi:10.1108/026444400710718556.

## Bibliography

---

- [79] H. Kreuzinger. Flächentragwerke: Platten, Scheiben, Schalen, Berechnungsmethoden und Beispiele. *Informationsdienst Holz, Brücken aus Holz*, pages 43 – 60, Nov. 1999.
- [80] H. Kreuzinger and H. J. Blass. Calculation models for prefabricated wood-based load bearing stressed skin panels for use in roofs. Technical Report TR 019, European Organisation for Technical Approvals, Feb. 2005.
- [81] O. D. Krieg, T. Schwinn, A. Menges, J.-M. Li, J. Knippers, A. Schmitt, and V. Schwieger. Biomimetic Lightweight Timber Plate Shells: Computational Integration of Robotic Fabrication, Architectural Geometry and Structural Design. In P. Block, J. Knippers, N. J. Mitra, and W. Wang, editors, *Advances in Architectural Geometry 2014*, pages 109–125. Springer International Publishing, Cham, 2015. doi:10.1007/978-3-319-11418-7\_8.
- [82] J. Köhler, J. D. Sørensen, and M. H. Faber. Probabilistic modeling of timber structures. *Structural Safety*, 29(4):255 – 267, 2007. doi:10.1016/j.strusafe.2006.07.007.
- [83] R. La Magna, M. Gabler, S. Reichert, T. Schwinn, F. Waimer, A. Menges, and J. Knippers. From nature to fabrication: Biomimetic design principles for the production of complex spatial structures. *International Journal of Space Structures*, 28:27–39, 2013. doi:10.1260/0266-3511.28.1.27.
- [84] R. La Magna, F. Waimer, and J. Knippers. Nature-inspired generation scheme for shell structures. In *Proceedings of the International Symposium of the IASS-APCS Symposium, Seoul, South Korea*, 2012. doi:10.18419/opus-105.
- [85] J. N. Lee and Q. Wu. Continuum modeling of engineering constants of oriented strandboard. *Wood and fiber science*, 35(1):24–40, 2007. Available online: <https://wfs.swst.org/index.php/wfs/article/viewFile/1844/1844> (accessed on January 2020).
- [86] Leitz. Leitz user lexicon. Lexicon Edition 6 (2011) p 428. Available online: <https://www.hoechsmann.com/en/lexikon/23836/Leitz-Anwenderlexikon> (accessed on January 2020).
- [87] M. Lenzen and G. Treloar. Embodied energy in buildings: wood versus concrete—reply to Börjesson and Gustavsson. *Energy Policy*, 30(3):249 – 255, 2002. doi:10.1016/S0301-4215(01)00142-2.
- [88] J.-M. Li and J. Knippers. Segmental Timber Plate Shell for the Landesgartenschau Exhibition Hall in Schwäbisch Gmünd—the Application of Finger Joints in Plate Structures. *International Journal of Space Structures*, 30(2):123–139, 2015. doi:10.1260/0266-3511.30.2.123.
- [89] P. Martin. *Etude du comportement des poutres lamellées clouées boulonnées en flexion*. PhD thesis, ENGREF (AgroParisTech), 2006. Available online: <https://pastel.archives-ouvertes.fr/pastel-00003306/> (accessed on January 2020).

- 
- [90] B. C. Michelfelder. *Structural and deformation behaviour of grooves in composites of nail-laminated board stacks and concrete*. PhD thesis, Institut für Konstruktion und Entwurf, University of Stuttgart, 2006. doi:10.18419/opus-249.
- [91] K. Möhler. Über einige Grundlagen und Entwicklungsmöglichkeiten des Holznagelbaues. *Holz als Roh- und Werkstoff*, 13(10):388–397, Oct. 1955. doi:10.1007/BF02605565.
- [92] K. Möhler. *Über das Tragverhalten von Biegeträgern und Druckstäben mit zusammengesetztem Querschnitt und nachgiebigen Verbindungsmitteln*. PhD thesis, Karlsruhe Institute of Technology, 1956.
- [93] P. Morlier. *Creep in Timber Structures*. Rilem Reports, No 8. Taylor & Francis, 2004.
- [94] E. S. Musselman, D. W. Dinehart, S. M. Walker, and M. L. Mancini. The effect of holes on the creep behavior and flexural capacity of laminated veneer lumber (lvl) beams. *Construction and Building Materials*, 180:167 – 176, 2018. doi:10.1016/j.conbuildmat.2018.05.186.
- [95] G.-J. Nabuurs, M. Lindner, P. J. Verkerk, K. Gunia, P. Deda, R. Michalak, and G. Grassi. First signs of carbon sink saturation in European forest biomass. *Nature Climate Change*, 3(9):792–796, Sept. 2013. doi:10.1038/nclimate1853.
- [96] J. Nässén, F. Hedenus, S. Karlsson, and J. Holmberg. Concrete vs. wood in buildings – An energy system approach. *Building and Environment*, 51:361 – 369, 2012. doi:10.1016/j.buildenv.2011.11.011.
- [97] J. Natterer. *Analyse non-linéaire des coques géodésiques multicouches à joints semi-rigides*. PhD thesis, École Polytechnique Fédérale de Lausanne, Lausanne, 2010. doi:10.5075/epfl-thesis-4499.
- [98] H. Neuhaus. *Lehrbuch des Ingenieurholzbaus*. Vieweg+Teubner Verlag, 1994. doi:10.1007/978-3-322-96714-5.
- [99] NF B51-032:1981. Laminated bonded wood - Test of compression shear. French Association for Standardization.
- [100] A. C. Nguyen. *A Structural Design Methodology for Freeform Timber Plate Structures Using Wood-Wood Connections*. PhD thesis, ENAC, Lausanne, 2020.
- [101] A. C. Nguyen, P. Vestartas, and Y. Weinand. Design framework for the structural analysis of free-form timber plate structures using wood-wood connections. *Automation in Construction*, 107:102948, 2019. doi:10.1016/j.autcon.2019.102948.
- [102] Norbord Europe, South Molton, England. Technical document for OSB type 4. Available online: [http://norbord.fr/downloads/documents/NORBORD\\_SterlingOSB-Zero\\_TechnischeBrochure\\_FR.pdf](http://norbord.fr/downloads/documents/NORBORD_SterlingOSB-Zero_TechnischeBrochure_FR.pdf) (accessed on January 2020).
- [103] NZS 3603:1993. Timber structures standard. Standards New Zealand.

## Bibliography

---

- [104] OECD. *Global Material Resources Outlook to 2060: Economic Drivers and Environmental Consequences*. OECD Publishing, Paris, Feb. 2019. doi:10.1787/9789264307452-en.
- [105] C. O’Loinsigh, M. Oudjene, E. Shotton, A. Pizzi, and P. Fanning. Mechanical behaviour and 3d stress analysis of multi-layered wooden beams made with welded-through wood dowels. *Composite Structures*, 94(2):313 – 321, 2012. doi:10.1016/j.compstruct.2011.08.029.
- [106] A.-M. Olsson, L. Salmén, M. Eder, and I. Burgert. Mechano-sorptive creep in wood fibres. *Wood Science and Technology*, 41(1):59–67, 2007. doi:10.1007/s00226-006-0086-5.
- [107] S.-J. Pang, J.-K. Oh, J.-S. Park, C.-Y. Park, and J.-J. Lee. Moment-carrying capacity of dovetailed mortise and tenon joints with or without beam shoulder. *Journal of Structural Engineering*, 137(7):785–789, 2011. doi:10.1061/(ASCE)ST.1943-541X.0000323.
- [108] M. A. Parisi and C. Cordié. Mechanical behavior of double-step timber joints. *Construction and Building Materials*, 24(8):1364–1371, 2010. doi:10.1016/j.conbuildmat.2010.01.001.
- [109] C. Pirazzi. *Zur Berechnung von Holzschalen in Brettrippenbauweise mit elastischem Verbundquerschnitt*. PhD thesis, École Polytechnique Fédérale de Lausanne, 2005. doi:10.5075/epfl-thesis-3229.
- [110] Python Software Foundation. Python Language Reference, version 2.7. Available online: <https://www.python.org> (accessed on January 2020).
- [111] A. R. Rad, Y. Weinand, and H. Burton. Experimental push-out investigation on the in-plane force-deformation behavior of integrally-attached timber through-tenon joints. *Construction and Building Materials*, 215:925 – 940, 2019. doi:10.1016/j.conbuildmat.2019.04.156.
- [112] M. H. Ramage, H. Burridge, M. Busse-Wicher, G. Fereday, T. Reynolds, D. U. Shah, G. Wu, L. Yu, P. Fleming, D. Densley-Tingley, J. Allwood, P. Dupree, P. Linden, and O. Scherman. The wood from the trees: The use of timber in construction. *Renewable and Sustainable Energy Reviews*, 68:333 – 359, 2017. doi:10.1016/j.rser.2016.09.107.
- [113] A. Ranta-Maunus. The viscoelasticity of wood at varying moisture content. *Wood Science and Technology*, 9(3):189–205, 1975. doi:10.1007/BF00364637.
- [114] S. Reichel and M. Kaliske. Hygro-mechanically coupled modelling of creep in wooden structures, Part I: Mechanics. *International Journal of Solids and Structures*, 77:28–44, 2015. doi:10.1016/j.ijsolstr.2015.07.019.
- [115] L. Resch. *Développement d’éléments de construction en bois de pays lamellés assemblés par tourillons thermo-soudés*. PhD thesis, École Nationale Supérieure des Technologies et Industries du Bois, 2009. Available online: <http://www.theses.fr/2009NAN10142> (accessed on January 2020).



- 
- [116] A. Rezaei Rad, J. Gamero, G. Ghion, and Y. Weinand. Initial experimental tests, setups, discussions and challenges for osb connections. Technical report, EPFL, 2016. Available online: <http://infoscience.epfl.ch/record/275873> (accessed on February 2020).
- [117] C. Robeller. *Integral Mechanical Attachment for Timber Folded Plate Structures*. PhD thesis, ENAC, Lausanne, 2015. doi:10.5075/epfl-thesis-6564.
- [118] C. Robeller. *Timber Plate Shell Structures: A Digital Resurgence of Traditional Joining Methods*, pages 1117–1133. Springer International Publishing, 2019. doi:10.1007/978-3-030-03676-8\_45.
- [119] C. Robeller, V. Helm, A. Thoma, F. Gramazio, M. Kohler, and Y. Weinand. Robotic integral attachment. *FABRICATE*, pages 92–97, 2017. Available online: <http://infoscience.epfl.ch/record/227410> (accessed on January 2020).
- [120] C. Robeller, M. A. Konakovic, M. Dedijer, M. Pauly, and Y. Weinand. A double-layered timber plate shell - computational methods for assembly, prefabrication, and structural design. *Advances in Architectural Geometry 2016*, 5:19. 104–122, 2016. doi:10.3218/3778-4\_9.
- [121] C. Robeller, P. Mayencourt, and Y. Weinand. Snap-fit joints - cnc fabricated, integrated mechanical attachment for structural wood panels. *ACADIA 2014 Design Agency: Proceedings of the 34th Annual Conference of the Association for Computer Aided Design in Architecture*, pages 189–198, 2014. Available online: <http://infoscience.epfl.ch/record/203065> (accessed on January 2020).
- [122] C. Robeller, S. S. Nabaei, and Y. Weinand. Design and fabrication of robot-manufactured joints for a curved-folded thin-shell structure made from clt. *Robotic Fabrication in Architecture, Art and Design 2014*, pages 67–81, 2014. doi:10.1007/978-3-319-04663-1.
- [123] C. Robeller, A. Stitic, P. Mayencourt, and Y. Weinand. Interlocking folded plate: Integrated mechanical attachment for structural wood panels. In *Advances in Architectural Geometry 2014*, pages 281–294. Springer International Publishing, 2015. doi:10.1007/978-3-319-11418-7\_18.
- [124] C. Robeller and Y. Weinand. Interlocking folded plate – integral mechanical attachment for structural wood panels. *International Journal of Space Structures*, 30(2):111–122, 2015. doi:10.1260/0266-3511.30.2.111.
- [125] C. Robeller and Y. Weinand. A 3d cutting method for integral 1dof multiple-tab-and-slot joints for timber plates, using 5-axis CNC cutting technology. In *Proceedings of the World Conference of Timber Engineering WCTE*, 2016. Available online: <https://infoscience.epfl.ch/record/222484> (accessed on January 2020).
- [126] C. Robeller and Y. Weinand. *Fabrication-Aware Design of Timber Folded Plate Shells with Double Through Tenon Joints*, pages 166–177. Springer International Publishing, Cham, 2016. doi:10.1007/978-3-319-26378-6\_12.

## Bibliography

---

- [127] S. Roche. *Semi-Rigid Moment-Resisting Behavior of Multiple Tab-and-Slot Joint for Freeform Timber Plate Structures*. PhD thesis, ENAC, Lausanne, 2017. doi:10.5075/epfl-thesis-8236.
- [128] S. Roche, J. Gamarro, and Y. Weinand. Multiple tab-and-slot joint : Improvement of the rotational stiffness for the connection of thin structural wood panels. In *Proceedings of the World Conference of Timber Engineering*, Vienna, 2016. doi:10.5075/epfl-ibois-221012.
- [129] S. Roche, G. Mattoni, and Y. Weinand. Rotational Stiffness at Ridges of Timber Folded-Plate Structures. *International Journal of Space Structures*, 30(2):153–167, 2015. doi:10.1260/0266-3511.30.2.153.
- [130] S. Roche, C. Robeller, L. Humbert, and Y. Weinand. On the semi-rigidity of dovetail joint for the joinery of lvl panels. *European Journal of Wood and Wood Products*, 73(5):667–675, Sep 2015. doi:10.1007/s00107-015-0932-y.
- [131] C. Sandhaas. *Mechanical behaviour of timber joints with slotted-in steel plates*. PhD thesis, Technische Universiteit Delft, 2012. Available online: <http://resolver.tudelft.nl/uuid:df5dbd8f-d19e-407d-aadd-48ad29a5fe97> (accessed on January 2020).
- [132] C. Sandhaas, A. K. Sarnaghi, and J.-W. van de Kuilen. Numerical modelling of timber and timber joints: computational aspects. *Wood Science and Technology*, 54:31–61, 2020. doi:10.1007/s00226-019-01142-8.
- [133] L. Sass. A wood frame grammar: A generative system for digital fabrication. *International Journal of Architectural Computing*, 4(1):51–67, 2006. doi:10.1260/147807706777008920.
- [134] L. Sass and M. Botha. The instant house: A model of design production with digital fabrication. *International Journal of Architectural Computing*, 4(4):109–123, 2006. doi:10.1260/147807706779399015.
- [135] W. Schelling. Die Berechnung nachgiebig verbundener, zusammengesetzter Biegeträger. *Ingenieurholzbau*, 1968.
- [136] W. Schelling. Zur Berechnung nachgiebig zusammengesetzter Biegeträger aus beliebig vielen Einzelquerschnitten. *Ingenieurholzbau in Forschung und Praxis*. Karlsruhe: Bruderverlag, pages 155–162, 1982.
- [137] C. Schindler. Information-Tool-Technology: Contemporary digital fabrication as part of a continuous development of process technology as illustrated with the example of timber construction. In *Proceedings of the 27th ACADIA Conference.*, Halifax, Canada, 2007. Available online: <https://documents.pub/document/information-tool-technology-contemporary-digital-fabrication-as-.html> (accessed on January 2020).

- 
- [138] T. Schmidt and H. J. Blass. Contact joints in engineered wood products. In *World Conference on Timber Engineering*, pages 1289–1296, Vienna, Austria, 2016.
- [139] T. Schmidt and H. J. Blass. Recent development in CLT connections part I: in-plane shear connection for CLT bracing elements under static loads. *Wood and Fiber Science*, 50(CLT Mass Timber):48–57, 2018. Available online: <https://wfs.swst.org/index.php/wfs/article/view/2635/2422> (accessed on January 2020).
- [140] T. Schmidt and H. J. Blass. Recent development in CLT connections part II: in-plane shear connections for CLT bracing elements under cyclic loads. *Wood and Fiber Science*, 50(CLT Mass Timber):58–67, 2018. Available online: <https://wfs.swst.org/index.php/wfs/article/view/2636/2423> (accessed on January 2020).
- [141] A. P. Schniewind. Recent progress in the study of the rheology of wood. *Wood Science and Technology*, 2(3):188–206, Sept. 1968. doi:10.1007/BF00350908.
- [142] A. P. Schniewind and J. D. Barrett. Wood as a linear orthotropic viscoelastic material. *Wood Science and Technology*, 6(1):43–57, Mar. 1972. doi:10.1007/BF00351807.
- [143] A. Scholz. *Ein Beitrag zur Berechnung von Flächentragwerken aus Holz*. PhD thesis, Technische Universität München, Dec. 2003. Available online: <https://mediatum.ub.tum.de/doc/601069/601069.pdf> (accessed on January 2020).
- [144] A. Scholz. Eigenspannungszustände an Verbundquerschnitten infolge von Dehnungsunterschieden– Anwendung eines neueren Rechenverfahrens auf einen bewährten Lösungsansatz. *Bautechnik*, 81(3):180–188, Mar. 2004. doi:10.1002/bate.200490042.
- [145] T. Schwinn, O. D. Krieg, and A. Menges. *Robotically Fabricated Wood Plate Morphologies*, pages 48–61. Springer Vienna, Vienna, 2013. doi:10.1007/978-3-7091-1465-0\_4.
- [146] SIA 265:2012. Timber Structures. Swiss society of engineers and architects.
- [147] J. Siem and A. Jorissen. Can traditional carpentry joints be assessed and designed using modern standards. In *International Conference on Structural Health Assessment of Timber Structures*, pages 9–11, 2015.
- [148] R. Sikkema, J. F. Dallemand, C. T. Matos, M. van der Velde, and J. San-Miguel-Ayanz. How can the ambitious goals for the EU’s future bioeconomy be supported by sustainable and efficient wood sourcing practices? *Scandinavian Journal of Forest Research*, pages 1–8, 2016. doi:10.1080/02827581.2016.1240228.
- [149] Sim[PLY] Building Framing System, Institute for Intelligent Materials, Systems and Environments, Clemson University School of Architecture, USA. Available online: [https://www.clemson.edu/centers-institutes/cuimse/02research/Materials/materials\\_projects/mat\\_01\\_simply.html](https://www.clemson.edu/centers-institutes/cuimse/02research/Materials/materials_projects/mat_01_simply.html) (accessed on January 2020).

## Bibliography

---

- [150] S. Smith. Wikihouse 4.0: Towards a smart future. In *IABSE Symposium Report*, volume 105, pages 1–6. International Association for Bridge and Structural Engineering, 2015.
- [151] W. Steffen, W. Broadgate, L. Deutsch, O. Gaffney, and C. Ludwig. The trajectory of the Anthropocene: The Great Acceleration. *The Anthropocene Review*, 2(1):81–98, 2015. doi:10.1177/2053019614564785.
- [152] H. Stehling, S. Fabian, and R. Jean. Bridging the gap from cad to cam: concepts, caveats and a new grasshopper plug-in. In *Proceedings of the FABRICATE conference*, Zurich, 2014. Available online: [https://www.jstor.org/stable/j.ctt1tp3c5w.10?seq=2#metadata\\_info\\_tab\\_contents](https://www.jstor.org/stable/j.ctt1tp3c5w.10?seq=2#metadata_info_tab_contents) (accessed on January 2020).
- [153] A. Stitic, A. C. Nguyen, A. Rezaei Rad, and Y. Weinand. Numerical simulation of the semi-rigid behaviour of integrally attached timber folded surface structures. *Buildings*, 9(2):55, 2019. doi:10.3390/buildings9020055.
- [154] T. Svilans, M. Tamke, M. R. Thomsen, J. Runberger, K. Strehlke, and M. Antemann. *New Workflows for Digital Timber*, pages 93–134. Springer International Publishing, 2019. doi:10.1007/978-3-030-03676-8\_3.
- [155] The DfMA Housing Manual. A general introduction to design for manufacture & assembly for homes, including design principles and procurement approaches. Technical report, Open Systems Lab<sup>®</sup>, 2019. Available online: <https://www.wikihouse.cc/Resources> (accessed on February 2020).
- [156] The Shift Project. *Décarbonons! : 9 propositions pour que l'Europe change d'ère*. Odile Jacob, Paris, 2017.
- [157] D. Thorby. 5 - damping. In D. Thorby, editor, *Structural Dynamics and Vibration in Practice*, pages 99 – 118. Butterworth-Heinemann, Oxford, 2008. doi:10.1016/B978-0-7506-8002-8.00005-5.
- [158] UNTC. Framework Convention on Climate Change. Adoption of the Paris Agreement, 21st Conference of the Parties, Paris: United Nations, 2015. Available online: [https://treaties.un.org/pages/ViewDetails.aspx?src=TREATY&mtds\\_g\\_no=XXVII-7-d&chapter=27&clang=\\_en](https://treaties.un.org/pages/ViewDetails.aspx?src=TREATY&mtds_g_no=XXVII-7-d&chapter=27&clang=_en) (accessed on January 2020).
- [159] M. Verbist, J. M. Branco, E. Poletti, T. Descamps, and P. B. Lourenço. Single Step Joint: overview of European standardized approaches and experimentations. *Materials and Structures*, 50(2), Apr. 2017. doi:10.1617/s11527-017-1028-4.
- [160] P. Vestartas, N. Rogeau, J. Gamero, and Y. Weinand. Modelling workflow for segmented timber shells using wood-wood connections. In C. Gengnagel, O. Baverel, J. Burry, M. Ramsgaard Thomsen, and S. Weinzierl, editors, *Impact: Design With All Senses*, pages 596–607, Cham, 2020. Springer International Publishing. doi:10.1007/978-3-030-29829-6\_46.

- [161] J. R. Villar-García, J. Crespo, M. Moya, and M. Guaita. Experimental and numerical studies of the stress state at the reverse step joint in heavy timber trusses. *Materials and Structures*, 51(1):17, 2018. doi:10.1617/s11527-018-1144-9.
- [162] M. Völz, J. Natterer, and T. Herzog. *Construire en bois*. Atlas de la Construction. Presses Polytechniques et Universitaires Romandes, 2ème éd., réimpr. edition, 1988.
- [163] VTT Technical Research Centre of Finland. Certificate No. 184/03 for structural laminated veneer lumber, 2004. Updated 17 May 2016. Available online: <https://www.metsawood.com/global/Tools/MaterialArchive/MaterialArchive/Kerto-VTT-C-184-03-Certificate.pdf> (accessed on January 2020).
- [164] Walter + Bai AG. Universal testing machine model LFV, 2020. Available online: [https://www.walterbai.com/page/products/Materials\\_Testing\\_Systems/Combined\\_Axial-Torsional\\_Testing\\_System/LFV\\_Series\\_Servohydraulic\\_Systems.php](https://www.walterbai.com/page/products/Materials_Testing_Systems/Combined_Axial-Torsional_Testing_System/LFV_Series_Servohydraulic_Systems.php) (accessed on January 2020).
- [165] WikiHouse Project, Open Systems Lab<sup>®</sup>, England. Available online: <https://www.wikihouse.cc> (accessed on January 2020).
- [166] J. Willmann, M. Knauss, T. Bonwetsch, A. A. Apolinarska, F. Gramazio, and M. Kohler. Robotic timber construction — Expanding additive fabrication to new dimensions. *Automation in Construction*, 61:16–23, Jan. 2016. doi:10.1016/j.autcon.2015.09.011.
- [167] B. Wisniewski and H. B. Manbeck. Residential floor systems: Wood i-joint creep behavior. *Journal of Architectural Engineering*, 9(1):41–45, 2003. doi:10.1061/(ASCE)1076-0431(2003)9:1(41).
- [168] X-Frame Limited<sup>®</sup>, New-Zealand. Available online: <https://x-frame.org> (accessed on January 2020).
- [169] B. Zhang, B. Rasmussen, A. Jorissen, and A. Harte. Comparison of vibrational comfort assessment criteria for design of timber floors among the european countries. *Engineering Structures*, 52:592 – 607, 2013. doi:10.1016/j.engstruct.2013.03.028.
- [170] Y. Zhang, H. Yao, C. Ortiz, J. Xu, and M. Dao. Bio-inspired interfacial strengthening strategy through geometrically interlocking designs. *Journal of the Mechanical Behavior of Biomedical Materials*, 15:70–77, 2012. doi:10.1016/j.jmbbm.2012.07.006.
- [171] E. Zhu, Z. Guan, P. Rodd, and D. Pope. A constitutive model for osb and its application in finite element analysis. *Holz Als Roh - Und Werkst*, 63:87–93, 2005. doi:10.1007/s00107-004-0513-y.
- [172] E. Zhu, Z. Guan, P. Rodd, and D. Pope. Finite element modelling of osb webbed timber i-beams with interactions between openings. *Advanced Engineering Software*, 36:797–805, 2005. doi:10.1016/j.advengsoft.2005.03.027.

## Bibliography

---

- [173] A. Štitić. *Integrally attached timber folded surface structures geometrical, experimental and numerical study*. PhD thesis, ENAC, Lausanne, 2017. doi:10.5075/epfl-thesis-8114.

# Julien Gamerro

TIMBER ENGINEERING · R&D · MANAGEMENT

Avenue de la Poste 18, 1020 Renens, Canton of Vaud, Switzerland

☎ (+41) 76-397-01-96 | ✉ julien.gamerro@gmail.com | 🌐 www.juliengamerro.com | 📱 juliengamerro | Orcid: 0000-0001-7802-5345

## Education

### University Degrees

#### EPFL (École Polytechnique Fédérale de Lausanne)

Lausanne, Switzerland

##### PHD CANDIDATE IN CIVIL AND ENVIRONMENTAL ENGINEERING

Sept. 2016 - Present

- Thesis: Development of Novel Standardized Structural Timber Elements Using Wood-Wood Connections.
- Supervisors: Prof. Y. Weinand and Dr. J. F. Bocquet.
- [www.epfl.ch/labs/ibois/](http://www.epfl.ch/labs/ibois/)

#### ENSTIB (École Nationale Supérieure des Technologies et Industries du Bois)

Epinal, France

##### MASTER IN ENGINEERING SCIENCES

Sept. 2013 - Sept. 2016

- Specialization: Timber engineering and Structural analysis.
- [www.enstib.univ-lorraine.fr/en/](http://www.enstib.univ-lorraine.fr/en/)

#### IAE Nancy - School of Management

Nancy, France

##### MASTER IN BUSINESS ADMINISTRATION - MBA

Sept. 2015 - Sept. 2016

- Program: Business law, management and marketing.
- [www.iae-nancy.univ-lorraine.fr](http://www.iae-nancy.univ-lorraine.fr)

### Technical Degrees

#### Apprenticeship in a timber company

Pringy, France

##### TIMBER CONSTRUCTION - BTEC HIGHER NATIONAL DIPLOMA

Sept. 2010 - Sept. 2012

- Performed tasks: carpenter, prefabrication (CAD/CAM), design and structural analysis of timber structures.

#### Les Compagnons du Tour de France

Seynod, France

##### YOUTH TRAINING IN CARPENTRY

Sept. 2009 - Sept. 2010

- One year apprenticeship to learn the carpentry trade.
- [www.compagnonsdutourdefrance.org](http://www.compagnonsdutourdefrance.org)

## Work Experience

#### NCCR Digital Fabrication

EPFL & ETHZ, Switzerland

##### PHD RESEARCHER

Nov. 2016 - Present

- The National Centre of Competence in Research Digital Fabrication is Switzerland's initiative to lead the development and integration of digital technologies within the field of architecture.
- Collaborative projects with other institutions and researchers on prefabrication possibilities and structural analysis of timber constructions.
- [www.dfab.ch](http://www.dfab.ch)

#### PopUp House

Aix-en-Provence, France

##### RESEARCH & DEVELOPMENT ENGINEER

Aug. 2015 - Mar. 2016

- PopUp House is an innovative research and design office specialized in the construction industry. Its aim is to build high-performance and well-insulated buildings effectively and efficiently. My work was to perform an in-depth analysis of the mechanical properties of this new timber construction system.
- [www.popup-house.com/en/](http://www.popup-house.com/en/)

#### EGP Bat

Annecy, France

##### ASSISTANT PROJECT MANAGER

Apr. 2015 - Jul. 2015

- Internship in a company specialized in project management of residential buildings.
- My duties were the organization and planning processes of concrete buildings sites.

#### Dunoyer / Labat & Sierra

Annecy, France

##### TIMBER CONSTRUCTION APPRENTICE

Sept. 2009 - Sept. 2012

- Duties included: Design, structural analysis, fabrication and site supervision of timber constructions projects.
- [www.dunoyer.com/](http://www.dunoyer.com/) [www.labat-et-sierra.com](http://www.labat-et-sierra.com)

## Skills

---

	Timber Engineering, Structural Analysis
<b>Specific Skills</b>	Design for Manufacture and Assembly (DfMA), Digital Fabrication
	Innovative structure, Sustainable constructions
<b>CAD &amp; CAM Softwares</b>	Cadwork, Rhinoceros
<b>Structural Analysis Softwares</b>	AcordBat, Abaqus, MD Bat
<b>Programming</b>	Python, Matlab, Gcode, Latex
<b>Languages</b>	French (Native), English (C1), Spanish (A1)

## Presentation

---

<b>International Conference on Computational Methods in Wood Mechanics</b>	<i>Linnaeus University, Växjö, Sweden</i>
SIMPLIFIED CALCULATION MODEL FOR INTERCONNECTED TIMBER ELEMENTS USING WOOD-WOOD CONNECTIONS	Jun. 2019
<b>European Cooperation in Science and Technology: COST FP1402 Workshop</b>	<i>ETHZ, Zürich, Switzerland</i>
FUTURE CHALLENGES AND NEED FOR RESEARCH IN TIMBER ENGINEERING	Oct. 2018
<b>European Cooperation in Science and Technology: COST FP1402 Workshop</b>	<i>TUM, Munich, Germany</i>
HOW WILL WE PLAN AND BUILD IN 25 YEARS AND HOW WILL THIS PROCESS BE REGULATED?	Sept. 2018
<b>World Conference on Timber Engineering (WCTE)</b>	<i>NIFOS, Seoul, South Korea</i>
MECHANICAL CHARACTERIZATION OF TIMBER STRUCTURAL ELEMENTS USING INTEGRAL MECHANICAL ATTACHMENTS	Aug. 2018
<b>8th International Wood Construction Forum</b>	<i>Dijon, France</i>
THE NEW VIDY THEATRE: AN INNOVATIVE TIMBER STRUCTURE	Apr. 2018

## Publications

---

<b>Le Pavillon en Bois du Théâtre de Vidy (fr)</b>	<i>Book</i>
BAUDRILLER, V., GAMERRO, J., JACCARD, M., ROBELLER, C., WEINAND, Y. (2017). "LE PAVILLON EN BOIS DU THÉÂTRE DE VIDY." PRESSES POLYTECHNIQUES ET UNIVERSITAIRES ROMANDES.	2017
<b>Experimental investigations on the load-carrying capacity of digitally produced wood-wood connections</b>	<i>Journal Paper</i>
GAMERRO, J., BOCQUET, J.F., WEINAND, Y. (2020). "EXPERIMENTAL INVESTIGATIONS ON THE LOAD-CARRYING CAPACITY OF DIGITALLY PRODUCED WOOD-WOOD CONNECTIONS." ENGINEERING STRUCTURES, 213, PP. 110576. DOI:10.1016/J.ENGSTRUCT.2020.110576	2020
<b>A Calculation Method for Interconnected Timber Elements Using Wood-Wood Connections</b>	<i>Journal Paper</i>
GAMERRO, J., BOCQUET, J.F., WEINAND, Y. (2020). "A CALCULATION METHOD FOR INTERCONNECTED TIMBER ELEMENTS USING WOOD-WOOD CONNECTIONS." BUILDINGS, 10, NO. 3: 61. DOI:10.3390/BUILDINGS10030061	2020
<b>Rotational mechanical behaviour of wood-wood connections with application to double-layered folded timber-plate structure</b>	<i>Journal Paper</i>
GAMERRO, J., ROBELLER, C., WEINAND, Y. (2018). "ROTATIONAL MECHANICAL BEHAVIOUR OF WOOD-WOOD CONNECTIONS WITH APPLICATION TO DOUBLE-LAYERED FOLDED TIMBER-PLATE STRUCTURE." CONSTRUCTION AND BUILDING MATERIALS. 165. PP. 434-442. DOI:10.1016/J.CONBUILDMAT.2017.12.178	2018



## Théâtre Vidy Lausanne - A Double-Layered Timber Folded Plate Structure

Journal Paper

ROBELLER, C., GAMERRO, J., WEINAND, Y. (2017). "THÉÂTRE VIDY LAUSANNE - A DOUBLE-LAYERED TIMBER FOLDED PLATE STRUCTURE." JOURNAL OF THE INTERNATIONAL ASSOCIATION FOR SHELL AND SPATIAL STRUCTURES. 58. PP. 295-314. DOI:10.20898/J.IASS.2017.194.864

2018

## Modelling Workflow for Segmented Timber Shells Using Wood-Wood Connections

Conference Paper

VESTARTAS, P., ROGEAU, N., GAMERRO, J., WEINAND, Y. (2020). "MODELLING WORKFLOW FOR SEGMENTED TIMBER SHELLS USING WOOD-WOOD CONNECTIONS", IN: GENGNAGEL, C., BAVEREL, O., BURRY, J., RAMSGAARD THOMSEN, M., WEINZIERL, S. (EDS.), IMPACT: DESIGN WITH ALL SENSES. SPRINGER INTERNATIONAL PUBLISHING, CHAM, PP. 596-607. DOI:10.1007/978-3-030-29829-6\_46

2019

## Mechanical Characterization of Timber Structural Elements Using Integral Mechanical Attachments

Conference Paper

GAMERRO, J., LEMAÎTRE I., WEINAND, Y. (2018). "MECHANICAL CHARACTERIZATION OF TIMBER STRUCTURAL ELEMENTS USING INTEGRAL MECHANICAL ATTACHMENTS." WORLD CONFERENCE ON TIMBER ENGINEERING, SEOUL, SOUTH KOREA.

2018

## Multiple Tab-and-Slot Joint : Improvement of the Rotational Stiffness for the Connection of Thin Structural Wood Panels

Conference Paper

ROCHE, S., GAMERRO, J., WEINAND, Y. (2016). "MULTIPLE TAB-AND-SLOT JOINT: IMPROVEMENT OF THE ROTATIONAL STIFFNESS FOR THE CONNECTION OF THIN STRUCTURAL WOOD PANELS." WORLD CONFERENCE ON TIMBER ENGINEERING.

2016

## Teaching

### Master's Project Supervision: Numerical modeling of timber joints

EPFL, Switzerland

NUMERICAL MODEL OF A TIMBER TAB-AND-SLOT JOINT

Fall 2019

- Student: Vincent Lestang
- Student University: EPFL

### Bachelor's Course

EPFL, Switzerland

DESIGN OF STRUCTURE

Fall 2018

- Teaching Assistant, lectures and exercises.

### Master Project's Supervision: Numerical modeling of timber structures

EPFL, Switzerland

MECHANICAL CHARACTERIZATION OF A PREFABRICATED ORTHOTROPIC SLAB MADE OUT OF OSB PANELS USING WOOD-WOOD CONNECTIONS

Spring 2017

- Student: Ingebrigt Lemaître
- Student University: ENSTA Paris Tech

## Scientific Committees, Editorials, and Societies

2019 **Member**, Restaurons Notre-Dame Association

Paris

2019 **Reviewer**, Construction and Building Materials journal

Elsevier

2018 **Participant**, COST Action FP1402 "Basis of Structural Timber Design" - from research to standards

TUM, Germany

## Grants

### Digital fabrication techniques for timber constructions / CHF 378 000

Swiss National Science Foundation

ACQUISITION OF A CUSTOM 5 AXIS COMPUTER NUMERICAL CONTROL (CNC) MACHINE

2019 – 2020

- Grant name: R'Equip
- Subside no: 205021\_189596 / 1
- R'Equip is aimed at researchers in Switzerland who need top-quality, innovative equipment for their research work. The SNSF awards grants for the acquisition and development of large-scale apparatuses in all areas of science.
- Manage the full grant application on the behalf of Prof. Weinand and Prof. Brühwiler for the Structural Engineering Group of EPFL.

## Extracurricular Activity

---

### Structural Engineering Group of EPFL

*Lausanne, Switzerland*

LABORATORY REPRESENTATIVE

*Jan. 2017 – Present*

- The Structural Engineering Group represents seven laboratories of the Civil Engineering Institute (IIC) of EPFL.
- I represent the chair of timber constructions to manage and invest in scientific equipment in order to perform high quality research.
- The Structural Engineering Platform offers a wide range of experimental facilities for testing structural materials and components at various scales (micrometers to meters) and under a large range of loadings (static and dynamic forces and displacement, temperature). It comprises at present four testing halls, four climatic rooms, and three workshops.

### Faculty Council ENAC EPFL

*Lausanne, Switzerland*

MEMBER

*Sept. 2018 – Present*

- The Council approves strategic proposals related to the education of Bachelors and Masters, research and planning of the faculty.
- Education (creation and suppression of diplomas, determination of educational evaluation methodology).
- Research (annual Report, Research general policy).
- Planification (Strategic planification, creation or closure of institutes or centers).
- Faculty policy and approval of nomination proposals according to each faculty policy.

### Lausanne Youth Support Center (CVAJ)

*Lausanne, Switzerland*

TEACHER

*Jan. 2017 – Jan. 2018*

- Teacher of children from 10 to 15 years old in basic sciences (mainly mathematics, physics, and biology).
- Member of this association serving children and young people in the canton of Vaud. Its complementary mission to public action aims to help promote support for children and young people.